DOE/ER-0313/73
ORNL/TM-2023/2934

FUSION MATERIALS
SEMIANNUAL PROGRESS REPORT
FOR THE PERIOD ENDING

December 31, 2022

Prepared for
DOE Office of Fusion Energy Sciences
(AT 60 20 10 0)

DATE PUBLISHED: May 2023

Prepared by
OAK RIDGE NATIONAL LABORATORY
Oak Ridge, Tennessee 37831
Managed by
UT-Battelle, LLC
For the
U.S. DEPARTMENT OF ENERGY

FOREWORD

This is the seventy-third in a series of semiannual technical progress reports on fusion materials science activity supported by the Fusion Energy Sciences Program of the U.S. Department of Energy. It covers the period ending December 31, 2022. This report focuses on research addressing the effects on materials properties and performance of exposure to the neutronic, thermal and chemical environments anticipated in the chambers of fusion experiments and energy systems. This research is a major element of the national effort to establish the materials knowledge base for an economically and environmentally attractive fusion energy source. Research activities on issues related to the interaction of materials with plasmas are reported separately.

The results reported are the products of a national effort involving a number of national laboratories and universities. A large fraction of this work, particularly in relation to fission reactor irradiations, is carried out collaboratively with partners in Japan, Russia, and the European Union. The purpose of this series of reports is to provide a working technical record for the use of program participants, and to provide a means of communicating the efforts of fusion materials scientists to the broader fusion community, both nationally and worldwide.

This report has been compiled by Stephanie Melton, Oak Ridge National Laboratory. Her efforts, and the efforts of the many persons who made technical contributions, are gratefully acknowledged.

Daniel Clark
Research Division
Office of Fusion Energy Sciences

TABLE OF CONTENTS

TABLE OF CONTENTS

TABLE OF CONTENTS

1. FERRITIC/MARTENSITIC STEEL DEVELOPMENT

1.1 X-RAY DIFFRACTION MICROSTRUCTURAL INVESTIGATION OF CNA SPECIMENS—D.J. Sprouster, L.L Snead (Stony Brook University), W. Zhong, Y. Yang (Oak Ridge National Laboratory)

OBJECTIVE

This work is a direct follow on from our previous Fiscal Year (FY) 20 and FY21 synchrotron characterization analysis of advanced steels for Fusion energy applications. In this report, we extend and demonstrate the utility of high-energy x-ray diffraction to identify and capture minor phases in a series of Castable nanostructured alloys (CNAs). Additional phases identified include $M_{23}C_6$ and MX. Subtle differences in the BCC host, MX and $M_{23}C_6$ precipitates were also apparent from the quantitative x-ray diffraction (XRD) results for the different alloys investigated. Changes in the XRD peak shape position, height, and full-width-at-half-maximum (FWHM), indicate changes in the atomic structure (lattice parameters) and microstructure (dislocation density, coherent grain size, weight fraction of minor phases). These results highlight that synchrotron based XRD is appreciably sensitive to the different microstructural features in CNAs with subtle variations in the starting powder and alloying elements and can be effectively employed to quantitatively extract changes in the atomic and microstructural features of both the BCC host and minor precipitate populations. Future work could include investigating the effects of mechanical deformation and elevated thermal treatments on the precipitate populations.

Experimental Procedure

The XRD measurements were performed at the National Synchrotron Light Source-II (NSLS-II) using the high-energy X-rays available at The Pair Distribution Function (PDF) beamline. All measurements were performed in transmission mode with an amorphous Silicon-based flat panel detector (Perkin-Elmer) mounted orthogonal to and centered on the beam path. The sample-to-detector distances and tilts of the detector relative to the beam were refined using a LaB_6 powder standard (National Institute of Standards and Technology [NIST] standard reference material 660c). The wavelength of the incident X-rays was 0.1665 Å (74.46 keV). The sample-to-detector distance was calculated to be 1000.44 mm. There were 600 XRD patterns collected with detector exposures of 0.1s. Specimens were vertically scanned to improve averaging, and to sample a large fraction of the individual specimens. All raw two-dimensional patterns were background corrected by subtracting a dark current image, and the air and Kapton scattering background within Igor Pro (Wavemetrics). Noticeable artefact regions of the detector (like the beam stop, dead pixels) were masked. The corrected and masked two-dimensional detector images were then radially integrated to obtain one-dimensional powder diffraction patterns.

Phase identification was performed using Match3! (Crystal Impact, Bonn, Germany). The background subtracted XRD patterns were Rietveld refined within the TOPAS software package. The peak profiles were modeled by a modified pseudo-Voigt function. The instrument contribution to the broadening of the measured profiles was quantified by fitting the LaB_6 NIST powder standard, with a known coherent grain size and negligible micro strain contribution. The Gaussian and Lorentzian-based broadening parameters were subsequently fixed during the analysis of the alloys under investigation to quantify the microstructure (coherent grain size, phase quantification and lattice parameters). The phase fraction, lattice parameter, and coherent grain size (CGS) components were allowed to vary for the different crystal phases present. The micro strain (μs) components for the $M_{23}C_6$ and MX phases were not included in the refinements. Therefore, the refined coherent grain size parameters of are lower limits.

Results

The XRD patterns for the four specimens are shown in Figure 1. The phases identified in the samples include MX (MN and/or MC), $M_{23}C_6$ and a minor FCC Fe phase in the CNA7 powder specimens. For The CNA7 and CNA8 specimens, the MX and $M_{23}C_6$ peaks are similar in position and height. The positions of the MX peaks from the phase identification are like VC, VN or TaC. Exact identification of the phase with the aid of alloy chemistry and electron microscopy is possible in the future. The CNA9 specimen only shows peaks from the MX and BCC phase. The quantitative phase analyses for all specimens are given in Table

1. The XRD analysis resulted in residual weights parameters (RWPs) less than 8%, indicative that he fits are of high quality. The microstructure, including lattice parameters, coherent grain size and micro strain are sample-dependent. The micro strain parameter is directly attributable to two-dimensional defects (such as dislocations), and the coherent grain size is the amount of defect free material (and is thus usually smaller than the grain size from SEM). The CNA7 is the least defective material (with lowest micro strain and highest coherent grain size). The lattice parameters show subtle variations among the different specimens and is potentially related to the processing/alloy chemistry. The weight fraction of the MX phase is consistent across the sample set, potentially due to strong scattering associated with the TaC phase used in the Rietveld refinements. This phase could be re-refined with a different structure based on alloy chemistry and electron microscopy results. The $M_{23}C_6$ phase fraction increases slightly from 1.2 % in CNA7 to ~1.8 % CNA8. It is interesting to note that the microstructural based broadening (μs) for CNA8 and CNA9 specimens is similar, indicative that the dislocation microstructures are potentially similar. Comparing to Transmission Electron Microscopy (TEM) results is a logical next step.

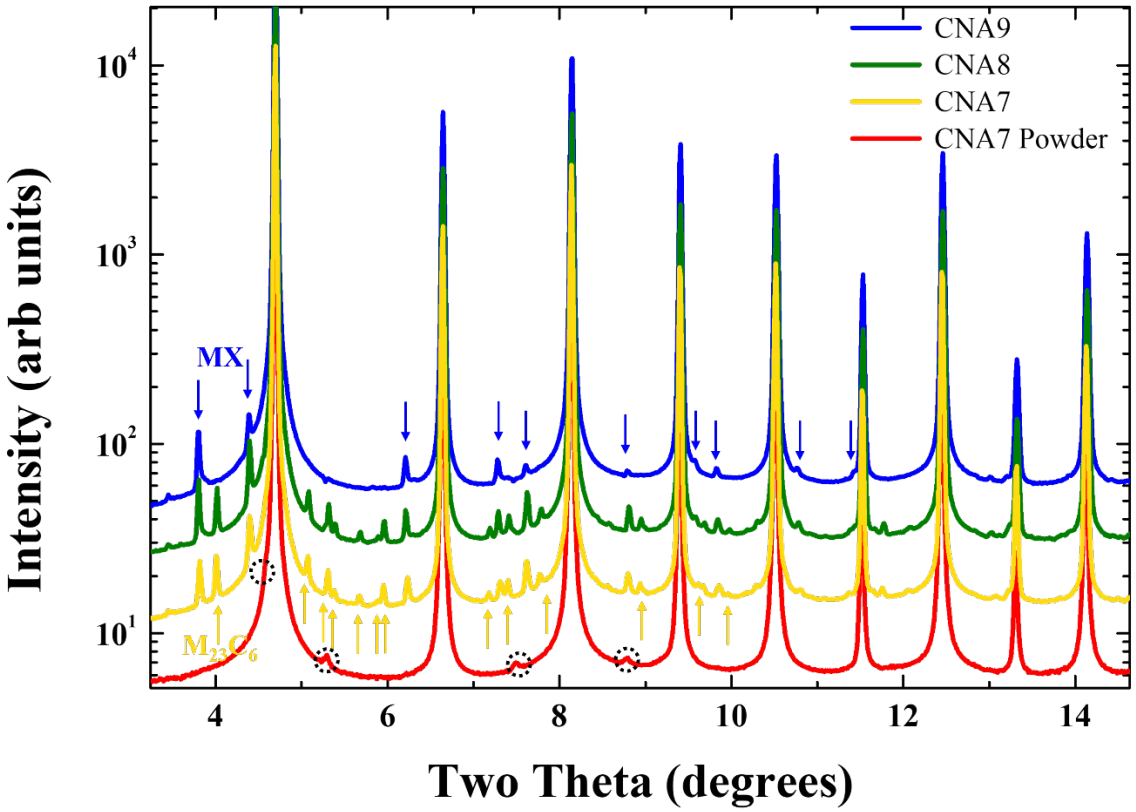

Figure 1. The XRD patterns for the four CNA specimens. The multiple phases identified for reference are labelled with Blue (MX) and yellow ($M_{23}C_6$) arrows and broken black circles (FCC Fe).

Table 1. Results from quantitative XRD analysis. CGS is coherent grain size, us is the XRD-based micro strain

Sample	Phase	a		CGS		μs		Wt.		R_{wp}
		(Å)		(nm)		(-)		(%)		(%)
CNA7 Powder	BCC	2.87328	0.00003	152.3	5.6	0.224	0.005	99.7	0.7	6.0
	FCC	3.60518	0.00301	15.0	6.0			0.3	0.1	
CNA7	BCC	2.87162	0.00002	744.6	52.0	0.174	0.003	98.7	0.1	5.1
	$M_{23}C_6$	10.62679	0.00114	42.6	5.7			1.2	0.1	
	MX	4.32613	0.00104	40.3	7.8			0.1	0.1	
CNA8	BCC	2.86968	0.00003	565.0	43.0	0.228	0.003	98.1	0.2	5.6
	$M_{23}C_6$	10.61027	0.00142	52.3	8.2			1.8	0.1	
	MX	4.33942	0.00077	61.7	3.0			0.1	0.1	
CNA9	BCC	2.87007	0.00003	531.2	39.0	0.243	0.003	99.8	0.2	6.0
	MX	4.34253	0.00092	45.1	8.7			0.1	0.1	

Conclusion

The nm-scale phases in a series of CNA specimens were quantitively captured from the XRD analysis. The minor MX and $M_{23}C_6$ phases were the best match to experimental data. The comparison with TEM results is a potential next step to uncover the effects of processing on the precipitates in the castable alloys. Collection of 2D XRD patterns for a series of specimens from extruded rods and plates were collected at the NSLS-II in later 2022. Analysis of the 2D mapping results, utilizing dedicated analysis scripts will continue in next quarter, to quantify the size and fraction of the MX and $M_{23}C_6$ precipitates as a function of heat treatment and position. Subtle atomic and microstructural differences were quantified for the different CNA specimens.

Acknowledgements

The work was funded under Grant DE-SC0018332 to the Research Foundation at State University of New York, Stony Brook by the United States Department of Energy (DOE) Office of Fusion Energy Sciences. Use of the 28-ID-1 (PDF) beamline at the NSLS-II, Brookhaven National Laboratory, was supported by the DOE under Contract No. DE-SC0012704.

1.2 THERMOMECHANICAL PROCESSING FOR IMPROVED MECHANICAL PROPERTIES OF Fe-12Cr FERRITIC-MARTENSITIC STEELS—T.S. Byun, D.A. Collins (Oak Ridge National Laboratory)

OBJECTIVE

The high-chromium ferritic-martensitic (FM) steels such as Fe-12Cr alloys have been considered as candidate materials for high-temperature reactor applications. This research is to investigate the effects of modified heat treatments to improve mechanical properties of the existing alloys without significant compositional change. In this work, the high chromium steels were rapidly quenched and tempered in a variety of conditions and tensile properties were evaluated.

SUMMARY

Normalizing, quenching, and tempering are the final heat treatment stages of thermomechanical processing (TMP) for the FM steels including the test materials (i.e., Fe-12Cr-1MoWV steels). It was attempted to produce a quenched and tempered martensitic structure with ultrafine laths and precipitates by combining rapid quenching and nontraditional tempering treatments, which was guided by phase stability data from thermodynamics calculation. Mechanical test results show that both the strength and ductility of the steels vary widely depending on processing route, particularly on the degree of tempering. Some tailored TMP routes, combining rapid quenching and limited tempering, significantly increased their strength to a level comparable to those of the nano-oxide strengthened ferritic alloys.

PROGRESS AND STATUS

Experimental Procedure

To evaluate the effects of thermomechanical treatments on the microstructural and mechanical characteristics, two 12Cr-1MoVW alloys (HT9 or HT9-modified steels) were selected and thermomechanically treated in various conditions. Table 1 lists the chemical compositions of these alloys, where it is noted that the Fe-12Cr heat-4 is a N-doped version of the standard Fe-12Cr steel (Heat-3). The starting materials of ~10.5 mm thick plates were produced by the traditional TMP for Fe-12Cr materials.

Table 1. Chemical compositions of Fe-12Cr ferritic-martensitic steels with and without N addition (in wt.%)

Material	Fe	Cr	Mn	Mo	Ni	W	V	Si	C	N
Fe-12Cr Heat-3	Bal.	11.07	0.55	1.0	0.51	0.47	0.3	0.25	0.2	0.001
Fe-12Cr Heat-4	Bal.	11.42	0.56	1.0	0.52	0.48	0.3	0.26	0.2	0.044

Table 2 lists the heat treatment routes designed for this research, which include various combinations of different after-quench treatments. Thin (2.5–4 mm) coupons were produced via hot rolling after normalizing at 1100°C for 30 min and used for the final heat treatments to achieve a high cooling rate of 100°C/s or higher, which can produce a nanoscale martensitic lath structure in quenching. In the last step, we attempted to reduce the degree of tempering, from the traditional full tempering, to yield finer precipitates within the ultrafine lath structure from rapid quenching so that both higher strength and fracture toughness could be achieved. The tempering processes include both single-step and double-step tempering treatments, after the same normalization and water quenching treatment.

Table 2. Various thermomechanical processing routes that have been used in this research

#	TMP Route	Normalization + Quenching	Tempering-1	Tempering-2
1	#AR (As Rolled)	1100°C/30 min & Hot Rolling	None	None
2	#WQ (Water Quench)	1070°C/1h & WQ	None	None
3	#WQ-300°C	1070°C/1h & WQ	300°C/1h & AC	None
4	#WQ-400°C	1070°C/1h & WQ	400°C/1h & AC	None
5	#WQ-500°C	1070°C/1h & WQ	500°C/1h & AC	None
6	#WQ-600°C	1070°C/1h & WQ	600°C/1h & AC	None
7	#WQ-650°C	1070°C/1h & WQ	650°C/1h & AC	None
8	#WQ-750°C	1070°C/1h & WQ	750°C/1h & AC	None
9	#WQ-300°C-650°C	1070°C/1h & WQ	300°C/1h & AC	650°C/0.5h & AC
10	#WQ-400°C-650°C	1070°C/1h & WQ	400°C/1h & AC	650°C/0.5h & AC
11	#WQ-500°C-650°C	1070°C/1h & WQ	500°C/1h & AC	650°C/0.5h & AC
12	#WQ-600°C-650°C	1070°C/1h & WQ	600°C/1h & AC	650°C/0.5h & AC
13	#WQ-300°C-750°C	1070°C/1h & WQ	300°C/1h & AC	750°C/0.5h & AC
14	#WQ-400°C-750°C	1070°C/1h & WQ	400°C/1h & AC	750°C/0.5h & AC
15	#WQ-500°C-750°C	1070°C/1h & WQ	500°C/1h & AC	750°C/0.5h & AC
16	#WQ-500°C-650°C-S	1070°C/1h & WQ	500°C/1h & AC	750°C/0.25h & AC
17	#WQ-600°C-750°C	1070°C/1h & WQ	600°C/1h & AC	750°C/0.5h & AC
18	#WQ-600°C-750°C-S	1070°C/1h & WQ	600°C/1h & AC	750°C/0.25h & AC

Note that the # in front of the TMP routes indicates the heat number (i.e., the number 3 & 4 will indicate the Heat-3 and Heat-4, respectively).

Uniaxial tensile testing was performed using the SS-3 specimens for the two Fe-12Cr steels after various heat treatments, including rapid water quenching and one-step or two-step tempering (see Table 2). Tensile testing was conducted at 25, 200, 300, 400, 500, and 600°C in a screw-driven testing machine equipped with an elevated temperature furnace at a displacement rate of 0.5 mm/min, which corresponds to a nominal strain rate of 0.0011/sec.

Tensile Strength and Ductility

The strength data of the Fe-12Cr steels after various TMP routes are compiled in the yield stress (YS) versus test temperature plots in Figures 1 and 2. As commonly observed in the phase transformable ferritic steels, a wide range of strengths were measured depending on their thermal processing route, on the degree of tempering. Among the room-temperature data, the highest YS was found in the as-rolled (AR) condition: about 1320 MPa and 1470 MPa for the Fe-12Cr heat-3 and heat-4, respectively. It is notable that both alloys before tempering or after single tempering below 600°C can demonstrate yield stresses above the 1 GPa mark. Further, low-temperature tempering treatments resulted in the YS values higher than those of the as-quenched materials.

The two-step tempering treatments with the 650°C/0.5h and 750°C/0.5h final tempering resulted in the strength data in a narrow range in respective alloys. These strength data are also close to those after single tempering, respectively, at 650°C and 750°C for 1 hour, which indicates that the final tempering temperature is the single most key factor controlling the strength of Fe-12Cr steels as far as the duration of tempering is long enough for near equilibrium (i.e., 0.5 h and 1 h). Such a strong tempering temperature effect on strength may also confirm that the traditional tempering at ~750°C is more than enough for inducing proper tempering effect because the high internal residual stress in the rapid-quenched microstructure can provide more free energy for precipitation and stress-relaxation. Indeed, the tempering at lower temperature or 650°C for 1 hour has induced enough degree of tempering effect: a high strength can be obtained without losing significant ductility.

It is also worth noting that the effect of elevated temperature (750°C) tempering is stronger in the Fe-12Cr heat-3 than in the heat-4 as shown in the different YS ranges, e.g., ~600 MPa versus 440–520 MPa, respectively, for heat-3 and heat-4 at room temperature. Overall, the Fe-12Cr heat-4 demonstrates a larger range of strength for the same variety in the TMP route, and addition of nitrogen lowers the strength of Fe-12Cr steel in certain conditions. The origin of such strength changes with N-doping is not well understood at the moment, and hence the pursuit of a thorough understanding on the effect of nitrogen addition will require further efforts, including an investigation on the role of nitrogen in the austenite formation below the calculated A3 temperature as well as in the total amount of precipitates formed and dissolved during the heat treatment routes.

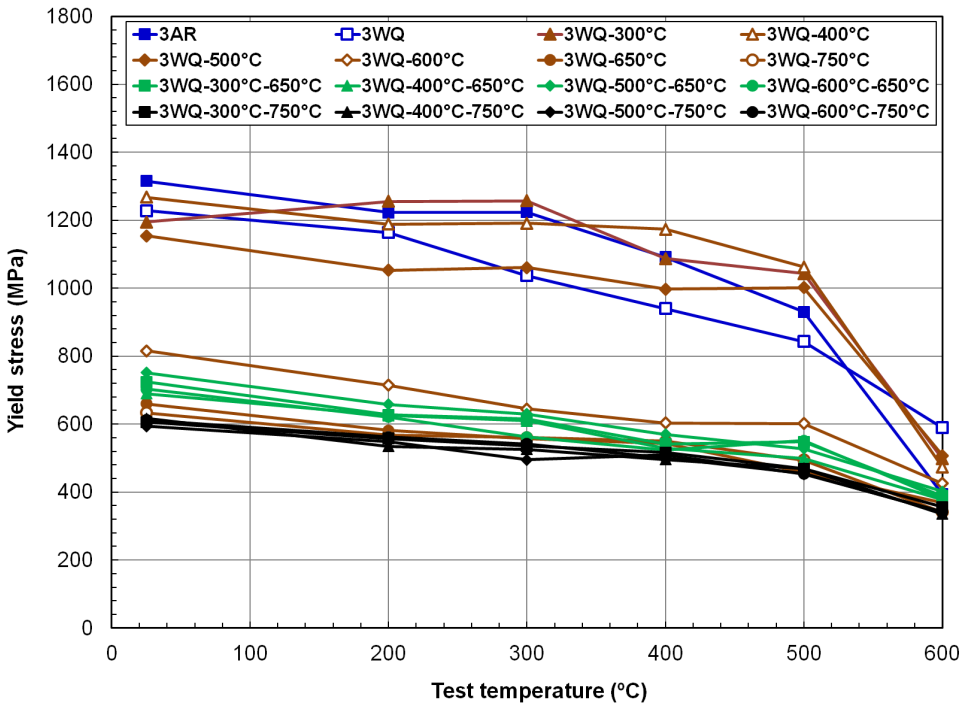

Figure 1. Temperature dependence of yield stress in Fe-12Cr steel heat-3 (low N) after various thermal treatment routes.

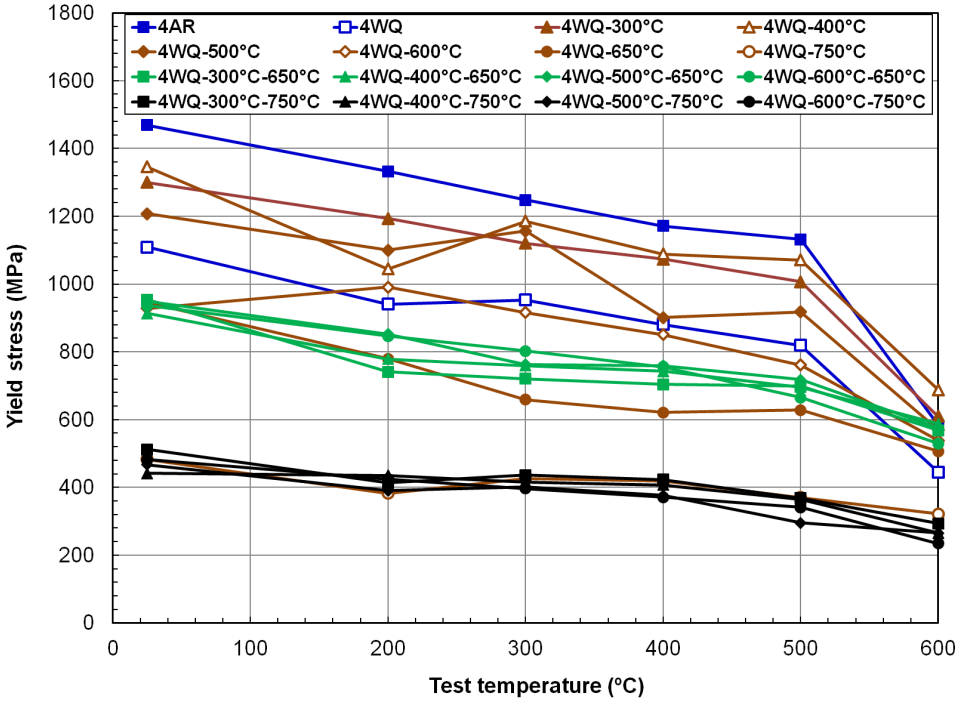

Figure 2. Temperature dependence of yield stress in Fe-12Cr steel heat-4 (high N) after various thermal treatment routes.

The temperature dependence of ductility for the two Fe-12Cr steels is summarized in Figures 3 and 4, respectively, for the total elongation (TE) data of heat-3 and heat-4 specimens. In contrast to the monotonic temperature dependence of YS, the ductility parameter show complex temperature dependencies as their temperature dependence depends strongly on processing route and hence on the strength of the materials. In general, the rankings of room temperature (RT) strengths are reversed in the ductility parameter, and their temperature dependence curves form either a monotonically decreasing line, a curve with maximum or a curve with minimum over the test temperature range. As the total elongation of an alloy represents its ability to resist failure, a temperature dependence curve of TE data can display significantly different behavior from that of uniform ductility. That is, the total ductility might represent more practical ductility characteristics of ferritic-martensitic steels since these steels usually absorb more plasticity in the necking deformation than in the uniform deformation and the TE data include both necking and final fracture information. The ductility data in Figures 3 and 4 confirm, therefore, that, except for the near-embrittled case (3WQ at RT), all processing routes attempted can obtain at least 5% TE and the vast majority more than 10% TE. Notably, the TE values at the highest test temperature of 600°C are as high as those at RT, with majority falling in the range of 16–18% for the heat-3 and 10–20% for the heat-4.

Another behavior of TE is the formation of clear ductility minimum in its temperature dependence curve. Except for the less tempered conditions (i.e., AR, WQ, WQ-300°C, or WQ-400°C), which resulted in very low TE at low temperatures < 300°C, the TEs of both Fe-12Cr steels have respectively high elongations at room temperature, i.e., 12–20%, and they decrease with temperature to form minimum at 400±100°C, and then increase with temperature, forming U shape curves. This ductility behavior having a minimum point is believed to be caused by the dynamic strain aging (DSA) phenomenon. With the DSA dislocation movements can be less glissile because of the repeated pinning–unpinning motions by interstitial atoms, primarily by carbon atoms, which results in reduction of ductility and toughness in metallic materials. Such an agreement on the DSA effect occurring at ~400°C in multiple HT9 alloys indicates that it is a fundamental phenomenon that might be controlled by the key steel elements such as iron and carbon (and nitrogen).

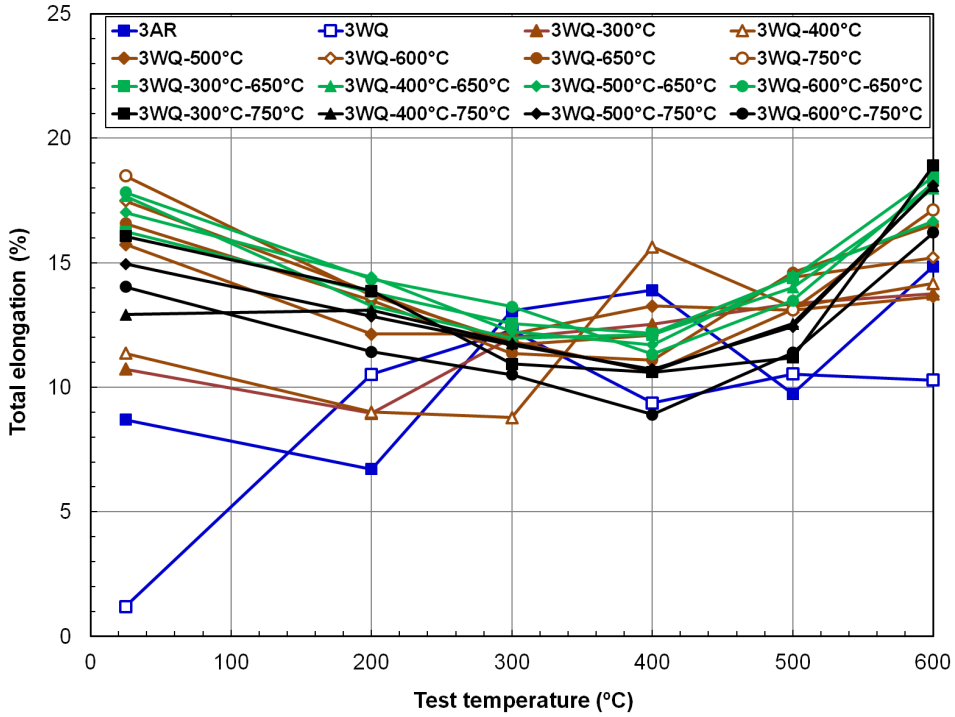

Figure 3. Temperature dependence of total elongation in Fe-12Cr steel heat-3 (low N) after various thermal treatment routes.

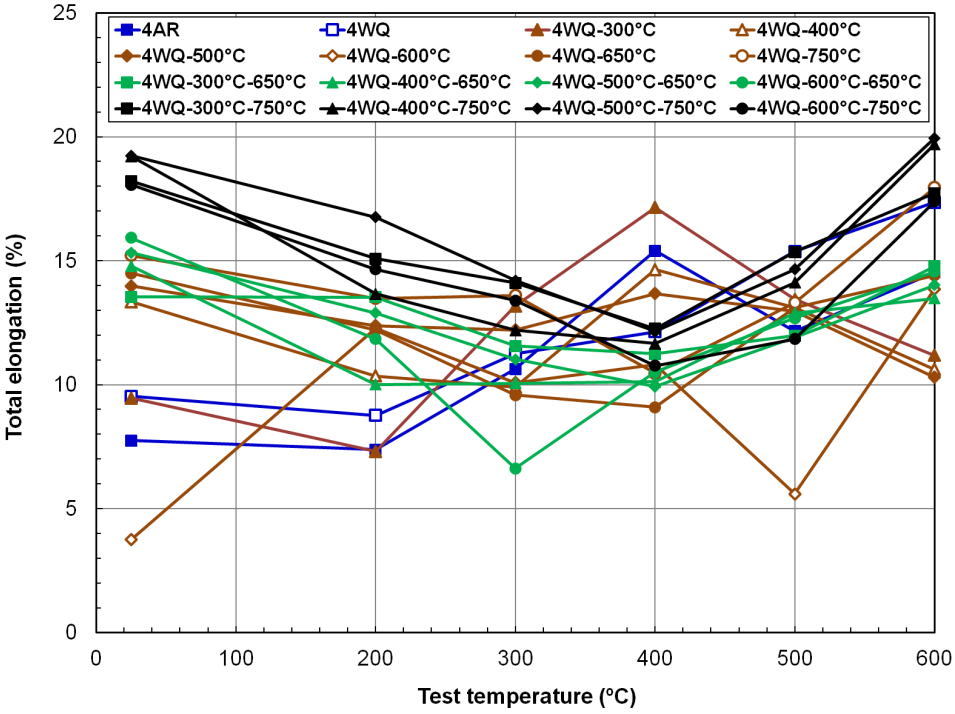

Figure 4. Temperature dependence of total elongation in Fe-12Cr steel heat-4 (high N) after various thermal treatment routes.

Results

A wide range of strength was measured from the Fe-12Cr alloys depending on thermomechanical processing route, on the degree of tempering. It is notable that the Fe-12Cr alloys before tempering or after single tempering below 600°C can achieve ultrahigh yield stresses above the 1 GPa mark. The final tempering temperature turned out to be the single most key factor for controlling the strength of the FM steels. The total ductility of the alloys (TE) showed complex behavior as their temperature dependence relied on processing route, and thus on the strength of the materials. It was concluded that the strength of Fe-12Cr can be conveniently controlled by modification of TMP route with retaining a reasonable amount of ductility.

The mechanical properties of the Fe-12Cr alloys, including fracture toughness over low-to-high temperature range, will be analyzed to determine an optimized TMP route for the high-chromium steels. The results will provide guidance in application of 12Cr steels to fusion reactor technologies and in TMP development for other FM steels.

Acknowledgement

This research was supported by the United States Department of Energy (US DOE), Fusion Materials Program at Oak Ridge National Laboratory (ORNL), under contract DE-AC05-00OR22725 with UT-Battelle, LLC. The prior alloy development and testing effort was sponsored by the former US DOE's Nuclear Energy Program.

1.3 PERFORMANCE EVALUATION OF MODIFIED 3Cr-3WVTa BAINITIC STEELS—Y. Yamamoto (Oak Ridge National Laboratory)

OBJECTIVE

This work aims to evaluate the advantages in the mechanical performance of newly proposed, modified 3Cr-3WVTa bainitic steels developed at Oak Ridge National Laboratory (ORNL). The proposed steel was designed to eliminate the need for post-weld heat treatment (PWHT), as well as providing improved mechanical properties of both base metal and weldments compared to those of existing commercial bainitic steels or ferritic-martensitic (FM) steels. The target applications are high-temperature structural components in fusion reactors, such as helium-cooled vacuum vessels operating up to 450°C and blanket support structures operating up to 550°C.

SUMMARY

Optimization of thermomechanical treatment (TMT) was applied to the modified 3Cr-3WVTa steel to target the refinement of prior-austenite grains (PAG). New TMT process achieved an average PAG size less than 100 μm. A significant improvement of the base metal creep-rupture performance was observed in the process-optimized steel with doubled creep-rupture life at 550°C and 295MPa in the normalized-and-tempered condition. The creep-rupture performance evaluation of the as-normalized condition has also been initiated. The process-optimized steel achieved significant improvements of the creep strength with >34% in the base metal and >20% across the weldments to date. Charpy impact toughness tests indicated that the weld metal exhibited low ductile-brittle transition temperature (DBTT), -45°C in the as-welded condition. On the other hand, the base metal DBTT was above room-temperature 55°C.

PROGRESS AND STATUS

A compositionally modified 3Cr-3WVTa bainitic ferritic steel (Mod. 3Cr-3WVTa steel, ID: MLC02T) was proposed with an advanced alloy design to achieve a reduced property inhomogeneity across the weldment in as-welded condition, targeting a PWHT-free bainitic ferritic steel for fusion structural applications. The nominal compositions of the original and modified steels are summarized in Table 1. Initial property evaluation of the modified steel suggested that the as-normalized MLC02T exhibited an improved room-temperature impact toughness compared to as-tempered, opposite to the response in typical low-alloyed bainitic steels. Based on the initial results, the focus of systematic performance evaluation has been shifted to the as-normalized condition. In addition, a refinement of the PAG was conducted through optimization of thermomechanical treatments as well as normalization temperature, as reported previously, targeting the improved room-temperature mechanical properties including both tensile and toughness. The present report summarizes the progress of property evaluation of MLC02T with the refined PAG in the as-normalized condition.

Table 1. Nominal composition of 3Cr-3WVTa base bainitic steels (balanced Fe)

Name	Alloy composition, wt.%	Remarks
MLC02T	3Cr-3W-0.2V-0.16Si-2.0Mn-0.1Ta-0.05C	Modified (newly proposed)
Original	3Cr-3W-0.2V-0.16Si-0.4Mn-0.1Ta-0.1C	Require PWHT, proposed in 1990's [ref.]

[ref.] R.L. Klueh et al., Int. J. Pressure Vessels and Piping, 84 (2007) 29-36.

A cast ingot of MLC02T, produced through vacuum-induction-melting, was homogenized at 1200°C, followed by hot-rolling and normalization at 1000°C to prepare an as-normalized plate with ~15 mm thickness and average PAG size of ~40 μm. A small piece was sectioned from the plate which applied tempering at 700°C to compare the mechanical performance with and without tempering. Uni-axial tensile creep-rupture tests of the base metal in the as-normalized and normalized-and-tempered conditions were conducted at 500 and 550°C. A part of the as-normalized plate was machined to have a single V groove

and then applied a gas tungsten arc weld (GTAW) with a compositionally matched weld filler metal strip. The creep-rupture performance across the weldment was also evaluated at 500 and 550°C.

Four creep-rupture tests at 500 and 550°C of the as-normalized MLC02T base metal with refined PAG and as-welded GTAW specimens are currently in progress, as summarized with Larson-Miller Parameter (LMP) in Figure 1a. The creep-rupture strength of the as-normalized base metal showed 34-38% improvement to date compared to that of previously evaluated MLC02T (normalized at 1100°C + tempered). Direct comparison of the creep-rupture curves of the normalized-and-tempered MLC02T evaluated at 550°C and 295MPa (Figure 2a) indicated an apparent improvement of creep-deformation resistance by applying normalization at 1000°C, followed by tempering, with more than double creep-rupture life compared to the previously tested specimens. The test of the as-normalized material (A) is in progress and now its tertiary creep regime after >12,000h testing, expecting significantly longer creep-rupture life than the tempered material. Two creep-rupture tests at 500°C/475MPa and 550°C/275MPa of the cross-weld MLC02T specimens in the as-GTAW condition are also in progress (Figure 2b). They have been testing for more than 2,500 h and 3,500 h, respectively, which are still in the secondary creep regime. By comparing with previously evaluated cross-weld properties with non-optimized base metal, the creep strength of the present weldment exhibited ~21% improvement (Figure 1), indicating the effectiveness of the process optimization of the modified 3Cr-3WVTa steel in the creep performance of both base metal and the weldment.

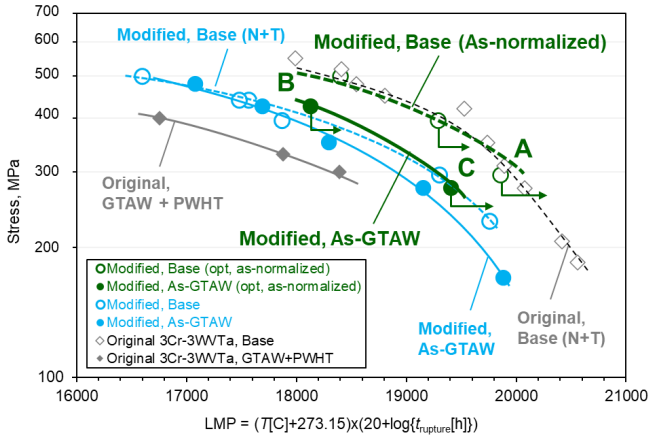

Figure 1. The LMP plot of newly processed modified 3Cr-3WVTa steel base metal and as-GTAW specimens, comparing with previously evaluated materials.

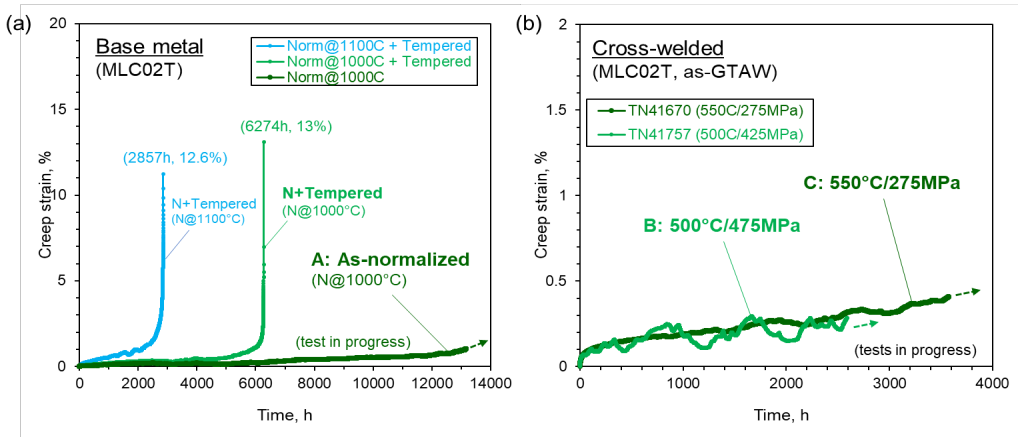

Figure 2. (a) creep-rupture curves of the modified 3Cr-3WVTa steel before and after re-normalization at 1,000°C, evaluated at 550°C and 295MPa, and (b) creep curves of cross-weld MLC02T specimens evaluated at 500°C/475MPa and 550°C/275MPa.

Charpy impact toughness of the weld metal in the as-GTAW condition revealed the room-temperature (RT) absorbed energy of more than 300J, together with a low DBTT -45°C. The results imply the proposed alloy design will be effective for improvement of the impact toughness of the weld metal in the as-welded condition, as opposed to the weld metal of the original 3Cr-3WVTa steel or any other typical steel weldments. On the other hand, the as-normalized base metal showed the DBTT above RT (~55°C), which was unexpected from the results of the as-welded material. This result was also unmatched with previously reported DBTT (-11°C) obtained from a half-size Charpy specimens, so that additional tests are planned to evaluate the observed gap.

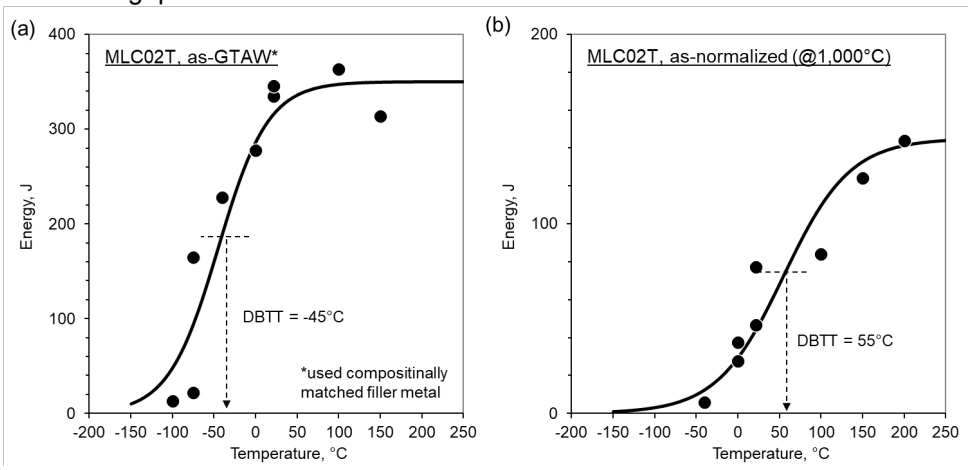

Figure 3. Charpy absorbed energy of MLC02T plotted as a function of test temperature: (a) as-GTAW specimens, and (b) as-normalized base metal specimens.

Isothermal aging at 500°C in a laboratory air, targeting for up to 10,000h, has been completed for evaluation of long-term thermal stability in microstructure and mechanical performance of the as-normalized MLC02T plate. The hardness, tensile, and short-term creep properties are to be evaluated as a function of isothermal aging time.

Results

Microstructure characterization of the as-welded, creep-ruptured and isothermally aged MLC02T will be conducted to be correlated with the process or test conditions. Evaluation of the creep-rupture performance and Charpy impact toughness of the base metal and cross-weld specimens will also be continued/ conducted. A production of compositionally matched metal-core wire has been completed, which will be used for wire-arc additive manufacturing process to build a test wall made of the modified 3Cr3WVTa steel.

2. ODS AND NANOCOMPOSITED ALLOY DEVELOPMENT

2.1 UNDERSTANDING THE PROCESSING AND RESULTING PHASE STRUCTURE OF TITANIUM BERYLLIDES ($Be_{12}Ti$) AS POTENTIAL FUSION MULTIPLIER MATERIALS—D. Bhardwaj, D. Sprouster, B. Cheng, M. A. Shawon, L.L. Snead (Stony Brook University)

OBJECTIVE

As compared to Be-metal, Be-intermetallic are promising multiplier materials due to their combined high Be density, relatively low chemical reactivity, tritium retention, and He swelling, and their good compatibility with blanket materials. Significant literature is available for different beryllide systems (Be-Ti, Be-V, Be-Zr, etc.) with the most studied system being Be-Ti as it contains the highest beryllium number density, and highest multiplication. However, by inspection of the literature it is apparent that control of the phase purity of $Be_{12}Ti$ is quite difficult. The objective of this study is to quantify the phase structure of materials in the open literature, to those we have fabricated via direct current.

SUMMARY

In this task, we have reviewed the available literature specific to phase structure of $Be_{12}Ti$ and while many researchers correctly indicate the presence of a wide array of phases in the Be-Ti systems, the processing, and properties of $Be_{12}Ti$ from X-ray diffraction (XRD) patterns clearly contains additional phases. As a first finding, while published work (example Kim [1]) indicated the mixture of phases (Be,Ti,$Be_{12}Ti$,$Be_{17}Ti_2$, etc) achievable through DCS or sintering the Be-Ti system. An additional number of recent papers on the $Be_{12}Ti$ system also present “phase pure” materials, while analysis of the XRD patterns do show evidence of second Be and BeO phases [2] [3]. This trend is confirmed in our own DCS work to achieve $Be_{12}Ti$, where stoichiometric powders invariably resulted in combined $Be_{12}Ti$/ $Be_{17}Ti_2$. The obvious takeaway from this observation is that any tritium breeding ratio calculation assuming phase pure $Be_{12}Ti$ is currently not appropriate.

Beryllium-Titanium stabilizes into distinct phases depending upon the Ti concentration and temperature. As shown in the phase diagram [4], most of these phases are line compounds. The Ti-based beryllide phase of most interest is the $Be_{12}Ti$, as this phase has the most desirable mechanical and thermomechanical properties, and optimal Be content. To achieve the $Be_{12}Ti$ phase, 7.77 at.% of Ti is added in the Be phase.

Here, $Be_{12}Ti$-rich composites were realized, with XRD showing minor trace levels of Be, BeO and unreacted Ti. Be: $Be_{12}Ti$ composite structures were realized by increasing Be concentration within a processing window of temperature and pressure, until complete reaction of Ti was observed. Simultaneous application of XRD and X-ray tomography was used to determine the as-sintered microstructure. The two-phase structure results in a decreased hardness with increasing Be concentration.

PROGRESS AND STATUS

The $Be_{12}Ti$ was synthesized using direct current sintering and optimizing the powder processing of Be and Ti powders. The powder was measured in the stoichiometric ratio (Be, 7.7 at. % Ti) and speed mixed at 800 rpm for 1 minute. 2 gm of the mixed powder was loaded into a 13 mm die and pressed at 100MPa to create a green body. The pressed green body was subsequently loaded into a 13 mm graphite die and sintered at 1100 ˚C. We report here the effect of hold time (20-80 min) on optimizing the density, final composition, and microstructure. Two phase Be:$Be_{12}Ti$ structures were formed by mixing 5-20 vol% excess Be. The sintering parameters are listed in the Table below:

Table 1. Sintering parameters

Vacuum	<10 Pa
Thermometer	K-type
Heating Rate	100 °C/min
Cooling Rate	Normal cooling
Sintering pressure	6.6 kN/ 50 MPa

After cooling, the pellet was taken out of the graphite die and polished to remove the sacrificial graphite and Be_2C layer (formed after reaction between Be and graphite sheet).

The XRD patterns (Figure 1a) of the specimens synthesized at different hold times. For the compact synthesized with a hold-time of 20 min, peaks were indexed to four different crystal phases; $Be_{12}Ti$ (space group: I4/mmm); BeO (space group: $P6_3/mc$); Be (space group: $P6_3/mc$); and Ti (space group: $P6_3/mmc$). As the hold time increases from 20 min to 80 min, the Ti peaks disappear due to the complete reaction with Be to form $Be_{12}Ti$. To confirm this, weight fraction (Figure 1b) and lattice parameters (Table 2) of the phases was determined using quantitative XRD analysis.

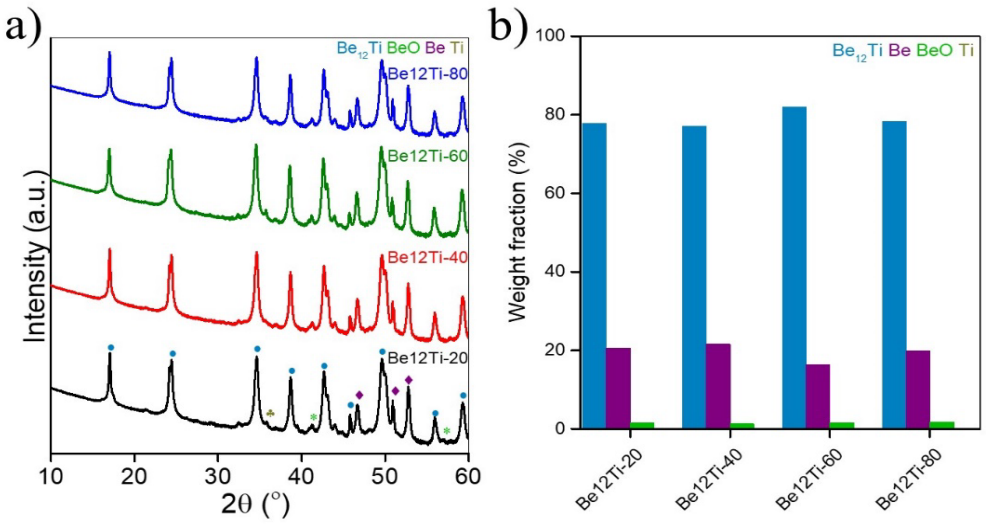

Figure 1. a) XRD pattern of compacts synthesized at different hold-time; b) Weight fraction of phases determined from XRD.

Table 2. Lattice parameters of compacts synthesized at different hold-time

Sample code	$Be_{12}Ti$		Be		BeO	
	a = b	c	a = b	c	a = b	c
Be12Ti-20	7.362	4.198	2.288	3.586	2.694	4.379
Be12Ti-40	7.362	4.198	2.288	3.586	2.694	4.379
Be12Ti-60	7.362	4.198	2.288	3.586	2.694	4.379
Be12Ti-80	7.362	4.198	2.288	3.586	2.694	4.379

The reconstructed x-ray computed tomography (XCT) cross sections through the different compacts are shown in Figure 2 (a)-(d). The features seen in the XCT images are attributed to presence of distinct phases seen from the XRD patterns. The light grey, dark grey, white, and black regions are attributed to $Be_{12}Ti$, Be, Ti and open porosity, respectively. The XCT results show additional evidence that the Be and Ti concentration reduce as the hold time increases, thereby confirming the completion of reaction. It can also be seen from the change in weight fraction obtained from the XRD data.

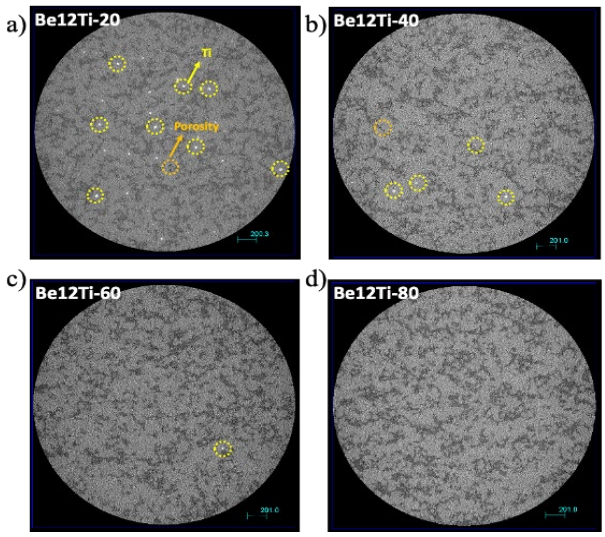

Figure 2. (a)-(d) XCT images of $Be_{12}Ti$ synthesized at different hold time.

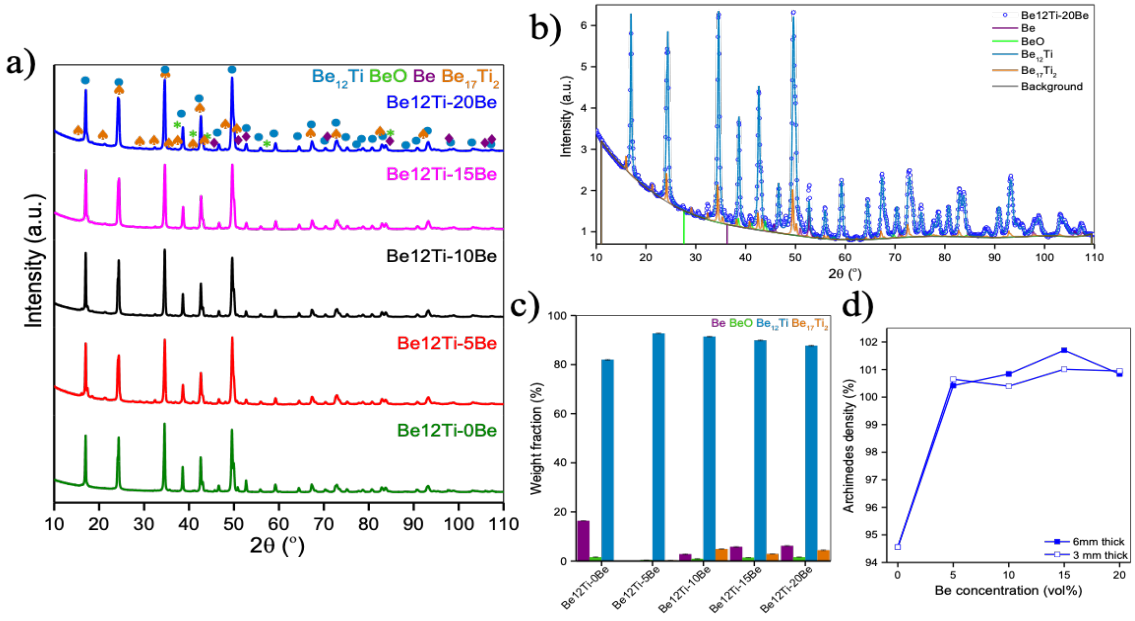

Figure 3. a) XRD pattern of compacts synthesized with different Be concentration; b) Fitted XRD pattern for Be12Ti-20Be; c) Weight fractions of distinct phases determined from XRD; c) Archimedes' density of the 6mm and 3mm compacts.

Following these optimization studies, further processing parameters were used to fabricate the two-phase composites with the addition of additional Be above the values of stoichiometry (e.g., Additional 5, 10, 15, and 20 vol.%). With increasing concentration of Be, the $Be_{17}Ti_2$ phase stabilized along with $Be_{12}Ti$. Figure 3(b) shows the XRD patterns and phases for the highest Be concentration. The $Be_{12}Ti$ phase is maximized with the addition of 5 vol.% of Be. With increasing concentration of Be, the weight fraction (Figure 3c) of $Be_{12}Ti$ decreased and weight fraction of Be increased. Thus, 5 vol.% is the solid solution limit. Archimedes density of the samples, 6mm thick and 3mm thick are shown in Figure 3d. Upon changing the Be concentration from 5 vol.% to 20 vol.%, only minor changes in the density are observed.

The scanning electron microscope (SEM) images of the Be-modified compacts are shown in Figure 4. It is observed that with increasing Be concentration, a clear morphological change is observable with Be channels. These Be channels are found to be located at grain boundaries. For the $Be_{12}Ti$-0Be, unreacted Ti can also be seen. Complete reaction of Ti particles can be seen upon addition of Be.

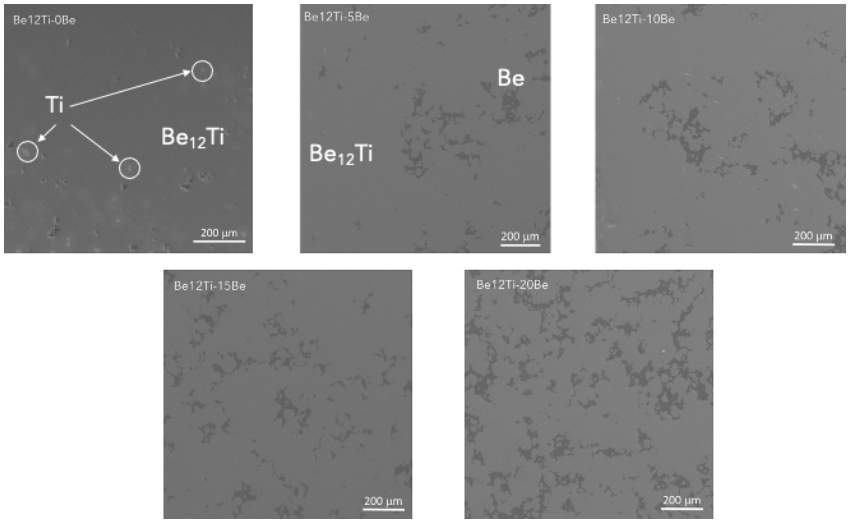

Figure 4. SEM images of the samples containing different Be concentration.

Vickers hardness measurements on the samples using compression load of 0.5Kg. The indents on each sample are shown in Figure 5(b). The Vickers hardness peaks for the Be12Ti-5Be and further increasing Be results in a decrease in hardness. This softening is attributed to the additional Be channels at the grain boundaries.

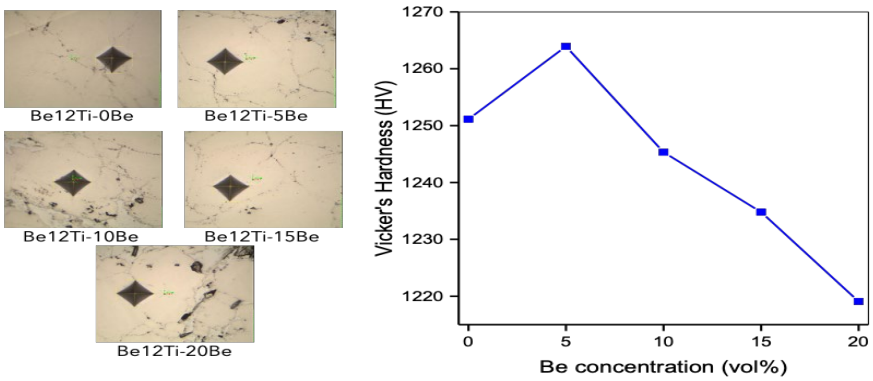

Figure 5. Optical images of the indents along with change in the Vickers's Hardness as a function of Be concentration.

Future Work

- Determine the neutronic impact of inability to realize phase pure $Be_{12}Ti$. Contrast with alternative beryllide line compounds whose stoichiometry is more easily achieved.
- Thermophysical properties of the compacts containing extra Be will be studied.
- Electrical resistivity of compacts containing extra Be will be quantified to understand the nature of thermal conductivity.
- Examples of more easily controlled beryllides for further processing include Cr, V and Zr beryllide using similar powder methods and DCS.
- Samples of $Be_{12}Ti$ are currently undergoing post-irradiation cool-down following irradiation in the MITR. Post irradiation examination studies to determine the effect of second phases will be studied.
- Thermal creep, plasticity, and irradiation effects of composited $Be_{12}Ti$ will be studied.

References

[1.] Kim, J.-H. and M. Nakamichi, *Optimization of synthesis conditions for plasma-sintered beryllium–titanium intermetallic compounds.* Journal of Alloys and Compounds, 2013. **577**: p. 90-96.
[2.] Hwang, T., et al., *Mechanical properties of beryllium-titanium intermetallic compounds fabricated by plasma sintering.* Nuclear Materials and Energy, 2022. **30**: p. 101117.
[3.] Gaisin, R., et al., *Synthesis of Be12Ti compound via arc melting or hot isostatic pressing.* Journal of Alloys and Compounds, 2019. **818**(7): p. 152919.
[4.] Okamoto, H., *Be-Ti (Beryllium-Titanium).* Journal of Phase Equilibria and Diffusion, 2008. **29**(2): p. 202-202.

3. CERAMIC COMPOSITE STRUCTURAL MATERIAL DEVELOPMENT

3.1 FABRICATION OF CERAMIC AND METAL MATRIX ENHANCED SHIELD THROUGH DIRECT CURRENT SINTERING—B. Cheng, D. Bhardwaj, D.J. Sprouster, J. R. Trelewicz, L.L. Snead (Stony Brook University)

OBJECTIVE

Elevated temperature superconductor coils in compact fusion reactor require high performance shielding materials to protect them from combined neutron damage and deposited heat from radiation. Here, we propose a two-phase composite shielding design with MgO ceramic as the matrix and metal hydride as a neutron absorbing entrained phase. The metal hydride provides excellent moderation and absorption of neutrons, while dense, irradiation stable MgO ensures a full encapsulation of metal hydrides to prevent hydrogen loss during elevated temperature operation. The co-sintering the MgO with temperature sensitive metal hydrides requires substantial reduction of sintering temperature. In our previous Advanced Research Projects Agency (ARPA-E) MEITNER program, we developed a strategy to lowing the sintering temperature of MgO using a bimodal size distribution of MgO feedstocks and a nano LiF sintering additives. The significant reduction of MgO sintering temperature (by ~600°C) enables the low temperature co-sintering of MgO with HfH_2 particles. Following on from our initial demonstration of densification of MgO:HfH_2 ceramic matrix composites (CMCs) through direct current sintering, here we show improvements in the hydride retention through engineering a “sandwich-like” structure with MgO:HfH_2 encapsulated between layers of MgO. We describe our recent success in retaining high hydride fractions in these hierarchical MgO:HfH_2 composites and directly compare to monolithic non-hierarchical compact microstructures utilizing quantitative X-ray Diffraction (XRD). This paper will review the processing and thermophysical properties of this class of composite material as well as describing its performance as fusion shield.

PROGRESS AND STATUS

Introduction

Hierarchical MgO:HfH_2 composites was synthesized using direct current sintering. Pre-mixed MgO powder (MgO, nano MgO (8:2 ratio) + 1wt.% LiF) was speed mixed at 800rpm, 1 minute with 25 vol.% of HfH_2. Then 3 gm of the pre-mixed MgO powder was loaded into a 25 mm stainless steel die and pressed slightly to for a smooth and homogeneous bottom layer. The punch was removed and 12.5g of MgO:HfH2 powder was loaded and again pressed slightly. After removing the punch, 3g of the MgO pre-mixed powder is again added to form the top final layer of the structure. The compacts were then pressed at 100MPa to create a green body (shown in the image below). The pressed green body was subsequently loaded into a 25 mm graphite die and sintered at 1100 ˚C. The sintering parameters are listed in the Table below:

Table 1. Sintering parameters

Vacuum	<10 Pa
Thermometer	K-type
Heating Rate	100^{o}C/min
Cooling Rate	Normal cooling
Sintering pressure	9.8 kN/ 20 MPa
Hold time	10 mins

Experimental Procedure

The sintering traces for standard MgO:HfH_2 and hierarchical MgO-MgO:HfH_2-MgO structure are shown in Figure 1a. The in-situ vacuum pressure for the two different specimens is shown in Figure 1b. The low temperature displacement and lower sintering onset temperature in hierarchical CMC is apparent relative to the non-hierarchical composite. The reduced second peak at 600°C and elimination of the higher temperature peaks (~750 – 1000 °C) is also apparent in the hierarchical composite. The hierarchical CMC design thus aids in reducing the hydride loss during sintering, due to the MgO matrix acting as an efficient hydrogen barrier.

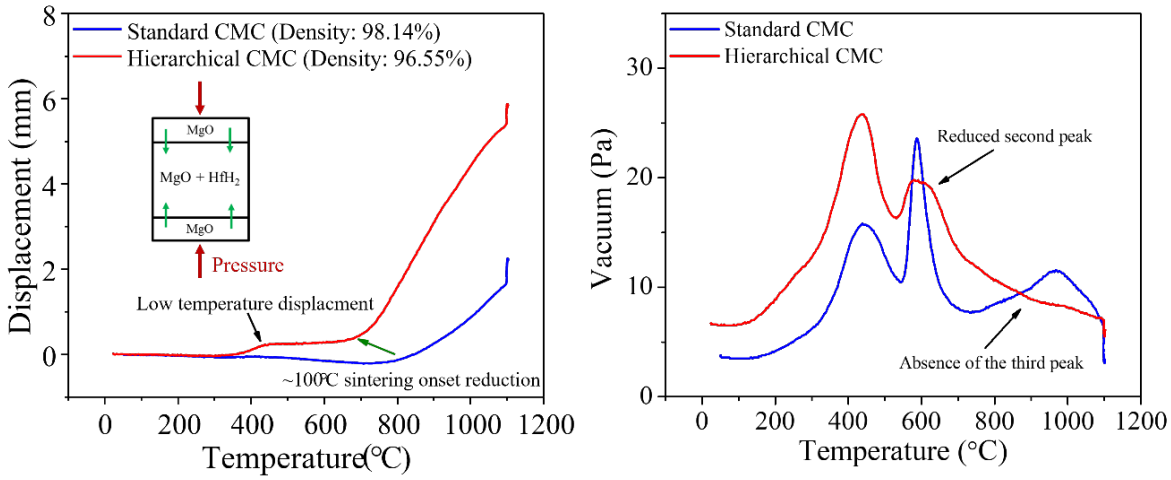

Figure 1. (a) sintering curve and (b) in situ vacuum pressures for standard and hierarchical MgO:HfH_2 compacts.

Optical microscopy was performed on cross sections of the sintered CMC structures, and results are shown in Figure 2. Figure 2a shows a representative image of the whole hierarchical cross-section. Figure 2b shows a higher magnification of the MgO:HfH_2 and top MgO interface. . The lighter contrast at the interface indicates that an interlayer has former. Higher magnification (Figure 2 c) shows that this interlayer, and regions close to the interface have minor microcracks due to a thermal expansion mismatch between the two layers. No visible cracks are observable in the center of the hydride-rich region of the CMC (Figure 2 d).

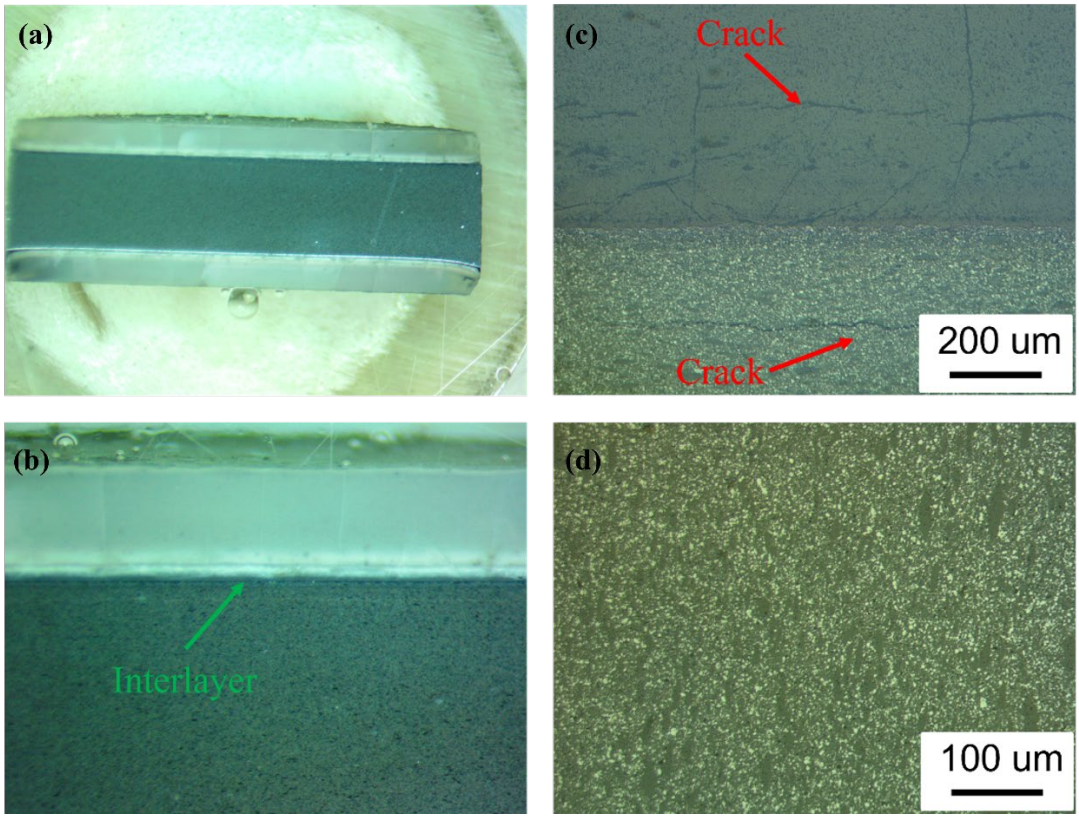

Figure 2. Optical microscopy images of the CMC showing (a) the sandwich structure (b) apparent interlayer region between the MgO:HfH2 and barrier MgO layers, (c) minor microcracks around interfaces in the hierarchical structures (d) uniform HfH_2 distribution and crack free center of the composite.

The XRD patterns for the two different CMCs are shown in Figure 3. For both specimens, the Hafnium hydride phases are clearly retained, even after the high sintering temperatures above 1000°C. The rapid sintering process, and potentially passivation of the HfH_2 particles with excess O of the MgO matrix act to limit the reduction of the hydride phase. Additional minor phases are observable in the XRD patterns and include HfO_2 (~5wt %) and Hf metal (~1 at %). The XRD results also indicate that the initial HfH_2 phase transforms into two components following sintering, specifically HfH_2 and HfH_x ($x<2$). The HfH_x phase is composed of both $HfH_{1.6}$ and $HfH_{1.44}$. The quantitative phase analysis, and total hydride fraction after sintering for both CMCs is shown in Figure 3b. It is interesting to note that while similar HfH_2 concentrations are quantified in both CMCs, the hierarchical CMC has double the $HfH_{x(<2)}$ concentration, further evidence that the hierarchical CMC design helps to reduce hydride decomposition during sintering.

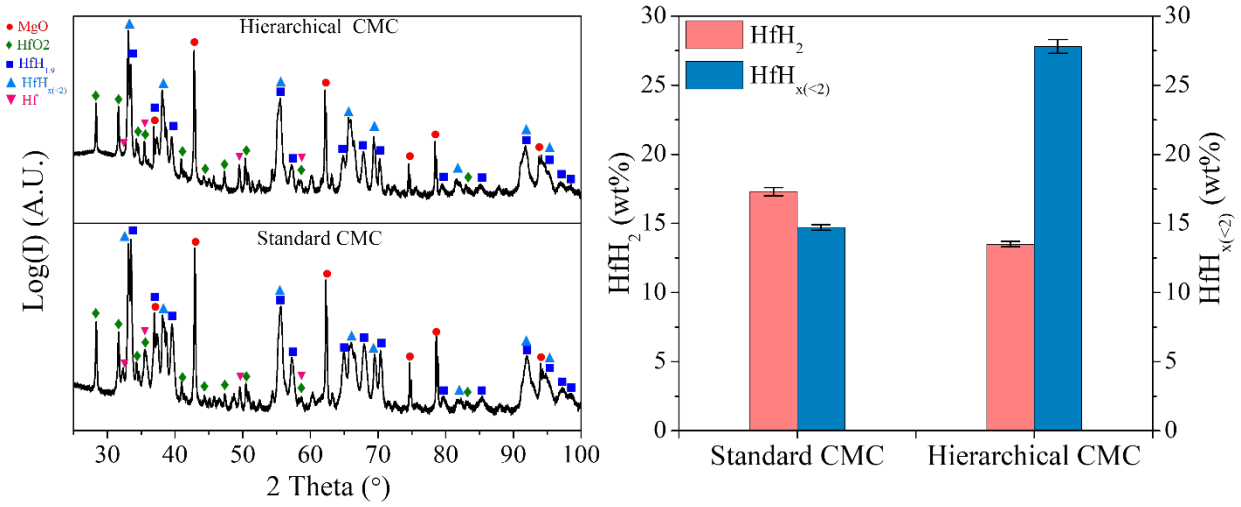

Figure 3. (a) The XRD patterns and (b) quantitative crystalline hydride fractions determined from the XRD refinements.

Results

In this report, we build on our initial success and progress in developing CMCs. We show that adopting a hierarchical CMC design can improve the retention of crystalline hydride phases in final compacts fabricated through direct current sintering methods. Quantitative X-ray diffraction effectively captured this increase in $HfH_{x<2}$ hydride fraction. Future work will incorporate investigating the elevated temperature stability of the two CMC designs, and isolation of non-crystalline hydrogen through inert gas fusion. A publication is under preparation reviewing the processing and thermophysical properties of this class of composite materials as well as describing their performance as fusion shields.

Acknowledgments

Ceramic Matric Composite Shields were conceptualized at Stony Brook University with all subsequent fabrication effort supported by the ARPA-E GAMOW program under contract DE-AR0001381.

4. PLASMA-FACING AND HIGH HEAT FLUX MATERIALS AND COMPONENT TESTING

4.1 X-RAY DIFFRACTION MICROSTRUCTURAL INVESTIGATION OF CCNZ SPECIMENS—D.J. Sprouster, M. Ouyang, L.L Snead (Stony Brook University), W. Zhong (Oak Ridge National Laboratory), L. Yang, S. Zinkle, Y. Yang (University of Tennessee, Knoxville)

OBJECTIVE

This work is a direct follow on from our previous FY20 and FY21 synchrotron characterization analysis of advanced alloys for Fusion energy applications. In this report, we extend and demonstrate the utility of high-energy x-ray diffraction (XRD) to identify and capture minor phases in a series of CCNZ alloys, including those manufactured at Oak Ridge National Laboratory (ORNL) and Stony Brook University (SBU). Changes in the XRD peak shape position, height, and full-width-at-half-maximum (FWHM), indicate changes in the atomic structure (lattice parameters) and microstructure (dislocation density, coherent grain size, weight fraction of minor phases). These results highlight that synchrotron based XRD is appreciably sensitive to the different microstructural features in the different generation of CCNZ alloys with subtle variations in the starting powder and alloying elements. Furthermore, the results and can be effectively employed to quantitatively extract changes in the atomic and microstructural features of the FCC host and minor precipitate populations. Future work could include investigating the effects of mechanical deformation and elevated thermal treatments on the precipitate populations and micro XRD mapping to spatially profile the precipitate populations from undeformed tab to Gauge region.

PROGRESS AND STATUS

Introduction

The XRD measurements were performed at the National Synchrotron Light Source-II (NSLS-II) using the high-energy X-rays available at The Pair Distribution Function (PDF) beamline. All measurements were performed in transmission mode with an amorphous Silicon-based flat panel detector (Perkin-Elmer) mounted orthogonal to and centered on the beam path. The sample-to-detector distances and tilts of the detector relative to the beam were refined using a LaB_6 powder standard (National Institute of Standards and Technology [NIST] standard reference material 660c). The wavelength of the incident X-rays was 0.1665 Å (74.46 keV). The sample-to-detector distance was calculated to be 1000.44 mm. 600 XRD patterns were collected with detector exposures of 0.1s. Specimens were vertically scanned to improve averaging, and to sample a large fraction of the individual specimens. All raw two-dimensional patterns were background corrected by subtracting a dark current image, and the air and Kapton scattering background within Igor Pro (Wavemetrics). Noticeable artefact regions of the detector (like the beam stop, dead pixels) were masked. The corrected and masked two-dimensional detector images were then radially integrated to obtain one-dimensional powder diffraction patterns.

Phase identification was performed using Match3! (Crystal Impact, Bonn, Germany). The background subtracted XRD patterns were Rietveld refined within the TOPAS software package. The peak profiles were modeled by a modified pseudo-Voigt function. The instrument contribution to the broadening of the measured profiles was quantified by fitting the LaB_6 NIST powder standard, with a known coherent grain size (CGS) and negligible micro strain contribution. The Gaussian and Lorentzian-based broadening parameters were subsequently fixed during the analysis of the alloys under investigation to quantify the microstructure (CGS, phase quantification and lattice parameters). The phase fraction, lattice parameter, and CGS components were allowed to vary for the different crystal phases present. The micro strain (μs) components for the minor phases were not included in the refinements. Therefore, the refined coherent grain size parameters of are lower limits.

Experimental Procedure

The XRD patterns for the four CCNZ HZ 500 °C specimens are shown in Figure 1. The phases identified in the samples include FCC Cu matrix, BCC Cr and Cr_2Nb peaks. Minor nanocrystalline phases (Cu_5Zr and or α') phases are also observable in the XRD patterns, with diffuse background-like structures around the FCC matrix reflections. This nanocrystalline phase was found to be necessary to include to properly refine the XRD patterns and to keep the background splines within physical range. An additional CuO phase was observable in 500°C 125MPa specimen (yellow trace with green arrows in Figure 1). It is interesting to note that the coherent grain size (X-ray crystallite size) for the FCC host was large (greater than the 700 nm and above the sensitivity range). The aged-stressed specimens, however had appreciably lower coherent grain sizes, and comparable micro strain based broadening components indicative of a different dislocation substructure. The quantitative XRD results are given in Table 1 for all specimens. The Cu_5Zr phase was refined twice; i) with ~3 nm crystallite sizes, and ii) fixed to larger ~23nm sizes. The 3 nm refinements resulted in lower residual weight parameters (and better fits). The small sizes are comparable to the transmission electron microscope (TEM) results.

The aged CCZ, CCNZ-HP, CCNZ-HZ, and stressed CCZ specimen (125 MPa at 500°C) are shown in Figure 2. Like Figure 1, FCC Cu, BCC Cr, Cr_2Nb (only in HP and HZ alloys), and nano-Cu_5Zr phases are observable in the XRD patterns. Surprisingly, strong reflections from a Cr_2Zr component with identical space group to Cr_2Nb are observable in the stressed CCZ specimen (125 MPa at 500°C), due to phase formation at elevated temperature. Again, nanoscale Cu_5Zr precipitates are present in the different specimens and needed to refine the XRD patterns. Quantitative XRD results are given in Table 1 for all specimens.

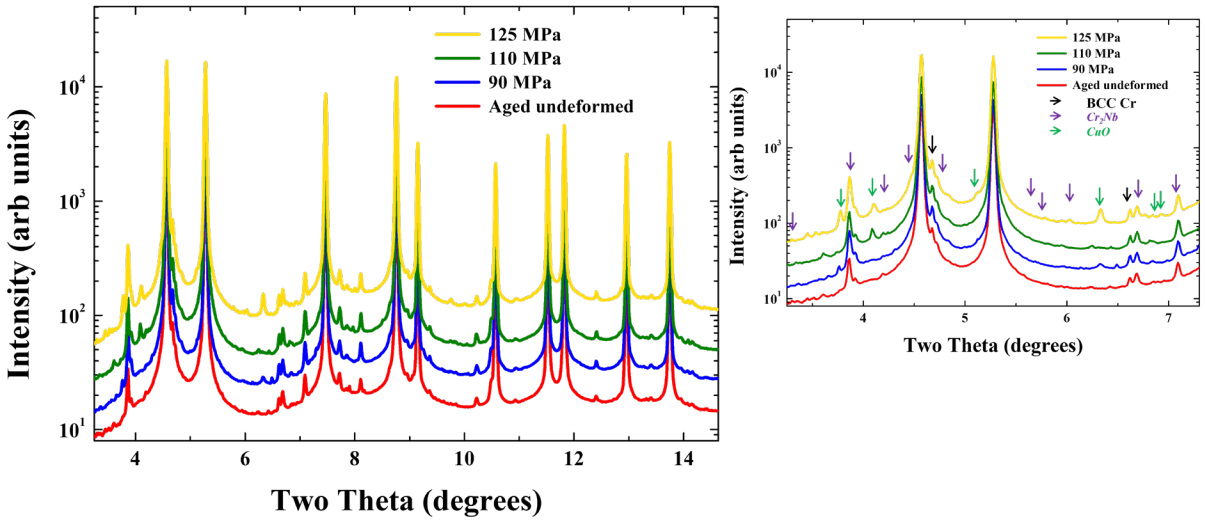

Figure 1. The XRD patterns for the four CCNZ specimens. The multiple phases identified for reference are labelled in the panel for reference.

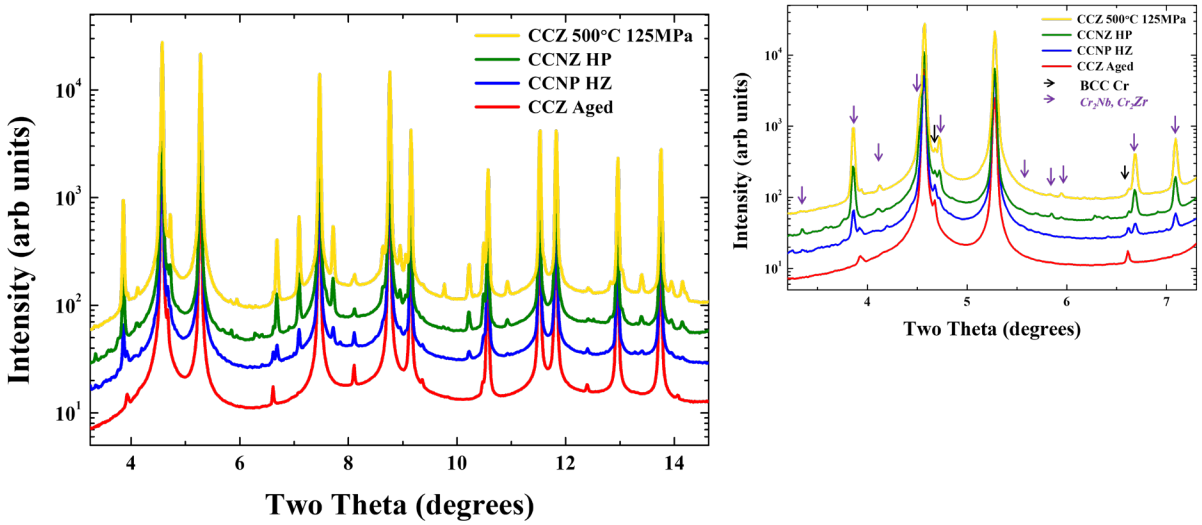

Figure 2. The XRD patterns for the CCZ Aged and Stressed (500C 125MPa) specimens and CCNZ-HP and CCNZ-HZ specimens. The panel on the right has the phases identified for reference with arrows. Note the similar diffraction peaks for the Cr_2Zr and Cr_2Nb.

Table 1. Results from quantitative XRD analysis. CGS is coherent grain size, μs is the XRD-based micro strain.

Sample	*Phase*	space group	a		CGS		μs		Weight fraction		Rwp
name			(Å)		(nm)		-		%		%
CCNZ SPS SBU	*Cu*	*Fm3m*	3.61480	0.00008	180	6.0	0.130	0.007	96.8	0.3	7.0
	Cr	*Im3m*	2.88372	0.00045	95	12.0	-	-	1.1	0.2	
	Cr_2Nb	*Fd-3m*	6.96928	0.00147	40.9	11.2	-	-	1.1	0.2	
CCNZ HZ aged undeformed	*Cu*	*Fm3m*	3.61644	0.00005	-	-	0.113	0.003	95.3	0.1	6.9
	Cr	*Im3m*	2.88226	0.00133	58.6	29.8			0.4	0.1	
	Cr_2Nb	*Fd-3m*	6.99515	0.00043	34.1	1.5			4.2	0.1	
CCNZ HZ 500°C 90MPa	*Cu*	*Fm3m*	3.61489	0.00004	104.6	5.2	0.058	0.002	96.9	0.1	6.9
	Cr	*Im3m*	2.88314	0.00055	44.0	7.9			0.9	0.1	
	Cr_2Nb	*Fd-3m*	6.98861	0.00103	26.4	1.6			1.7	0.1	
	Cu_5Zr	*F-43m*	6.87113	0.00356	23.0	-			0.5	0.1	
CCNZ HZ 500°C 110MPa	*Cu_5Zr*	*F-43m*	6.86465	0.00393	23.0				0.5	0.1	7.3
	Cr	*Im3m*	2.88264	0.00062	42.5	8.2			0.9	0.1	
	Cr_2Nb	*Fd-3m*	6.98827	0.00096	29.1	1.9			1.8	0.1	
	Cu	*Fm3m*	3.61420	0.00005	107.9	9.7	0.075	0.003	96.8	0.1	
CCNZ HZ 500°C 125MPa	*Cu_5Zr*	*F-43m*	6.90211	0.01154	3.2	0.2			2.5	0.2	10.5
	Cr	*Im3m*	2.88319	0.00057	65.8	19.6			0.8	0.1	

	Cr_2Nb	*Fd-3m*	6.98888	0.00102	34.2	3.3			1.5	0.1	
	Cu	*Fm3m*	3.61485	0.00005	92.3	6.1	0.098	0.003	94.9	0.3	
	CuO	*C1c1 (a)*	4.68501	0.00784	40.2	16.1			0.4	0.1	
		(b)	3.42597	0.00538							
		(c)	5.13560	0.00843							
CCZ SBU	*Cu_5Zr*	*F-43m*	6.82488	0.00650	40	5.0	-	-	0.7	0.1	9.0
	Cr	*Im-3m*	2.88299	0.00107	35.3	10.3	-	-	1.7	0.2	
	Cu	*Fm-3m*	3.61584	0.00092	-	-	0.213	0.006	97.7	0.2	
CCZ aged	*Cu_5Zr*	*F-43m*	6.66708	0.02239	5.7	1.3			0.3	0.1	5.7
	Cr	*Im-3m*	2.88555	0.00067	165.0	86.0			0.3	0.0	
	Cu	*Fm-3m*	3.61669	0.00004	90.3	6.4	0.127	0.003	99.4	0.1	
CCZ 500°C 125MPa	*Cu_5Zr*	*F-43m*	6.94497	0.02430	3.2				0.8	0.3	6.6
	Cr	*Im3m*	2.88200	0.00102	65.2	28.0			0.3	0.1	
	Cu	*Fm3m*	3.61405	0.00004			0.074	0.002	92.6	0.4	
	Cr_2Zr	*Fd-3m*	6.99324	0.00027	41.6	1.3			6.3	0.3	
CCNZ HZ aged	*Cu5Zr*	*F-43m*	6.91932	0.01212	2.9	0.2			1.8	0.2	5.5
	Cr	*Im-3m*	2.88394	0.00060	64.2	18.4			0.5	0.0	
	Cr_2Nb	*Fd-3m*	6.99289	0.00085	45.2	5.0			1.0	0.1	
	Cu	*Fm-3m*	3.61610	0.00004	104.4	8.9	0.078	0.002	96.6	0.2	
CCNZ HP aged	*Cu_5Zr*	*F-43m*	6.95888	0.01863	2.7	0.3			1.7	0.2	6.5
	Cr	*Im-3m*	2.88239	0.00108	129.9	292.1			0.3	0.1	
	Cr_2Nb	*Fd-3m*	6.99516	0.00043	38.7	1.8			3.8	0.1	
	Cu	*Fm-3m*	3.61646	0.00004			0.109	0.003	94.2	0.2	

Results

The microstructure of the CCNZ specimens (all generations) with and a without applied stress were analyzed with high energy XRD. Quantitative phase identification and microstructures were captured from the XRD analysis. The minor Cr, Cr_2Nb, Cu_5Zr_2, $ZrCr_2$, and CuO phases were identified in the different specimens. The comparison with TEM results is a potential next step to uncover and compare the effects of composition on the precipitates. An additional nanocrystalline component could also be present and co-refined (α' Cr), again guided by TEM results. Specimens are currently undergoing cool-down following neutron irradiation in MITR. A post-irradiation examination campaign, incorporating electron microscopy, XRD (at a synchrotron light source), electrical resistivity and mechanical property evaluation (creep and tensile) is anticipated in mid-2023.

Acknowledgements

The work was funded under Grant DE-SC0018332 to the Research Foundation at State University of New York, SBU by the United States Department of Energy (DOE) Office of Fusion Energy Sciences. Use of the 28-ID-1 PDF beamline at the NSLS-II, Brookhaven National Laboratory, was supported by the DOE under Contract No. DE-SC0012704.

4.2 IDENTIFICATION OF IRRADIATION ASSISTED PHASE PRECIPITATION IN HEAVY ION IRRADIATED TUNGSTEN HEAVY ALLOYS—J.V. Haag IV, M.J. Olszta, W. Jiang, W. Setyawan (Pacific Northwest National Laboratory)

This is an extended abstract of a manuscript titled "Characterization of boundary precipitation in a heavy ion irradiated 90W-7Ni-3Fe tungsten heavy alloy" to be submitted to Acta Materialia

An elevated temperature (700 °C) Ni^+ and He^+ ion irradiated 90W-7Ni-3Fe tungsten heavy alloy (WHA) has been observed in its as-sintered state as well as post-thermomechanical treatment to determine the effects of processing upon the expression of irradiation damage. Prior analyses of these materials' pre-irradiation have revealed there are no measurable changes in the chemistry of the specimens or in their relative phase compositions, but the domain morphologies and boundary densities change significantly with the introduction of hot-rolling [1]. To quantify these effects upon irradiation behavior, it has become necessary to observe the responses of an as-sintered and an 87% rolling reduction WHA to the simulated fusion reactor environment. Details on the irradiation conditions can be found in prior semiannual reports [2,3], but have been selected and applied to mimic the damage incurred from five years of service in DEMO. Specimens from the Ni^+ and He^+ exposed regions have been lifted out using a focused ion beam and analyzed through the application of scanning transmission electron microscopy (STEM) and energy dispersive x-ray spectroscopy (EDS) to determine the crystallographic structure and chemistry. These analyses have revealed the presence of two distinct forms of irradiation assisted phase precipitation: a hexagonal tungsten rich phase and a surface-lying η-phase; both of which are found at interfaces between the BCC tungsten phase and the FCC ductile phase. The crystal structure of the η-phase is consistent with that of carbides observed in alloys of W, Co, Ni, and Fe and is measured to have an elemental ratio of approximately 62:22:16 (W:Ni:Fe) in at.%. Due to the experimental difficulties in determining exact carbon compositions through STEM-EDS, the crystal structure and relative metal atomic ratios have been used to assign the surface lying phase as the *η*-carbide. The composition of the hexagonal tungsten rich phase has been estimated to be 90:5:5 (W:Ni:Fe) also in at.% and is noted to be structurally consistent with the α-W_2C phase. The domain morphology and manipulation of boundary conformations is expected to mediate the manifestation and density of these precipitates, an effect which is noted to be even more pronounced in the short penetration range from heavy ion implantation as compared to neutrons. These precipitates are assumed to result from the combined effects of surface carbon contamination and ballistic mixing of interfacial regions during irradiation, leading to a localized chemical environment with a sufficient driving force for precipitate nucleation at heterogeneous boundary sites. There does exist a possibility that the nature of the precipitation is due to the extreme dose rates necessary to mimic five years of fusion neutrons through a shorter timescale with heavy ion irradiation. Results from the current study have led to the implementation of a dose rate dependence study. The implications of this precipitate formation upon material performance in the fusion environment remain unknown, but the nucleation of tertiary and quaternary phase precipitation along WHA phase boundaries is anticipated to lead to a deterioration of fracture toughness over time.

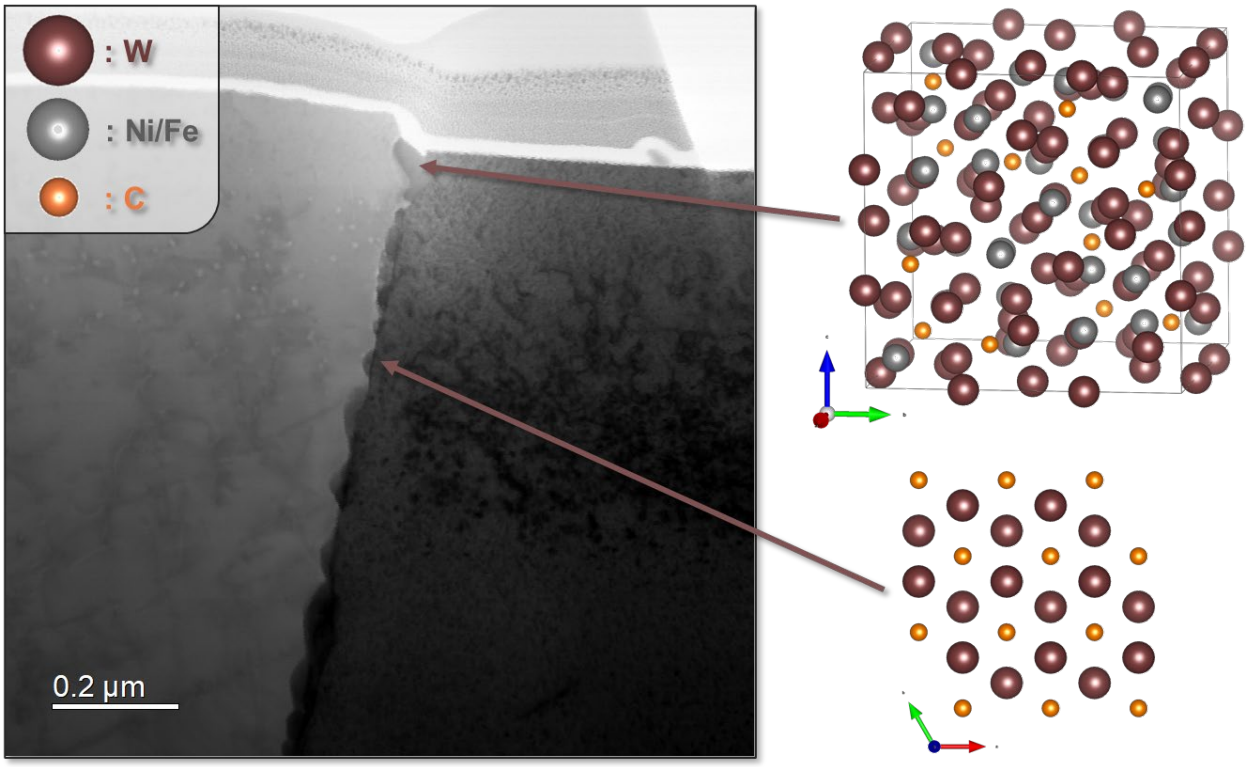

Figure 1. Bright field STEM image of a TEM liftout acquired from a Ni^{+} and He^{+} exposed as-sintered WHA. There are two distinct forms of precipitation, the surface lying η-phase shown top right and hexagonal α-W2C phase shown bottom right.

Acknowledgements

This research was supported by the Office of Fusion Energy Sciences, U.S. Department of Energy and performed at Pacific Northwest National Laboratory under Contract DE-AC05-76RL01830. We are grateful to Zhihan Hu at Texas A&M University for ion irradiation.

References

[1] J.V. Haag, J. Wang, D. J. Edwards, W. Setyawan, and M. Murayama, “A boundary-based approach to the multiscale microstructural characterization of a W-Ni-Fe tungsten heavy alloy,” *Scripta Materialia*, vol. 213, p. 114587, May 2022, doi: 10.1016/j.scriptamat.2022.114587.

[2] W. Jiang, W. Setyawan, K. Kruska, L. Kovarik, D. Zhang, “Self-ion and He ion irradiation of ductile phase toughened tungsten composites,” DOE Fusion Reactor Materials Program Semiannual Progress Report. DOE/ER-0313/68 (2020) 96-101.

[3] J.V. Haag IV, M. Murayama, M.J. Olszta, D.J. Edwards, W. Jiang, W. Setyawan, “Transmission electron microscopy analysis of a heavy ion irradiated tungsten heavy alloy,” DOE0313/71 (2021), pp. 98-104.

4.3 SURFACE CHEMISTRY OF NEUTRON IRRADIATED TUNGSTEN IN A HIGH-TEMPERATURE MULTI-MATERIAL ENVIRONMENT—C.N. Taylor, M. Shimada (Idaho National Laboratory), Y. Nobuta (Hokkaido University), M. Kobayashi (National Institute for Fusion Science), Y. Oya (Shizuoka University), Y. Hatano (University of Toyama), T. Koyanagi (Oak Ridge National Laboratory)

Abstract of a manuscript in Nuclear Materials and Energy 34 (2023) 101323

Deuterium retention was measured on neutron irradiated tungsten samples where one side of the samples had a visually clean metallic luster and the opposite side appeared to have a reacted surface film. Deuterium plasma exposure and subsequent thermal desorption from the reacted surface side produced spectra with larger total deuterium desorption at lower temperatures than from the clean surface side. For neutron irradiation, these W disk samples were installed in an irradiation capsule in such a way that one side of W sample was in contact with the surface of another W sample, and the opposite side was in contact with a SiC temperature monitor. The composition of the reacted surface was investigated using x-ray photoelectron spectroscopy and showed that SiC had inter-diffused into the W samples. Neutron enhanced diffusion likely contributed to this as SiC and W are stable at temperatures exceeding the irradiation temperature. Results highlight the need to consider the surface chemistry of samples in drawing conclusions on hydrogen isotope retention of W materials and illustrate the complexity of multi-material nuclear environments expected in fusion devices.

4.4 QUANTIFICATION OF HELIUM CAVITY NUMBER DENSITIES IN 87R DPT W IRRADIATED WITH He^+ IONS AT 973 K—W. Jiang, L. Kovarik, K. Kruska, Y. Fu, W. Setyawan (Pacific Northwest National Laboratory)

OBJECTIVE

This work explores and applies convergent-beam scanning transmission electron microscopy (CB-STEM) and STEM electron energy loss spectrometry (EELS) methods to study behavior and quantify the properties of He cavities in 87R DPT W irradiated with He^+ ions at elevated temperatures.

SUMMARY

This report presents the results on the quantification of cavity number density as a function of depth in a hot-rolled, 87% thickness reduced, ductile-phase toughened (DPT) tungsten (87R DPT W) composite (90W-7Ni-3Fe) irradiated with 90 keV He^+ ions to 1.0×10^{17} He^+/cm^2 at 973 K. A relative cavity number density was determined as a function of depth using CB-STEM. The images are processed in several steps, including removing atom grids, enhancing contrast, and removing statistical noise. Cavities are identified based on the contrast. Stacking cavities from different depths are retrieved to two or more cavities using a self-developed code. Subsequent calibration for the number density profiles was made based on STEM-EELS measurements in an extremely thin area. These results, along with the cavity diameter and volume distributions as well as the He density and pressure in the cavities, are being finalized for a journal article.

PROGRESS AND STATUS

Introduction

Tungsten (W) has outstanding thermomechanical properties for plasm-facing components of fusion power systems [1-6]. However, pure W has low fracture toughness at room temperature and its ductile to brittle transition temperature (DBTT) increases with irradiation damage [7,8]. The DPT W composites, such as 90W-7Ni-3Fe, can exhibit significantly higher fracture toughness than pure W [9-13], while retaining the favored W properties. Irradiation of DPT W with 14.1 MeV neutrons from the $^3T(d,n)^4He$ fusion reaction produces atomic displacements, resulting in the generation of lattice defects and creation of foreign elements, including He, by transmutation of Ni, Fe and W [14,15]. Diffusion and interaction of He atoms and vacancies will lead to nucleation and growth of He cavities in DPT W. The critical parameters controlling the evolution of the number density and size of the cavities during He introduction by He^+ ion implantation or elemental transmutation are temperature, He production rate, displacement rate, accumulated He concentration, and dose [16]. In general, the presence of He cavities in metals has considerable concerns because it could deteriorate the mechanical properties, including dramatic embrittlement. This embrittlement results from He cavity formation at grain boundaries and may occur even at low He concentrations [17,18]. Therefore, it is crucial to study the He behavior of candidate fusion materials, such as DPT W [9].

Conventional transmission electron microscopy (TEM) in a defocus condition has been extensively used to characterize the size of He cavities in various materials. A defocus condition is necessary because the bubble edges create hardly any contrast at focus, even if a contrast aperture is used. In defocus conditions, Fresnel fringe contrast reveals the cavity edges. However, using this technique, the actual He cavity size is obscured by the defocus conditions, and the observed cavity size must be corrected. The correction of measured values based on the simulation results has been demonstrated in our previous study [18]. If the cavity number density is extremely high, there is a high probability for cavity images to be overlapped across a typical TEM foil (~100 nm thick) due to projection. Therefore, projection can lead to an error in estimating the cavity number density and size distributions when some small cavities are completely shielded and become invisible. This study explores a CB-STEM method to minimize the

probability for the projection effects. In contrast to the conventional TEM [18,19], the CB-STEM methodology uses a converging beam that only images a depth of field in the 20-40 nm range. The resulting image will have the actual size of the cavity with a significantly lower probability of cavity overlap, thus allowing for a more accurate analysis of the number density and size distributions. The remaining stacked cavities from different depths are separated into two or more by reconstructing the partially visible cavities via boundary segments using a self-developed code. In this study, we attempted to apply CB-STEM and STEM-EELS to quantify the distributions of He cavity number densities as a function of depth in both W and NiFeW phases within hot-rolled, 87R DPT W in an emulated fusion environment.

Experimental Procedure

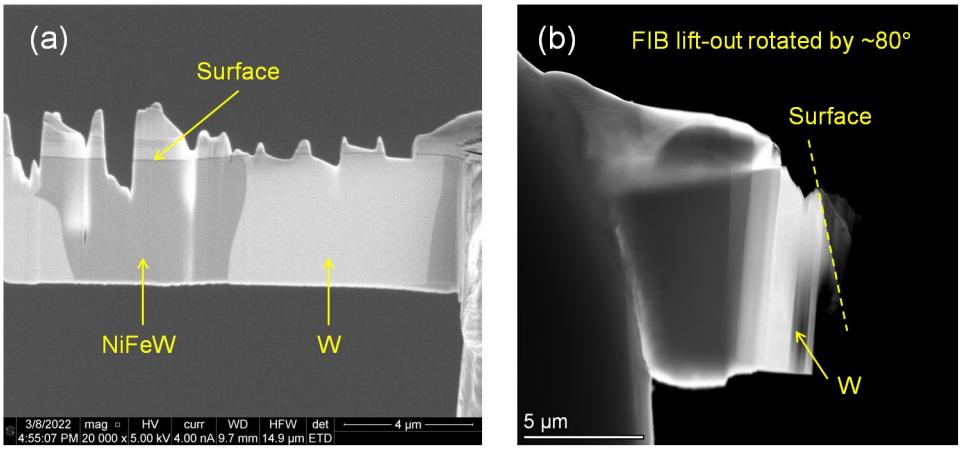

NiFeW FIB Sample W FIB Sample

Figure 1. The FIB samples for CB-STEM and STEM-EELS characterizations of (a) NiFeW and (b) W in 87R DPT W irradiated with 90 keV He^+ ions to 1.0×10^{17} He^+/cm^2 at 973 K.

Ion irradiation was performed with 90 keV He^+ ions at normal incidence to 1.0×10^{17} He^+/cm^2 at 973 K. The low ion energy for irradiation was chosen for the convenience of damage profiling near the surface region. A resistance heater was located behind a copper plate on which the sample was mounted. A thermocouple was clamped on the sample surface for temperature measurement. Irradiation was manually interrupted every ~15 min to check and, if necessary, adjust the beam current, which was found to be stable. The beam current was arithmetically averaged over the time period. Despite this procedure, the absolute ion fluence is still subject to an error of up to 10% or greater. The average ion flux over a rastered area of 5 mm × 10 mm was $\sim2\times10^{13}$ $(He^+/cm^2)/s$.

Two separate cross-sectional TEM samples were prepared to examine He cavities in the irradiated 87R DPT W using a Field Electron and Ion Company (FEI) Quanta dual-beam focused ion beam (FIB) microscope. Figure 1 shows the secondary electron microscopy (SEM) images for the two FIB samples, each having a distinct contrast of W (white) and NiFeW (dark) phases. Regions with NiFeW and W interphases were selected to cap with electron- and ion-deposited Pt layers to protect the surface prior to the FIB process. One lamella for cavity examination in NiFeW was extracted using a standard lift-out procedure with a Ga^+ ion beam and attached to a Cu grid. Windows in the lamella were thinned with the Ga^+ ion beam at 30 kV. Surface damage was removed in a final low-energy polishing step with the beam energy reduced to 2 kV. The sample in Figure 1a has thin NiFeW regions (~100 nm) over the entire irradiation region and some extremely thin zones (20-30 nm) suitable for CB-STEM and STEM-EELS of He cavities, respectively. As an even thinner foil is required for STEM-EELS of the He cavities in W that has a much lower sputtering rate than NiFeW, additional FIB sample for examination of cavities in W was

prepared, as shown in Figure 1b. Because the W phase is more resistant to the ion beam sputtering than the protective Pt cap, it proved difficult to obtain the ultra-thin samples necessary for STEM EELS analysis without losing the He irradiated surface layer. Therefore, a modified lift-out process was used by mounting the lift-out on a Cu grid with a rotation by ~80° and thinning along a direction parallel to the sample surface. It was found that rather than thinning the new "surface" of the sample, the best results were obtained when the lowest portion of the rotated FIB lamella was thinned, producing a zone with ~10 nm thick W foil suitable for STEM-EELS.

The FIB samples were examined using a probe aberration-corrected 300 kV Thermo Fisher Scientific Themis STEM microscope with a spatial resolution of 0.05 nm, which was equipped with a high-performance EELS detection system. High-angle annular dark-field (HAADF) CB-STEM with a convergence semi-angle of 25 mrad and an inner collection semi-angle of 52 mrad was performed at an accelerating voltage of 300 kV and a scanning increment step of 0.032 – 0.140 nm. The STEM-EELS mapping was performed also at 300 kV with a collection semi-angle of 38.5 mrad and a scanning step of 0.073 - 0.23 nm. Compared to lower voltage (e.g., 200 kV) imaging, utilization of 300 kV STEM-EELS for He cavities provides a number of advantages, including (1) a smaller loss of He atoms in a cavity due to ballistic collisions [20] during EELS measurement, (2) occurrence of primarily He K-shell ionization for the He atoms in the cavities of this study, and (3) less stringent requirement for minimal foil thicknesses. The STEM and EELS data were analyzed using the Gatan Microscopy Suite 3.

Results

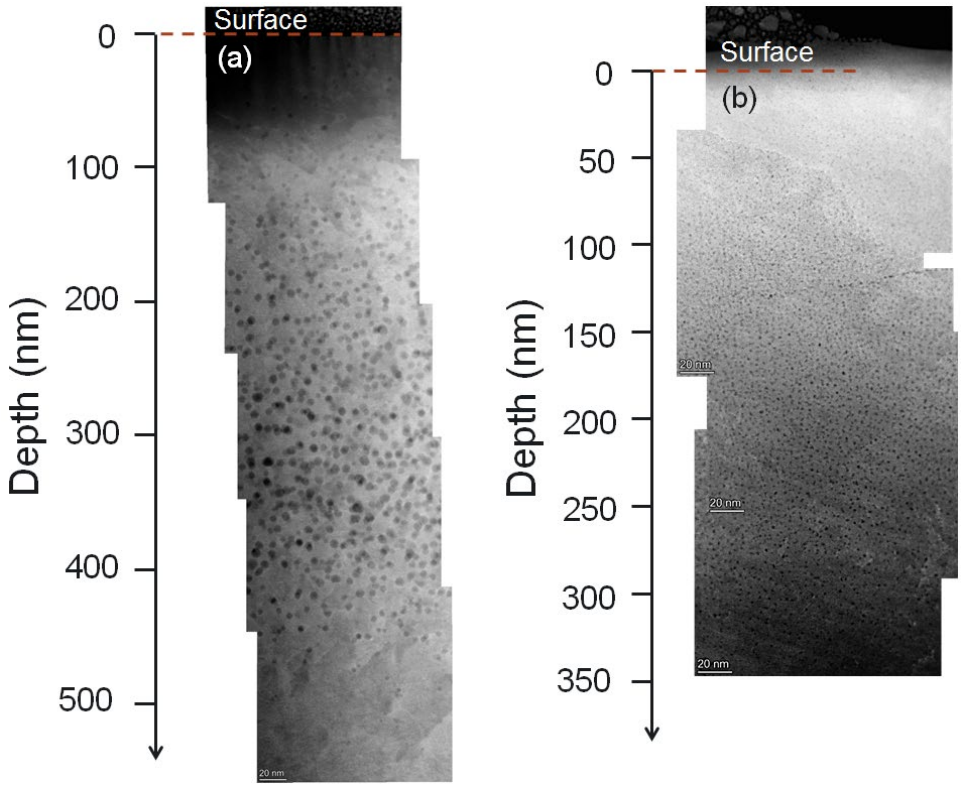

Figure 2. Stitched CB-STEM images for depth profiles of the He cavities in (a) NiFeW and (b) W within 87R DPT W irradiated with 90 keV He^+ ions to 1.0×10^{17} He^+/cm^2 at 973 K.

Stitched depth-dependent HAADF CB-STEM images of He cavities in NiFeW and W within the irradiated DPT W are shown in Figures 2a and 2b, respectively. It is immediately apparent that He cavities in the W phase are much smaller and have a much greater density than in the NiFeW phase. Over the depth of focus starting from the foil surface, cavities are observed in actual size at an atomic-level resolution [21]. The cavity contrast is stronger closer to the top surface of the foil. The cavity contrast emerges as a result

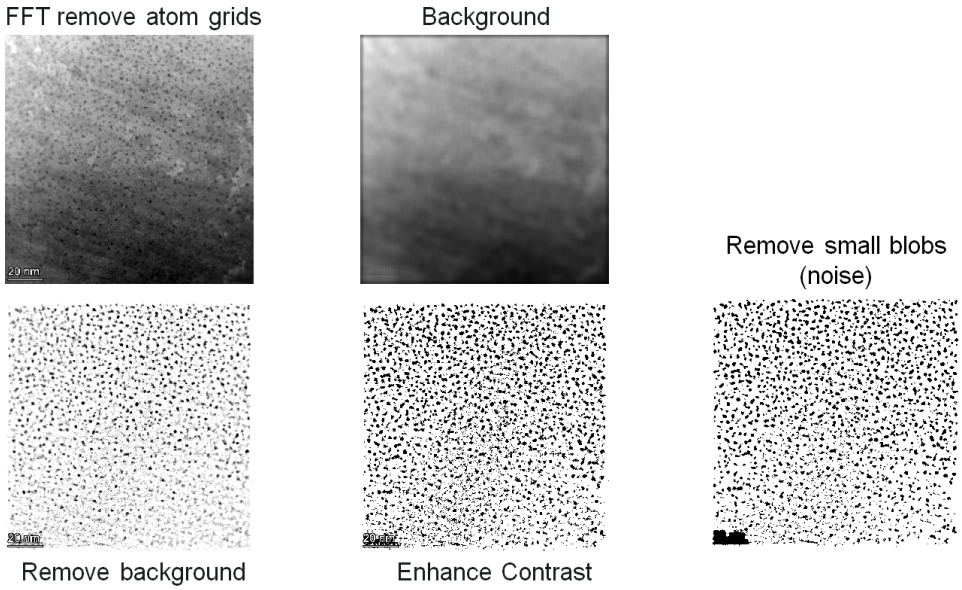

Figure 3. Procedure for CB-STEM image processing: an example of W over the depth region from 250 to 300 nm in 87R DPT W irradiated with 90 keV He^+ ions to 1.0×10^{17} He^+/cm^2 at 973 K.

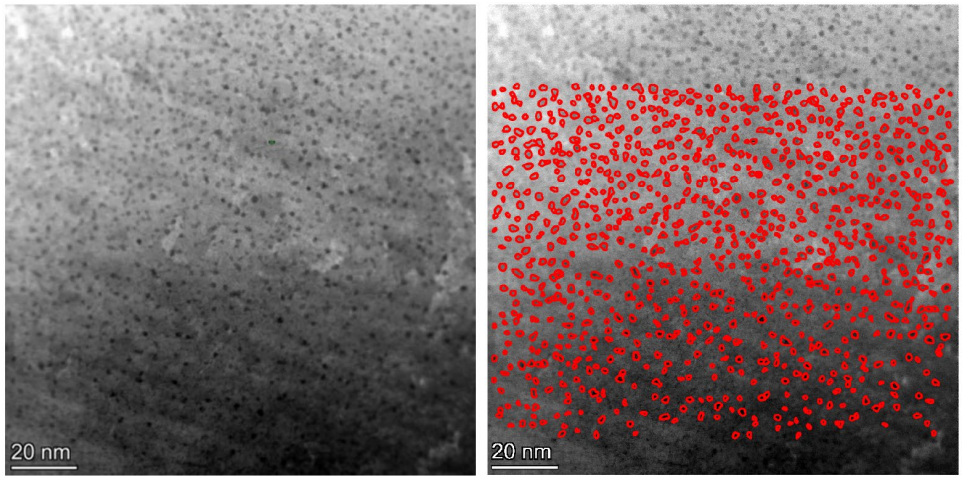

Figure 4. Contrast-based identification of the cavities in W over the depth region from 250 to 300 nm in 87R DPT W irradiated with 90 keV He^+ ions to 1.0×10^{17} He^+/cm^2 at 973 K.

of the foil thickness difference. In general, He cavities show a darker contrast compared to the surrounding metal in HAADF imaging due to smaller thickness in the cavity region. Figure 2a shows that He cavities are distributed over the depth region from 100 to 400 nm and nearly disappear at ~450 nm, consistent with SRIM prediction [21]. The cavities are small with a typical diameter between 3 and 5 nm. Their sizes vary little with depth over a large depth region. Compared to the conventional Fresnel diffraction fringe contrast from a defocus beam, the CB-STEM technique exhibits a reduced probability of

projection effects in a thinner slab (depth of focus). Hence, the technique has a greater accuracy in counting the absolute cavity numbers and determining the number density as a function of depth. Figure 2(b) shows a similar depth profile of the He cavities in W within the irradiated 87R DPT W. Compared to NiFeW, the He cavities are smaller on average, typically ~1.5 nm in diameter, in

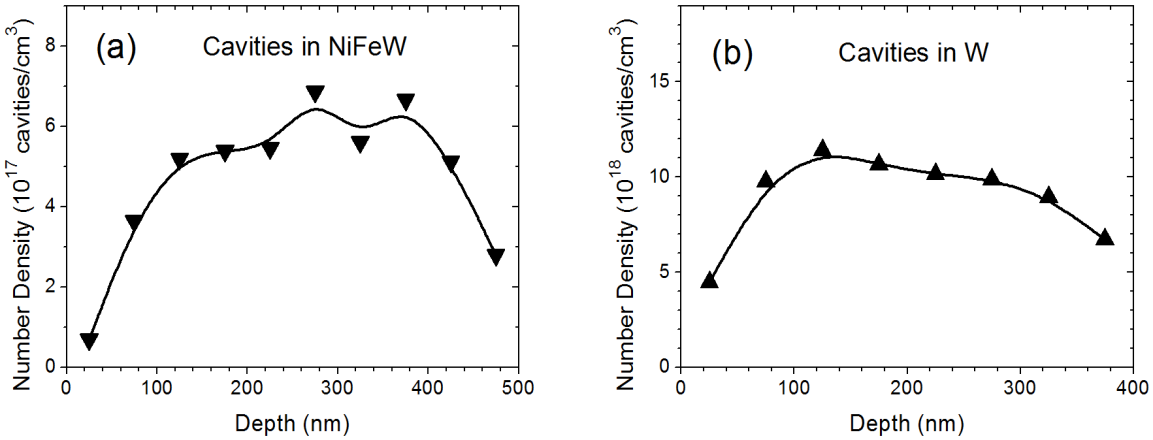

Figure 5. Depth profiles of the cavity number densities in (a) NiFeW and (b) W within 87R DPT W irradiated with 90 keV He^+ ions to 1.0×10^{17} He^+/cm^2 at 973 K.

agreement with our previous reports [18,19]. The cavities nearly disappear beyond the depth of ~350 nm, which is again consistent with the SRIM prediction [21].

The CB-STEM images were processed through several steps, as shown in Figure 3. First, the atomic lattice contrast in the image of the host material was removed by masking the lattice spots in a fast-Fourier transformed (FFT) image and subsequent reverse transformation. Then, the contrast of the remaining features was enhanced. Finally, tiny specs from statistical noise were removed, leading to a high-contrast cavity image.

Detailed analysis of the He cavity diameter distributions as a function of depth has been performed using a self-developed code that identifies the cavity areas based on the contrast in the processed image. An example of the cavity identification results in W is shown in Figure 4, where the red loops for identified cavities are superimposed with the original image for clarity. Overlapping cavities at different depths are deconvoluted into two or more cavities by reconstructing partially covered cavities via boundary segments. Each individual cavity is assumed to be a sphere.

The relative number densities of He cavities as a function of depth in NiFeW and W are determined based on the data analysis of CB-STEM images shown in Figure 2. The depth of focus in different areas under a fixed CB-STEM condition remains constant for each material, NiFeW or W. This length is much smaller than the local foil thickness, which can help minimize cavity image stacking from different depths. Instead of calculating the absolute value of the depth of focus, additional CB-STEM and STEM-EELS in extremely thin region was performed. This technique ensures all the cavities throughout the entire foil thickness are imaged. The imaging areas in NiFeW and W have the average depths (designated as the center of the image) of 318 nm and 250 nm with foil thickness values of ~23 nm and ~10 nm, respectively, determined by EELS thickness mapping [22]. The total number of He cavities corresponds to 77 over an area of 5.93×10^3 nm^2 in NiFeW and 341 over 3.36×10^3 nm^2 in W, leading to the number densities of 5.6×10^{17} cm^{-3} in NiFeW and 1.0×10^{19} cm^{-3} in W. As the number density is the same at the same depth in ion-irradiated samples, these values are used to calibrate the relative number density profiles with the results shown in Figure 5.

The number densities in both NiFeW and W are lower in the surface region and near the end of the He concentration profile, which is consistent with the prediction from the Stopping and Range of Ions in Matter (SRIM) simulation. Compared to the He number densities in NiFeW and W within an 87R DPT W irradiated to 6.5×10^{15} He^+/cm^2 at 973 K [18**Error! Bookmark not defined.**], which were analyzed with conventional TEM under a defocus condition, this study shows a comparable He number density in W, but a little higher value in NiFeW. Part of the reason for the latter case might be that some of the small He cavities could be effectively shielded by larger ones in front of them due to larger imaging thickness in our previous study [18].

Ongoing Efforts

The final number density results, along with the cavity diameter and volume distributions as well as the He density and pressure in the cavities, are currently being summarized for a journal article. The new results will also be presented at The Minerals, Metals & Materials Society (TMS) 2023 meeting in March 2023. In addition, we have completed sequential irradiation with Ni^+ and He^+ ions for 87R DPT W at room temperature and 1000 °C. The samples are being examined and preliminary data are being evaluated. Updates about the results will be reported in our next semiannual report.

Acknowledgements

This research was supported by the Office of Fusion Energy Sciences, United States Department of Energy (DOE) and performed at Pacific Northwest National Laboratory (PNNL) under Contract DE-AC05-76RL01830. A portion of the research was performed using the Environmental Molecular Sciences Laboratory, a DOE Office of Science User Facility. We are grateful to Charles Henager at PNNL for providing the 87R DPT W sample and to Zhihan Hu at Texas A&M University for ion irradiation.

References

[1] R.A. Causey, T.J. Venhaus, Phys. Scr. T94 (2001) 9.
[2] E. Lassner, W.S. Schubert, Tungsten: Properties, Chemistry, Technology of the Element, Alloys and Chemical Compounds, Springer, New York, NY, 1999. P.30.
[3] D.M. Duffy, Phil. Trans. R. Soc. A 368 (2010) 3315.
[4] M. Rieth, S.L. Dudarev, S.M. Gonzalez de Vicente, J. Aktaa, T. Ahlgren, S. Antusch *et al*., J. Nucl. Mater. 432 (2013) 482.
[5] R.G. Abernethy, Mater. Sci. Technol. 33 (2017) 388.
[6] S.J. Zinkle, J.T. Busby, Mater. Today 12 (2009) 12.
[7] H. Ullmaier, F. Carsughi, Nucl. Instrum. Methods Phys. Res. B. 101 (1995) 406.
[8] M. Rieth , J.L. Boutard, S.L. Dudarev, T. Ahlgren, S. Antusch, N. Baluc *et al*., J. Nucl. Mater. 417 (2011) 463.
[9] C.H. Henager, Jr., W. Setyawan, T.J. Roosendaal, N.R. Overman, B.A. Borlaug, E.L. Stevens *et al*., Int. J. Powder Metall. 53 (2017) 53.
[10] R. Neu , H. Maier , M. Balden , R. Dux , S. Elgeti , H. Gietl *et al*., J. Nucl. Mater. 511 (2018) 567.
[11] M.E. Alam , G.R. Odette , Acta Mater. 186 (2020) 324.
[12] J.V. Haag IV, D.J. Edwards, C.H. Henager Jr., W. Setyawan, J. Wang, M. Murayama, Acta Mater. 204 (2021) 116523.
[13] J.V. Haag IV, J. Wang, K. Kruska, M.J. Olszta, C.H. Henager Jr., D.J. Edwards, W. Setyawan, M. Murayama, Sci. Rep. 13 (2023) 1.
[14] M.R. Gilbert, J.-Ch. Sublet, Nucl. Fusion 51 (2011) 043005.
[15] Fusion Evaluated Nuclear Data Library Ver.3.1d (FENDL-3.1d) at https://www-nds.iaea.org/fendl/.
[16] H. Trinkaus, B.N. Singh, J. Nucl. Mater. 323 (2003) 229.
[17] H. Ullmaier, Nucl. Fusion 24 (1984) 1039.
[18] W. Jiang, D. Zhang , D. Li, J. Heo, Z. Wang, L.M. Zhang, N. Overman, T. Varga, Z. Hu, X. Wang, L. Shao, W. Setyawan, J. Nucl. Mater. 561 (2022) 153565.

[19] W. Jiang, Y. Zhu, L. Zhang, D.J. Edwards, N.R. Overman, G. Nandipati, W. Setyawan, C.H. Henager Jr., R.J. Kurtz, J. Nucl. Mater. 550 (2021) 152905.
[20] M.-L. David, K. Alix, F. Pailloux, V. Mauchamp, M. Couillard, G.A. Botton, *and* L. Pizzagalli, J. Appl. Phys. 115 (2014) 123508.
[21] W. Jiang, L. Kovarik, K. Kruska, W. Setyawan, Fusion Materials Semiannual Progress Report for Period Ending June 30, 2022, DOE/ER-0313/72, U.S. Department of Energy.
[22] T. Malis, S.C. Cheng, R.F. Egerton, J. Electron Microsc. Tech. 8 (1988) 193.

4.5 APPLICATION OF MICROCANTILEVER BENDING TESTS TO LOCAL FRACTURE TOUGHNESS DETERMINATION IN W-Ni-Fe DUCTILE-PHASE TOUGHENED TUNGSTEN—A.V. Garcia Caraveo, T. Chen (Oregon State University), W. Setyawan (Pacific Northwest National Laboratory)

OBJECTIVE

This project aims to evaluate the radiation-induced property changes in the ductile phase toughened (DPT) W-NiFe alloys to inform computational models for performance prediction and microstructure manipulation. The key technical challenge lies in the application of small-scale mechanical testing to measuring microstructure-specific fracture properties, especially with the presence of plasticity.

SUMMARY

In order to calculate and understand the microstructure-specific fracture toughness, in-situ bending tests on notched microcantilevers containing single-phase W or Ni was performed. The W microcantilever showed elastic deformation followed by an elastic-plastic transition, strain hardening, and stable crack growth. The Ni microcantilever showed slip development during the bending test without crack growth. The J-integral-based crack resistance curve was derived for W to demonstrate the application of microcantilever bending to characterize microstructure-specific fracture toughness. The reported work proves the concept of microscopic testing for microstructure-specific fracture toughness in DPT alloys. Within the context of literature, our results warrant the plastic-zone effect for future considerations in experimental design.

PROGRESS AND STATUS

Introduction

The DPT W-NiFe alloys have significantly improved fracture toughness compared to tungsten, mitigating the brittle challenge of W-based plasma-facing materials. With the strong interface between the hard and the ductile phases, microcracks imitate in the hard W phase are arrested and blunted by the ductile NiFeW phase, which also bridges co-planar microcracks [1, 2]. However, after ion irradiation (which emulates helium accumulation and radiation damage effects of 14 MeV neutrons), helium cavities were observed at the W/NiFeW interface[3], raising concerns about possible interfacial debonding, which impairs the above toughening mechanisms. Further development, evaluation, and qualification of DPT alloys for fusion applications require answering the following questions. (1) To what extent does the radiation evolution of the W/NiFeW interface affect the interfacial mechanical properties, microcrack initiation, and propagation? (2) Should we expect new toughening mechanisms to emerge due to the local mechanical property changes? And (3) Can we tailor the microstructure of the DPT alloys for better performance in radiation environments? One critical step to answering these questions and understanding the mechanisms is quantifying the microstructure-specific properties, which will also provide input to computational models for performance prediction and microstructure optimization. Yet, probing the mechanical responses to irradiation damage at specific microstructural features is challenging, especially in ion-irradiated samples with shallow irradiated zones.

Nanomechanical testing has demonstrated success in characterizing mechanical responses to ion irradiation. Prior studies applied hardness, stress relaxation, and nanoindentation creep tests to understand irradiation hardening effects [4, 5]. Recent studies showed the promise of obtaining fracture properties of ion-irradiated samples using nanomechanical bending tests [6, 7]. Yet, the specimen size effect has been recognized as one of the challenges in the quantitative assessment of fracture properties at micro scales [8]. First, the plastic zone usually extends beyond the vicinity of the crack tip, the so-called K-dominated zone, invalidating the small-scale yielding condition for the application of linear elastic fracture mechanics (LEFM) even in brittle materials [9]. Thus, J-integral must be employed to describe crack propagation. Second, the sample size dependence of the fracture resistance is hard to eliminate because of the small

sample dimensions relative to the plastic zone and the characteristic microstructural length scales governing certain fracture resistance mechanisms [8, 10]. On one hand, extending microscale data to the macroscale requires additional interpretation based on rigorous size-dependent analysis. On the other hand, the correlation between operating resistance mechanisms and specimen size can be utilized to investigate microstructure-specific toughening mechanisms that are hard to separate from macroscale testing.

Experimental Procedure

The DPT alloy used for this research is W-NiFe alloy sample W90, which contains 90W-7Ni3Fe (by wt%) supplied and mechanically polished by Pacific Northwest National Laboratory (PNNL). The microstructure and crystal orientation relationships of the W and NiFe phases were characterized by electron backscattered diffraction (EBSD), Figure 1. This practice allows for crystal orientation-dependent studies. For fracture studies, microcantilevers can be orientated to fracture on dedicated crystal planes.

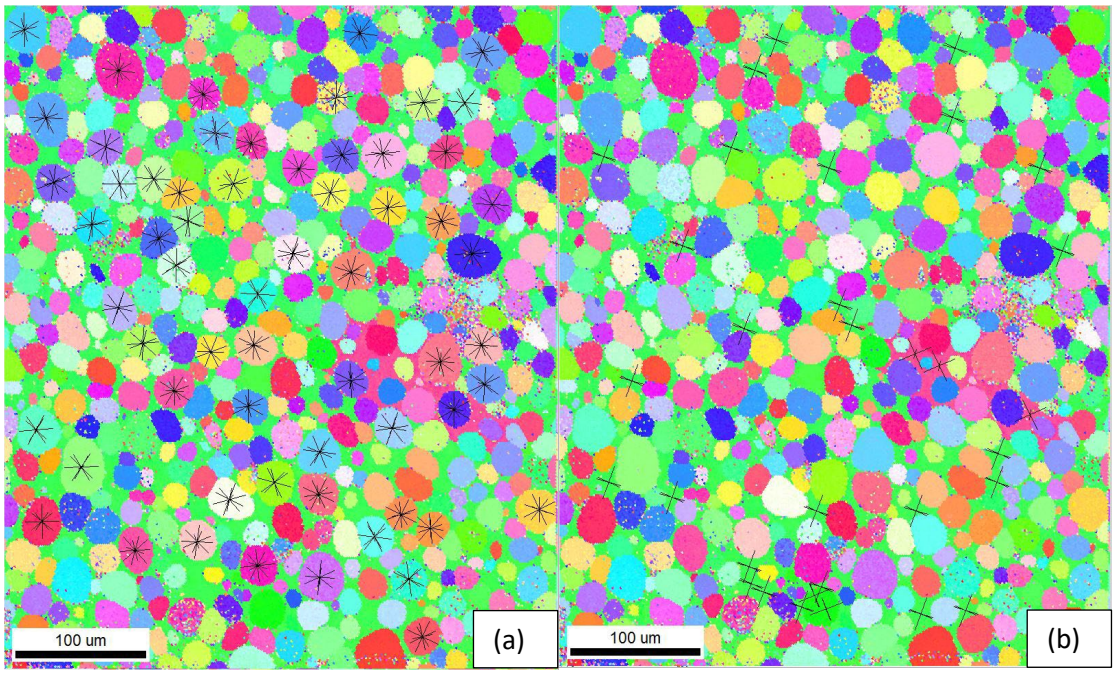

Figure 1. The EBSD analysis with the W [011] and Ni [001] orientations marked in (a) and (b), respectively.

Free-standing notched microcantilevers were employed to evaluate microstructure-specific fracture toughness. A straight-trough notch (STN) geometry was employed for the easiness of fabrication and the existence of reference protocols in the literature. The microcantilever geometry and dimensions are defined by the following ratios ($\frac{a}{b}, \frac{w}{b}, \frac{L_0}{b}, \frac{L_1}{b}$) where b = 2 μm, a = 0.4 μm, L_0 = 0.2 μm, L1 = 10 μm and w = 2 μm, as shown in Figure 1. [11].

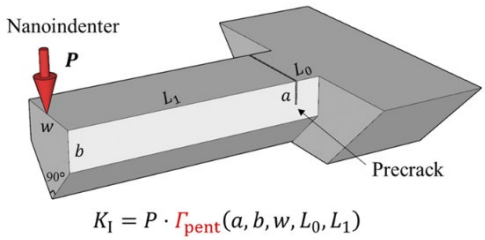

Figure 2. Free-standing notched microcantilever dimension diagram reference. [11]

Guided by the EBSD survey shown in Figure 2, microcantilevers containing single-crystal W and Ni were prepared with the {011} and {001} crack planes, respectively, normal to the beam longitudinal direction. The notched microcantilevers were micro-milled using a Field Electron and Ion Company (FEI) Quanta 3D scanning electron microscope (SEM)/focused ion beam (FIB) dual beam system. Gradually, the beam current decreases from 15 nA to 0.5 nA for trenching, cutting, and polishing the cantilevers. The notches were introduced by FIB machining using a beam current of 10 pA with a line pattern.

In-situ SEM bending experiments were performed with a FemtoTools (FT)-NMT04 nano indenter. An in-situ set-up allows the investigation of the cantilever displacement, fracture propagation, plastic deformation, and slip band development. A conical tip with a diameter of 2 µm was chosen to apply the load to the notched microcantilevers. The displacement control mode was employed to warrant stable crack growth to obtain the crack growth resistance curve (R-Curve). Continuous stiffness measurement (CSM) was performed to obtain the stiffness evolution for crack length estimation. The testing parameters are as follows. The displacement rate equals 5 nm/s, the CSM frequency 200 Hz, and the CSM oscillation amplitude 2 nm.

Results

Figure 3 a-c and d-f show fracture initiation and propagation in the W microcantilever and slip band development without fracture initiation in the Ni microcantilever, respectively. The fractography of the W microcantilever, Figure 3c, indicates plastic-energy dissipation during fracture. Slip band development was observed at quite early stage in the bent Ni microcantilever. Plastic deformation continued until the end of the test when the displacement reached around 4 µm, corresponding to a strain of ~0.4. Both the number density and the step depths of the slip bands were observed to increase during the test. Fracture initiation in the Ni microcantilever was not observed.

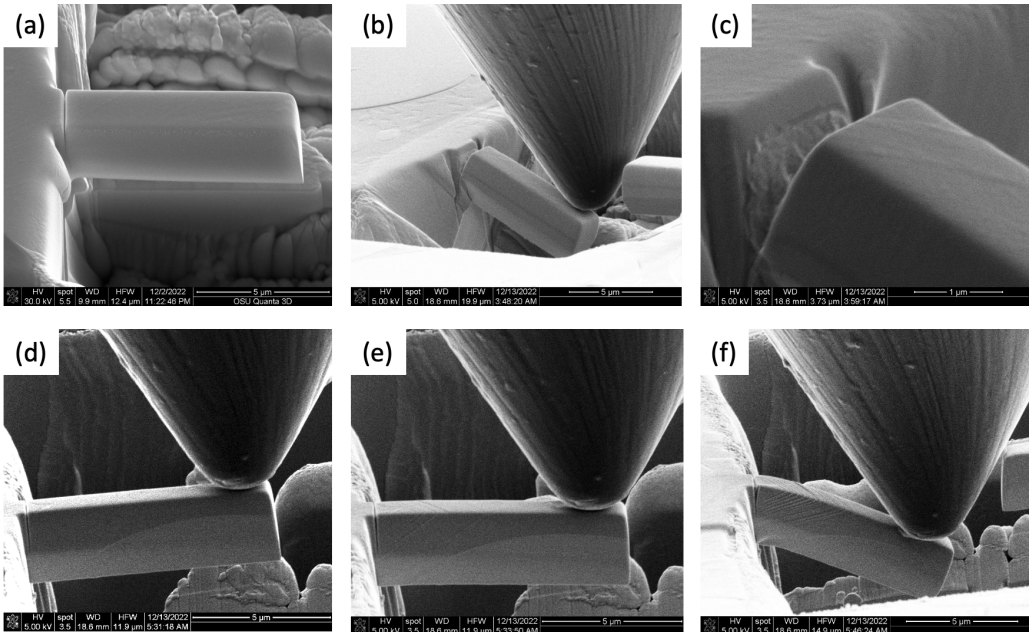

Figure 3. Snapshots during the in-situ bending tests of notched microcantilevers of W (a-c) and Ni (d-f).

Figure 4a and b present the load and stiffness curves with increasing displacement for the W and Ni cantilevers. In Figure 4a. the single-phase W microcantilever shows linear elastic and plastic behavior, whereas the single-phase Ni microcantilever shows almost flat load in the plastic regime with load drops due to slip bursts. In Figure 4b the initial rapid increase in stiffness happened as the indenter came in full contact with the microcantilever. A flat stiffness curve, as shown by the Ni microcantilever, corresponds to a constant notch depth through the test. On the other hand, stiffness decreases with the decreasing length of *(b-a)* in Figure 2, corresponding to fracture growth. The initial drop of stiffness in the W curve marks the fracture initiation.

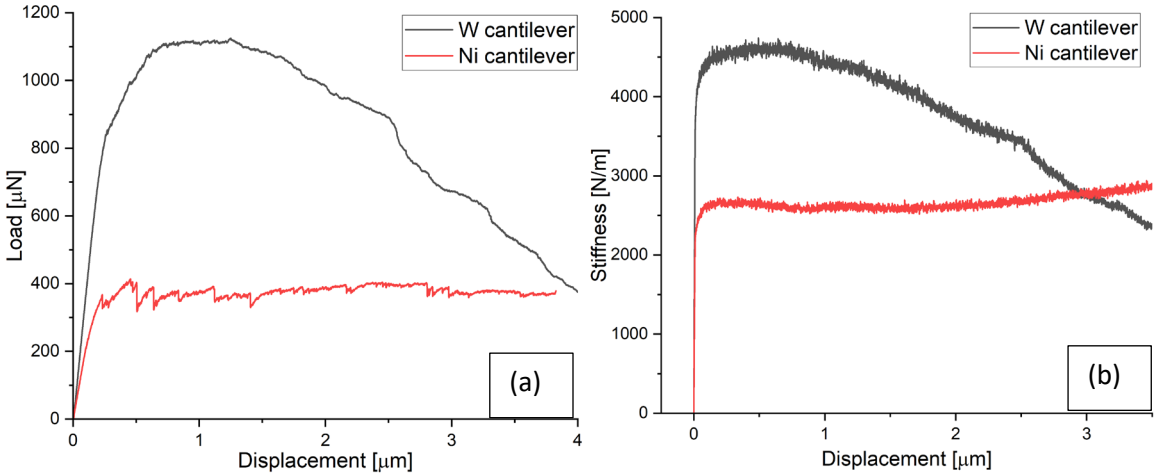

Figure 4. Single-phase W microcantilever (black) and single-phase Ni microcantilever (red) raw data load-displacement curves shown on the left and stiffness-displacement curves shown on the right.

The J-integral-based crack resistance was evaluated with the input of the raw data of load (P), displacement (u), time (s) and stiffness (k) according to elastic plastic fracture mechanics (EPFM) and using the iterative method described in ASTM International (ASTM) 1820 [14]:

$$J(a) = J^{el}(a) + J^{pl}(a) \quad (1)$$

$$J_n^{el} = \frac{K_{q,n}^2(1-v^2)}{E} \quad (2)$$

$$J_n^{pl} = \left\{J_{n-1}^{pl} + \frac{\eta_n}{b-a_n}\frac{A_n^{pl} - A_{n-1}^{pl}}{w}\right\}\left\{1 - \gamma_n\frac{a_n - a_{n-1}}{b - a_n}\right\} \quad (3)$$

where $J^{el}(a)$ and $J^{pl}(a)$ are the elastic and plastic J-integral values at specific crack lengths a. For W, the $J^{el}(a)$ was evaluated using the values of E = 410 GPa and *v* = 0.28. The number of iteration steps is *n* and the stress intensity factor K_q was evaluated following ASTM 399 [15]:

$$K_{q,n} = \frac{P_n L_1}{wb^{1.5}} f\left(\frac{a_n}{b}\right) \quad (4)$$

Here *b, w* and L_1 are geometric dimensions as shown in Figure 2, *P* is the Force and *f(a/b)* is a geometry factor specified for the cantilever geometry. For this study *f(a/b)* employs a polynomial function proposed by Alfreider *et al.* [16] in which the crack length a_n was found by the following correlation:

$$\left(\frac{a_n}{b}\right) = 1 - 2.897\left(\frac{k_n}{k_{max}}\right) + 10.618\left(\frac{k_n}{k_{max}}\right)^2 - 23.620\left(\frac{k_n}{k_{max}}\right)^3 + 24.497\left(\frac{k_n}{k_{max}}\right)^4 - 9.600\left(\frac{k_n}{k_{max}}\right)^5 \quad (5)$$

where a_n is the crack length, k_n is stiffness and k_{max} is the maximum value of stiffness obtained during the bending test.

The plastic part of the J-integral was calculated using geometry independent pre-factors η = 1.9 and γ = 0.9 as proposed for straight-trough notch bend specimen in ASTM 1820 [14]. The plastic work A^{pl} was computed numerically from the load-displacement curve for each point *n* where u_n, P_n and k_n are the respective displacement, load and stiffness shown in the following equation:

$$A_n^{pl} = A_n - A_n^{el} = \int_0^{u_n} P du - \frac{P_n^2}{2k_n} \quad (6)$$

Since J-integral is a function of the crack length *a*, using equation 5, the crack extension during the bending test was calculated using the measured stiffness *k*. Figure 5, shows the calculated crack length compared with the load-displacement curve for the single-phase W microcantilever, as well as a snapshot of W microcantilever cross-section after the bending test.

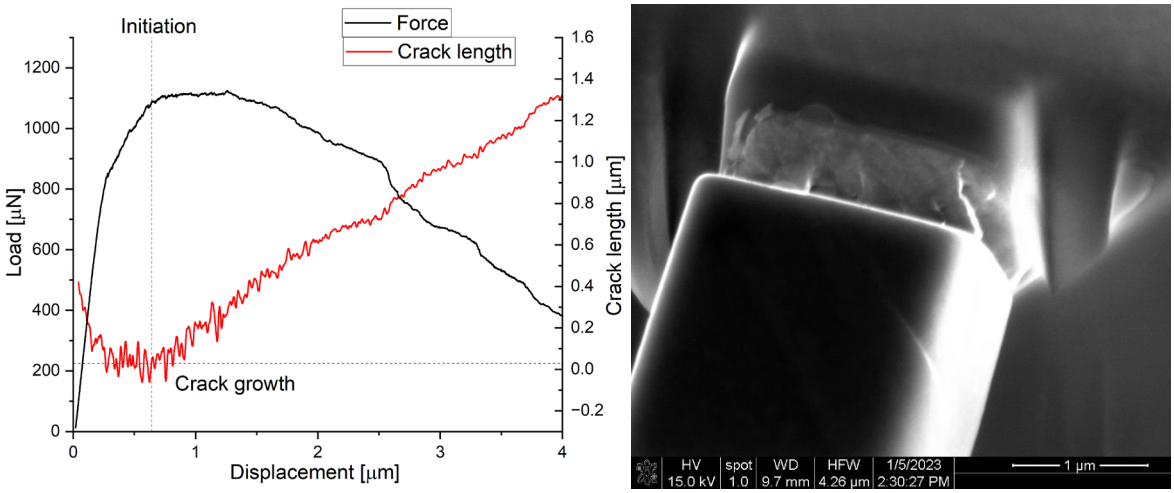

Figure 5. Load-displacement curve (black) and crack length curve (red) show crack initiation and growth shown on the left. Snapshot of W cantilever cross-section after bending test shown on the right.

J-Integral curve was generated from Eq. 1, where the J elastic component was calculated using Eq. 2, and the J plastic component was calculated from Eq. 3. Figure 6 shows the plot of the result and the J initiation obtained from the crack initiation value.

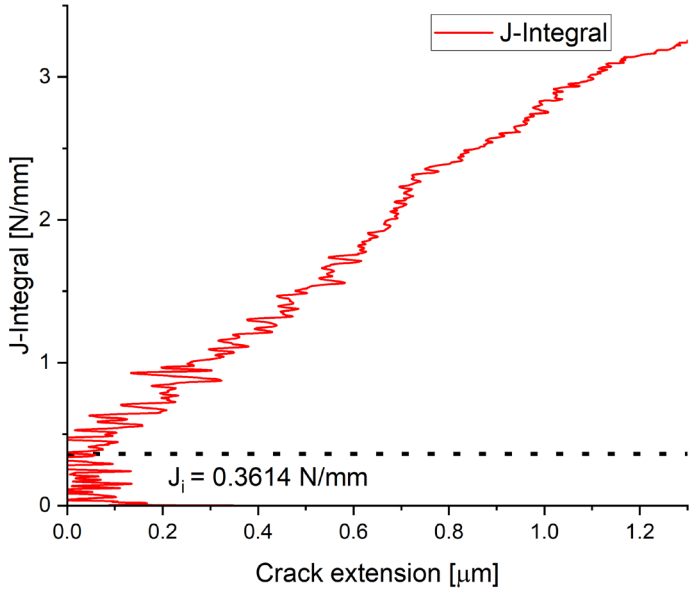

Figure 6. J(a)-integral results for single-phase W microcantilever, where J_i is the initiation J value.

The K toughness for fracture initiation was determined to be 12.7 $MPa \cdot m^{1/2}$ using the following equation:

$$K_i = \sqrt{\frac{EJ_i}{(1-\nu^2)}} \quad (7)$$

Future Work

In-situ displacement controlled bending tests were performed on a single-phase W and Ni straight-trough notch microcantilevers. Fracture initiation and plastic growth were observed in the W microcantilever along the {011} crack plane. While for the single-phase Ni microcantilever, slip-band development without cracking was observed because of its ductile characteristics. The high surface-volume ratio favors the escape of dislocations without dislocation piling up. As a result, plastic deposition of energy prevails over the formation of new fracture surfaces. This sample-size effect has led to the absence of fracture in the Ni microcantilever, and the high J-integral in W as shown in Figure 6. On the other hand, the fracture initiation toughness of W obtained by the microcantilever bending test is in good agreement with literature [12].

The preliminary examination proved the concept of J-integral- based crack resistance approach using microcantilever bending tests. Crack evolution can be derived from the measured stiffness from the CSM nanoindentation measurement. The results are in good agreement with that of Bohnert *el al.* [12] who took into consideration the house-shape geometry for the J-integral-based crack resistance calculation and used similar a/b and w/b ratios, which are the predominant factors influencing the fracture behavior in straight-trough notch microcantilevers [11]. It is worth noting that the geometry factor function and the crack length-stiffness correlation are sensitive to the specimen geometry. Rectangular-shaped microcantilevers with simpler geometry will be fabricated in future experiments in the hope of improving the accuracy and reliability of the fracture toughness values.

The future work includes tuning up the testing method for improved reliability and accuracy, applying this microscopic fracture toughness testing to W/Ni interface, and investigating radiation effects on fracture property changes in this W90 alloy. The methodology tunning up will focus on sample geometry and fabrication procedure optimization, calibration of the stiffness-notch depth relationships, and understanding the loading rate effects on plasticity. The main challenge in applying this microscopic fracture toughness testing to W/Ni interface is the plasticity in Ni, as suggested by the results of Ni microcantilevers reported above. We propose to fabricate a microcantilever with a narrow Ni layer bounded between the tungsten segments to limit plasticity. Relationships among the measured interfacial toughness, width of the Ni ligament, and plastic energy dissipation will be generated and understood to allow for data extension. The developed and verified testing protocol will then be applied to helium-irradiated samples to characterize the fracture property change as a function of damage microstructure development.

Other Progresses

Different microscale sample geometries and testing protocols, including the above notched microcantilever bending, double-clamped beam deflection, and pillar compression, have been evaluated. Systematic comparison and evaluation has led to the choice of the notched microcantilever bending method.

This project has enabled the recruitment and training of Ana Garcia, a first-year Ph.D. student in the materials science program. With the project's support, Ana has finished her training on SEM, FIB, and nanomechanical testing and can work independently.

Acknowledgements

The research was supported by the Office of Fusion Energy Science, United States Department of Energy and performed under the Contract DE-AC05-76RL01830. The authors acknowledge Ramprashad Prabhakaran for providing the samples and James V. Haag IV and Weilin Jiang for meaningful discussion.

References

[1.] Alam ME, Odette GR (2020) On the remarkable fracture toughness of 90 to 97W-NiFe alloys revealing powerful new ductile phase toughening mechanisms. *Acta Materialia*, 186:324–340. https://doi.org/10.1016/j.actamat.2020.01.012.

[2.] Haag JV, Edwards DJ, Henager CH, Setyawan W, Wang J, Murayama M (2021) Characterization of ductile phase toughening mechanisms in a hot-rolled tungsten heavy alloy. *Acta Materialia*, 204:116523. https://doi.org/10.1016/j.actamat.2020.116523.

[3.] Jiang W, Zhang D, Li D, Heo J, Wang Z, Zhang L, Overman N, Varga T, Hu Z, Wang X, Shao L, Setyawan W (2022) Behavior of helium cavities in ion-irradiated W-Ni-Fe ductile-phase toughened tungsten. *Journal of Nuclear Materials*, 561:153565. https://doi.org/10.1016/j.jnucmat.2022.153565.

[4.] Hosemann P (2018) Small-scale mechanical testing on nuclear materials: bridging the experimental length-scale gap. *Scripta Materialia*, 143:161–168. https://doi.org/10.1016/j.scriptamat.2017.04.026.

[5.] Chen T, He L, Cullison MH, Hay C, Burns J, Wu Y, Tan L (2020) The correlation between microstructure and nanoindentation property of neutron-irradiated austenitic alloy D9. *Acta Materialia*, 195:433–445. https://doi.org/10.1016/j.actamat.2020.05.020.

[6.] Armstrong DEJ, Hardie CD, Gibson JSKL, Bushby AJ, Edmondson PD, Roberts SG (2015) Small-scale characterization of irradiated nuclear materials: Part II nanoindentation and micro-cantilever testing of ion irradiated nuclear materials. *Journal of Nuclear Materials*, 462:374–381. https://doi.org/10.1016/j.jnucmat.2015.01.053.

[7.] Chen T, Frazer D, Cullison M, Teng F, Mo K, Cappia F (2023) The effects of radiation-induced grain subdivision and dislocations on the fracture properties of uranium dioxide. *Journal of Nuclear Materials*, Accepted.

[8.] Pippan R, Wurster S, Kiener D (2018) Fracture mechanics of micro samples: Fundamental considerations. *Materials & Design*, 159:252–267. https://doi.org/10.1016/j.matdes.2018.09.004.

[9.] Jaya BN, Jayaram V (2016) Fracture Testing at Small-Length Scales: From Plasticity in Si to Brittleness in Pt. *JOM*, 68(1):94–108. https://doi.org/10.1007/s11837-015-1489-2.

[10.] Ast J, Göken M, Durst K (2017) Size-dependent fracture toughness of tungsten. *Acta Materialia*, 138:198–211. https://doi.org/10.1016/j.actamat.2017.07.030.

[11.] Liu X, Athanasiou CE, Padture NP, Sheldon BW, Gao H (2021) Knowledge extraction and transfer in data-driven fracture mechanics. *Proceedings of the National Academy of Sciences*, 118(23):e2104765118. https://doi.org/10.1073/pnas.2104765118.

[12.] Bohnert C, Schmitt NJ, Weygand SM, Kraft O, Schwaiger R (2016) Fracture toughness characterization of single-crystalline tungsten using notched micro-cantilever specimens. *International Journal of Plasticity*, 81:1–17. https://doi.org/10.1016/j.ijplas.2016.01.014.

[13.] Lavenstein S, Crawford B, Sim G-D, Shade PA, Woodward C, El-Awady JA (2018) High frequency in situ fatigue response of Ni-base superalloy René-N5 microcrystals. *Acta Materialia*, 144:154–163. https://doi.org/10.1016/j.actamat.2017.10.049.

[14.] ASTM (2013) ASTM Standard E1820-13, Standard Test Method for Measurement of Fracture Toughness. *ASTM*.

[15.] ASTM (2009) Standard E399-09, Standard Test Method for Linear-Elastic Plane-Strain Fracture Toughness KIC of Metallic Materials. *ASTM*.

[16.] Alfreider M, Kozic D, Kolednik O, Kiener D (2018) In-situ elastic-plastic fracture mechanics on the microscale by means of continuous dynamical testing. *Materials & Design*, 148:177–187. https://doi.org/10.1016/j.matdes.2018.03.051.

4.6 STATUS OF THE ELEVATED TEMPERATURE MECHANICAL TEST FACILITY, HOT ROLLING AND TENSILE TESTING AT PACIFIC NORTHWEST NATIONAL LABORATORY

—R. Prabhakaran, J. V. Haag IV, W. Setyawan (Pacific Northwest National Laboratory)

OBJECTIVE

The objective of this task is to setup an elevated temperature mechanical test facility at Pacific Northwest National Laboratory (PNNL), design appropriate mechanical test fixtures, perform hot rolling (with different thickness reductions) to obtain tensile samples and conduct various types of mechanical testing (microhardness, tensile, bend, fracture toughness) to understand the mechanical behavior of ductile phase toughened tungsten heavy alloys, such as W-NiFe, for applications in plasma-facing components.

SUMMARY

This report summarizes the status of the elevated temperature mechanical test facility setup, hot rolling operations (with different thickness reductions) to fabricate a new batch of ductile phase-toughened (DPT) W-NiFe tensile specimens to obtain elevated temperature mechanical properties, and tensile testing of 90W (as sintered and hot rolled), 95W (as sintered) and 97W (as sintered) alloys at PNNL.

PROGRESS AND STATUS

Introduction

Tungsten (W) is a promising candidate material for plasma-facing components (PFCs) due to its excellent high-temperature strength, low sputtering rate, good thermal conductivity, and high melting temperature. [1-2] However, the potential application of tungsten as a structural material in PFCs is limited due to its low ductility which will further degrade after irradiation. [3] Therefore, introducing a ductile phase (DP) to develop a tungsten composite could serve as an alternative route to overcome its limitations. The DPT is a fracture toughness improvement concept that is being utilized to develop tungsten-based composites for fusion reactor divertor and plasma-facing materials. Liquid-phase sintered tungsten heavy metal alloys (WHAs), due to their balance of strength, ductility and toughness, are being considered to be a suitable alternative to monolithic polycrystalline W for fusion applications.

The low melting point of the alloying elements Fe and Ni being 1538°C and 1455°C, respectively, could restrict the operational space. However, in order to avoid recrystallisation of tungsten to preserve its original mechanical properties, the temperature should be kept anyway below 1300°C, which means that the improvement in ductility and toughness by using Fe and Ni remains expected, though to a lesser extent compared to room-temperature mechanical property improvement. [4] Determining the mechanical properties of DPT-W at elevated temperatures is indeed an important aim of this research.

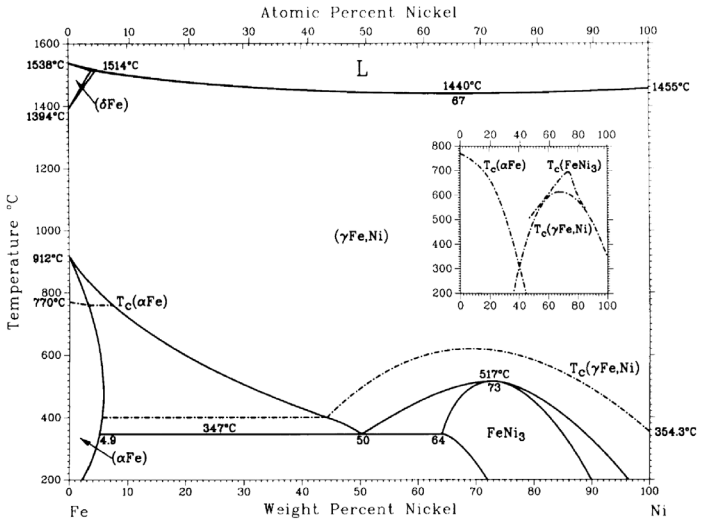

Figure 1. Iron-Nickel phase diagram [19].

Different thermomechanical plastic deformation processing routes, such as hot-rolling (HR), extrusion and swaging, can increase the strength of WHAs. [5-11] Researchers at PNNL have characterized the effects of the composite architecture on deep notch bend bar toughness for a 90 wt.% W–Fe–Ni WHA, hot rolled to different thickness reductions of 62, 74 and 87%. [12] As per our previous study, the deformed W and DP phases that form a 'brick-and-mortar (BAM)' like microstructure could improve strength by hot working, while enhancing the ductility and toughness, by creating a more distributed damage zone under deep notch bar loading. [12,13]

As per the literature, the maximum service temperature for divertors is likely 1200-1300°C [4,14,15], and hence it is critical to obtain the elevated temperature mechanical properties of WHA. The issue of W fuzz has not been fully resolved and, if significant, it might lower the maximum temperature to about 700°C. [16-18] The melting temperature of the DP phase (near Ni:Fe weight ratio of 7:3) is ~1440C, as shown in Figure 1. [19]

Previous mechanical tests have been performed at room temperature using an Instron 5582 servomechanical test frame equipped with an Epsilon ONE optical extensometer, and the results could be found in our previous reports. [20-22] Currently, efforts are ongoing to understand the mechanical behavior of DPT W-NiFe alloys at elevated temperatures (590°C, 880°C and ~1200°C) and this report is focused in documenting the status of the elevated temperature mechanical test facility setup, hot rolling operations to fabricate a new batch of tensile specimens to obtain elevated temperature mechanical properties, and tensile testing at PNNL.

Experimental Procedure

Elevated Temperature Mechanical Test Facility Setup

Instron 8801 Servohydraulic Mechanical Test System

Instron 8801 is a compact servohydraulic fatigue testing system that could be employed to perform static and dynamic mechanical tests. This frame has been used to evaluate several materials at ambient and elevated temperatures (600°C) using a Mellen clamshell furnace that can be purged with argon gas (to minimize oxidation). This system has both the Bluehill Universal and WaveMatrix software for performing

axial static and dynamics tests. Additional information on this test frame can be found in the previous report. [23] This mechanical test system is available for performing elevated temperature mechanical testing.

Figure 2. The MRF furnace (1600°C) along with Instron 8801 mechanical test frame and tensile test fixture.

MRF Model M-4x6-M-1600-V&G Furnace

The PNNL has a Materials Research Furnaces, Inc. (MRF) Model M-4x6-M-1600-V&G front-loading furnace with a usable work zone of 3.5" dia. x 4.0" high, and a maximum operating temperature of 1600°C. The hot zone is a 180° split design with tungsten mesh heating elements for operation in vacuum (50-100 milliTORR) and inert gas (Ar, N_2 or Ar/O_2 gas mixture). Additional information about this furnace can be found in previous reports. [23, 24]

This furnace was purchased several decades ago and has not been used for an exceptionally long time. Recently, efforts were made to replace multiple components such as tungsten mesh heating elements, water-cooled power cords, water lines, argon lines, water sensor, and vacuum gage. After demonstrating the furnace's safety features, necessary approvals were obtained from various subject matter experts (SMEs), in order to turn on the furnace and check its heating elements. Trial testing of the furnace was performed for temperatures up to 600°C, since the initial batch of tensile testing are being planned to be performed at 590°C. The furnace vacuum level at 600°C was about 9.5 mTorr (without fixture and sample). Figure 2 shows the photos of the MRF furnace along with the Instron 8801 mechanical test frame.

Elevated Temperature Tensile Test Fixture

Currently, efforts are also ongoing to perform tensile testing of DPT W-NiFe (as-sintered and rolled) at 590°C (~1/2 Tm, where Tm is the melting temperature of the ductile phase), 880°C (~2/3 Tm of the ductile phase) and slightly higher (1000-1200°C). The MRF furnace has a usable work zone of 3.5" dia. x 4.0" high. It has water-cooled pull rods (17-4 PH stainless steel) on either side of the furnace, and a tensile fixture that can withstand elevated temperatures without any water cooling is required. The silicon carbide (SiC) fixtures can perform well at these elevated temperatures (>1000°C), however, the cost of machining is high, and durability is low, especially under tensile loading. During 2022, efforts were made to identify a metallic material and fixture design that would allow us to utilize the furnace and perform tensile testing at the maximum possible operating temperature (based on a metallic fixture).

Extensive research was conducted by looking at the literature and communicating with various vendors of mechanical test equipment to identify a suitable metallic fixture material. Based upon material availability,

machinability, cost, and mechanical properties at elevated temperatures, titanium-zirconium-molybdenum (TZM) was chosen as the fixture material. The acronym TZM stands for the molybdenum alloy 'titanium-zirconium-molybdenum', and is a molybdenum alloy containing 0.5% titanium, 0.08% zirconium, 0.02% carbon and the balance molybdenum. The alloy TZM has a higher recrystallization temperature than pure molybdenum, thus reducing the likelihood of embrittlement at higher temperatures. And in elevated temperature applications, TZM's higher strength, hardness, creep resistance and ductility ensure that it will not weaken or soften.[25]

According to the vendor (Rembar), the recommended temperatures for using TZM is between 700 and 1400°C. [25] However, like pure molybdenum, TZM begins to oxidize at 400°C and oxides rapidly in oxidizing atmospheres above 500°C. Similar in strength to pure molybdenum at room temperatures, at operating temperatures exceeding the recrystallization temperature of pure molybdenum (900 to 1100°C), TZM is much stronger. And in load-bearing applications exceeding 1300°C, TZM is twice as strong as pure molybdenum, as shown in Figure 3 (left). [25] The TZM material was procured from Ed Fagan Inc., and the tensile fixture fabrication was performed at PNNL. The fabricated TZM tensile fixture is shown in Figure 3 (right).

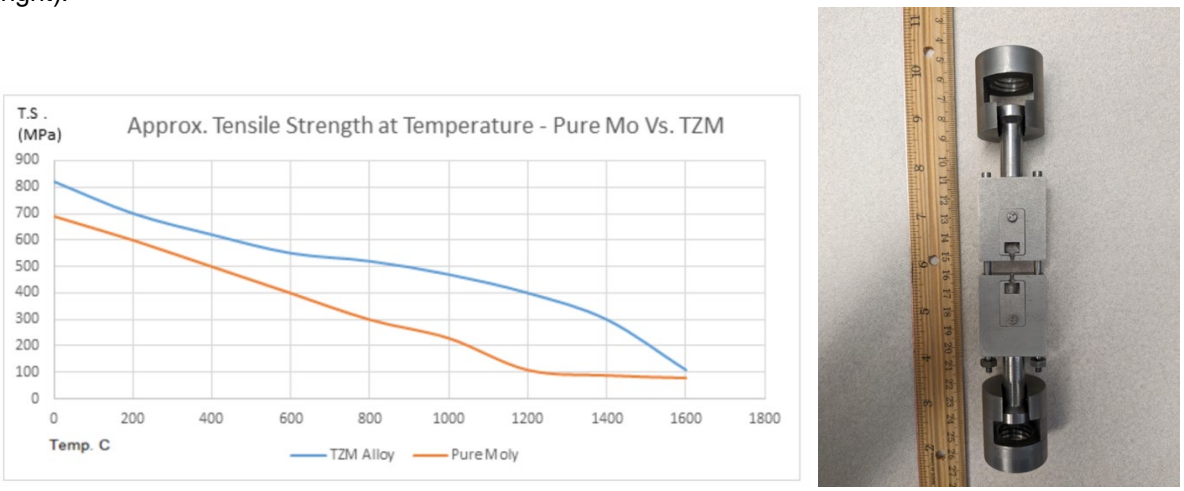

Figure 3. Left: Tensile strength of TZM and pure Mo at various temperatures [25]; Right: Shoulder-loaded TZM tensile fixture.

Procurement of 90 wt.%, 95 wt.% and 97 wt.% W–Fe–Ni alloys

Sintered 90 wt.%, 95 wt.% and 97 wt.% W-Fe–Ni alloys were procured from MiTech, in order to fabricate tensile specimens for room and elevated temperature mechanical testing. Table 1 shows the lot information of these WHA alloys.

Table 1. Sintered W–Fe–Ni alloys procured from MiTech

Material	Vendor	Vendor Code	Lot Number	Lot Chemistry (wt.%)
90W	MiTech	HD 17D	36124	90.37 W; 6.82 Ni and 2.81 Fe
95W	MiTech	HD 18D	36843	95.11 W; 3.45 Ni; 1.44 Fe
97W	MiTech	HD 18.5	36910	97.08 W; 2.05 Ni; 0.87 Fe

Hot rolling of 90 wt.% W–Fe–Ni WHA

Table 2. Hot rolling schedule of sintered 90 wt.% W–Fe–Ni alloy

Target Reduction 10% per pass									
Pass #	Thickness (Inches)		Buck (Inches)		Mill Set	Reduction %		Notes	
	Desired	Actual	Estimate	Actual	(inches)	Pass	Total		
Start		1.00						Started with 2 pieces of nearly identical size 1" ±.002"	
1	0.900	0.891	0.025	0.016	0.875	10.90%	10.90%	1150C 15 min preheat	
2	0.802	0.798	0.020	0.016	0.782	10.44%	20.20%	1150C 10 min preheat	
Annealed 3 hours 1200C, Ar Purge then 100% H2					2 bars on 3/23/22				
		0.794						Remeasured after cooling, annealing and descaling with a wire brush	
3	0.715	0.718	0.020	0.015	0.699	9.57%	28.20%	900C 15 min preheat	
4	0.646	0.652	0.020	0.014	0.630	9.19%	34.80%	900C 6 min preheat	
5	0.587	0.588	0.015	0.020	0.565	9.82%	41.20%	900C 6 min preheat	
Annealed 3 hours 1200C, Ar Purge then 100% H2					2 bars on 3/29/22				
		0.584						Remeasured after cooling, annealing and descaling with a wire brush	
6	0.526	0.528	0.020	0.022	0.506	9.59%	47.20%	900C 15 min preheat	
7	0.476	0.477	0.022	0.021	0.454	9.66%	52.30%	900C 6 min preheat	
8	0.429	0.426	0.022	0.019	0.407	10.69%	57.40%	900C 6 min preheat	take this as the 57R
Annealed 3 hours 1200C, Ar Purge then 100% H2 2 bars on 4/6/22								Only 1 piece continued to next rolling steps.	
		0.422						Remeasured after cooling, annealing and descaling with a wire brush	
9	0.380	0.380	0.022	0.022	0.358	9.95%	62.00%	900C 15 min preheat	
10	0.342	0.346	0.022	0.026	0.320	8.95%	65.40%	900C 6 min preheat	
11	0.311	0.311	0.028	0.028	0.283	10.12%	68.90%	900C 6 min preheat	Some edge cracking was noticed
Annealed 3 hours 1200C, Ar Purge then 100% H2 1 bar 4/11/22									
		0.300						Remeasured after cooling, annealing and descaling with a wire brush	
12	0.270	0.273	0.022	0.025	0.248	9.00%	72.70%	900C 15 min preheat	
13	0.246	0.243	0.025	0.022	0.221	10.99%	75.70%	900C 6 min preheat	
14	0.219	0.222	0.022	0.019	0.197	8.64%	77.80%	900C 6 min preheat	take this as the 78R
Annealed 3 hours 1200C in Ar Purge then 100% H2 2 bars 4/15/22								The rolled strip was cut in half, only one half was rolled to final dimension	
		0.215						Remeasured after cooling, annealing and descaling with a wire brush.	
16	0.194	0.192	0.025	0.023	0.169	10.70%	80.80%	900C 15 min preheat	
17	0.173	0.175	0.025	0.027	0.148	8.85%	82.50%	900C 6 min preheat	
18	0.157	0.155	0.030	0.028	0.127	11.43%	84.50%	900C 6 min preheat	
19	0.150	0.145	0.030	0.025	0.120	6.45%	85.50%	900C 6 min preheat	take this as the 86R
Annealed 3 hours 1200C, Ar Purge then 100% H2 1 bar 4/20/22									
		0.139				86.10%		Final dimension after annealing and descaling	
Average reduction per pass						9.21%			
Then, the 57R, 78R, and 86R final materials were degassed to remove H2, 1 hr at 900 C									

Hot rolling was performed on the sintered 90 wt.% W–Fe–Ni alloy procured from MiTech (HD 17D; Lot # 36124). In order to perform hot rolling, the material (approximately 2” thick x 2” wide x 4” long) was sectioned into approximately 1” thick x 1” wide x 2.25” long pieces.

Prior to hot rolling, samples were preheated in a Lucifer model 7GT-M48 furnace (see Figure 4) at 1150°C for a minimum of 15 minutes. Hot rolling was performed employing a Waterbury Farrell Two High/Four High 755 Rolling Mill using a 10% reduction for each pass (Table 2), as shown in Figure 4. During the hot rolling process, the rolled material was annealed (purged with Argon for 70 minutes, followed by hydrogen purge and heating cycle; ramp up @5°C/min; dwell at 1200°C for 3 hours; ramp down via natural cooling @ 3-5°C/min; hydrogen purge continued until the furnace reached under 100°C while cooling down; followed by

70 minutes of Argon purge) using a CM Furnaces (CM) model 1516GSH2FL furnace (see Figure 5) during various stages of the rolling process, as shown in the Table 2. The hot rolled samples (with different thickness reductions: 57R, 78R and 86R) were finally degassed (to remove hydrogen) using a Thermal Technologies/Brew furnace (model 121224MMS; see Figure 5) at 908°C for 60 minutes (vacuum level before heating was around 2E-4 mTorr; ramp up rate @ 3-4°C/min and ramp down via natural cooling @ ~4°C/min).

Two samples were hot rolled as shown in the Table 2. It took 8 passes to obtain 57R samples. After annealing, one of these 57R samples were stored separately for hydrogen degassing and tensile specimen fabrication. Additional hot rolling was performed on the second 57R sample. Some edge cracking was observed after 11th pass (68.9% reduction). This sample was hot rolled further and successfully obtained 78R sample after 14 passes (total). Some edge cracking was observed on one half of the 78R sample. This 78R sample was sectioned into two pieces and annealed was performed. One half of the sample with some edge cracking was stored separately as a 78R sample for hydrogen degassing and tensile specimen fabrication. The second half (with no edge cracking) of the 78R sample was hot rolled further to obtain an 86R sample after 19 passes (total). This 86R sample was then annealed. Finally, the 86R was degassed to remove hydrogen along with 78R and 57R hot rolled WHA samples. Figure 6 shows 90 wt.% W–Fe–Ni samples at the various stages of hot rolling and annealing process. Figure 7 shows hot rolled (with different thickness reductions: 57R, 78R and 86R) and annealed 90 wt.% W–Fe–Ni plates/foils.

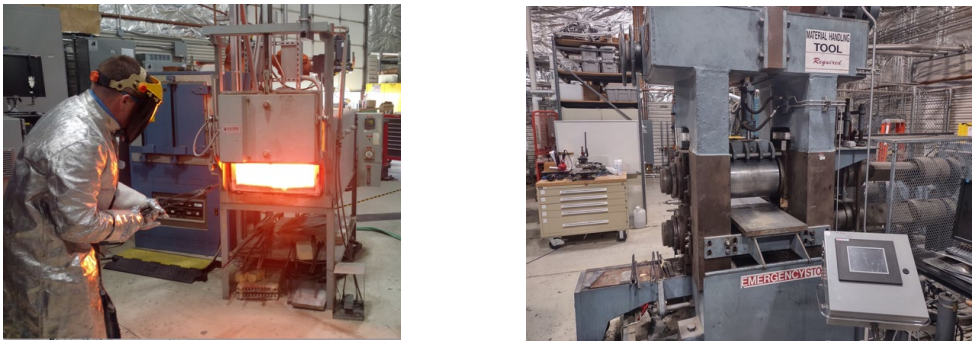

Figure 4. Preheating Lucifer Furnace and Waterbury Farrell Rolling Mill.

Figure 5. The CM Furnace (annealing) and Thermal Technologies/Brew Furnace for degassing hydrogen.

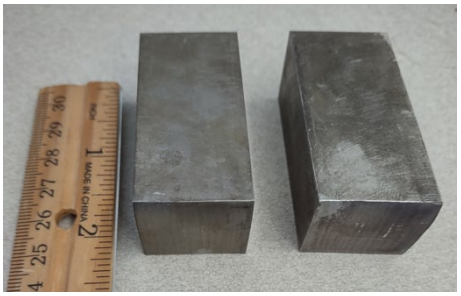

(a) Before hot rolling

(b) 2nd pass 20.2% reduction

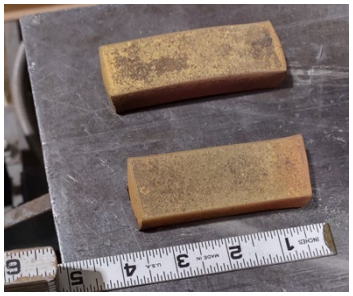

(c) 5th pass 41.2% reduction

(d) 8th pass 57.8% reduction post anneal

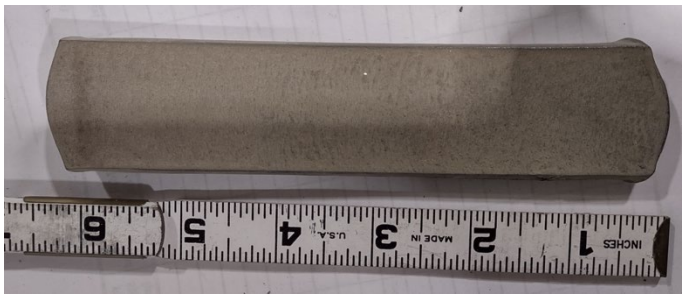

(e) 11th pass 68.9% reduction pre anneal

(f)14th pass 77.8% reduction pre anneal sectioned

(g) 19th pass 85.5% reduction pre anneal

Figure 6. Sintered 90 wt.% W–Fe–Ni samples before and during hot rolling.

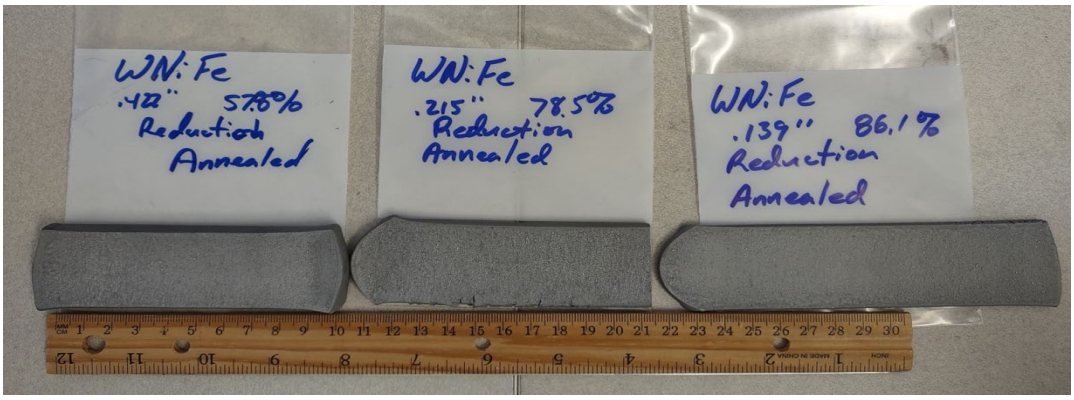

Figure 7. Hot rolled (thickness reductions: 57R, 78R and 86R) and annealed 90W–Fe–Ni plates/foils.

Tensile Specimen Fabrication

Sub-size tensile specimens, as shown in Figure 8, were machined (single orientation) using an EDM (electrical discharge machining) from as sintered 90W, 95W and 97W samples. Tensile specimens (multiple orientations, as shown in Figure 9) were also fabricated from hot rolled (57R, 78R and 86R), annealed and degassed 90 wt.% W–Fe–Ni plates/foils. Tensile specimens were fabricated in order to perform tensile testing at room and elevated temperatures (590°C, 880°C and higher). The nominal gage width, gage thickness and reduced length of a sub-size tensile specimen are 1.684 mm, 0.762 mm and 5.029 mm, respectively. The total length and shoulder width of the sub-size tensile specimen are 16.104 mm and 4.013 mm, respectively. Tensile specimens were polished (top and bottom wide faces; not on thickness direction) to at least 1200 grit condition to remove minor cracks and local residual stresses die to EDM.

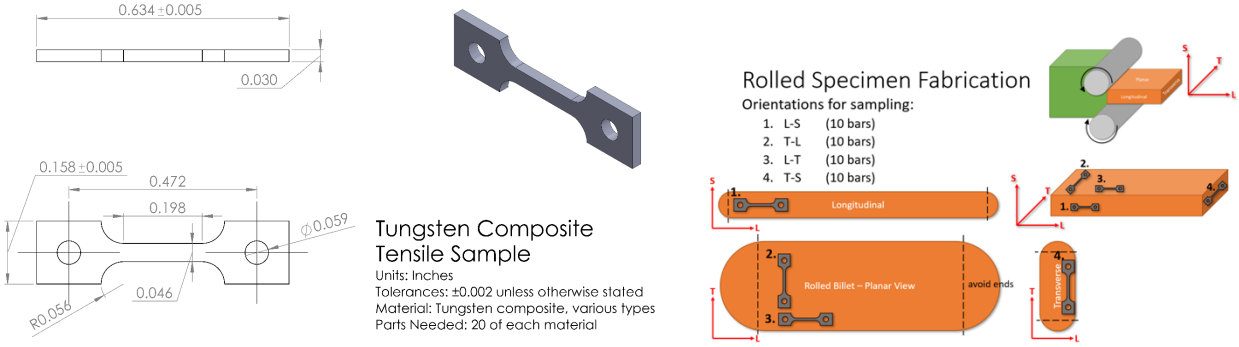

Figure 8. Left: Subsize tensile specimen design; Right: Specimen orientations for rolled specimens.

Tensile Testing at Room Temperature

An Instron 8801 servo-hydraulic mechanical testing system was utilized for conducting tensile testing in the displacement control mode. The specimen gage width and thickness were measured using calipers prior to tensile testing. The displacement rate during tensile testing was constant at a crosshead speed of 0.06 mm/min (1 micron/s), which can be converted to an estimated strain rate of 1.99E-4/s for specimens with a 5.029 mm reduced length. Subsize tensile specimens were shoulder loaded instead of pin loaded to avoid tear out at the pin hole and warping of the pins.

ASTM International (ASTM) Standard E8/E8M was utilized for performing tensile testing and data analysis.[26] Load, displacement and time were recorded during tensile testing. The displacement was measured from the crosshead movement. The load data was obtained from the load cell. Engineering stress-strain curves were generated by using load-displacement data recorded during testing along with initial specimen gage width, thickness and reduced length. These curves were used to determine 0.2% offset yield strength (YS), ultimate tensile strength (UTS), uniform elongation (UE), and total elongation (TE). Table 3 shows the room temperature tensile properties of as-sintered 90W, 95W and 97W W–Fe–Ni alloys.

The 0.2% offset YS values were similar for all samples, and it was slightly lower for 97W. However, the UTS increased significantly as W% reduced (see Figure 9). There is no significant difference between uniform and total elongations for a particular %W, and these values (UE and TE) increased significantly as W% reduced (i.e., as the percent of ductile phase increased), as expected. Representative engineering stress vs strain curves are shown in Figure 10. These are all preliminary results and additional testing (such as increasing the number of tensile specimens per condition; grind and polish the thickness side in addition to the top and bottom faces of specimens) and analysis will soon be completed.

Tables 4, 5 and 6 show the room temperature tensile properties of 90W-57R, 90W-78R and 90W-86R W–Fe–Ni samples in two orientations (#3 refers to L-T and #2 refers to T-L; see Figures 8 and 9). Representative engineering stress vs strain curves for various conditions are shown in Figures 10-12. As the rolling reduction was increased from 0R→57R→78R→86R, the YS and UTS increased along with it. Various thermomechanical plastic deformation processing routes such as hot rolling, extrusion, and swaging, can increase the strength of WHAs. [5-11] The difference between the uniform and total elongation gradually improved as the rolling reduction was increased. In addition, both UE and TE increased (more significant at 57R and 86R) as the rolling reduction was increased.

Table 3. Room temperature tensile properties of as sintered 90W, 95W and 97W W–Fe–Ni alloys

Sample Information	Specimen ID	0.2% offset Yield Strength (MPa)	UTS (MPa)	Uniform Elongation (%)	Total Elongation (%)
90W-0R_MiTech_Lot 36124	Sp 1	650	875	10.10	10.15
	Sp 2	650	855	8.65	9.00
	Sp 3	650	865	10.90	11.37
	AVERAGE	650	865	9.88	10.17
	SD	0	8	0.93	0.97
95W-0R-MiTech_Lot 36843	Sp 1	665	809	5.80	5.97
	Sp 2	655	785	4.45	4.65
	Sp 3	650	765	3.32	3.87
	Sp 4	655	779	3.83	4.27
	AVERAGE	656	785	4.35	4.69
	SD	5	16	0.93	0.79
97W-0R_MiTech_Lot 36910	Sp 1	632	661	0.51	0.70
	Sp 2	638	671	0.90	1.10
	Sp 3	652	681	1.00	1.20
	AVERAGE	641	671	0.80	1.00
	SD	8	8	0.21	0.22

Table 4. Room temperature tensile properties of 90W-57R W–Fe–Ni alloy.

Sample Information	Specimen ID	0.2% offset Yield Strength (MPa)	UTS (MPa)	Uniform Elongation (%)	Total Elongation (%)
90W-57R_MiTech_Lot 36124_Orientation 2	Sp 1	755	971	12.50	13.15
	Sp 2	767	985	14.48	17.82
	AVERAGE	761	978	13.49	15.49
	SD	6	7	0.99	2.34
90W-57R_MiTech_Lot 36124_Orientation 3	Sp 1	760	952	12.28	14.30
	Sp 2	758	945	13.75	17.40
	AVERAGE	759	949	13.02	15.85
	SD	1	4	0.74	1.55

Table 5. Room temperature tensile properties of 90W-78R W–Fe–Ni alloy

Sample Information	Specimen ID	0.2% offset Yield Strength (MPa)	UTS (MPa)	Uniform Elongation (%)	Total Elongation (%)
90W-78R_MiTech_Lot 36124_Orientation 2	Sp 1	845	1042	12.64	14.05
	Sp 2	835	1041	13.15	14.30
	AVERAGE	840	1042	12.90	14.18
	SD	5	1	0.26	0.13
90W-78R_MiTech_Lot 36124_Orientation 3	Sp 1	810	980	13.28	15.95
	Sp 2	810	975	13.30	16.15
	AVERAGE	810	978	13.29	16.05
	SD	0	3	0.01	0.10

Table 6. Room temperature tensile properties of 90W-86R W–Fe–Ni alloy

Sample Information	Specimen ID	0.2% offset Yield Strength (MPa)	UTS (MPa)	Uniform Elongation (%)	Total Elongation (%)
90W-86R_MiTech_Lot 36124_Orientation 2	Sp 1	860	1050	14.82	19.72
	Sp 2	865	1055	14.40	17.00
	AVERAGE	863	1053	14.61	18.36
	SD	3	3	0.21	1.36
90W-86R_MiTech_Lot 36124_Orientation 3	Sp 1	825	1011	16.00	20.72
	Sp 2	852	1013	15.85	22.55
	Sp 3	810	995	15.40	22.57
	AVERAGE	829	1006	15.75	21.95
	SD	17	8	0.25	0.87

Researchers at PNNL have previously characterized the effects of the composite architecture on deep notch bend bar toughness for a 90 wt.% W–Fe–Ni WHA, hot rolled to different thickness reductions of 62, 74 and 87%. [12] As per our previous study, the deformed W and DP phases that form a BAM like microstructure could improve strength by hot working, while enhancing the ductility and toughness, by creating a more distributed damage zone under deep notch bar loading. [12,13]

Table 7 and Figure 9 shows the difference in tensile properties based upon two orientations (#3 and #2). These results showed that the properties remained quite similar for both orientations (#2 and #3), except UTS and TE that showed a smaller difference at higher rolling reductions.

Table 7. Difference in tensile properties based on orientations #3 (L-T) vs #2 (T-L) for 90W–Fe–Ni alloy

HR	Difference in YS (MPa)	Difference in UTS (MPa)	Difference in UE (%)	Difference in TE (%)
57%	-2	-30	-0.48	0.37
78%	-30	-64	0.40	1.88
86%	-34	-46	1.14	3.59

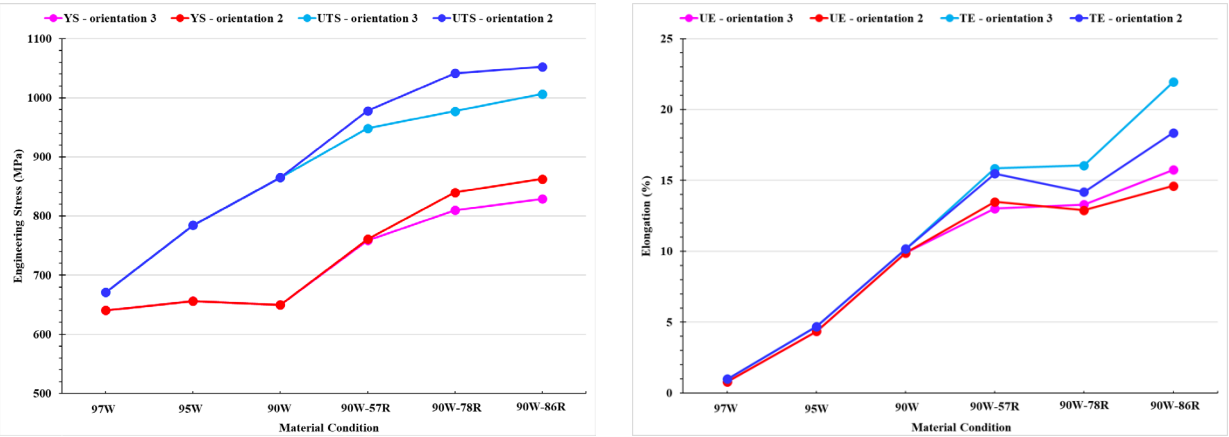

Figure 9. Left: 0.2% offset yield strength, ultimate tensile strength, uniform elongation, and total elongation of W-Fe-Ni alloys as a function W percent, hot rolling reduction and specimen orientation.

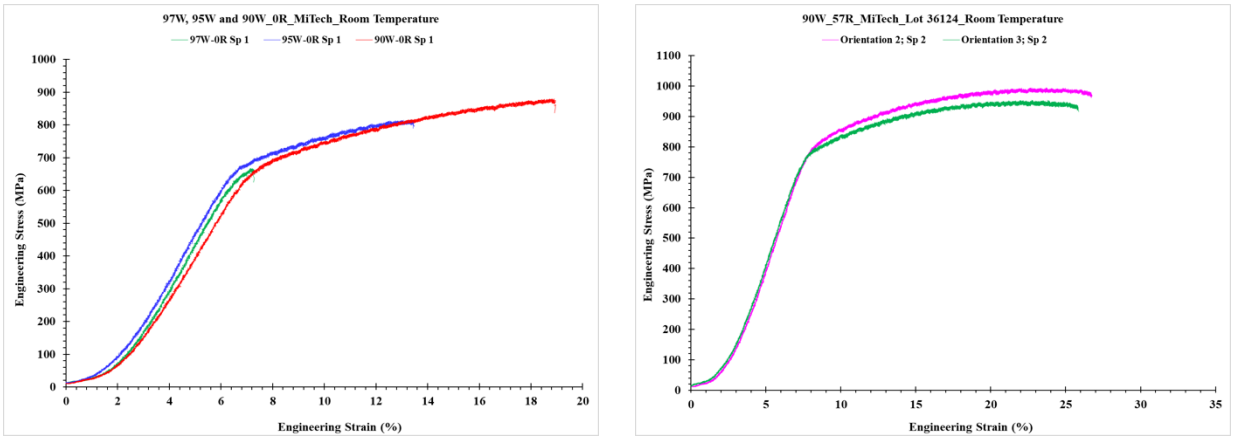

Figure 10. Representative engineering stress vs strain curves. Left: as sintered 97W, 95W and 90W WHA samples; Right: 90W-57R samples (orientations 2 and 3).

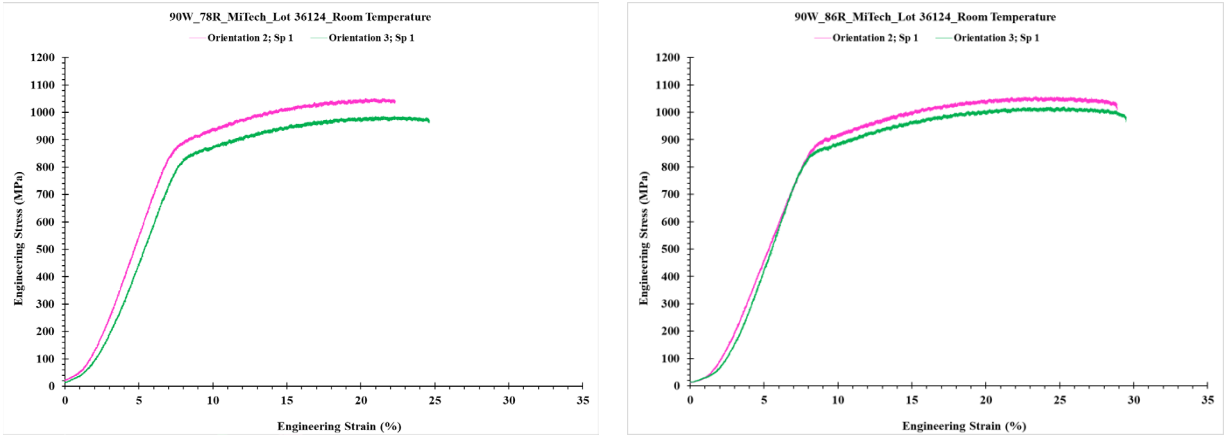

Figure 11. Representative engineering stress vs strain curves (orientations #2 and #3). Left: 90W-78R WHA samples; Right: 90W-86R samples.

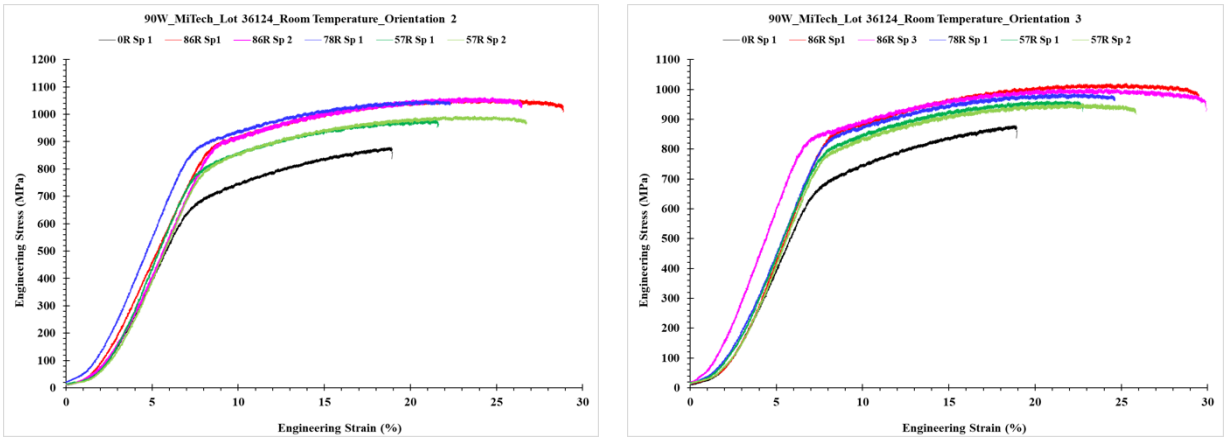

Figure 12. Representative engineering stress vs strain curves for 90W-0R, 90W-57R, 90W-78R and 90W-86R samples (orientations #2 and #3).

Future Work

The following activities are being planned to be performed during 2023:

- Publish a journal article based on existing room temperature tensile testing (PNNL sintered 90W, 90W, 95W and 97W from different vendors, and 90W-87R) and microstructural data.
- Perform additional tensile testing of polished 90W, 95W and 97W as-sintered samples (grind and polish the thickness side too, besides the top and bottom faces) at room temperature.
- Perform additional tensile testing of polished 90W-57R, 78R and 86R hot rolled samples (grind and polish the thickness side too, besides the top and bottom faces) at room temperature.
- Perform elevated temperature (590°C, 880°C and higher) tensile testing on as sintered and hot rolled samples.
- Perform additional hot rolling to fabricate fracture toughness samples.
- Perform room and elevated temperature toughness testing of as sintered and hot rolled samples.

Acknowledgments

The authors would like to acknowledge the support of Mark Rhodes for performing hot rolling of 90W WHA samples and coordinating the annealing and degassing operations. This research was supported by the United States Department of Energy (US DOE), Office of Science, Office of Fusion Energy Sciences, through Contract No. AT2030110-13784 and was performed at the PNNL, which is operated by Battelle for the US DOE under Contract No. DE-AC05-76RL0-1830.

References

[1.] S. Wurster, et al., *Recent progress in R&D on tungsten alloys for divertor structural and plasma facing materials.* Journal of Nuclear Materials, 442 (1-3): p. S181-S189, 2013.

[2.] D. Stork, et al., *Developing structural, high-heat flux and plasma facing materials for a near-term DEMO fusion power plant: the EU assessment.* Journal of Nuclear Materials, 455(1-3): p. 277-291, 2014.

[3.] A. Hasegawa, et al., *Neutron irradiation effects on the microstructural development of tungsten and tungsten alloys.* Journal of Nuclear Materials, 471: p. 175-183, 2016.

[4.] R. Neu, et al., *Investigations on tungsten heavy alloys for use as plasma facing material,* Fusion Eng. Des. 124 (2017) 450–454.

[5.] X. Gong, et al., *Effect of tungsten content on microstructure and quasi-static tensile fracture characteristics of rapidly hot extruded W-Ni-Fe alloys*, Int. J. Refract. Metals Hard Mater. 30 (2012) 71–77.

[6.] X. Gong, et al., *Microstructure and highly enhanced mechanical properties of fine-grained tungsten heavy alloy after one-pass rapid hot extrusion,* Mater. Sci. Eng. 528 (2011) 3646–3652.

[7.] Z.S. Levin, K. Ted Hartwig, *Hardness and microstructure of tungsten heavy alloy subjected to severe plastic deformation and post-processing heat treatment*, Mater. Sci. Eng. 635 (2015) 94–101.

[8.] Y. Yang, et al., *Microstructure and mechanical properties of a hothydrostatically extruded 93W-4.9Ni-2.1Fe alloy*, Mater. Sci. Eng. 435–436 (2006) 620–624.

[9.] Y. Yu, H. Hu, et al., *Microstructure evolution and recrystallization after annealing of tungsten heavy alloy subjected to severe plastic deformation*, J. Alloys Compd. 685 (2016) 971–977.

[10.] Y. Yu, et al., *Effect of heat treatment on microstructure and mechanical properties of hot-hydrostatically extruded 93W-4.9Ni-2.1Fe alloy*, J. Alloys Compd. 622 (2015) 880–884.

[11.] Z.H. Zhang, et al., *Deformation characteristics of the 93W-4.9Ni-2.1Fe tungsten heavy alloy deformed by hydrostatic extrusion*, Mater. Sci. Eng. 435–436 (2006) 632–637.

[12.] C. Henager Jr., et al., *Ductile-phase toughened tungsten for plasma-facing materials in fusion reactors*, Int. J. Powder Metall. 53 (2017) 53–69.

[13.] B.N. Nguyen, et al., *Tailoring ductile-phase toughened tungsten hierarchical microstructures for plasma-facing materials*, J. Nucl. Mater. 540 (2020) 152382.

[14.] R. Neu, et al., *Results on the use of tungsten heavy alloys in the divertor of ASDEX Upgrade*, J. Nucl. Mater. 511 (2018) 567–573.

[15.] M. Alam, et al., *The effect of hot rolling on the strength and fracture toughness of 90W-7Ni3Fe tungsten heavy metal alloys*, Materials Science & Engineering A 824, 141738, 2021.
[16.] G.M. Wright, et al., *Comparison of tungsten nano-tendrils grown in Alcator C-Mod and linear plasma devices*, J. Nucl. Mater. 438 (2013) S84–S89.
[17.] D. Dasgupta, et al., *Prediction of temperature range for the onset of fuzz formation in helium-plasma-implanted tungsten*, Surf. Sci. 698 (2020) 121614.
[18.] Q. Yang, et al., *Nanostructured fuzz growth on tungsten under low-energy and high-flux He irradiation*, Sci. Rep. 5 (2015) 1–9.
[19.] L.J. Swartzendruber, et al., Phase Diagrams of Binary Nickel Alloys, P. Nash, Ed., ASM International, 1991, p 110–132.
[20.] J. Wang, et al., *Tensile testing and microstructural characterization of ductile phase toughened W-NiFe alloys*, in Fusion materials Semiannual Progress Report for the Period Ending June 30, 2020. 2020.
[21.] J. Wang, et al., *Microstructural characterization and mechanical testing of ductile-phase toughened tungsten*, in Fusion materials Semiannual Progress Report for the Period Ending December 31, 2019. 2019.
[22.] J. Wang, et al., *Microstructure-Mechanical Property Correlation in Ductile Phase Toughened W-NiFe Heavy Alloy*, in Fusion Materials Semiannual Progress Report for the Period Ending December 31 2020, D. Clark, Editor. 2020.
[23.] R. Prabhakaran, et al., *Status of the elevated temperature mechanical test facility setup at PNNL*, PNNL-SA-170069, In Fusion Materials Semiannual Progress Report for period ending December 31, 2021, DOE/ER-0313/71, US Department of Energy, 2022.
[24.] R. Prabhakaran, et al., "*Status of the elevated temperature mechanical test facility setup at PNNL*", PNNL-SA-176100, In Fusion Materials Semiannual Progress Report for Period Ending June 30, 2022, DOE/ER-0313/72, U.S. Department of Energy, 2022.
[25.] Rembar website; https://www.rembar.com/when-to-use-tzm-alloy-instead-of-pure-molybdenum; updated July 30, 2020 (accessed 1 Aug 2022).
[26.] ASTM E8/E8M-21, Standard Test Methods for Tension Testing of Metallic Materials, ASTM International, West Conshohocken, PA, 2021.

5. ADVANCED MANUFACTURING

No contributions this reporting period.

6. EFFECTS OF IRRADIATION

6.1 THE ATOMIC STRUCTURE OF DISLOCATION LOOP WALLS AND Cr SEGREGATION ON DISLOCATION LOOPS IN IRRADIATED Fe-Cr ALLOYS—Y. Li, G. Duscher, Y. Zhao, A. Houston, S.J. Zinkle (University of Tennessee, Knoxville), J. Poplawsky, J. Burns (Oak Ridge National Laboratory)

OBJECTIVE

The objective of this project is to study the dislocation loop and Cr solute segregation processes in irradiated Fe-Cr alloys, including the formation of petal-shaped dislocation loops and dislocation loop walls.

SUMMARY

Atomic-resolution scanning transmission electron microscopy (STEM), energy-dispersive X-ray spectroscopy in STEM mode (STEM-EDS), and atom probe tomography (APT) were used to characterize a complex structure reported in preceding reports on the atomic scale, called dislocation loop walls, after 8 MeV Fe ion irradiation in high-purity Fe-5%Cr and Fe-8%Cr alloys. At 450 °C and 3.5 dpa, <001> 2-D dislocation loop walls were observed. A Z-contrast imaging collected by high angle annular dark field detector (STEM-HAADF) identified that different dislocation loops in the same loop wall were on adjacent and parallel atomic planes which have the same plane normal. Vacancy- and interstitial-type loops have been identified.

PROGRESS AND STATUS

Introduction

This report summarizes recent work on dislocation loop characterization in ion irradiated high-purity Fe-Cr alloys; prior work is summarized in previous progress reports [1-3]. The irradiations examined in this report were performed at 450°C and the midrange dose was 3.5 dpa. This investigation is a continuation of our previous work in which the same samples were irradiated by 8 MeV Fe ions at 0.35 dpa (midrange dose). The midrange safe analysis region is from 750 to 1250 nm, based on the method proposed by Zinkle [4]. Transmission electron microscopy (TEM) lamellae were lifted out from the desirable grains whose crystal directions had been determined by the electron Backscatter Diffraction (EBSD) technique. Afterward, samples discussed in this report were prepared by focus ion beam (FIB) milling followed by the flash polishing method reported previously [2].

Experimental Procedure

<u>The atomic structure of dislocation loop walls</u>

Figure1 displays the petal-shaped loops (Figure 1a) and 2-D dislocation walls (Figure 1e) created at 450°C. At the low dose (0.35dpa), under the on-zone condition (B = 001), all the loops are revealed, as shown in Figure 1a. Our hypothesis for this evolution process is shown in Figure 1b-1d. One [100] loop cluster is used as an example: At the very beginning of irradiation, multiple small [100] loops may form as a self-organized cluster aligned along {100} planes. There may be favorable strain fields at the periphery of the small loops that favor nucleation of another loop in the approximately same habit plane, thereby encouraging formation of ordered arrays of loops that have been reported by multiple research groups [5-9]. These observations of loop self-organization are sometimes called rafting or patterning. In reality, the individual loops may be sited on slightly different and parallel atomic habit planes which have the same plane normal (Figure 1b). As more defect clusters are created by irradiation, the small [100] loops absorb more defects and grow. Since [100] loops are immobile, their relative positions to each other remain unchanged (Figure 1c). With further growth, these [100] loops impinge other neighboring [100] loops, and

coalescence occurs (Figure 1a and 1d), forming the petal-shaped loops. With increasing doses, the petal-shaped loops coarsen and eventually become too large to be encompassed by a TEM foil. The inner region of a coarsened petal-shaped loop is similar to a 'perfect' crystal. New small <001> loops may nucleate inside of the coarsened petal-shaped loops and will form the next generation of petal-shaped loops once they impinge upon the [100] loops in their neighborhood. To evaluate our hypothesis, atomic-resolution STEM was conducted on Fe-8Cr irradiated to 3.5 dpa at 450°C. Figure 1f is the atomic resolution image by STEM-HAADF under B = 001 condition. The imaging was performed using a ThermoFisher Spectra 300 located at the Institute for Advanced Materials and Manufacturing (IAMM), University of Tennessee, Knoxville. The operation voltage was 300 kV. The camera length was 115 mm. The convergence angle was 30 mrad. The collection angle was 60-200 mrad. The atomic-resolution images were taken under the [001] zone(Figure 1f-h). The images in Figure 1f-h appear to support the hypothesis outlined above. The individual loops observed in a dislocation loop wall were confirmed to be located on different atomic planes, offset by ~1 atomic plane. In particular, for the two loops in Figure 1g, their habit planes were shifted by one atomic distance along the [010] direction. Besides the misfit of habit planes, the atomic resolution images in Figure 1f-h also demonstrated that the imaged two loops are vacancy type. In our previous study[3], 20 out of 22 characterized loops were identified as interstitial type.

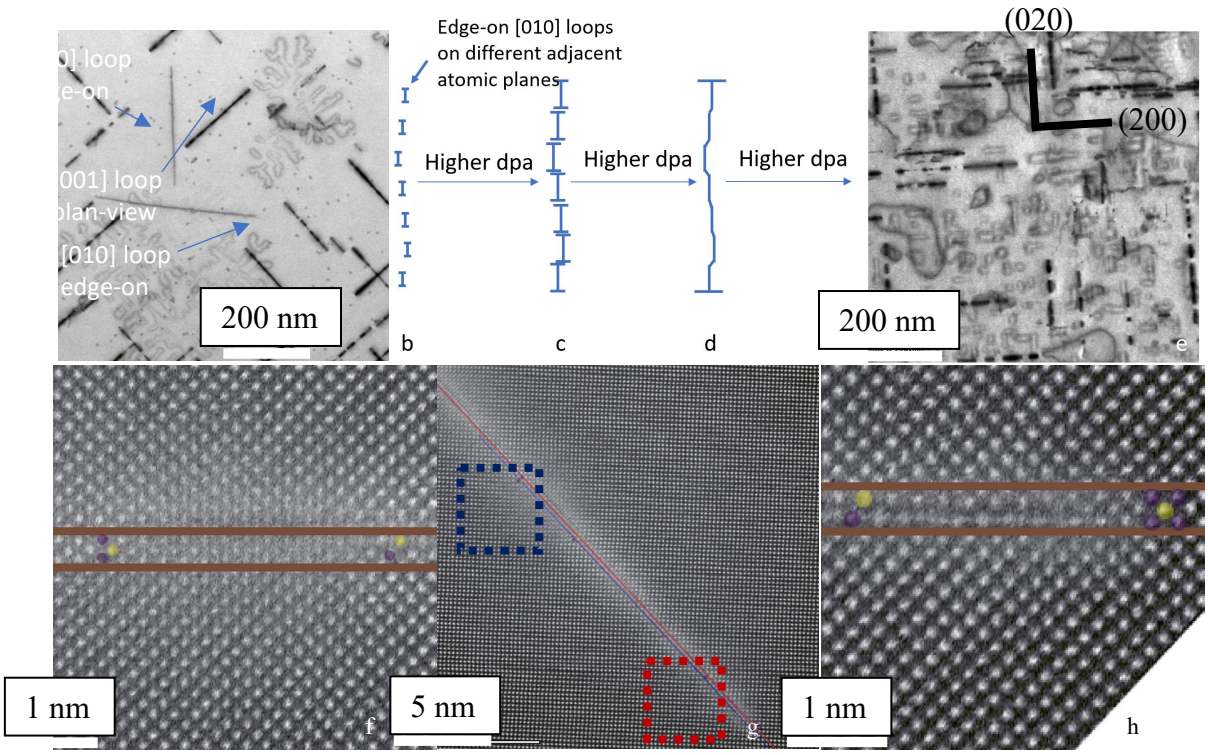

Figure 1. (a) Fe-8Cr STEM-BF imaged using on-zone, B =001 following irradiation at 450℃ to 0.35 dpa at 10^{-5} dpa/s. (b-d) a schematic illustration displays the evolution process of petal-shaped dislocation loops in separate phases from (b) nucleation, (c) growth, and (d) coalescence. (e) A Fe-5Cr irradiated at 450℃ to 3.5 dpa at 10^{-4} dpa/s is imaged with the STEM-BF technique. The diffraction condition was on-zone, B =001. (f) is the high magnification image of the marked region by the blue box in Figure 1g. Two brown guidelines sandwich three layers of atoms on the left side and two layers of atoms on the right side. (g) is the part of a dislocation loop wall. The marked regions are magnified in Figure 1f, corresponding to the blue box, and Figure 1h, corresponding to the red box. The red line denotes the habit plane of the loop in the red box and the blue denotes the habit plane of the loop in the blue box. (h) is the high magnification image

of the marked region by the red box in Figure 1g. Two brown guidelines sandwich two layers of atoms on the left side and three layers of atoms on the right side.

Cr segregation on dislocation loop walls

The STEM-EDS was performed on the same sample, Fe-8Cr irradiated to 3.5 dpa at 450℃. As shown in Figure 2, the Cr segregation occurred on some dislocation loops. By imaging all the Cr-enriched loops and regular loops with the atomic-resolution imaging technique, we observed that the Cr segregation occurred on the vacancy-type loops whereas no segregation was observed for the interstitial dislocation loops. However, we have only analyzed the Cr segregation and loop nature for a limited number of loops and further analysis is needed to provide better statistics. Nevertheless, our preliminary results imply that Cr segregation might only occur on vacancy loops.

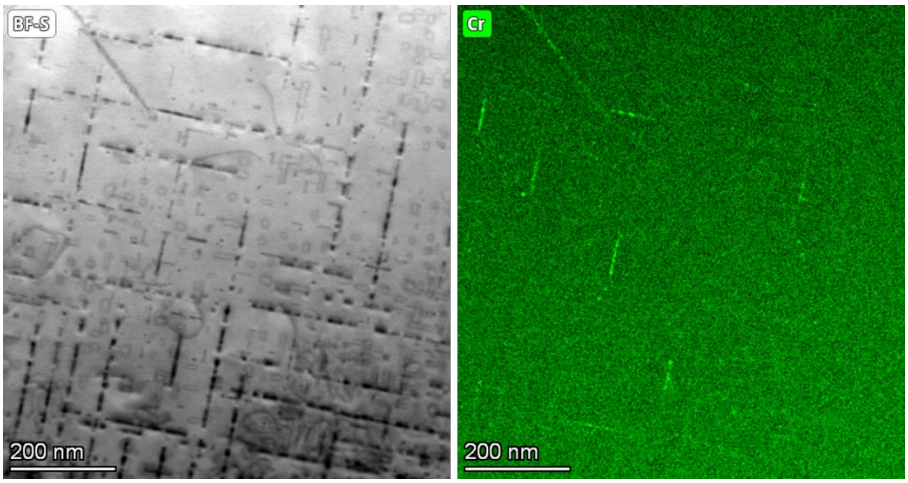

Figure 2. Cr concentration mapping by STEM-EDS. The STEM-EDS was performed under the on-zone condition with B=001.

The Cr segregation on dislocation loops was characterized by APT as well. Needles for APT were lifted out from Fe-5Cr irradiated to 3.5 dpa at 450℃ and Fe-8Cr irradiated to 3.5 dpa at 450℃. Two needles were lifted out from one bulk sample at different depths, ~1μm, and 1.8 μm, respectively (corresponding to the mid-range and peak damage/ Fe implanted ion region respectively) . No segregation was observed by APT at the 1.8-μm depth in Fe-5Cr or Fe-8Cr. In contrast, Cr-enriched regions were observed at the 1μm in Fe-5Cr and Fe-8Cr. The top panel of Figure 3 is the APT result extracted from the needle at 1μm from Fe-5Cr and the middle panel of Figure 3 is the APT result extracted from the needle at 1μm from Fe-8Cr. The bottom panel of Figure 3 is the measured Cr concentration profile of different clusters. The Cr iso-concentration interface in Figure 3b is 10 at% and the Cr iso-concentration interface in Figure 3d-3e is 11.5 at%. Three features are marked in Figure 3b. Number 1 is encompassed by two parallel segments. It is likely that feature 1 was a loop and its two tips were destroyed during the FIB sessions since feature 1 is close to the needle tip. Feature 2 and feature 3 are edge-on images of high Cr-concentration clusters. The measured angle between feature 2 and feature 3 is ~ 85°. Considering the distortion in APT analysis, these features are supposed to be perpendicular to each other. In each feature, two Cr concentration profiles were extracted. Profile 1 and 2 were from feature 3, profile 3 and 4 were from feature 2, and profile 5 and 6 were from feature 1, as shown in Figure 3. The concentration profiles in Figure 3f-h displayed the Cr concentration jumped to 20 at% around the detected features. Moreover, the mean loop diameter in Fe-5Cr is 28 nm and the mean loop diameter in Fe-8Cr is 13 nm. The diameter of objects in feature 2 is ~23 nm and the diameter of objects in feature 3 is ~21 nm. The diameter of feature 4 in Fe-8Cr is 20 nm. Their diameters are close to the mean values in the corresponding samples and the Cr-enriched features were

perpendicular to each other in the Fe-5Cr sample. Thus, we consider that the features observed in APT results may be dislocation loops with Cr segregation.

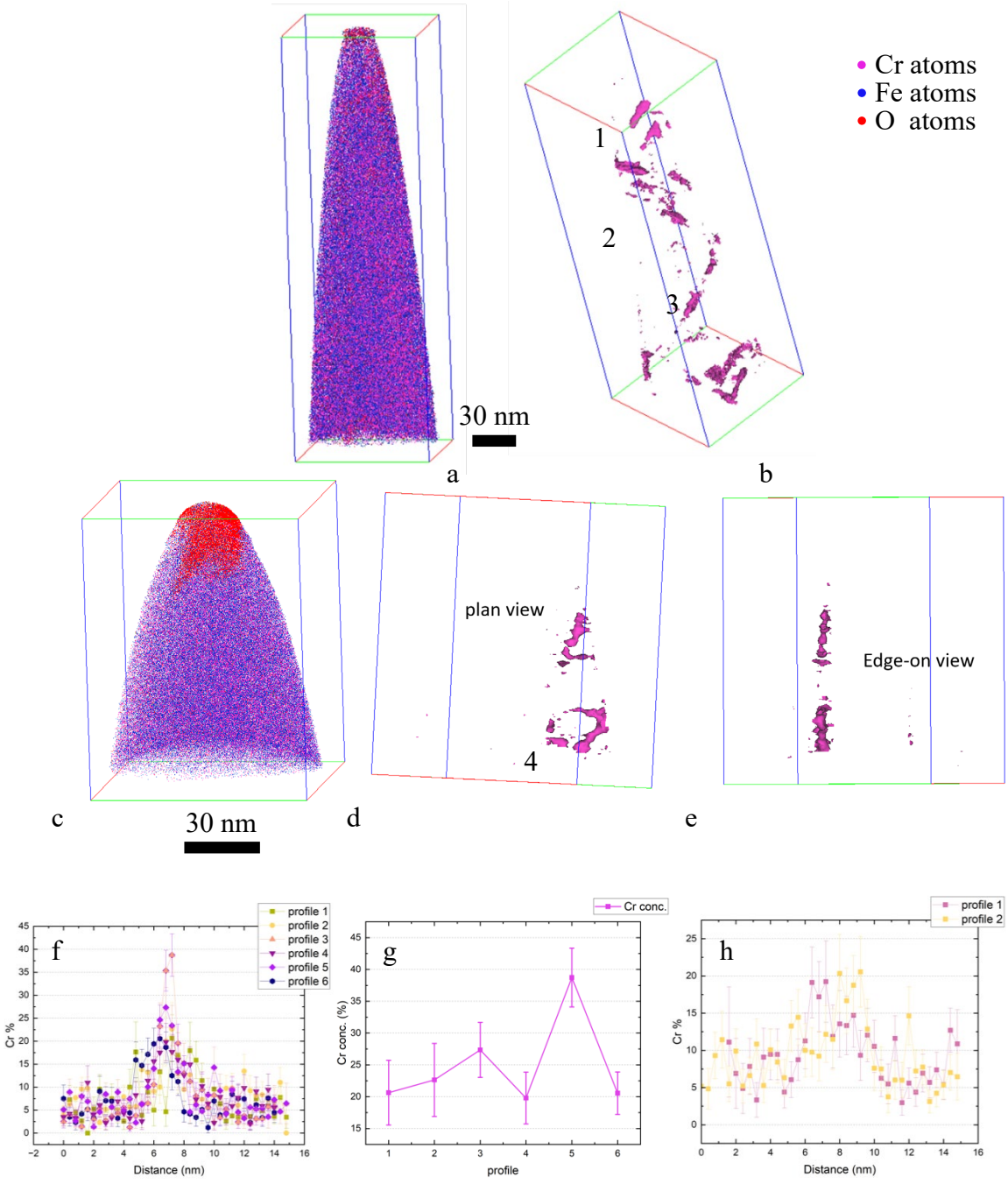

Figure 3. Atomic reconstruction of APT needles. (a) is the reconstruction displaying all atoms in the Fe-5Cr needle. (b) shows the Cr-enriched features. The Cr iso-concentration surfaces are 10 at%. (c) is the reconstruction displaying all atoms in the Fe-8Cr needle. (d) and (e) show the Cr-enriched features. (e) was achieved by rotating d by 90°. The Cr iso-concentration surfaces are 11.5 at% for (d) and (e).(f) is the Cr concentration profiles from six objects in (a) and (g) is the maximum Cr concentration from (f). (h) are the Cr concentration profiles from the features in (d).

References

[1] Y. Li, S.J. Zinkle, A. Bhattacharya, EFFECTS OF Cr AND C ON DISLOCATION LOOPS IN HEAVY ION IRRADIATED ULTRA-HIGH PURITY FeCr ALLOYS, in: F.W. Wiffen, S. Melton (Eds.) Fusion Materials Semiannual Progress Report For the Period Ending June 2019, Oak Ridge National Laboratory, 2019, pp. 15-19.

[2] Y. Li, S.J. Zinkle, L. Wang, A. Bhattacharya, EFFECT OF Cr ON DISLOCATION LOOPS IN HEAVY ION IRRADIATED ULTRA-HIGH PURITY FeCr ALLOYS, in: S. Melton (Ed.) Fusion Materials Semiannual Progress Report For the Period Ending June 2020, Oak Ridge National Laboratory, 2020, pp. 11-21.

[3] Y. Li, S.J. Zinkle, A. Bhattacharya, AN ELECTRON MICROSCOPE STUDY OF HEAVY ION IRRADIATED ULTRA-HIGH PURITY Fe AND Fe-Cr ALLOYS AT 350℃, in: S. Melton (Ed.) Fusion Materials Semiannual Progress Report For the Period Ending December 2020, Oak Ridge National Laboratory, 2020, pp. 186-198.

[4] S.J. Zinkle, L.L. Snead, Opportunities and limitations for ion beams in radiation effects studies: Bridging critical gaps between charged particle and neutron irradiations, Scripta Materialia 143 (2018) 154-160.

[5] J.L. Brimhall, B. Mastel, Neutron irradiated molybdenum-relationship of microstructure to irradiation temperature, Radiation Effects 3(2) (1970) 203-215.

[6] J.E. Westmoreland, J.A. Sprague, F.A. Smidt, P.R. Malmberg, Dose rate effects in nickel-ion-irradiated nickel, Radiation Effects 26(1-2) (1975) 1-16.

[7] J.O. Stiegler, K. Farrell, Alignment of dislocation loops in irradiated metals, Scripta Metallurgica 8(6) (1974) 651-655.

[8] N. Yoshida, M. Kiritani, E. Fujita, Electron radiation damge of iron in high voltage electron microscope, Journal of the physical society of Japan 39(1) (1975) 170-179.

[9] W. Jäger, H. Trinkaus, Defect ordering in metals under irradiation, Journal of Nuclear Materials 205 (1993) 394-410.

6.2 MICROSTRUCTURE OF NEUTRON-IRRADIATED BORON-11 ENRICHED ZIRCONIUM DIBORIDE AT ELEVATED TEMPERATURES—Y. Lin, T. Koyanagi, C.M. Petrie, M.G. Burke, Y. Katoh (Oak Ridge National Laboratory)

OBJECTIVE

The objective of this study is to investigate the microstructures of ^{11}B-enriched ZrB_2 ultra-high temperature ceramics neutron-irradiated at temperatures of 220 and 620°C. The Finite Element Method was employed to calculate the temperatures of the ZrB_2 at the beginning of the cycle (prior to residual ^{10}B burnout) and at the end of the cycle (following ^{10}B burnout).

SUMMARY

Polycrystalline ^{11}B-enriched ZrB_2 specimens were irradiated in the Oak Ridge National Laboratory (ORNL) High Flux Isotope Reactor (HFIR) at average temperatures of 220 and 620°C and fluences up to 2.4×10^{25} $n\cdot m^{-2}$ (E >0.1 MeV). Dislocation loops and dislocation networks were observed in both ZrB_2 samples that were irradiated at 220 and 620°C. The dominance of prism planar defects is unusual for hexagonal ceramics and may be linked to the lower "c" to "a" ratio of 1.12 in ZrB_2. Cavities were observed in samples that were irradiated at 620°C, but not in those that were irradiated at 220°C. It is suggested that the formation of these cavities in the matrix and at grain boundaries of samples irradiated at 620°C is caused by an increase in temperature from neutron absorption of residual ^{10}B, as well as the production of He from ^{10}B transmutation.

PROGRESS AND STATUS

Ultra-high temperature ceramics (UHTCs), such as ZrB_2 with a melting point of 3246°C, are being recognized as candidate materials for use in high heat and plasma-facing applications [1]. The ZrB_2 has several desirable properties for use in fusion plasma-facing components, but there are limited neutron/ion irradiation data for ZrB_2. Thus, there is concern that neutron irradiation of ZrB_2 may promote swelling and crack formation due to the accumulation of helium (He) from the $^{10}B(n, \alpha)^7Li$ transmutation reaction [2]. To mitigate this issue, isotopically-enriched ^{11}B can be used in the production of ZrB_2 materials. Using this approach, polycrystalline ZrB_2 samples with 99.37 wt.% isotopic enrichment in ^{11}B were produced for the present study, with a net concentration of B in the samples of 17.9 wt.%.

To investigate the impact of neutron irradiation on ^{11}B-enriched ZrB_2, disk specimens with a diameter of 6 mm and thickness of 0.5 mm were irradiated in sealed capsules in the HFIR at ORNL. These specimens were exposed to a total fluence of ~2.4×10^{25} $n\cdot m^{-2}$ (E>0.1 MeV) at intended temperatures of 200 and 600°C for capsules IMR-4 and IMR-6, respectively. Post-irradiation thermometry using silicon carbide (SiC) revealed that the actual end-of-cycle (EOC) temperature for the ZrB_2 samples in IMR-4 were between 210 and 230°C, and the IMR-6 samples varied between 600 and 630°C. All irradiation temperature results were calculated using thermal-only solutions with a temperature-dependent gas gap. For the purposes of this study, the average irradiation temperatures will be referred to as 220°C and 620°C.

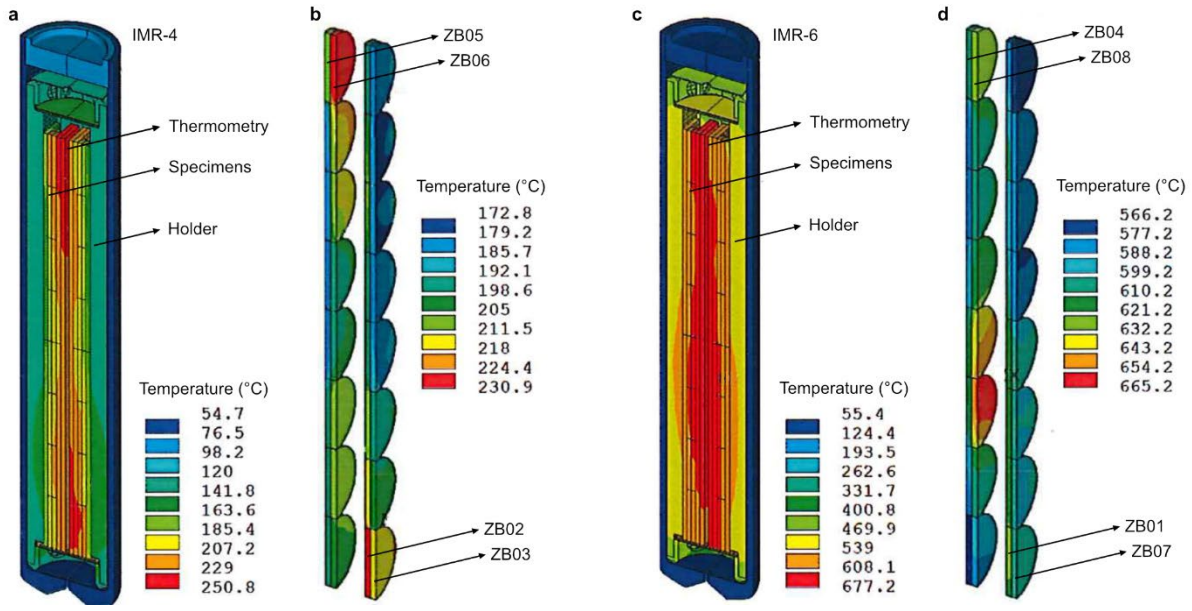

Figure 1. End-of-cycle temperature contour plot for (a) IMR-4 assembly and (b) IMR-4 specimens; (c) IMR-6 assembly and (d) IMR-6 specimens

To account for the temperature increase caused by ^{10}B transmutation, detailed finite element calculations were performed to estimate the ZrB_2 temperatures at the beginning-of-cycle (BOC), prior to ^{10}B burnout. The ZrB_2 samples in IMR-6 ran significantly hotter at the BOC compared to EOC, up to ~200°C increase, whereas the samples in IMR-4 showed a temperature increase of up to ~140°C. This difference is attributed to the use of He as the fill gas for IMR-4 and Neon for IMR-6, as He is more conductive, resulting in less sensitivity to temperature differences between the samples and surrounding materials. The ZB02 (220°C) and ZB04 (620°C) samples were selected for Transmission Electron Microscopy (TEM) analysis due to their grain size distribution being comparable to that of the non-irradiated sample.

The microstructure of the as-irradiated samples was subsequently characterized using TEM of Ga+ Focused ion beam (FIB)-prepared lift-out specimens. As shown in Figure 1, diffraction contrast TEM characterization revealed the presence of irradiation-induced defects such as dislocation loops and networks after irradiation at both 220 and 620°C. The specimens were imaged by tilting the foil close to the $[1\bar{2}10]$ zone axis and further tilted to two-beam conditions along $\langle 0001 \rangle$ and $\langle 10\bar{1}0 \rangle$ type diffraction vectors to identify the basal and prism loops, respectively. Similar microstructures were observed for the specimen irradiated at 220 and 620°C. At 220°C, the average diameter of basal loops was 13.3±6.3 nm and the number density was ~5±1×10^{21} m^{-3}. At 620°C, the diameter and the number density of the basal loops were 35±17 nm and 4.0±1×10^{21} m^{-3}, respectively. The size of the prism loops was 7±3 and 9±2 nm at 220 and 620°C, respectively. However, the prism loops had almost two orders of magnitude higher number density compared to the basal loops. For both irradiation temperatures, basal loops were larger with a lower density than the prism loops. The dislocation network density at 220 and 620°C was measured from the TEM images as 5±0.3 ×10^{14} m^{-2} and 10±0.5 ×10^{13} m^{-2}, respectively. The error considered the statistical counting errors.

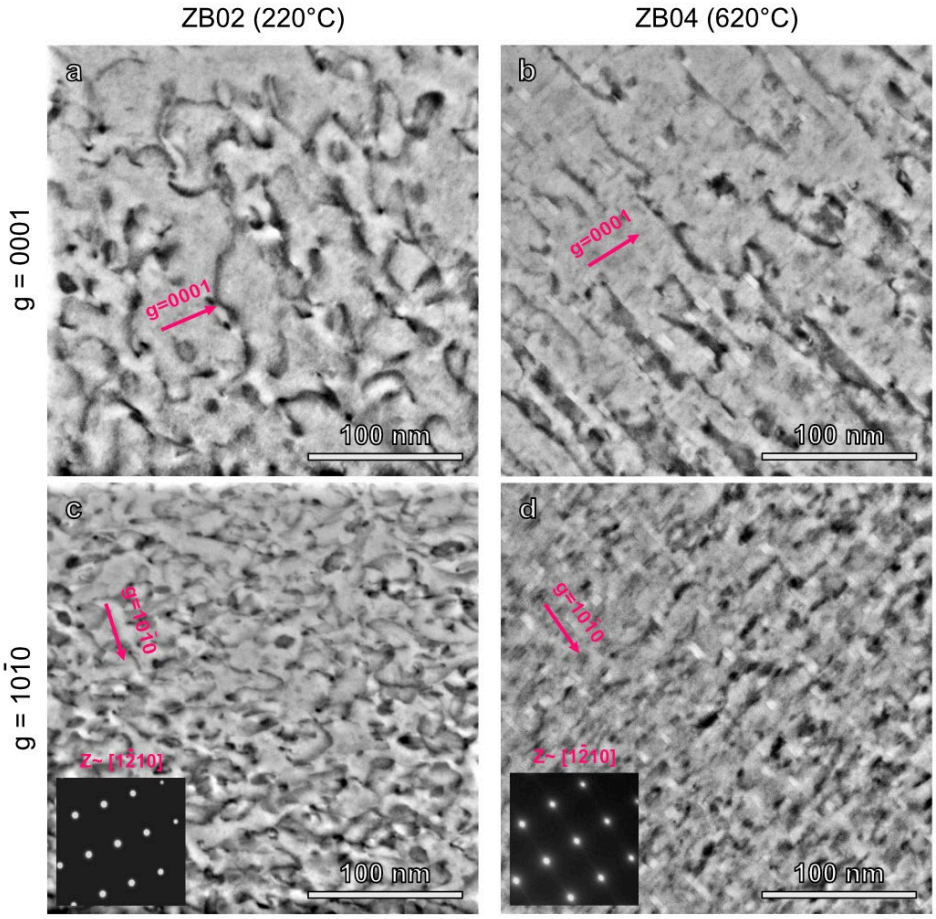

Figure 2. Dislocation loops and dislocation networks in two-beam condition scanning transmission electron microscope Bright-field (STEM-BF) images of ZrB_2 at 220 and 620°C, using g vectors of (a-b) $\langle 0001 \rangle$ and (c-d) $\langle 10\bar{1}0 \rangle$ diffraction conditions near the $[1\bar{2}10]$ zone axis. The diffraction patterns were obtained at $[1\bar{2}10]$ zone axis.

The TEM analysis revealed a homogeneous distribution of cavities in ZrB_2 after irradiation at 620°C, but not at 220°C. Under- and over-focused images taken from areas tilted away from diffraction conditions are shown in Figure 2. In the 620°C irradiated sample, larger cavities appeared faceted, whereas smaller ones were spherical in agreement with the bimodal cavity size distribution model for neutron-irradiated samples that produce trans mutant He gas atoms. As shown in Figure 2, the larger faceted cavities were elongated along the $\langle 10\bar{1}0 \rangle$ diffraction vector. The average length of the long and short sides of the faceted cavities was 6±2 and 4±1 nm, respectively. The diameter of the small spherical cavities was approximately 1 nm. The cavity number density was ~ 1×10^{22} m^{-3} and ~3×10^{22} m^{-3} for the large faceted and small spherical cavities. The magnitude of cavity swelling was estimated to be 0.15%.

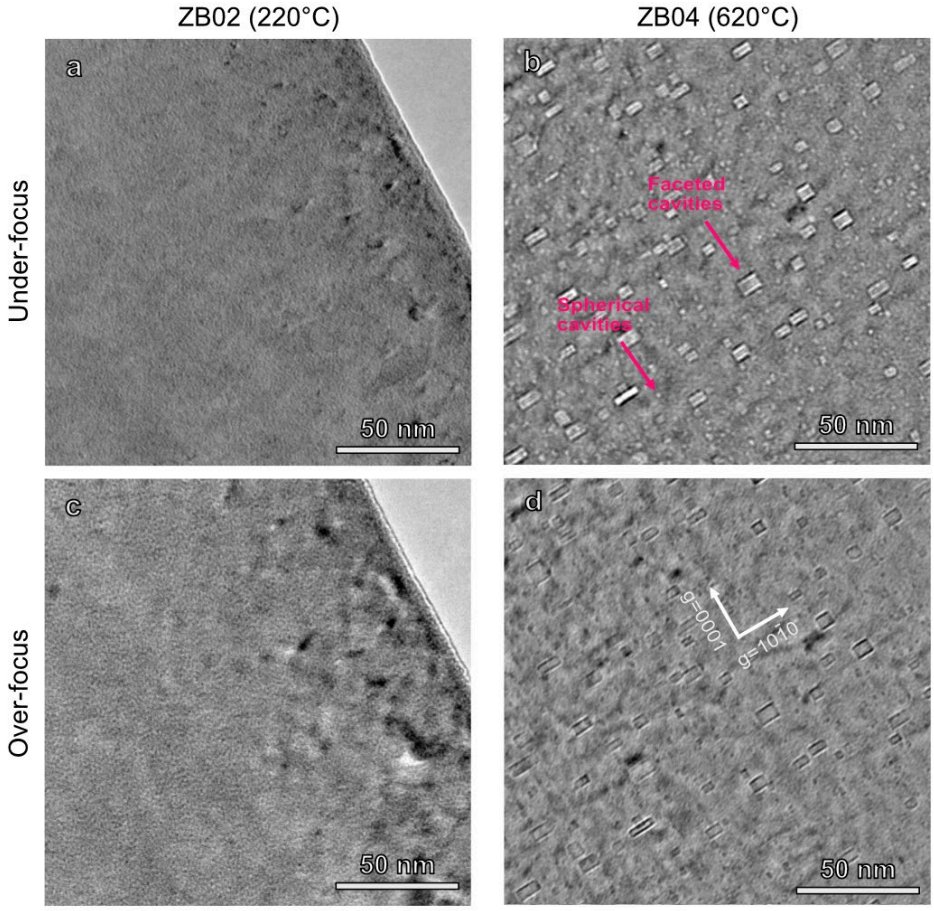

Figure 3. Under and over-focused TEM-BF images (±1 μm defocus) of cavities in ZrB_2 irradiated at (a & c) 220°C and (b & d) 620°C.

The dominance of prism dislocation loops in ZrB_2 differs from typical hexagonal ceramics in which dislocation loops primarily form on basal planes, resulting in c-lattice parameter swelling. This suggests a potential role of the c/a ratio of hexagonal materials in defect formation and aggregation. The high density of defect clusters on prism planes in ZrB_2 may explain the anisotropic a-lattice parameter swelling reported in literature [3] that leads to intergranular crack formation. The proportion of cracks decreased with increasing irradiation temperature, and grain boundary cavity segregation was only observed in the 620°C irradiated sample. This suggests that isotopic enrichment could reduce the production of He and be a viable approach to produce transition-metal diborides for potential nuclear structural applications. However, it is important to note that the significant temperature increase (up to ~200°C) due to residual ^{10}B transmutation was observed, resulting in the formation of matrix and grain boundary cavities in ZrB_2 at an irradiation temperature lower than the expected vacancy mobility temperature of 1/3 the melting point of ZrB_2 (~1100°C). To ensure proper operation temperature of ZrB_2 for nuclear applications, simulation studies of the vacancy and interstitial diffusivity as a function of temperature in ZrB_2 are recommended.

Results

To gain insight into the cause of the surface cracks observed in irradiated ZrB_2 materials, synchrotron X-ray diffraction will be used to examine the samples. This technique will enable the assessment of the expansion/shrinkage of the lattice parameters along the "a" and "c" axes, which is crucial in understanding

the formation of the prevalent prism loops and the microcracks in the samples. Besides, cracks were observed during SEM examination of the 620°C irradiated sample. Additional SEM analyses will be conducted to quantify the surface cracks per unit area.

References

[1] W.G. Fahrenholtz, G.E. Hilmas, I.G. Talmy, J.A. Zaykoski, Refractory diborides of zirconium and hafnium, J. Am. Ceram. Soc., 90 (2007) 1347-1364.
[2] V.F. Sears, Neutron scattering lengths and cross sections, Neutron News 3(2006) 26-37.
[3] A. Bhattacharya, C.M. Parish, T. Koyanagi, C.M. Petrie, D. King, G. Hilmas, W.G. Fahrenholtz, S.J. Zinkle, Y. Katoh, Nano-scale microstructure damage by neutron irradiations in a novel Boron-11 enriched TiB_2 ultra-high temperature ceramic, Acta Mater. 165 (2019) 26-39.

6.3 PRECIPITATE STABILITY IN HEAVY ION IRRADIATED Fe-Cr AND Fe-Cu ALLOYS—Y. Zhao, S.J. Zinkle (University of Tennessee, Knoxville)

OBJECTIVE

The objective of this work is to study the phase stability of Cr-rich and Cu-rich precipitates during heavy ion irradiations at temperatures where back diffusion of ejected solute is minimal.

SUMMARY

Displacement cascades that form during heavy ion irradiations are known to cause ballistic dissolution and affect the stability of precipitates. To quantify the rate of ballistic dissolution, both FeCu (containing ~0.7%Cu) and Fe-18Cr specimens were aged to form nm-scale solute precipitates. These aged specimens were then irradiated by 8 MeV Fe ions at -123°C – room temperature (RT) to final doses of 0.1 - 0.6 dpa. These low temperatures were chosen to minimize the effect of back diffusion of ejected solute. Solute atom distributions after irradiations were studied by Atom Probe Tomography (APT), the results of which are summarized here.

PROGRESS AND STATUS

Introduction

In order to study the dissolution rate of pre-existing precipitates, irradiations using 8 MeV Fe ions were conducted at -123°C (150K) to RT (below or near the onset temperature for vacancy migration), so the back diffusion of solute atoms can be suppressed. The irradiation doses were 0.1, 0.2 and 0.6 dpa, and thus the gradual dissolution of precipitates was expected to be observed. The specimens used for these irradiations were FeCu and Fe-18Cr alloys pre-aged to form Cu and Cr clusters, respectively. As a compromise to control the beam current and irradiation time more easily for the 0.1 dpa irradiation, the dose rate was set to 3×10^{-4} dpa/s. The same dose rate was used in the two other higher-dose irradiations for consistency. Therefore, the time for each irradiation ranged between 6 to 33 minutes. The irradiation conditions and specimen status before irradiation are summarized in Table 1.

Table 1. The details of cryogenic to room temperature heavy ion irradiation conditions. All materials were irradiated in a single sample holder for each condition. Pre-irradiation heat treatment conditions are listed in the Materials column.

Materials	Mid-range dose (dpa)	Fluence (ions* cm^{-2})	Flux/mid-range dose rate (ions*$cm^{-2}.s^{-1}$ / $dpa.s^{-1}$)	Temperature (°C)	Estimated time (minutes)
Fe18Cr S.S. Fe18Cr 475 °C 100h Fe18Cr 475 °C 900h FeCu S.S. FeCu 500 °C 1.5h FeCu 500 °C 10h FeCu 500 °C 100h FeCu 500 °C 1000h	0.1	$2.5x10^{14}$	$7.5x10^{11}$ / $3×10^{-4}$	-123 /150K	6
Fe18Cr 475 °C 100h Fe18Cr 475 °C 900h FeCu 500 °C 1.5h FeCu 500 °C 10h FeCu 500 °C 100h	0.2	$5x10^{14}$	$7.5x10^{11}$ / $3×10^{-4}$	Room temperature /~20	11
Fe18Cr 475 °C 100h Fe18Cr 475 °C 900h FeCu 500 °C 1.5h FeCu 500 °C 10h FeCu 500 °C 100h	0.6	$1.5x10^{15}$	$7.5x10^{11}$ / $3×10^{-4}$	Room temperature /~20	33

s.s.: as-received solid solution state
Temperatures and times in the Materials column are for the aging conditions prior to irradiations.
The FeCu 500°C 1.5h aging followed by 0.2 dpa irradiation specimen was irradiated in repeated irradiation due to unexpected issues.

Experimental Procedure

Precipitate formation after thermal aging

The distribution of solute atoms in Fe-18Cr and FeCu alloys after thermal aging is presented in Figure 1. The Cu clusters are clearly visible from the reconstructions at both aging conditions. After aging for 10 hours, strong coarsening of precipitates is accompanied by a decrease in number density, which agrees with the conventional Ostwald ripening mechanism. In the Fe-18Cr specimens, precipitates are not evident in the 100h aging condition due to both the high bulk solute concentrations and low contrast of solute contents between matrix and precipitates. However, they become easily distinguishable after aging for 900 hours. In general, the number densities of precipitates in Fe-18Cr are much higher than that in FeCu specimens. Sizes of Cu and Cr precipitates will be presented later.

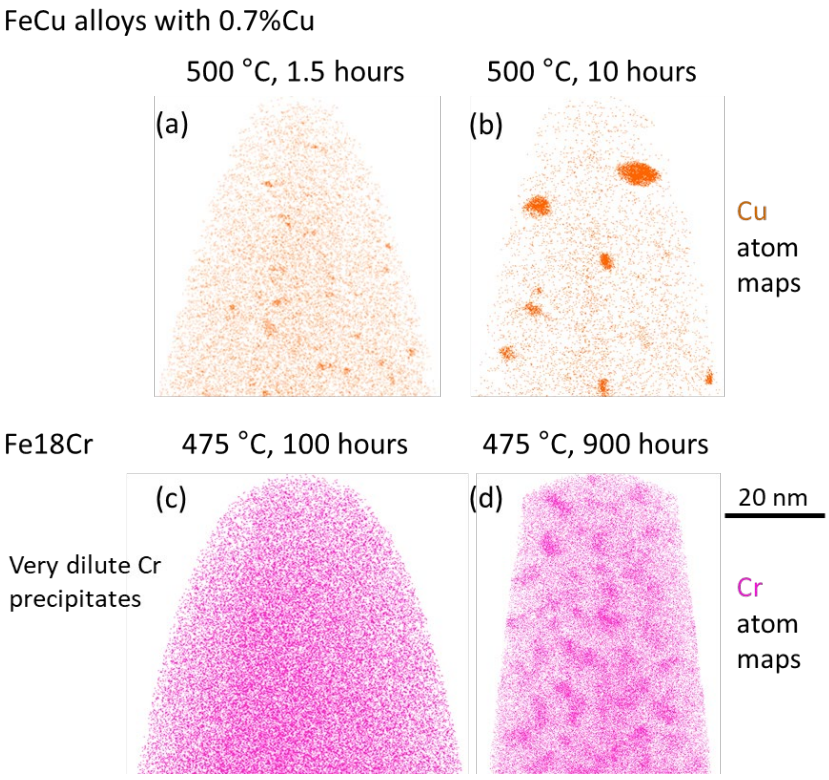

Figure 1. The APT reconstructions showing the distribution of (a, b) Cu atoms in FeCu alloys and (c, d) Cr atoms in Fe-18Cr specimens after thermal aging at indicated temperatures and times.

Dilution of Cu precipitates after ion irradiations

The FeCu alloys containing Cu precipitates were irradiated by 8 MeV Fe ions at conditions listed in Table 1. The status of Cu precipitates after each irradiation was characterized by APT and the results are given in Figure 2. Small Cu precipitates that formed from 1.5h aging became less distinct with increasing irradiation doses; only slight Cu-enriched regions can be observed at 0.6 dpa. However, the Cu atom distribution in the whole APT tip still shows some inhomogeneity compared to the uniform distribution in the as-received state. The large Cu precipitates formed from aging for 10 hours stayed stable without clear change (according to the atom maps) for doses up to 0.6 dpa.

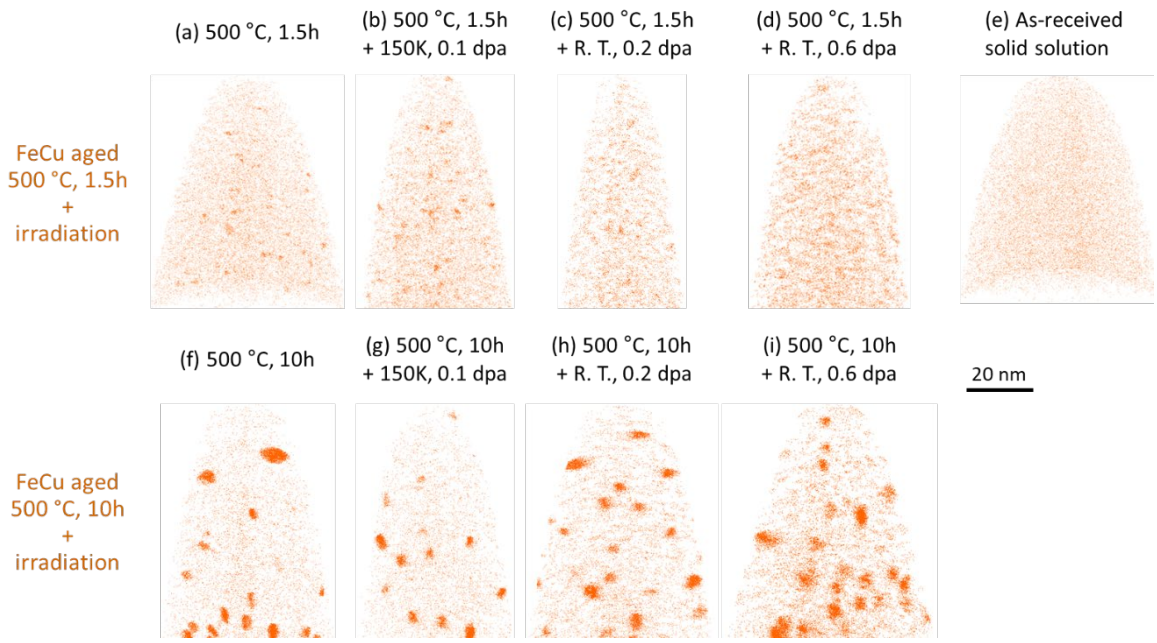

Figure 2. The APT reconstructions showing the distribution of Cu atoms in FeCu alloys (a-d) after aging at 500°C for 1.5h + irradiation at -123°C - RT to 0.1-0.6 dpa and (f-i) after aging at 500°C for 10h + irradiation at the same conditions. The Cu atom map in the as-received state is given in (e) for comparison.

The number density, average radius and volume fraction of Cu precipitates are plotted in Figure 3a-c as a function of dose for the two pre-aged conditions. These properties remain constant before and after irradiations. The slightly increasing volume fraction of Cu precipitates in the 10h aged specimen at 0.6 dpa is within statistical errors. Compared to the trendline for the as-aged and RT, 0.2 dpa irradiated specimens, the 150K, 0.1 dpa specimen appears to exhibit a slightly higher number density and a slightly reduced size. The 0.1 dpa irradiation temperature was -123°C, which was much lower than the RT value used for the other irradiation doses. The most important change induced by irradiations is the large decrease in precipitate core solute concentrations from as-aged to 0.6 dpa irradiated condition (34% to 22% for the 1.5h aged specimens and 65% to 26% for the 10h aged specimens). This is convincing evidence for significant ballistic mixing and cannot be attributed to an APT artifact since the precipitate size and number density were constant. Matrix Cu concentrations are plotted in Figure 3e. For the 1.5h aged specimens, matrix Cu concentration is slightly lower at 0.1 dpa and becomes lowest at 0.2 dpa, whereas as-aged and 0.6 dpa specimens gave similar values. The main reason for these two lower concentrations is the inhomogeneity of the FeCu alloy. Most APT measurements gave bulk Cu concentrations ~0.65 at.%, while the 0.1 dpa specimen has Cu contents of 0.59±0.08 at.%, and 0.2 dpa specimen only has 0.49±0.11% Cu (calculated from 4 APT datasets, which contain Cu concentrations of 0.47, 0.35, 0.66 and 0.48%, respectively). This inhomogeneity blurs the effect of irradiation, and thus no trend could be derived from the matrix solute concentration of the 1.5h aged specimen. On the other hand, 10h aged specimens show a clear increase in matrix Cu content with increasing irradiation dose, which is attributed to the dissolved Cu atoms from precipitates.

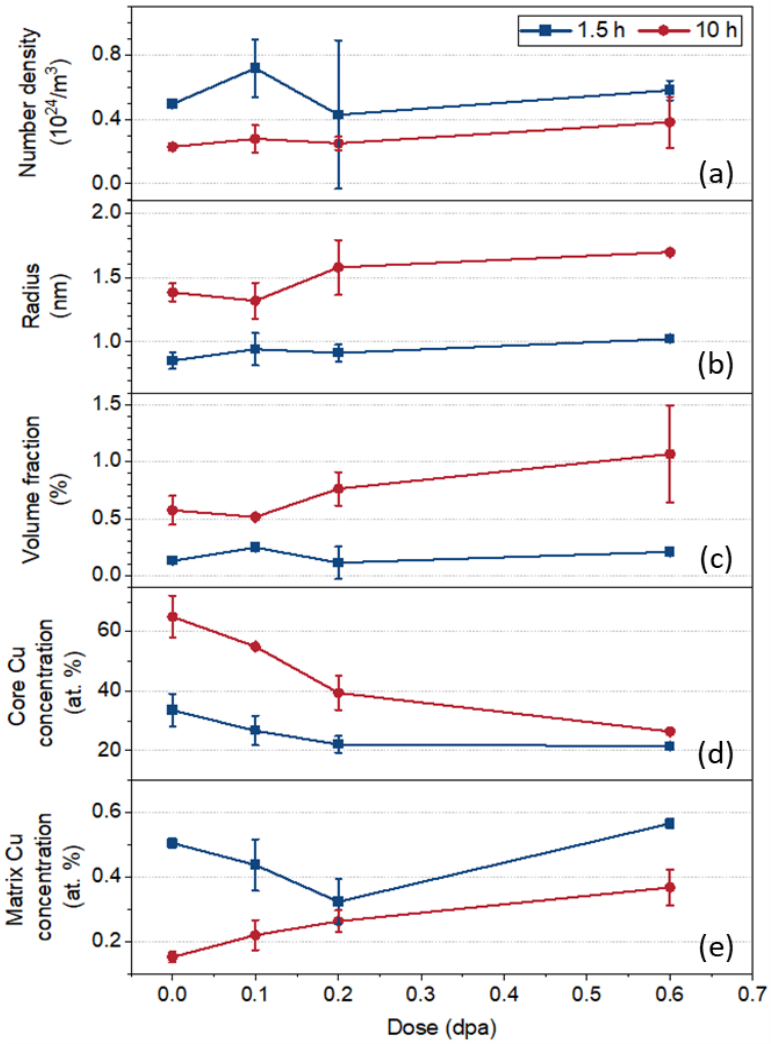

Figure 3. The evolution of (a) number density, (b) radius, (c) volume fraction, (d) precipitate core Cu concentrations and (e) matrix Cu concentration in FeCu alloys irradiated to 0.1-0.6 dpa.

Detailed analysis showing the distribution of Cu precipitate sizes is plotted in Figure 4a and c. For the specimens starting with small Cu precipitates formed from 1.5h aging, size distributions are remarkably close among the aged and aged + irradiated conditions. However, in the specimen aged for 10 hours, the size distribution of Cu precipitates slightly shifts to larger sizes at 0.2 dpa and shows an apparent slight bimodal distribution with a large number of small clusters after irradiation at 0.6 dpa, which may form from the partial dissolution of large Cu precipitates. As plotted in Figure 4b and d, Cu concentrations at the precipitate core decrease gradually with increasing irradiation dose, regardless of the cluster size. In Figure 4b, Cu concentrations decrease with increasing precipitate sizes in each specimen. This might be associated with their sizes that are comparable to the sizes of background clusters (~0.5-1 nm). In our cluster analysis algorithm, background clusters are removed based on their small sizes and low solute concentrations, so a smaller cluster can survive from the removal process only if it has a higher solute concentration, which leads to the higher measured solute concentrations in the smaller precipitates. Precipitates are much larger in the 10h aged specimens, so the effect of removing background clusters becomes less important, and Cu contents increase with precipitate sizes. This trend might be related to the blurring effect from trajectory aberration or the non-classical nucleation process [1, 2]. Further analysis is required to clarify this effect.

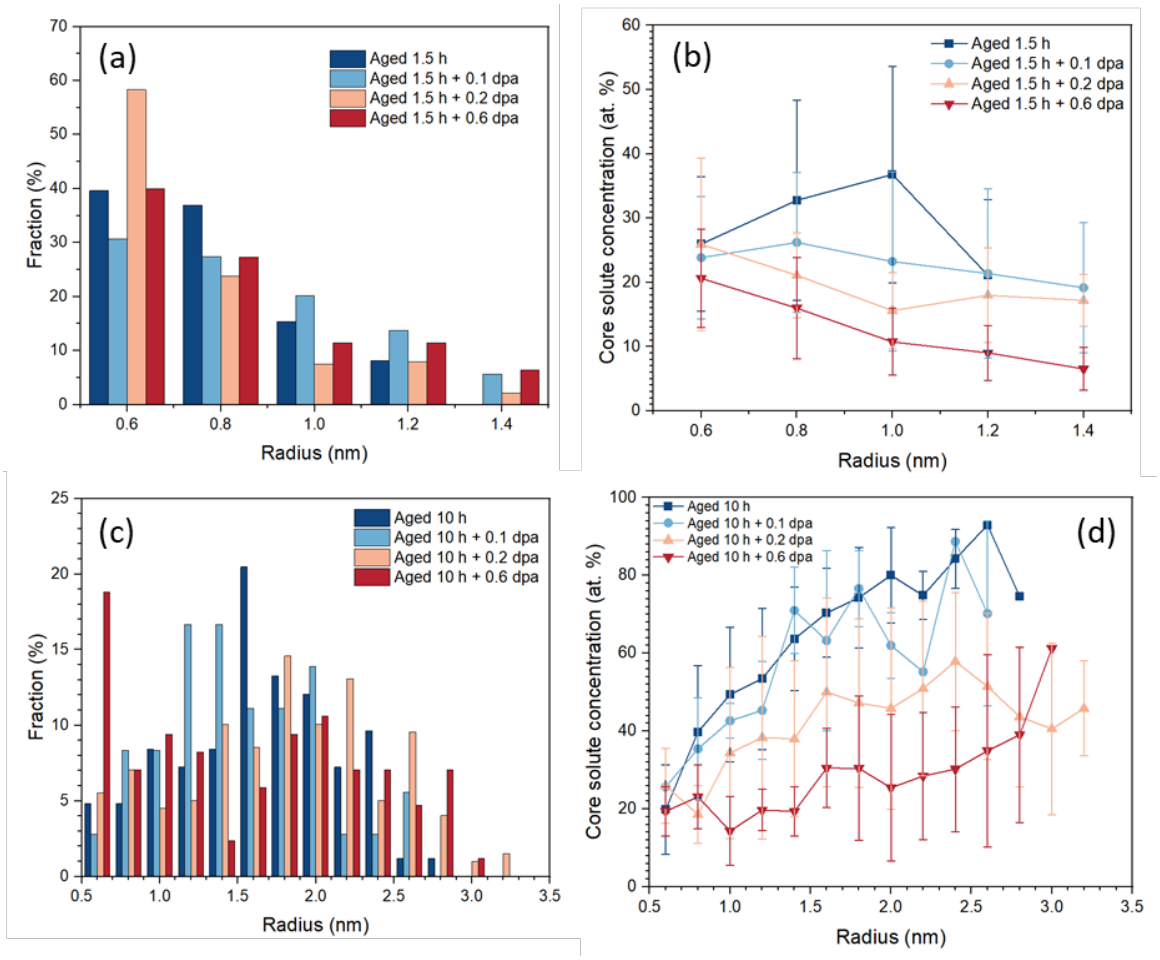

Figure 4. (a) Size distribution of Cu precipitate and (b) change of precipitate Cu concentration as a function of precipitate sizes in FeCu alloys after aged at 500°C for 1.5 hours and aged followed by irradiations to 0.1-0.6 dpa. (c) and (d) are similar plots to (a) and (b) respectively. The specimens were aged at 500°C for 10 hours followed by irradiation under the same conditions.

Evolution of Cr precipitates after ion irradiation

The Fe-18Cr specimens aged at 500°C for 100-900 hours to form pre-existing α' precipitates were irradiated in the same target stage as the FeCu specimens. The APT results showing the distribution of Cr atoms before and after irradiations are presented in Figure 5. Due to the high solute concentration of Fe-18Cr alloy and the dilute precipitates (~45% Cr) formed after the shorter time aging, the Cr precipitates are not readily visible from the atom maps, so the clusters identified using our analysis algorithms are also shown in the figure below for clarity. Surprisingly (based on the 300-450°C ion irradiation results presented in the previous work [3]), only negligible changes can be observed from these reconstructions. The Cr precipitates remain stable after RT and cryogenic irradiations up to 0.6 dpa. Similar trends can also be observed in the 900h aged specimens.

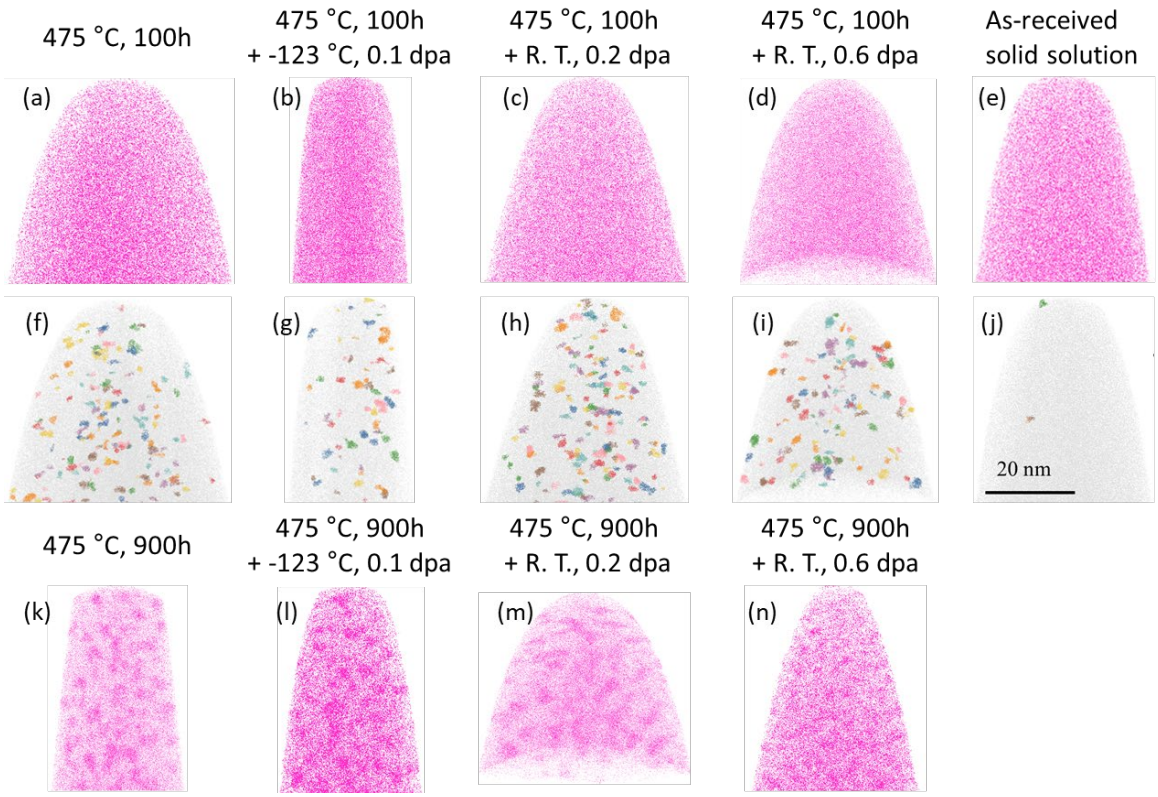

Figure 5. The APT reconstructions showing the distribution of Cr atoms in Fe-18Cr alloys (a-d) after aging at 475°C for 100h + irradiation at -123°C – RT to 0.1-0.6 dpa. For better visualization, Cr-rich clusters filtered by our algorithms are presented below each Cr atom map in (f-j). (k-n) Cr atom distribution after aging at 500°C for 10h + irradiation at the same conditions. The Cr atom map in the as-received state is given in (e) for comparison.

Statistical results comparing the evolution of quantitative properties of α' precipitates before and after irradiations are plotted in Figure 6. The number density, radius and volume fraction of precipitates are almost unchanged by irradiation up to 0.6 dpa. The only noticeable modification induced by irradiations is the gradual decrease of precipitate core Cr concentrations in the Fe-18Cr specimen aged at 475°C for 900 hours followed by irradiation at 0.1-0.6 dpa, which is similar to what was observed in the FeCu alloys. On the contrary, Cr concentrations of precipitates in Fe-18Cr samples aged for 100 hours remain unchanged (at a low value of ~45%) after irradiation up to 0.6 dpa. Matrix Cr concentrations were not changed by irradiations in the 100-hour-aged specimens, while in the 900-hour-aged specimen, it was increased by ~3% after irradiation to 0.6 dpa.

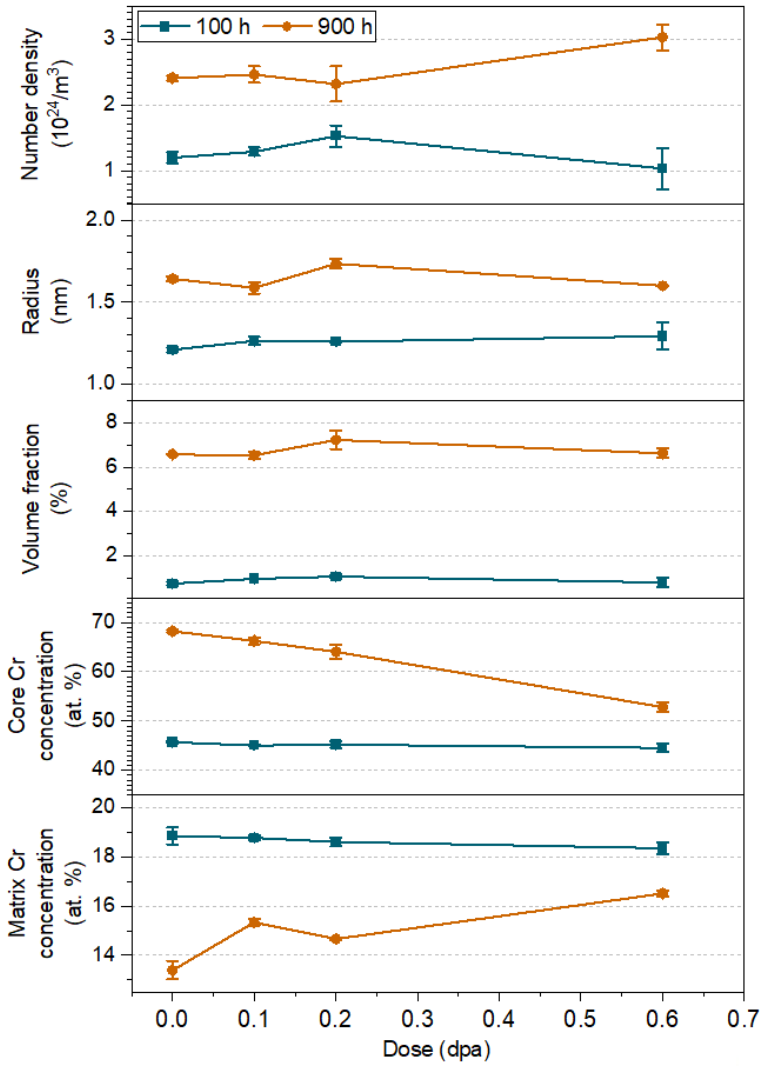

Figure 6. The evolution of (a) number density, (b) radius, (c) volume fraction and (d) precipitate core Cr concentrations of α' precipitates in Fe-18Cr alloys irradiated to 0.1-0.6 dpa.

The distribution of α' sizes for the 475°C, 100h aged Fe-18Cr specimen before and after irradiation is plotted in Figure 7a. Both the extents and peaks of all distributions are remarkably close to each other. This is also true for the same alloy aged for the longest time (900h) followed by irradiations at the same conditions (Figure 7c). Since a decrease of core Cu concentrations in precipitates of all sizes was observed in the FeCu alloy system, it is useful to confirm whether or not a similar trend was observed in Fe-18Cr. Distinct differences can be observed from the plots in Figure 7b and d. In the specimen aged for 100h, the Cr concentrations of precipitates after irradiation to 0.1-0.6 dpa are almost overlapped with the ones in the as-aged state, indicating there is no change in α' compositions. On the other hand, the larger and more concentrated precipitates formed after aging for 900h show gradual dilution of Cr concentrations inside precipitates with increasing irradiation doses, similar to what happened in the Cu precipitates.

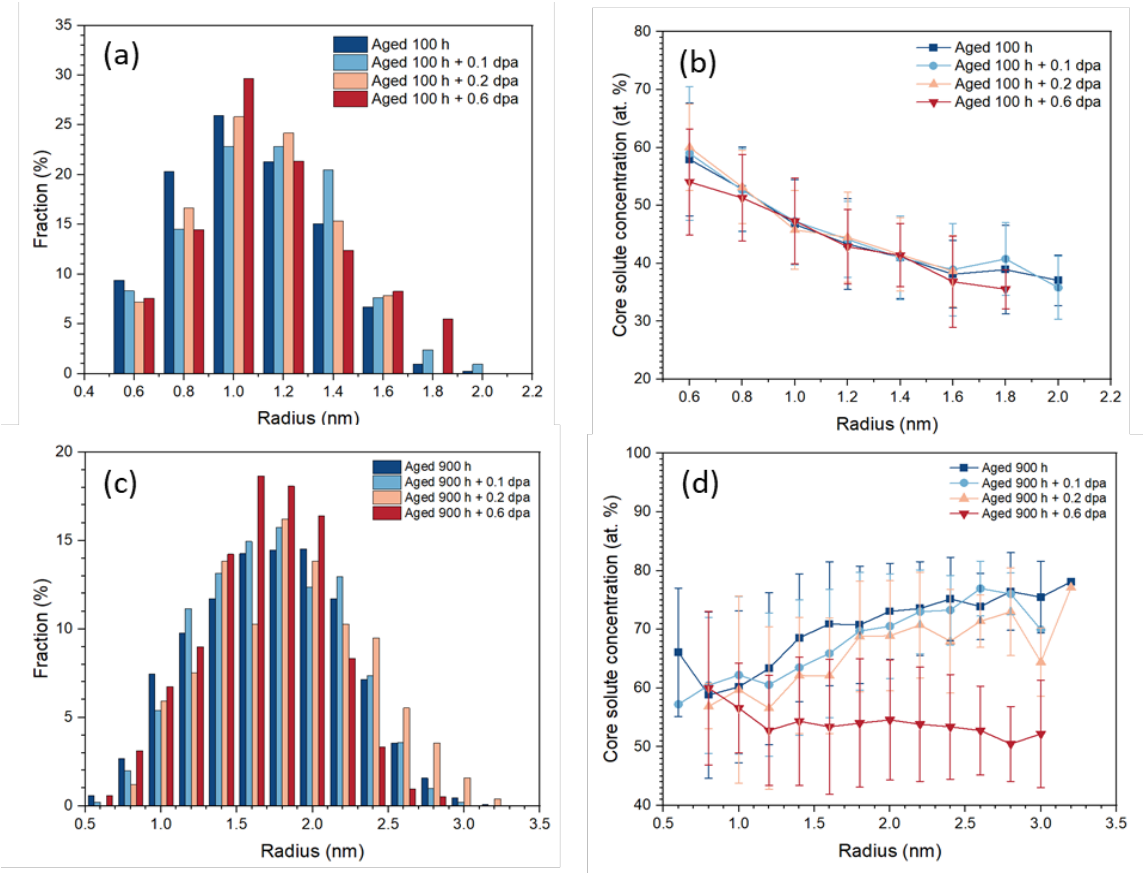

Figure 7. (a) Size distribution of Cr precipitate and (b) change of precipitate Cr concentration as a function of precipitate sizes in Fe-18Cr alloys after aged at 475°C for 100 hours and aged followed by irradiations to 0.1-0.6 dpa. (c) and (d) are similar plots to (a) and (b) respectively. The specimens were aged at 475°C for 900 hours followed by irradiation at the same conditions.

To identify possible local changes in Cr atom distributions that cannot be detected by the cluster analysis algorithm, nearest neighbor distribution analysis was performed in all Fe-18Cr datasets. Nearest neighbor distribution analysis measures the distance between two solute atoms and plots the cumulative counts at each distance range. Order is an input parameter in this analysis, where the nth order represents the nth nearest neighbors. Most frequently used orders are in the range of 1-10, and a higher order is usually selected when the inhomogeneity of solute distribution is minor, such as in the early stage of precipitation nucleation. Due to the low contrast between the precipitate and matrix phases in Fe-18Cr, the tenth order was used to generate the distributions, the results of which are plotted in Figure 8. Two peaks can be identified in the distribution curves if there is significant solute clustering, in which the short-distance part represents the inter-solute distances in precipitates, while the long-distance part represents that in the matrix. An example of this case can be observed in Figure 8b at aged and aged + irradiation up to 0.2 dpa conditions. The peak at ~0.4 nm signifies that the location of the 1st through 10th nearest Cr solute atoms in the solute clusters are all located within 0-0.4 nm of each other. For an ideal α' precipitate containing only Cr atoms, the position of the peak is expected to be slightly smaller than 0.4 nm. At the highest dose of 0.6 dpa, the two distinct peaks become less obvious due to their shifts to central positions. However, the specimens aged for 100h did not give clear double-peak distributions because the Cr precipitates are less mature and contain fewer Cr atoms. There is only one peak in the distributions calculated after aging or irradiation for all of the 100h pre-aged specimens, and their peak shapes and locations are not vastly different compared to the as-received state.

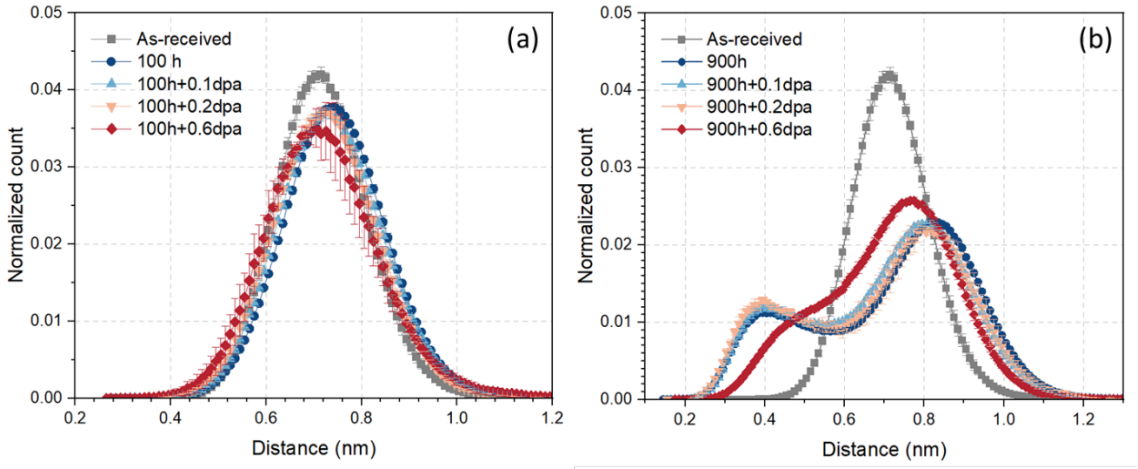

Figure 8. Tenth-order nearest neighbor distributions of Cr atoms in APT datasets. The specimens are Fe-18Cr aged at 475°C for 100 or 900 hours, and Fe-18Cr aged + irradiation to 0.1-0.6 dpa.

Results

Both FeCu and Fe-18Cr specimens were pre-aged to form nm-scale solute precipitates, and then irradiated by Fe ions at -123°C to RT, to final doses of 0.1 - 0.6 dpa. In both alloys, the precipitate size and number density were not significantly changed by irradiations up to 0.6 dpa. The largest difference induced by irradiations is the decrease in precipitate core solute concentrations. In FeCu alloy, the Cu concentrations in the 1.5h aged specimen was reduced from 34% (unirradiated) to 22% (irradiated). Precipitate sizes were ~0.9 nm with number densities of 4 to $7\times10^{23}/m^3$ before and after irradiation to different doses. In the 10h aged specimens, precipitate Cu concentrations decreased from ~65% to ~26%. Radii of precipitates were ~1.5 nm and number densities were $\sim3\times10^{23}$/m3 without clear difference with respect to irradiation dose.

This dilution process happened in all precipitates regardless of their sizes, which implies the gradual dissolution of Cu precipitates by displacement cascades. Our FeCu observations up to 0.6 dpa qualitatively agree with what was reported by Nicol et al., who found the radii of Cu precipitates to shrink by more than 1 nm after irradiation at 20°C to 1 dpa [4]. The difference in observed precipitate Cu concentration decrease in our study versus size shrinking in their work might be partially related to different characterization techniques. In our cluster analysis algorithm, the precipitate interface is defined as the midpoint of the concentration profile. Therefore, the interface of a concentrated precipitate would have a higher solute concentration than that of a dilute precipitate. Since Cu concentrations at precipitate cores became lower after irradiations, the precipitates are viewed as larger ones by our algorithm, which might compensate for the radius decrease observed by Nicol et al. However, both sets of results suggest a strong ballistic dissolution effect, where significant dissolution was observed after ≤1 dpa in FeCu alloy system during irradiation near RT.

On the contrary, Cr precipitates formed in Fe-18Cr after aging for 100h showed no difference in composition (~46%) after RT irradiations up to 0.6 dpa, and solute concentrations only decreased from 70% (unirradiated) to 54% (irradiated) in the 900h aged specimens at the highest dose. At all conditions, the sizes of precipitates were 1-2 nm and number densities were ~1 to 2×10^{24}/m3. These results suggest that larger and more solute-concentrated precipitates show larger irradiation-induced dilution rates, and Cr precipitates have higher stability than Cu precipitates under heavy ion irradiation conditions, which is counterintuitive.

In a simplified model, the stability of precipitates under irradiation conditions is determined by the competition between radiation-enhanced diffusion (promote precipitate formation) and ballistic dissolution

by displacement cascades (destroy precipitates) [5]. From our thermal aging results at 500°C, Cu precipitates grow and coarsen much faster than Cr precipitates in Fe-based binary alloys, which indicates that Cu atoms have a higher thermal diffusion rate at this temperature. However, our latest results suggest Cr precipitates are more stable, which indicates the thermal diffusion rate is not strictly relevant for irradiation conditions. Also, precipitate coarsening is not solely determined by matrix solute diffusion rate. Factors such as interface energy, etc., also may be important. Since the irradiation temperatures were low (-123°C to RT) where vacancy diffusion is sluggish, it is expected that ballistic dissolution effects would be dominant. Whether the difference in their stability can be related to different dissolution efficiencies of Cu vs. Cr precipitates by displacement cascades is unclear for now. Since the majority of FeCu and Fe-18Cr alloys are Fe atoms, and Cu and Cr both have similar atomic mass to Fe, the primary knock-on atom (PKA) energy and size of the displacement cascade should not be quite different. The Cu and Cr precipitates formed from thermal aging have similar radii of ~1-2 nm. The major difference is that Cu precipitates might be less coherent with Fe-rich matrix due to the 9R crystal structure transformation that occurs in larger precipitates, while Cr precipitates have a BCC structure and are coherent with the matrix. However, clear dilution of Cu precipitates formed from 1.5h aging versus no dissolution of Cr precipitates formed from 100h aging cannot be explained by this difference, since they are both coherent with the matrix.

The strong stability of Cr precipitates at ≤ RT also contradicts our previous heavy ion irradiation results performed at 300-450°C. We observed the dissolution of pre-existing α' by irradiation to 0.37 dpa at 300°C. Cr precipitates should be less stable at lower temperatures if their stability is simply controlled by the relative importance of radiation-enhanced diffusion vs. ballistic dissolution mechanisms. The conflicting results at RT and 300°C may suggest that other mechanisms are active at the low-temperature regime. One potential hypothesis is associated with the faster diffusion rate of Cr atoms at higher temperatures (300-450°C), so the dissolved Cr atom can quickly diffuse back and contribute to the formation of Cr-enriched nuclei. At the intermediate temperature of 300°C, the re-nucleated Cr clusters might be too small to be detected by APT. On the other hand, the diffusion rate is so slow at ≤ RT that the back diffusion of solute atoms is suppressed. During irradiation, the whole precipitate (including the core and outer region) is gradually diluted by displacement cascade. However, it remained as a solute-enriched region with a near-initial size since there is negligible diffusion to refine the size of the Cr-rich cluster. This size is above the detection limit of APT, so it is still detectable after irradiation. This would lead to a Cr cluster size close to the unirradiated size and a peak Cr concentration much less than the unirradiated value for the low temperature irradiations, and reduced Cr cluster sizes with a high Cr content in the cluster core for the higher temperature irradiations. This reasoning is obviously oversimplified. Further investigations by performing additional irradiations at intermediate temperatures such as 100 and 200°C will be helpful to generate a systematic trend, and simulation studies using molecular dynamics can also help understand the deviations between the conflicting observations at ≤ RT and 300-350°C.

Conclusions

In both FeCu and Fe-18Cr alloys, precipitate size and number density were not significantly changed by irradiations up to 0.6 dpa at RT. The largest difference induced by irradiations is the decrease in precipitate core solute concentrations, which changed from 34 to 22% in the 1.5h aged FeCu specimen and from 65 to 26% in the 10h aged FeCu specimen, respectively. This dilution process implies the gradual dissolution of Cu precipitates by displacement cascades in ≤1 dpa in FeCu alloy system.

On the contrary, the core concentration of Cr precipitates formed in Fe-18Cr after aging for 100h showed no difference in composition (46%) after irradiations up to 0.6 dpa at RT, and solute concentrations only decreased from 70 to 54% in the 900h aged specimens at 0.6 dpa. These results suggest that Cr precipitates have higher stability than Cu precipitates under heavy ion irradiation conditions, the reason for which is currently unclear.

The strong stability of Cr precipitates at temperatures ≤ RT also contradicts our previous irradiation results at 300-350°C (where strong dissolution of Cr-rich precipitates was observed), which may suggest the activation of different diffusion paths or other physical mechanisms.

References

[1] S. Shu, B.D. Wirth, P.B. Wells, D.D. Morgan, G.R. Odette, Multi-technique characterization of the precipitates in thermally aged and neutron irradiated Fe-Cu and Fe-Cu-Mn model alloys: Atom probe tomography reconstruction implications, Acta Materialia 146 (2018) 237-252.

[2] S. Novy, P. Pareige, C. Pareige, Atomic scale analysis and phase separation understanding in a thermally aged Fe–20at.%Cr alloy, Journal of Nuclear Materials 384(2) (2009) 96-102.

[3] Y. Zhao, A. Bhattacharya, C. Pareige, C. Massey, P. Zhu, J.D. Poplawsky, J. Henry, S.J. Zinkle, Effect of heavy ion irradiation dose rate and temperature on α′ precipitation in high purity Fe-18% Cr alloy, Acta Materialia 231 (2022) 117888.

[4] A. Nicol, M. Jenkins, N. Wanderka, C. Abromeit, Dissolution of Copper Precipitates in An Fe− 1· 3Wt% Cu Alloy Under Fe+ Ion Irradiation, MRS Online Proceedings Library (OPL) 540 (1998) 457-462.

[5] R. Nelson, J. Hudson, D. Mazey, The stability of precipitates in an irradiation environment, Journal of Nuclear Materials 44(3) (1972) 318-330.

6.4 RESPONSE OF F82H-IEA TO DOSE AND TEMPERATURE IN DUAL AND TRIPLE ION IRRADIATION TO UNDERSTAND THE SYNERGIES BETWEEN H, He AND RADIATION DAMAGE—L.N. Clowers, Z. Jiao, G.S. Was (University of Michigan)

OBJECTIVE

The objective of this project is to understand the synergy between transmutation gasses H and He on cavity evolution in ferritic/martensitic fusion blanket materials.

SUMMARY

The ferritic/martensitic alloy F82H-IEA was studied to understand the synergistic effects of H, He and radiation damage on cavity evolution and swelling via dual ion beam (Fe^{2+}+He^{2+}) and triple ion beam (Fe^{2+}+He^{2+}+H^{+}) irradiation. Irradiations were conducted across damage levels of 50 to 150 dpa and temperatures from 400°C to 600°C at 1x10^{-3} dpa/s with He/H injection rates of 10/40 appm/dpa. Across all conditions, hydrogen co-injection with helium resulted in an increased cavity number density and cavity size, producing an increase in swelling over that from helium injection alone that peaks between 450 and 500°C. Preceding work is published in Clowers, et al [1].

PROGRESS AND STATUS

Experimental Procedure

The reduced activation ferritic/martensitic (RAFM) steel F82H-IEA, a highly characterized heat provided by the National Institutes of Quantum and Radiological Science and Technology in Japan was irradiated in a series of dual and triple ion beam irradiations. Ion irradiations were conducted at the Michigan Ion Beam Laboratory (MIBL) using the 3 MV Pelletron accelerator to provide a defocused beam of 5 MeV Fe^{2+} for irradiation damage, the 1.7 MV Tandetron to provide a raster-scanned beam of 2.85 MeV He^{2+} to be passed through a ~6.2 μm thick Al degrader foil for helium implantation, and an ion implanter to provide a raster-scanned beam of 390 keV H^{+} through a second ~2.3 μm Al degrader foil for hydrogen implantation. Both types of ion irradiation, dual ion beam (Fe^{2+}+He^{2+}) and triple ion beam (Fe^{2+}+He^{2+}+H^{+}), were nominally conducted at 500°C to a damage level of 50 dpa with single value variations across each of these parameters. The damage profiles from self-ions and the concentration profiles of injected H/He calculated using a custom MATLAB script along with SRIM-2013 [2]. At a damage rate of ~1x10^{-3} dpa/s, the injection ratios for hydrogen and helium were 40 appm/dpa and 10 appm/dpa, respectively, at the depth of analysis (400-800nm from the surface). A narrower band of 500-700nm was used to minimize dpa variation in cavity data.

Following irradiation, transmission electron microscopy (TEM) samples were prepared using standard focused ion beam (FIB) lift-out methods in a TFS Nova 200 or a Helios 650 Nanolab scanning electron microscope (SEM)/FIBs at the Michigan Center for Materials Characterization (MC^2). Cavities greater than 5 nm were characterized using high-angle annular dark-field scanning transmission electron microscopy (HAADF-STEM) while cavities less than 5 nm were characterized using the bright field (BF) TEM focus-defocus technique with a defocus of +/- 1 μm in the TFS Talos TEM/STEM microscope. Typically, greater than 500 cavities were characterized in the region of interest (500-700nm) per irradiation condition. The foil thicknesses were measured to be in the range 50-80 nm via electron energy loss spectroscopy (EELS). Errors in cavity size, density and swelling were estimated to be 7%, 10% and 30%, respectively.

Results

To determine the effect of damage level on the resulting cavity microstructure, a series of dual and triple ion irradiations were conducted at 50, 100, and 150 dpa with otherwise equivalent conditions of 1x10^{-3}

dpa/s and 40/10 appm/dpa of H/He all at 500°C. A visual comparison of the microstructural evolution across each damage level is shown in the STEM-HAADF images in Figure 1. As expected, swelling increased with each increase in damage level for both dual and triple ion irradiation, as shown in Figure 2, where co-injection of H along with He and radiation damage resulted in as much as a two-fold increase in swelling, showing that these synergistic effects promote cavity swelling across wide damage regimes. The cavity size distributions shown in Figure 3 indicate that this increase in swelling between dual and triple ion irradiation is the result of both increases in maximum cavity size as well as increases in cavity density in the triple ion irradiated condition in comparison to that of dual ions.

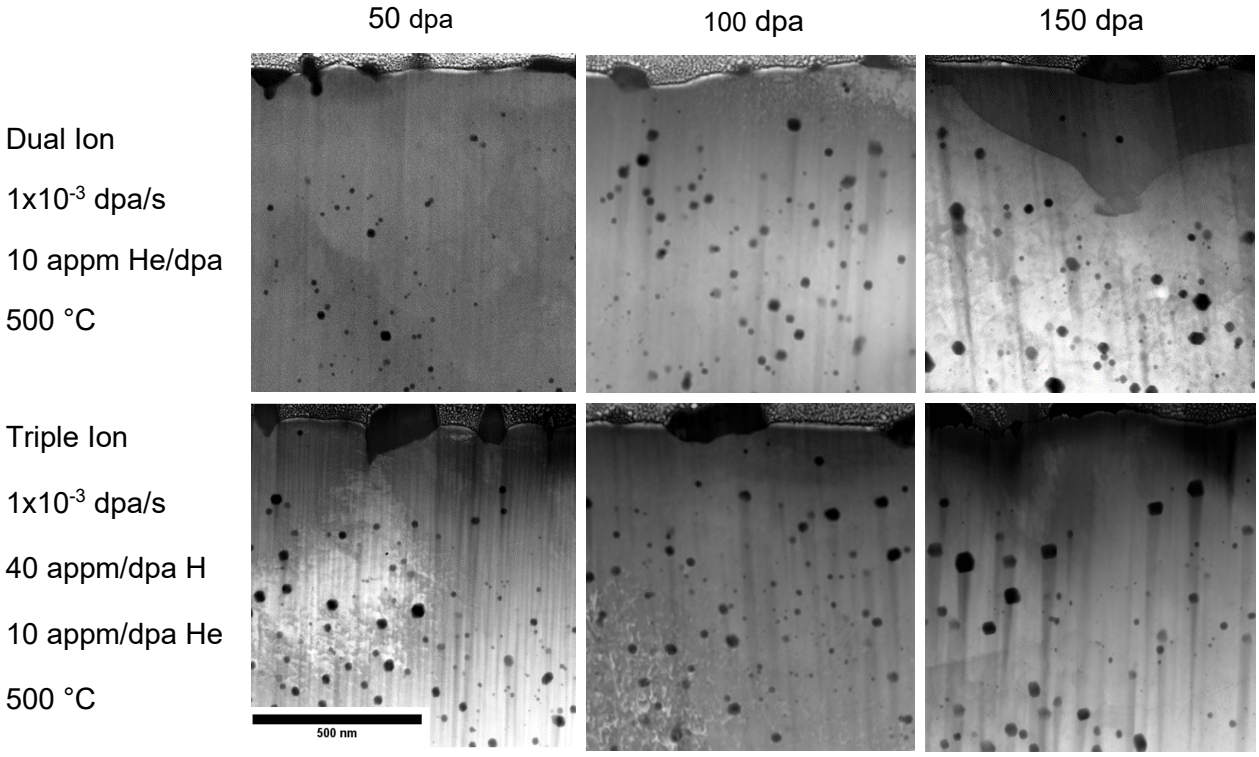

Figure 1. The HAADF images of cavities in dual beam (Fe^{2+}+H^{+}, Fe^{2+}+He^{2+}) and triple beam (Fe^{2+}+He^{2+}+H^{+}) irradiated F82H at 50, 100, and 150 dpa.

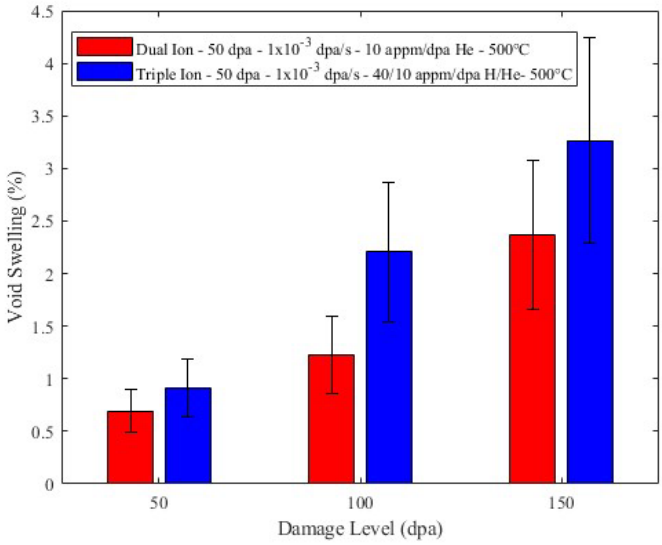

Figure 2. Evolution of cavity swelling across damage levels in dual and triple ion irradiated F82H.

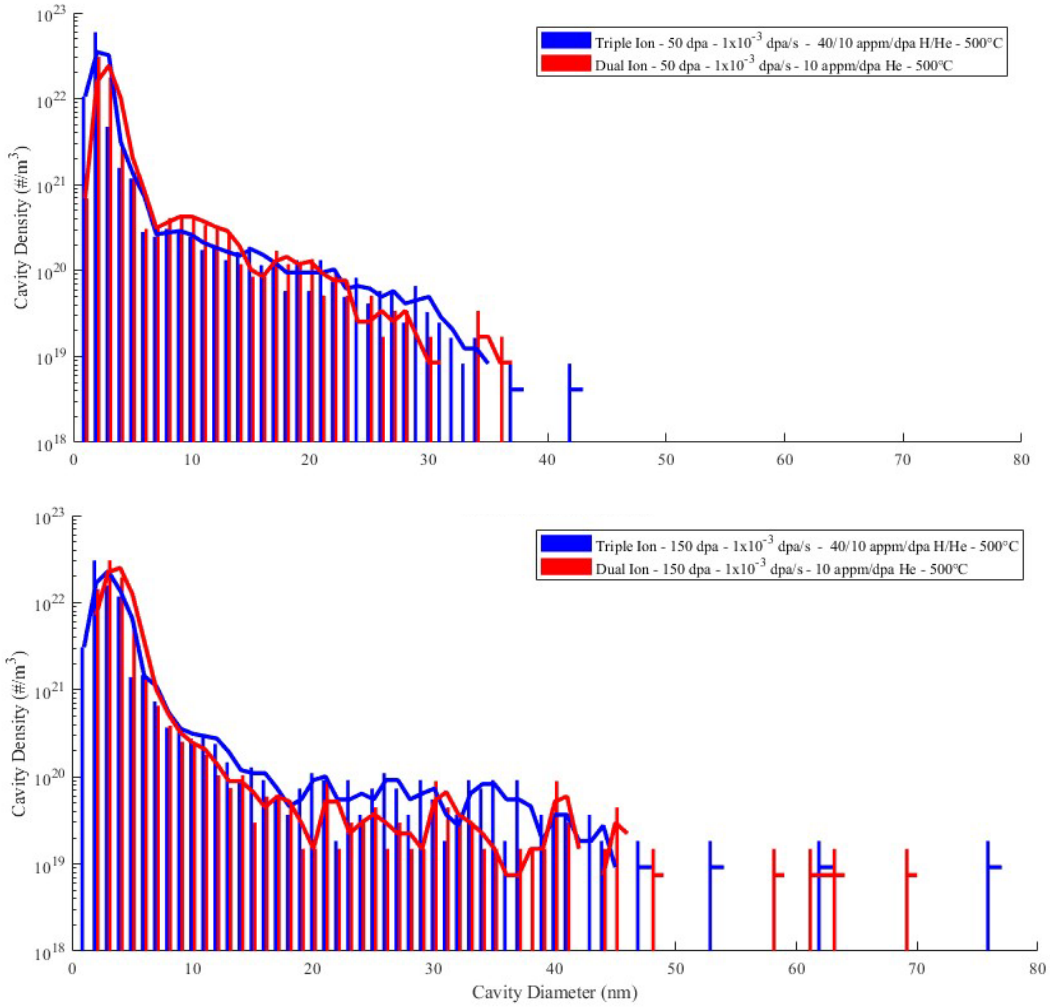

Figure 3. Comparison of the cavity size distributions resulting from dual and triple ion irradiated F82H at 50 and 150 dpa.

Another series of dual and triple ion irradiation experiments was done to determine the temperature dependence of the synergies between H, He and radiation damage. Starting at 400°C and going in 50°C steps to 600°C, these experiments were conducted at otherwise equivalent conditions of 50 dpa, $1x10^{-3}$ dpa/s, and 40/10 appm/dpa of H/He. A visual comparison of the irradiated microstructures across these temperature steps in triple ion irradiated F82H is shown in the TEM-BF images in Figure 4. At 400°C, swelling is significantly suppressed with high densities of small cavities of small 1-2 nm cavities spread homogeneously with the triple ion irradiated case having over double the cavity density. At the high end of 550°C to 600°C, swelling is again subdued in both the dual and triple ion irradiated cases with cavities residing primarily along dislocations and grain boundaries. At 450°C and 500°C, swelling was much higher with much more cavity growth occurring in these conditions, of which the triple ion irradiated case had larger cavity sizes and higher overall cavity densities as shown in the cavity size distributions in Figure 5. Swelling was observed to peak around 450°C to 500°C, as is observable in comparison to other similar studies in Figure 6 [3]–[5].

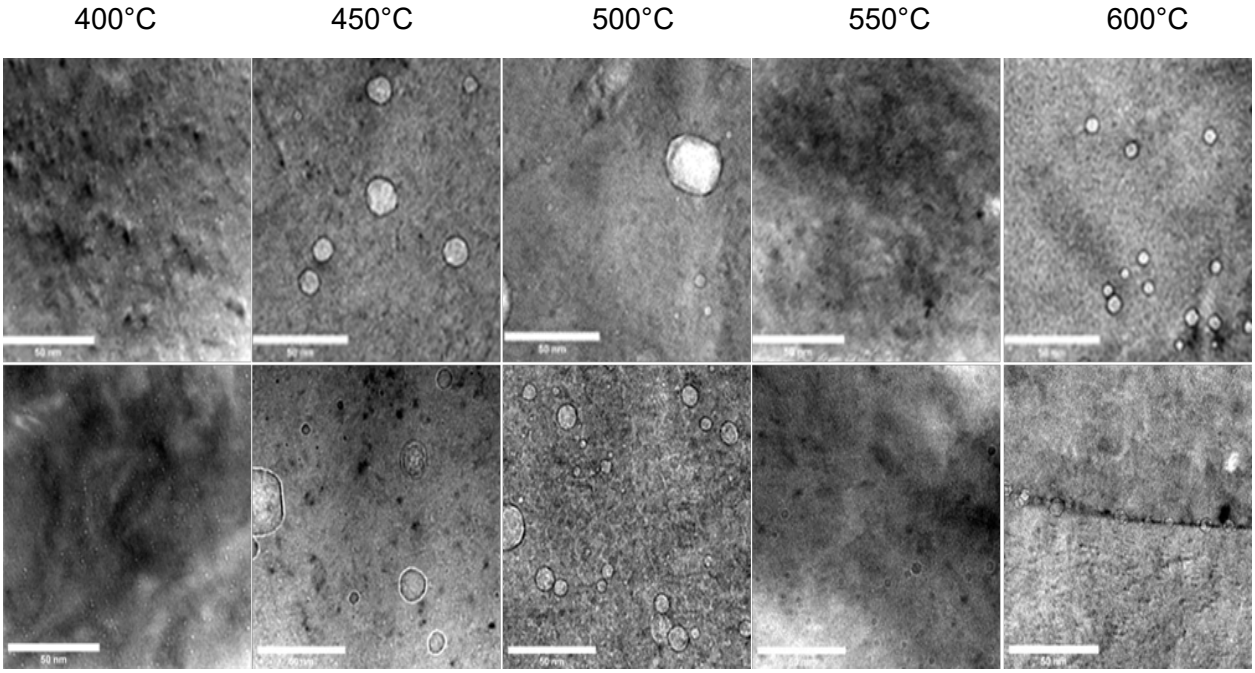

Figure 4. TEM-BF images of cavities in F82H dual and triple ion irradiated to 50 dpa, 1x10-3 dpa/s, and 40/10 appm/dpa of H/He from 400°C to 600°C.

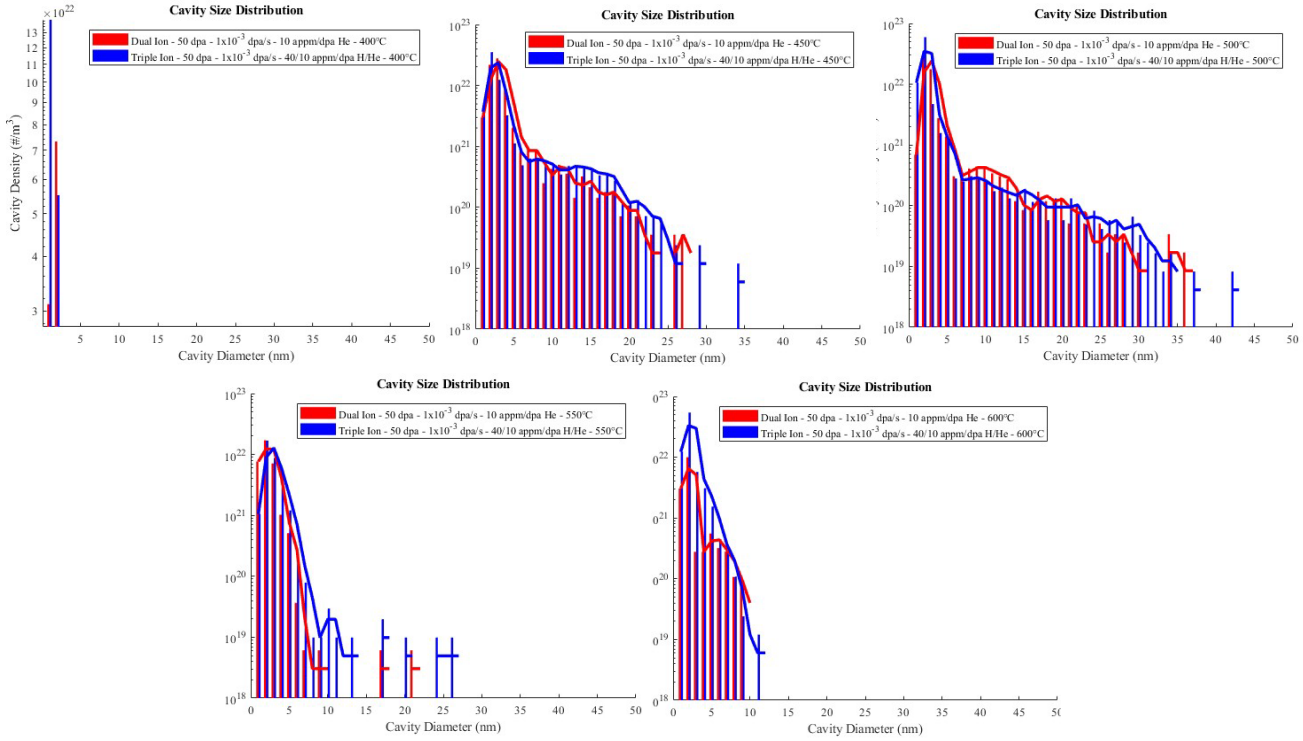

Figure 5. Cavity size distributions for dual and triple ion irradiated F82H from 400°C to 600°C.

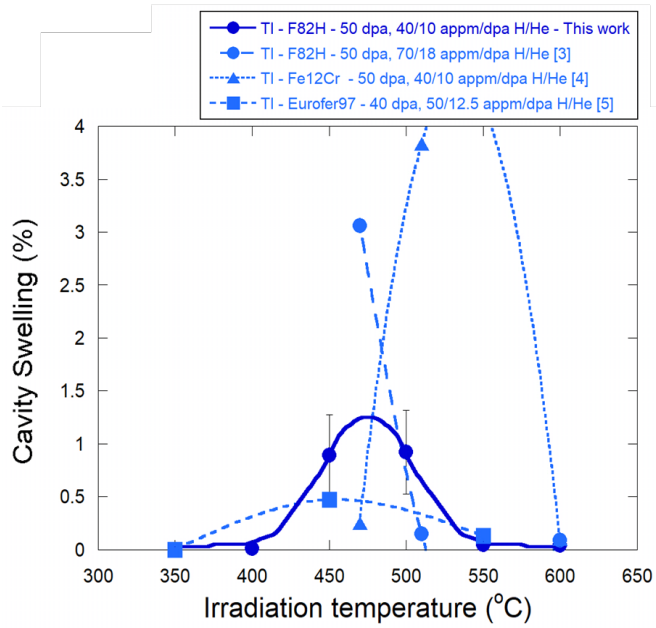

Figure 6. Evolution of cavity swelling across temperatures in triple ion irradiated F82H and similar RAFM steels.

Future Work

Further experiments are planned that include dual and triple ion irradiations to determine the dose rate dependence as well as to isolate the role of hydrogen in these phenomena. Future characterization will help understand the role of hydrogen in cavity swelling and its location in the microstructure through advanced microscopy techniques including elemental mapping and real-time observation through in-situ ion irradiation.

References

[1] L. N. Clowers, Z. Jiao, and G. S. Was, "Synergies between H, He and radiation damage in dual and triple ion irradiation of candidate fusion blanket materials," *Journal of Nuclear Materials*, vol. 565, p. 153722, 2022, doi: 10.1016/j.jnucmat.2022.153722.

[2] S. Taller *et al.*, "Multiple ion beam irradiation for the study of radiation damage in materials," *Nucl Instrum Methods Phys Res B*, vol. 412, pp. 1–10, 2017, doi: 10.1016/j.nimb.2017.08.035.

[3] E. Wakai *et al.*, "Swelling behavior of F82H steel irradiated by triple/dual ion beams," *Journal of Nuclear Materials*, vol. 318, no. SUPPL, pp. 267–273, 2003, doi: 10.1016/S0022-3115(03)00122-3.

[4] T. Tanaka *et al.*, "Synergistic effect of helium and hydrogen for defect evolution under multi-ion irradiation of Fe-Cr ferritic alloys," *Journal of Nuclear Materials*, vol. 329–333, no. 1-3 PART A, pp. 294–298, 2004, doi: 10.1016/j.jnucmat.2004.04.051.

[5] N. Zimber *et al.*, "Microstructural evolution of three potential fusion candidate steels under ion-irradiation," *Journal of Nuclear Materials*, vol. 535, 2020, doi: 10.1016/j.jnucmat.2020.152160.

6.5 INVESTIGATION OF HIGH TEMPERATURE HE EMBRITTLEMENT EFFECTS IN NICKEL-BASED AND IRON-BASED ALLOYS—Z. Qi, S.J. Zinkle (The University of Tennessee, Knoxville)

OBJECTIVE

The objective of this project is to study how tensile stress affects high temperature helium embrittlement (HTHE) behaviour by characterizing cavity size and number density in the matrix and at grain boundaries (GBs) in nickel-based and iron-based alloys after He irradiations at different temperatures, stresses and He implantation rates.

SUMMARY

An innovative specimen fixture was designed to provide tensile stress from zero to ~200 MPa during ion irradiation. Conventional Transmission Electron Microscopy (TEM) with bright field (BF) through-focus imaging technique was used to characterize cavity size and density in matrix and at GBs after 4.5 MeV He^{2+} irradiations to 200 appm peak implanted He concentration at 750℃ with zero stress and 100MPa stress in Fe-9%Cr, Haynes 230, Haynes 244 (standard [STD] aging) and Haynes 244 (solution annealed [SHT] and slow cooled). At zero stress, many cavities were observed in matrix for Fe-9%Cr and Haynes 244 STD aging, while sparse cavities were observed for Haynes 230 and no cavities was observed for Haynes 244 SHT in matrix. The GB cavities were observed for Haynes 244 SHT at zero stress. At 100 MPa stress, larger cavities were observed in matrix for Haynes 230, which demonstrates the importance of applied stress during He introduction.

PROGRESS AND STATUS

For fusion and Gen IV reactor concepts operating at high temperatures and doses, HTHE might be the lifetime limiting mechanism for potential structural materials. It is well accepted that tensile stress can dramatically enhance HTHE [1]. However, only limited creep test data of simultaneous He-implanted samples are available due to its drawback of high cost and long experimental time. In this project, an innovative specimen fixture was designed to passively provide tensile stress from zero to ~200 MPa during He implantation.

Three specimen fixtures with curved surfaces were machined to provide tensile stress by elastic bending. The schematic and the actual picture are shown in Figure 1a-b. The sample surface stress can be calculated with the equation $\sigma = \frac{Et}{2R}$, where E is elastic modulus of the sample, t is thickness of the sample and R is the radius of the curved surfaces. The radius of curvature for three specimen fixtures are 400, 1300 and 4300 mm. With sample thickness t varying from 0.3 to 1 mm, tensile stress from zero to ~200 MPa could be provided. During He implantation, stress relaxation from thermal and irradiation creep could take place due to the strain constraint effect from the substrate under the irradiated layer. Using the two peak dose rates (3.5e-7 and 3.5e-6 dpa/s) of our He implantations in Table 1, the initial tensile stress could relax by ~45% for He implantations #1 and #2, and ~20% for He implantation #3 over the course of the implantations, where thermal creep effect dominates the stress relaxation.

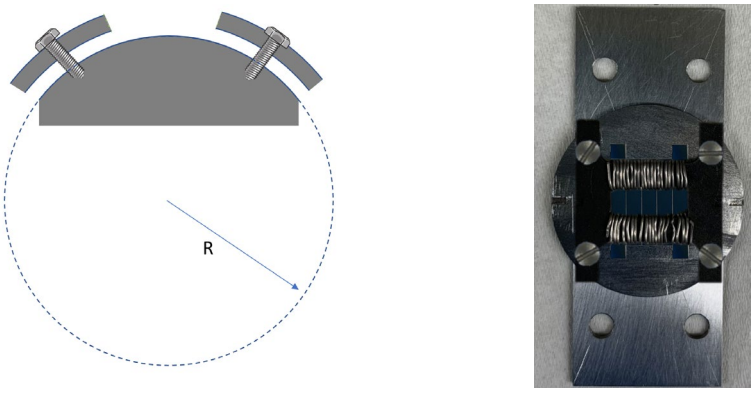

(a) *(b)*

Figure 1. (a) Schematic for specimen fixture with curved surfaces (b) Actual picture of specimen fixture with samples.

Table 1. Irradiation matrix of the alloys

Target holder	Material	Ion Species	Stress (MPa)	Fluence (ions/cm^2)	Flux (ions/cm^{2}s)	Temperature (°C)
#1	Haynes 244_SHT, Haynes 244_STD aging, Haynes 230, Fe-9%Cr and 316 SS	4.5 MeV He	0	6.8x10^{14} (200 appm)	2.36x10^{10} (0.007 appm/s)	750
#2	As above	4.5 MeV He	100	6.8x10^{14} (200 appm)	2.36x10^{10} (0.007 appm/s)	750
#3	As above	4.5 MeV He	100	6.8x10^{14} (200 appm)	2.36x10^{11} (0.07 appm/s)	750

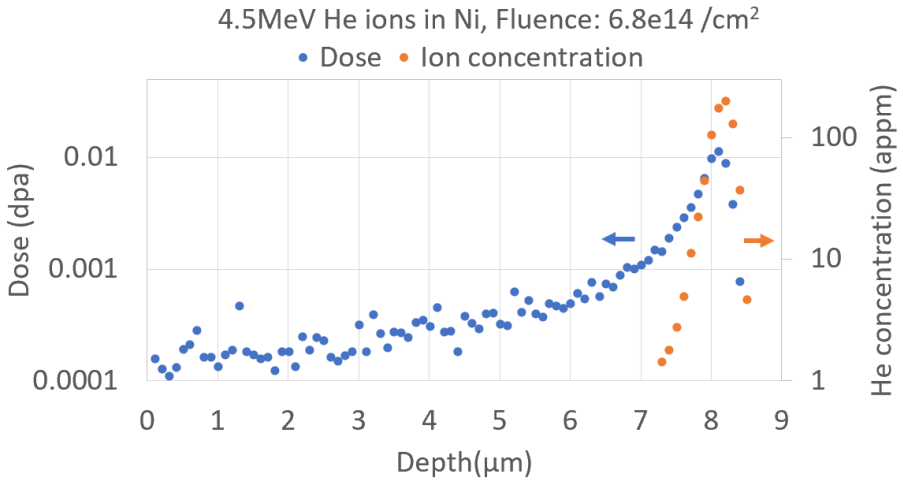

Figure 2. Dose and He concentration profile calculated by Stopping and Range of Ions in Matter (SRIM) for 4.5 MeV He ions in Ni with the fluence of 6.8x10^{14}/cm^2.

We performed 4.5 MeV He^{2+} irradiations on 316 stainless steel (SS), Fe-9%Cr and three high-performance commercial Ni-based alloys at 750℃ with peak implanted He concentration of 200 appm for different stresses and He implantation rates. The detailed irradiation conditions are shown in Table 1. The dose and He concentration profile calculated by SRIM full cascades using damage energy method are shown in Figure 2. The size and number density of cavities (matrix and GB) were characterized by conventional TEM with BF through-focus imaging technique to quantify cavity behavior versus applied stress and He implantation rate for different matrix precipitate distributions.

Experimental Procedure

Fe-9%Cr - zero-stress - 0.007 appm/s - 200 appm - 750℃

Small cavities were observed in the matrix at depths from 8.4 to 9.6 μm. By using though-focus imaging technique, small cavities are visible as lighter than background with dark fringes under underfocus condition while they exhibit dark centers with light fringes under overfocus condition, as shown in Figure 3 [2]. A total of 112 cavities were measured at depths of 8.8-9.3 μm, and the measured mean cavity diameter was $4.2 \pm 0.9\ nm$. The cavity size distribution is shown in Figure 4. Assuming the thickness of the TEM lamella is 100 nm, the cavity number density is about $1e15/cm^3$.

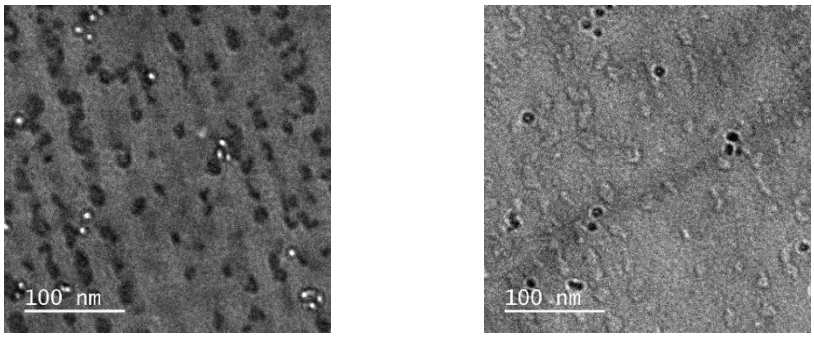

(a) *(b)*

Figure 3. The TEM BF images at depth of 8.8-9.3 μm for He cavities in matrix of Fe-9%Cr at zero-stress with He implantation rate of 0.007 appm/s and He peak concentration of 200 appm at 750℃: (a) underfocus condition. (b) overfocus condition.

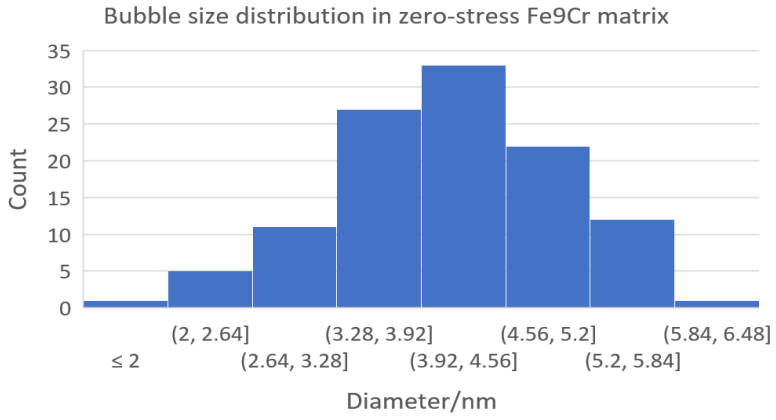

Figure 4. Cavity size distribution at depth of 8.8-9.3 μm for He cavities in matrix of Fe-9%Cr at zero-stress with He implantation rate of 0.007 appm/s and He peak concentration of 200 appm at 750℃.

Haynes 244 STD aging - zero-stress - 0.007 appm/s - 200 appm - 750℃

Small cavities were observed in the matrix at depths from 8 to 9.2 μm. A total of 159 cavities were measured at depths of 8.4-8.9 μm, and the measured mean cavity diameter was $3.4\pm0.9\,nm$. The underfocus and overfocus images for cavities are shown in Figure 5. The cavity size distribution is shown in Figure 6. Assuming the thickness of the TEM lamella is 100 nm, the cavity number density is about 1e15/cm^3.

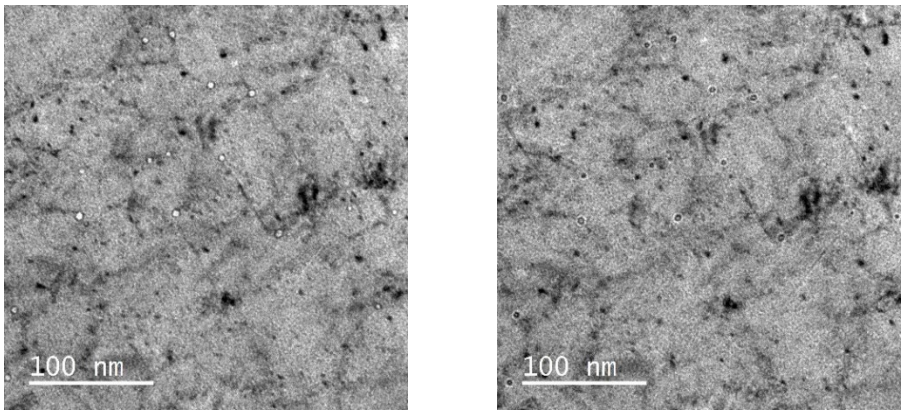

(a) *(b)*

Figure 5. The TEM BF images at depth of 8.4-8.9 μm for He cavities in matrix of Haynes 244 STD aging at zero-stress with He implantation rate of 0.007 appm/s and He peak concentration of 200 appm at 750℃: (a) underfocus condition. (b) overfocus condition.

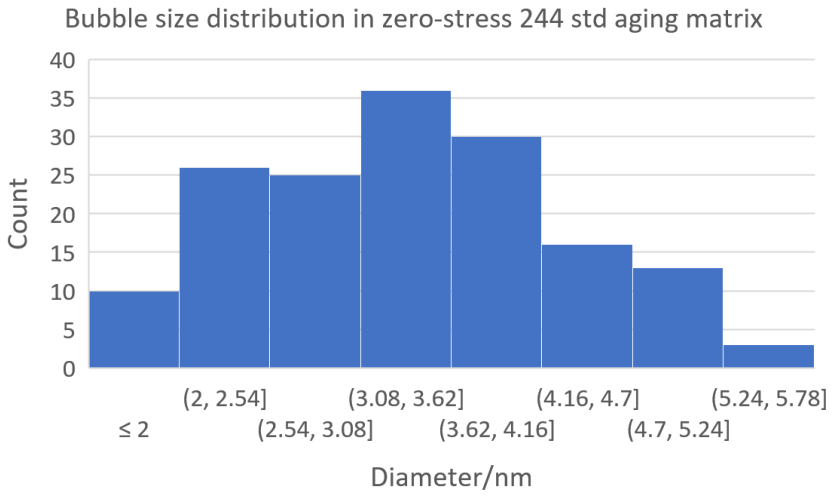

Figure 6. Cavity size distribution at depth of 8.4-8.9 μm for He cavities in matrix of Haynes 244 STD aging at zero-stress with He implantation rate of 0.007 appm/s and He peak concentration of 200 appm at 750℃.

On-zone STEM BF images ([101 zone axis]) were used to measure the pre-existing dislocation line density. By obtaining the average number of line intersections per unit length of randomly drawn lines N, the dislocation line density can be calculated by $\rho = 2N/t$, where t is the thickness of the TEM lamella [3]. Assuming the thickness of the TEM lamella is 100 nm, the pre-existing dislocation line density in Haynes 244 STD is 3e10/cm^2. By comparing the on-zone STEM BF images for dislocation lines and the underfocus

kinematic image for He cavities, it can be observed that the He cavities are predominantly located at dislocation lines, as shown in Figure 7.

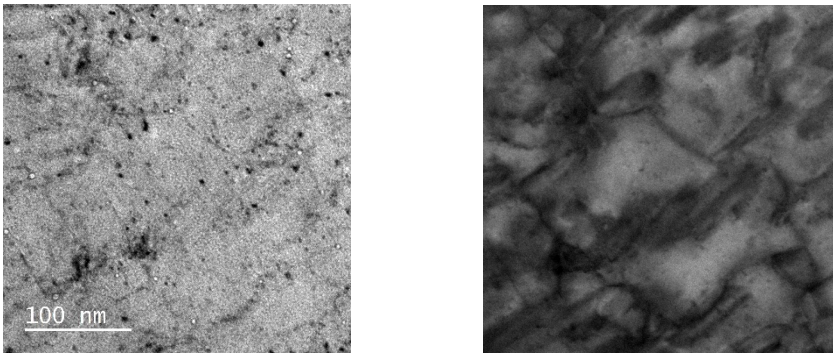

(a) *(b)*

Figure 7. Comparing the locations of He cavities and dislocation lines in matrix of Haynes 244 STD aging at zero-stress with He implantation rate of 0.007 appm/s and He peak concentration of 200 appm at 750℃: (a) TEM BF underfocus image for He cavities. (b) On-zone STEM ([101] zone axis) BF image for pre-existing dislocation lines.

Haynes 244 SHT - zero-stress - 0.007 appm/s - 200 appm - 750℃

No cavities were observed in the matrix of Haynes 244 SHT. Cavities were only observed at a GB, as shown in Figure 8. The GB in this figure extends from the surface to a depth of about 4.3 μm. 25. The GB cavities were measured, and the measured mean GB cavity diameter was $5.4 \pm 1.4\ nm$. The GB cavity size distribution is shown in Figure 9. Assuming the thickness of the TEM lamella is 100 nm, the GB cavity area number density is about 1e10/cm^2. As shown in Figure 8, large carbides (diameter ~140nm) were also observed at the GB. On-zone STEM BF images ([101 zone axis]) were also obtained, and no pre-existing dislocation lines were observed.

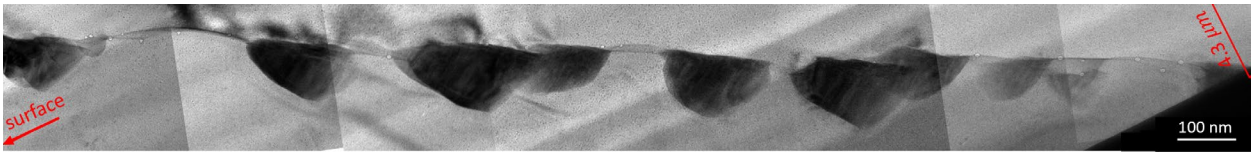

Figure 8. The TEM under focus BF images for GB cavities of Haynes 244 SHT at zero-stress with He implantation rate of 0.007 appm/s and He peak concentration of 200 appm at 750℃. Large carbides at the GB were also observed.

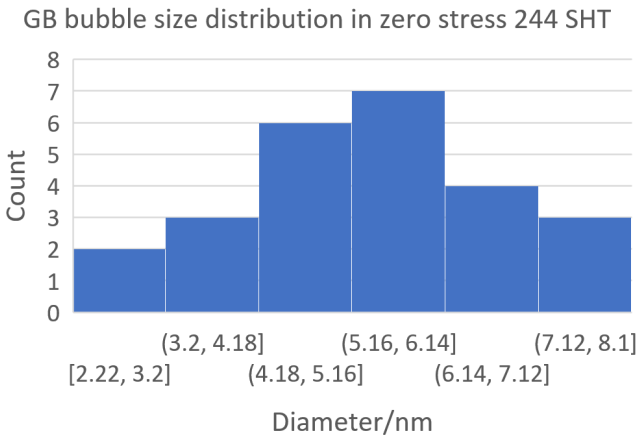

Figure 9. The GB cavity size distribution of Haynes 244 SHT at zero-stress with He implantation rate of 0.007 appm/s and He peak concentration of 200 appm at 750℃.

Haynes 230 - zero-stress - 0.007 appm/s - 200 appm - 750℃

Sparse small cavities were observed in the matrix from 8.2 to 9.5 μm. Only 6 cavities were observed at depths of 8.7-9.1 μm, and all the cavities are at dislocation lines, as shown in Figure 10. The measured mean cavity diameter was $6.2 \pm 1.5\ nm$. Assuming the thickness of the TEM lamella is 100 nm, the cavity number density is about $6e13/\mathrm{cm}^3$.

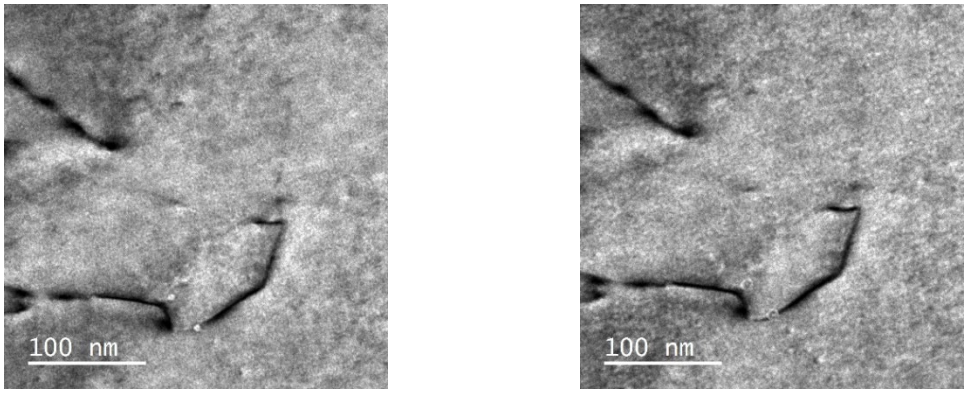

(a) *(b)*

Figure 10. The TEM BF images at depth of 8.7-9.1 μm for He cavities in matrix of Haynes 230 at zero-stress with He implantation rate of 0.007 appm/s and He peak concentration of 200 appm at 750℃: (a) underfocus condition. (b) overfocus condition.

Haynes 230 – 100MPa - 0.007 appm/s - 200 appm - 750℃

Sparse cavities were observed in the matrix at 1.8-7 μm and 10.6-16.8 μm. More cavities were observed at 7-10.6 μm. A total of 19 cavities were measured at depths of 8.5-9.2 μm, and the measured mean cavity diameter was $11 \pm 3\ nm$. The underfocus and overfocus images for cavities are shown in Figure 11. The cavity size distribution is shown in Figure 12. Assuming the thickness of the TEM lamella is 100 nm, the cavity number density is about $1e14/\mathrm{cm}^3$. This preliminary result suggests that applied stress promotes both growth and nucleation of helium bubbles in the grain matrix.

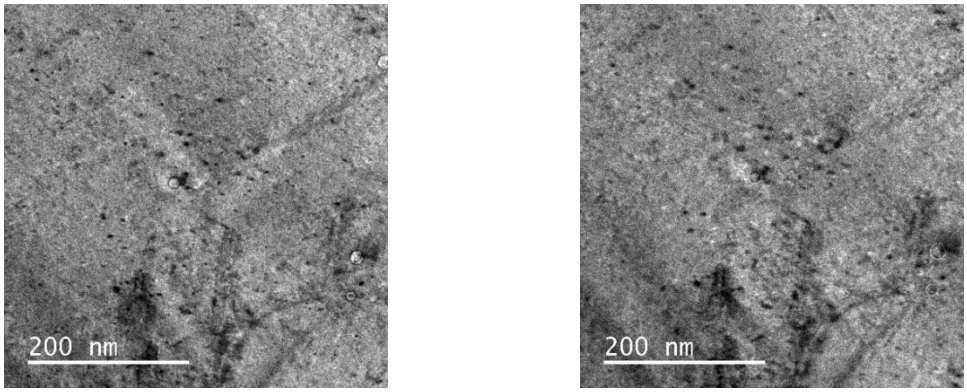

(a) *(b)*

Figure 11. The TEM BF images at depth of 8.5-9.2 μm for He cavities in matrix of Haynes 230 at 100MPa with He implantation rate of 0.007 appm/s and He peak concentration of 200 appm at 750℃: (a) underfocus condition. (b) overfocus condition.

On-zone STEM BF images ([101 zone axis]) were used to measure the pre-existing dislocation line density. Assuming the thickness of the TEM lamella is 100 nm, the pre-existing dislocation line density is 5e9/cm^2. By comparing the on-zone STEM BF images for dislocation lines and the underfocus kinematic image for He cavities, it can be observed that the He cavities are located along dislocation lines, as shown in Figure 13.

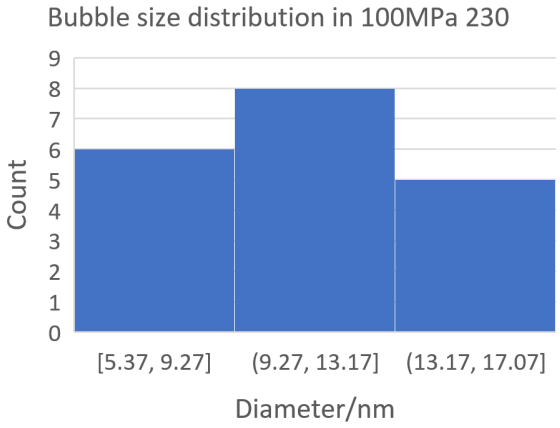

Figure 12. Cavity size distribution at depth of 8.5-9.2 μm for He cavities in matrix of Haynes 230 at 100MPa stress with He implantation rate of 0.007 appm/s and He peak concentration of 200 appm at 750℃.

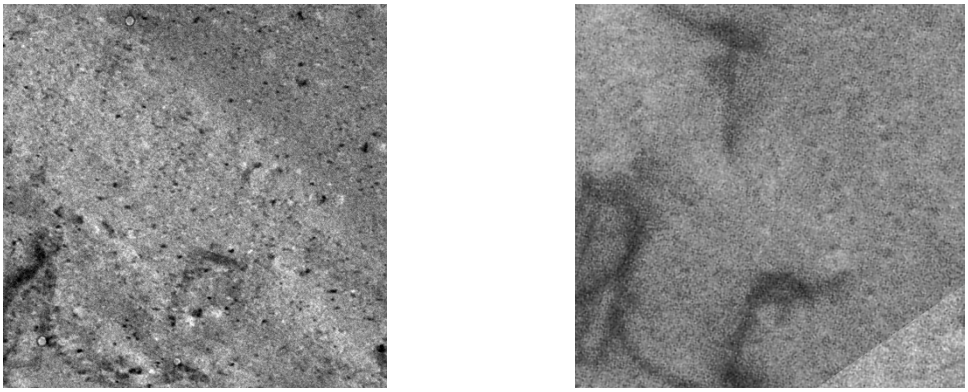

(a) *(b)*

Figure 13. Comparing the locations of He cavities and dislocation lines in matrix of Haynes 230 at 100 MPa with He implantation rate of 0.007 appm/s and He peak concentration of 200 appm at 750℃: (a) TEM BF underfocus image for He cavities. (b) On-zone STEM ([101] zone axis) BF image for pre-existing dislocation lines.

Future Work

In this report, most results are for cavities in the grain interior. We will characterize GB cavities for all the samples in the next reporting period. Also, more irradiations for different temperatures, stresses and implantation rates will be performed and characterized to get a comprehensive understanding of tensile stress effect on HTHE.

References

[1.] D. Braski, H. Schroeder, H. Ullmaier, The effect of tensile stress on the growth of helium bubbles in an austenitic stainless steel, Journal of Nuclear Materials 83(2) (1979) 265-277.
[2.] D.B. Williams, C.B. Carter, The transmission electron microscope, Transmission electron microscopy, Springer1996, pp. 3-17.
[3.] C.S. Smith, L.J.J. Guttman, Measurement of internal boundaries in three-dimensional structures by random sectioning, 5 (1953) 81-87.

7. PLASMA-MATERIAL INTERACTIONS

No contributions this reporting period.

8. CORROSION AND COMPATIBILITY IN FUSION SYSTEMS

8.1 EVALUATION OF LIQUID METAL EMBRITTLEMENT SUSCEPTIBILITY OF STEELS IN LIQUID LITHIUM—M. Romedenne, C. S. Hawkins, B.A. Pint (Oak Ridge National Laboratory)

OBJECTIVE

The goal is to inform the design of the United States (US)-based liquid metal divertor plasma-facing component (PFC) for the fusion nuclear science facility (FNSF) related to liquid metal embrittlement (LME). To that end, an experimental procedure to evaluate the susceptibility of steels to liquid Li embrittlement was established.

SUMMARY

Hollow tensile specimens of reduced activation ferritic/martensitic (RAFM) alloy F82H and low-alloy martensitic American Iron and Steel Institute (AISI) type 4340 steel were prepared and exposed to commercial liquid Li at 200 and 400°C. The 4340 specimens were tested and confirmed LME in liquid Li especially, when the specimens were heated to 400°C for 1 h before tensile testing at 200°C. In contrast, the F82H specimens did not demonstrate clear LME behavior even after pre-exposure to liquid Li for 500 h at 500°C. Characterization of the fractured specimens is in progress.

PROGRESS AND STATUS

Introduction

Liquid metals are being explored as a potential solution for the extreme environment experienced by PFCs (e.g., Li PFCs) and blanket systems (e.g., dual coolant lead lithium, [DCLL]) of the FNSF [1]. The FNSF involves several materials challenges [2] such as magnetohydrodynamics (MDH) effects [3], corrosion and mass transfer in flowing PbLi [4-6] and irradiation damage [7]. More recently, the failure of a Li-filled type 1018 steel preheater after a few minutes at 200°C [8] has pointed out the need for additional assessment of the potential LME for RAFM steels and relevant fusion structural materials.

The LME was studied for many liquid-materials pairs (Ga, Zn, Sn, Hg-, Al-, Cu-, Zn- alloys and steels) [9] and was defined as the abrupt reduction in elongation at rupture of an alloy that occurs in contact with liquid metals [9, 10]. In liquid Li, ferritic/martensitic stainless steels (Fe-9Cr-1Mo) and austenitic steel (Fe-18Cr-10Ni) were found insensitive to LME [10, 11], while mild steels 4130 and 1018 showed potential susceptibility to LME [8, 10]. However, in the former [10], short-term exposure to liquid Li was observed to result in grain boundary (GB) decarburization and therefore could more likely correspond to an impact of the environment on mechanical behavior. In general, LME is differentiated from the progressive impact of the environment on mechanical properties that concerns the long-term corrosion induced mass transfer and thermal aging [12]. Both Li LME and environmental embrittlement was investigated by Borgstedt and Grundmann [11]. The authors measured no reduction in elongation at rupture during tensile testing in air and liquid Li at 250°C for austenitic (Fe-18Cr-10Ni – 1.4301 (type 304)) steel and up to 25% reduction for ferritic steels (Fe-11Cr-Mo 1.4923 and 1.4914) attributed to GB attack. After pre-exposure to purified liquid Li (1,000 h exposure at 550°C), tensile tests in liquid Li at 250°C resulted in 41 and 36% reduction in elongation at rupture for the austenitic and ferritic steels respectively, that was also related to GB attack [11].

Within the development of the FNSF, new materials such as RAFM-type steels and oxide dispersion strengthened (ODS) steels will be in contact with the liquid metals and therefore their susceptibility to LME needs evaluation. In the present study, an LME evaluation and characterization of F82H (Fe-8Cr-2W) and 340 steels was performed using hollow Li-filled specimens. The fractures and polished surfaces were characterized.

Experimental Procedure

Tested materials

The ferritic steel type AISI 4340 and RAFM-type F82H steel were chosen for the experiments and their compositions are shown in Table 1). The starting materials were delivered in the form of plates. The F82H was normalized 40 min at 1040°C and tempered at 750°C for 60 min.

Table 1. Alloys chemical compositions analyzed by inductively coupled plasma atomic emission spectroscopy, combustion for carbon and inert gas fusion for nitrogen

Wt.%	**Fe**	**Cr**	**Ni**	**Mn**	**Mo**	**Si**	**C**	**W**	**Ta**	**V**	**N**	**Al**
4340	95.54	0.80	1.78	0.71	0.30	0.21	0.44	-	-	-	-	-
F82H	88.9	8.1	0.06	0.45	-	0.08	0.10	1.8	0.09	0.20	0.01	0.02

Cylindrical hollow tensile specimens and caps were machined from the plates with 57.2 mm gage length, 12.7 mm outer and 11.2 mm inner diameter (Figure 1). As a safety measure during the LME test, additional threads were machined at the bottom of the tensile specimen to attach a stainless-steel lid and cup made of type 316L stainless steel to catch the Li after fracture (Figure 1). The hollow tensile specimens were filled with 3 g of commercial Li from Sigma Aldrich (composition in Table 2) and sealed by welding the lid on the top in an Ar-filled glove box. The concentrations of nonmetallic impurities (C, O, N and H) in the Li were not measured.

Figure 1. Images of (bottom) Hollow tensile specimens (top) 316L catch cup for lithium.

Table 2. Lithium chemical composition (wt.%) analyzed by inductively coupled plasma atomic emission spectroscopy

Wt.%	**Li**	**K**	**Na**
Li	99.96	0.01	0.03

Tensile tests

High temperature tensile tests were performed according to ASTM International (ASTM) standard E21 by means of an MTS Servo-hydraulic load frame 312.31 coupled with an MTS model 407 controller and custom LabView control software. An ATS three zone furnace coupled with ATS temperature controller was utilized to control the temperature of the test specimen (Figure 2a). The temperature of the test specimen was monitored utilizing three type “S” thermocouples held in intimate contact to the specimen gauge length (Figure 2b). The Thermocouples were placed at the top, middle, and bottom of the gauge length to ensure a temperature gradient of no more than ± 3°C along the reduced section. A Ni-based alloy 600 retort was utilized for environmental control along with flowing ultra-high purity Ar (99.999%) through the retort while maintaining a positive atmosphere. Three different displacements rates were used, one to achieve the required strain rate at yield per ASTM E21 ($\varepsilon_1 = 5\times10^{-3}$ min^{-1}) and higher and lower strain rates ($\varepsilon_2 = 5\times10^{-2}$ min^{-1}, $\varepsilon_3 = 5\times10^{-4}$ min^{-1}) to evaluate the effect of strain rate.

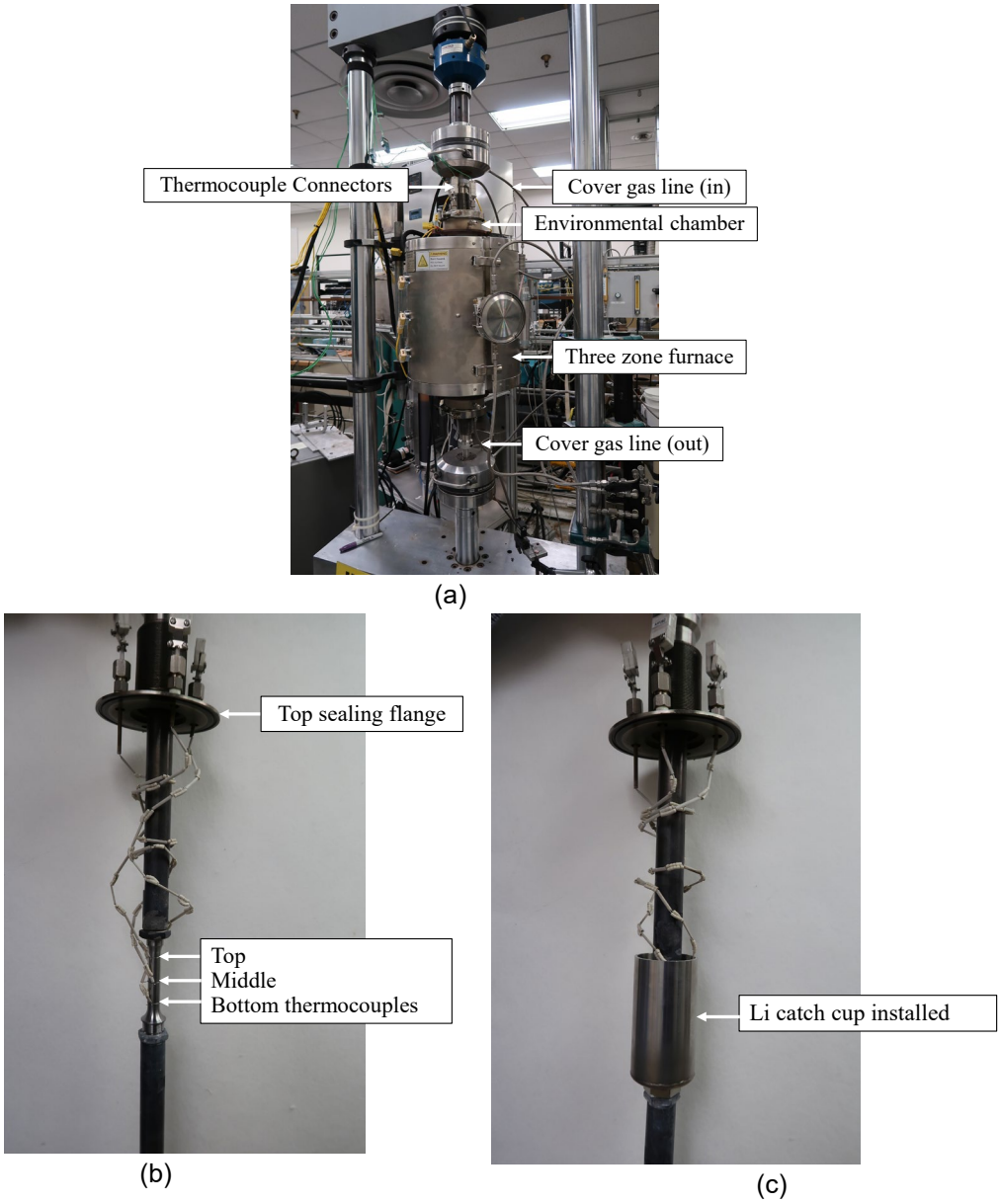

Figure 2. (a) Picture of the high temperature tensile test frame, (b) picture of the specimen and thermocouples and (c) picture of the specimen, thermocouples and Li catch cup.

Table 3 gives a summary of the test matrix for each material. Tests were performed with Ar- and Li-filled hollow tensile specimens at 200°C with 1 h heating at 200°C (henceforth named 200/200°C) or 1h heating at 400°C (henceforth named 400/400°C) and three different strain rates (ε_1, ε_2, ε_3). In addition, one hollow F82H specimen filled with Li was pre-exposed for 500 h at 500°C in a box furnace and then tensile tested in Li at 200°C.

Table 3. Number of specimens tested per experimental condition and strain rate (F82H and 4340)

Parameter of test	**200/200°C (F82H)**	**400/200°C (F82H)**	**200/200°C (4340)**	**400/200°C (4340)**
Number of specimens tested in: **Argon** **$\varepsilon_1 = 5 \times 10^{-3}$ min^{-1}**	2	-	1	-
Commercial Li **$\varepsilon_1 = 5 \times 10^{-3}$ min^{-1}**	4	1	2	2
Commercial Li **$\varepsilon_2 = 5 \times 10^{-2}$ min^{-1}**	1	-	-	-
Commercial Li **$\varepsilon_3 = 5 \times 10^{-4}$ min^{-1}**	1	-	-	-
Commercial Li after pre-exposure in Li (500h at 500°C) **$\varepsilon_1 = 5 \times 10^{-3}$ min^{-1}**	1	-	-	-

Characterizations

After tensile tests, the specimens were cleaned using ethanol. The fracture surface and polished cross-sections were characterized using secondary electron (SE) and backscattered electron (BSE) in a scanning electron microscope (SEM) (Tescan model MIRA3) equipped with energy dispersive X-ray spectroscopy (EDS).

Results

Stress-strain curves

Stress-strain curves are reported in Figure 3 for alloy 4340 and F82H for the specimens tested in Ar and Li at 200°C and a strain rate of 5 10^{-3} min^{-1}. For the 4340 specimens, a 77 ± 2% reduction in elongation at rupture was measured in Li compared to Ar (Figure 3a). For the F82H specimens, the results in Ar were more reproducible than the result in Li and a smaller reduction of elongation at rupture (25 ± 8%) was measured (Figure 3b) compared to the 4340 alloy (Figure 3a).

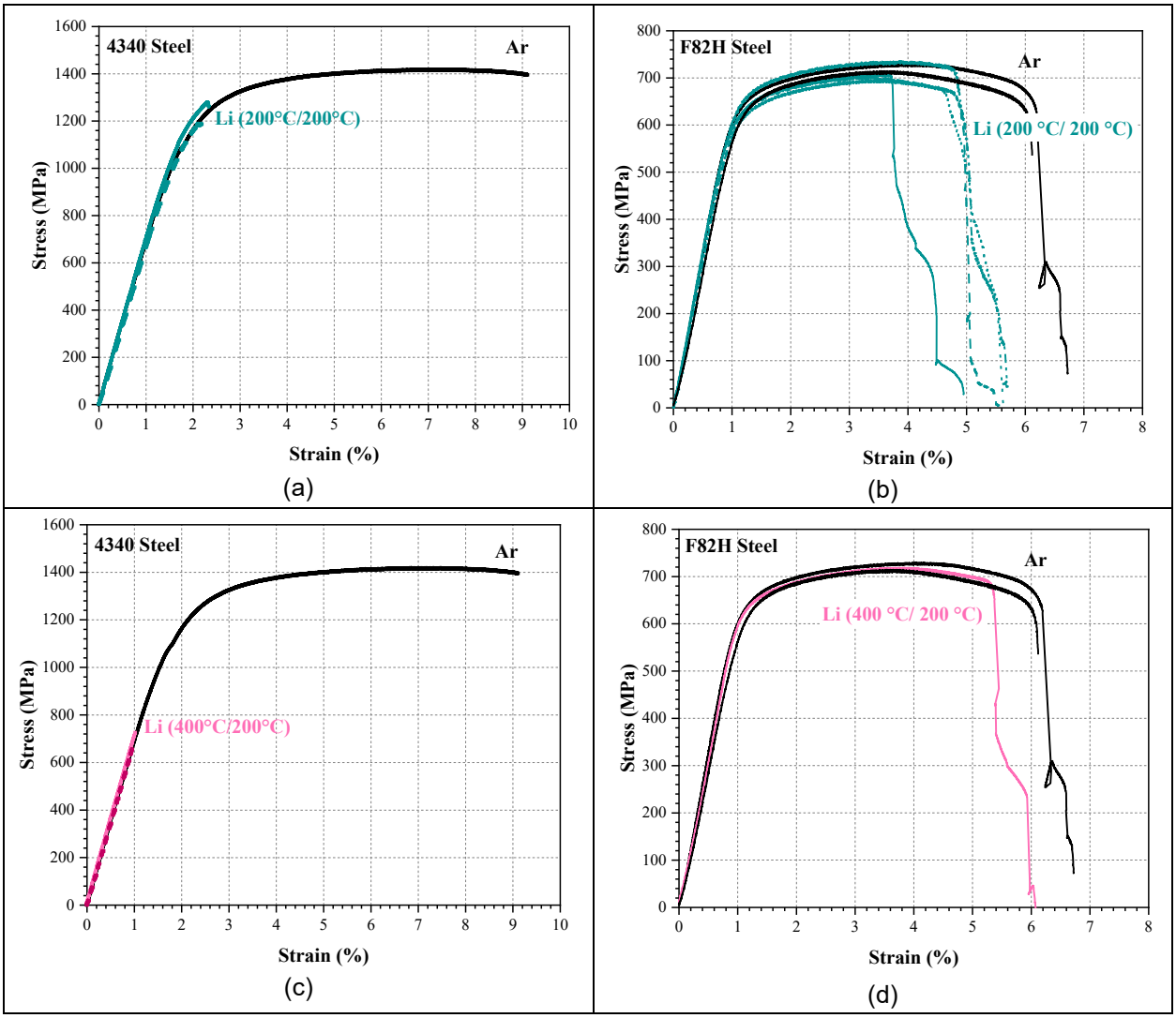

Figure 3. Stress-strain curves of (a, c) 4340 and (b, d) F82H after exposure in (a, b) Ar and Li at 200°C (200/200°C) and in Ar (200/200°C) and Li (400/200°C) ($\varepsilon_1 = 5 \times 10^{-3}$ min^{-1}).

When the specimen was pre-heated at 400°C for 1 h, the deformation at rupture was even lower for the Li-filled alloy 4340 specimens, with a 90% reduction in elongation at rupture in Li and little to no plastic deformation (Figure 3c). For the F82H specimens, pre-heating at 400°C for 1 h did not change the deformation at rupture compared to 200°C in Li or Ar (Figure 3d). In addition, tensile testing after a 500-h pre-exposure in Li at 500°C did not impact the strength and deformation at rupture for the F82H specimen (Figure 4). Similarly, increasing and decreasing the strain rate (Table 3) did not result in a significant reduction in deformation at rupture (Figures 3 and 4).

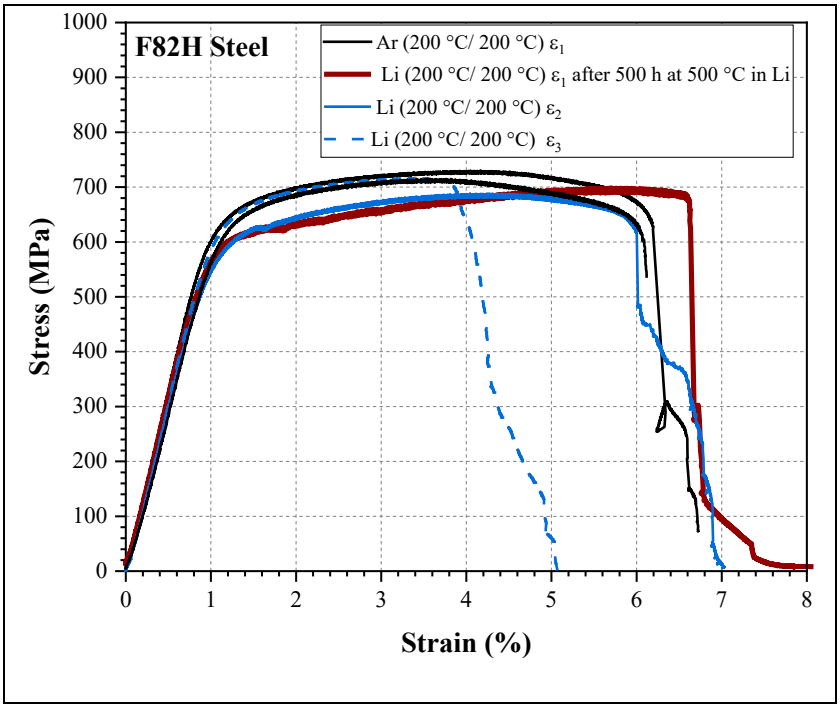

Figure 4. Strain-strain curve for F82H steel during exposure in Ar or Li (200°C/200°C), ε1, ε2, ε3 with and without pre-exposure in Li for 500 h at 500°C.

Fracture surfaces

The SEM observations of the fracture surfaces revealed ductile dimple fracture after tensile testing in Ar (Figure 5a) as well as in Li (200°C/200°C),Figure 5b and c, for the 4340 specimen. However, the presence of cracks throughout the 4340 specimen's thickness was noted (Figure 5b). Finally, a brittle fracture surface was observed after tensile testing in Li (400°C/200°C) for the 4340 specimen in Figure 5c.

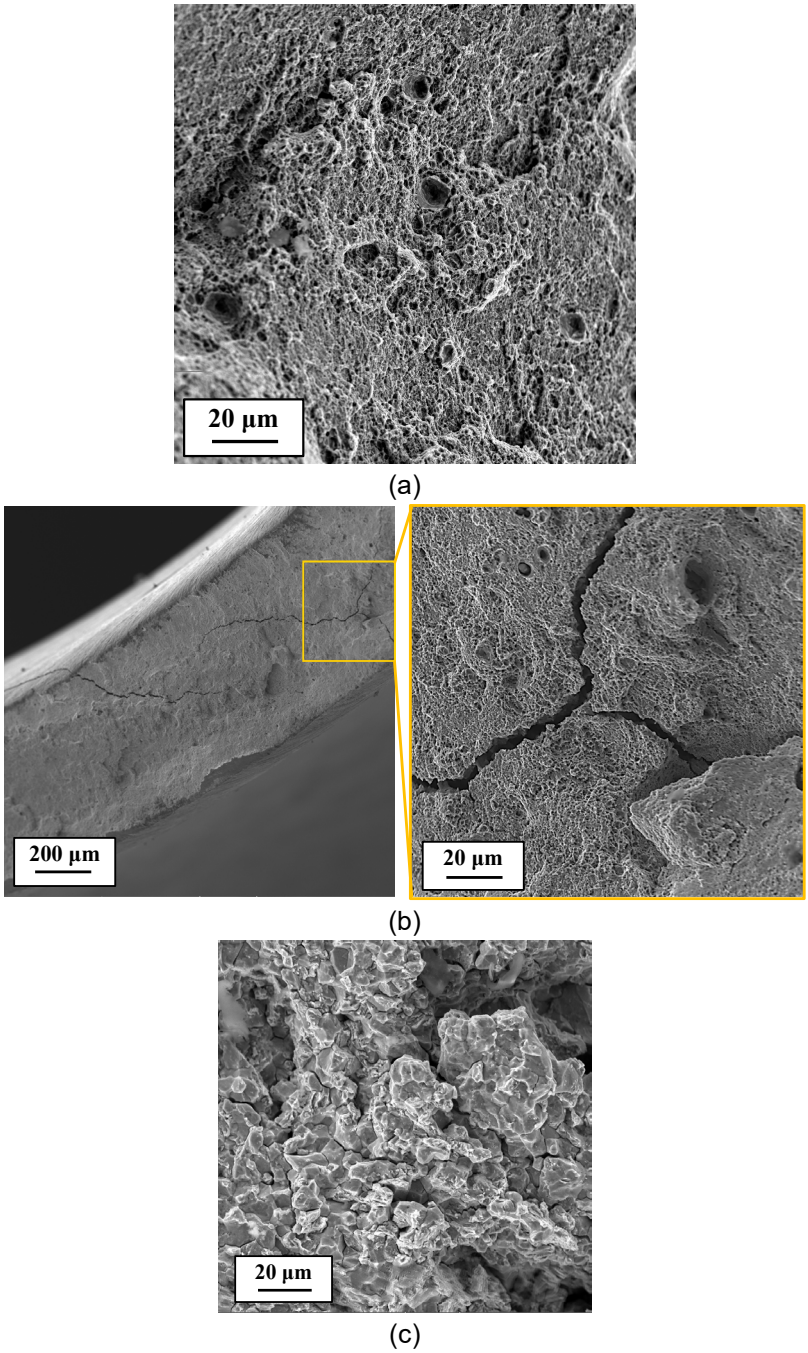

Figure 4. The SE images of fracture surfaces of 4340 specimens after exposure in (a) Ar (200/200°C), (b) Li (200/200°C) and (c) Li (400/200°C).

The F82H fracture surfaces are reported in Figure 6. Ductile fracture behavior was observed after tensile testing in Ar (200/200°C) in Figure 6a. After exposure in Li (200/200°C) mixed ductile (Figure 6b) and brittle (quasi-cleavage in Figure 6c) behaviors were identified in agreement with the slight reduction in elongation at rupture reported in Figure 3b. Tensile testing in Li after pre-exposure in Li for 500 h at 500°C also showed quasi-cleavage behavior (Figure 6d).

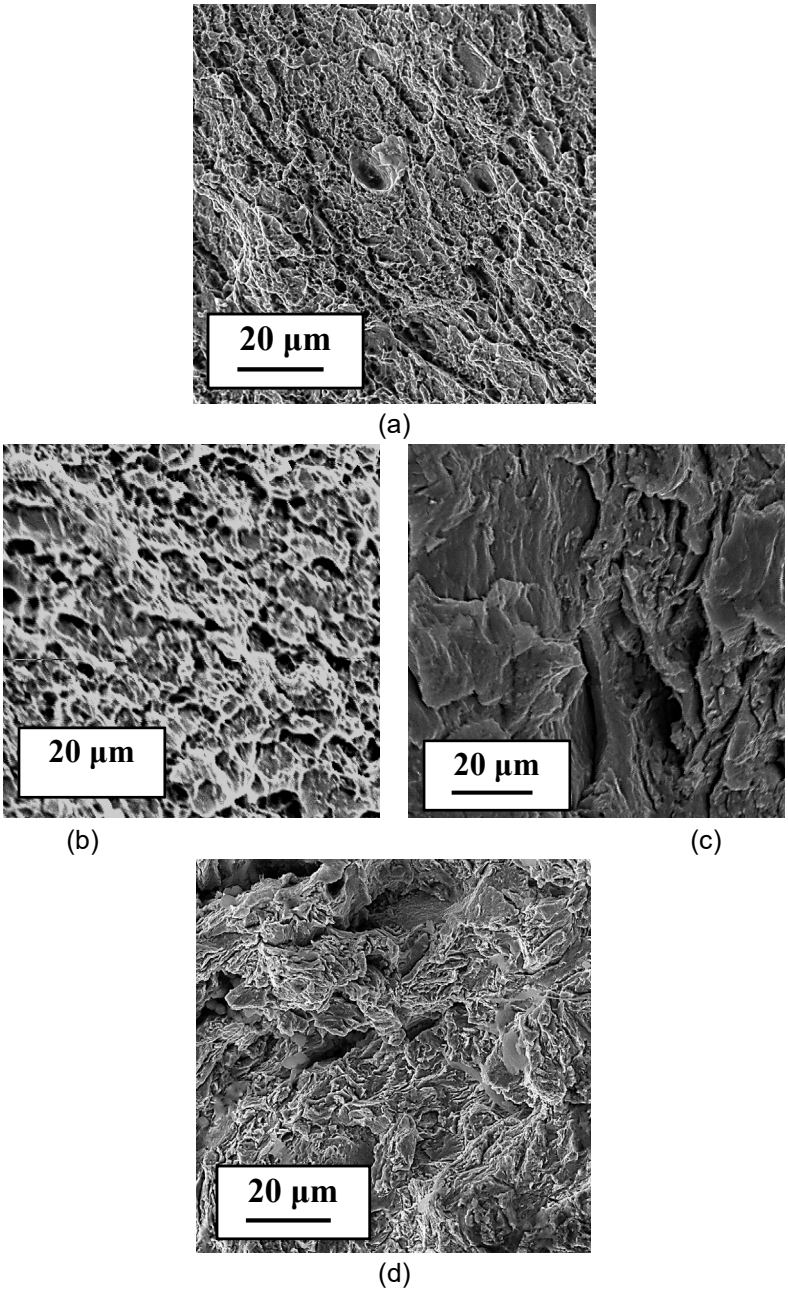

Figure 5. The SE images of fractured surface of F82H specimens after exposure in (a) Ar (200/200°C), (b, c) Li (200/200°C) and (d) Li (200/200°C) after pre-exposure in Li for 500 h at 500°C.

Future work

Polished cross sections of the specimens are being prepared and will be etched to evaluate the microstructure changes as a function of temperature and environment.

References

[1] Smolentsev, S., et al., *Integrated Liquid Metal Flowing First Wall and Open-Surface Divertor for Fusion Nuclear Science Facility: Concept, Design, and Analysis.* Fusion Science and Technology, 2019. **75**(8): p. 939-958.
[2] Rowcliffe, A.F., et al., *Materials-engineering challenges for the fusion core and lifetime components of the fusion nuclear science facility.* Nuclear Materials and Energy, 2018. **16**: p. 82-87.
[3] Smolentsev, S., et al., *MHD thermohydraulics analysis and supporting R&D for DCLL blanket in the FNSF.* Fusion Engineering and Design, 2018. **135**: p. 314-323.
[4] Pint, B.A., J. Jun, and M. Romedenne, *Compatibility of SiC with ODS FeCrAl in flowing Pb-Li at 600°–700 °C.* Fusion Engineering and Design, 2021. **166**: p. 112389.
[5] Pint, B.A. and J. Jun, *Pre-Oxidation to Improve Liquid Metal Compatibility.* Oxidation of Metals, 2021. **96**(3): p. 231-240.
[6] Pint, B.A. and K.A. Unocic, *Pb–Li compatibility issues for DEMO.* Journal of Nuclear Materials, 2013. **442**(1, Supplement 1): p. S572-S575.
[7] Bhattacharya, A., et al., *Irradiation damage concurrent challenges with RAFM and ODS steels for fusion reactor first-wall/blanket: a review.* Journal of Physics: Energy, 2022. **4**(3): p. 034003.
[8] Nygren, R.E., et al., *Failure of a lithium-filled target and some implications for fusion components.* Fusion Engineering and Design, 2021. **171**: p. 112664.
[9] Nicholas, M.G. and C.F. Old, *Liquid metal embrittlement.* Journal of Materials Science, 1979. **14**(1): p. 1-18.
[10] Old, C.F., *Liquid metal embrittlement of nuclear materials.* Journal of Nuclear Materials, 1980. **92**(1): p. 2-25.
[11] Borgstedt, H.U. and M. Grundmann, *The fracture of austenitic and martensitic steel in liquid lithium.* Nuclear Engineering and Design. Fusion, 1986. **3**(3): p. 273-286.
[12] Chopra, O.K. and P.F. Tortorelli, *Compatibility of materials for use in liquid-metal blankets of fusion-reactors.* Journal of Nuclear Materials, 1984. **123**(1-3): p. 1201-1212.

9. MODELING AND COMPUTATIONAL STUDIES

9.1 MODELING THE EFFECT OF HYDROGEN ON TUNGSTEN GRAIN BOUNDARY PROPERTIES

—T. Frolov, R.E. Rudd (Lawrence Livermore National Laboratory)

OBJECTIVE

The objective of this study is to assess the effect of hydrogen isotopes on mechanical properties of tungsten that are relevant to first-wall applications in a tokamak. We focus on the effects of hydrogen segregation to grain boundaries (GBs) and its impact on the GB structure and properties. Through molecular dynamics and other atomistic techniques, we are able to make predictions of GB structure and properties related to it, including GB mobility and impurity diffusivity along the GB. The GB structure can change significantly and abruptly as conditions change, including due to heating and radiation damage. These GB phase transformations can have a pronounced effect on mobility and impurity diffusivity, even when no hydrogen is present. How this behavior changes in the presence of hydrogen is not known. The phase may affect the level of hydrogen segregation and hydrogen storage, and the hydrogen may induce significant GB structure changes. Our objective is to predict whether they do. The results inform thermomechanical modeling of tungsten at tokamak conditions.

PROGRESS AND STATUS

We have applied molecular dynamics to determine whether hydrogen in tungsten segregates to GBs, whether that depends on the kind of GB and what effect it has on the structure of the boundary. The GBs are the interfaces in materials where two grains with different crystal orientations meet. The arrangement of atoms in a grain boundary is related to the crystal structure of the adjoining grains, but distinct. Many of the properties of metals and other crystalline materials are determined by their defects including GBs.

The GB structure has long been thought to be uniquely determined by the boundary's orientation and misorientation, up to defect content which would raise its energy. Here the misorientation is the angle between the lattices in the two abutting grains, and the orientation is the angle at which the boundary slices through the pair. The understanding of the thermodynamics of GBs has been based on that notion. Over the past decade computational work has predicted GB phase transformations in which a GB with fixed orientation and misorientation change's structure dramatically in a first order transformation [1]. That prediction has recently been observed in experiments using high resolution transmission electron microscopy [2]. A GB was caught in mid-transformation. The experiments were able to resolve the atomic structure of the GB, showing half of the boundary to be in the ground state structure and the other half in a high-temperature phase. The structures of both phases agreed with atomistic calculations.

The relevant time scales can be long compared to what is directly accessible to conventional molecular dynamics simulation, so special computational techniques are required to study these processes. Advanced genetic search algorithms coupled with machine learning have proved to be effective at generating a large ensemble of metastable GB structures and then automatically finding relations amongst them to reduce to a small number of distinct phases [3]. Genetic algorithms avoid getting trapped in local minima during the search on the configuration space by using a method inspired by evolution. Similar to the copper studied in the earlier computational work and high-resolution transmission electron microscopy, we have predicted a rich phase structure for GBs in tungsten [4,5]. Once the structures are associated with putative phases, molecular dynamics is used to investigate their high-temperature behavior [4,5] and free energy calculations can be done to determine free energies [6]. An example of GB phases for a 20° symmetric tilt GB in tungsten is shown in Figure 1.

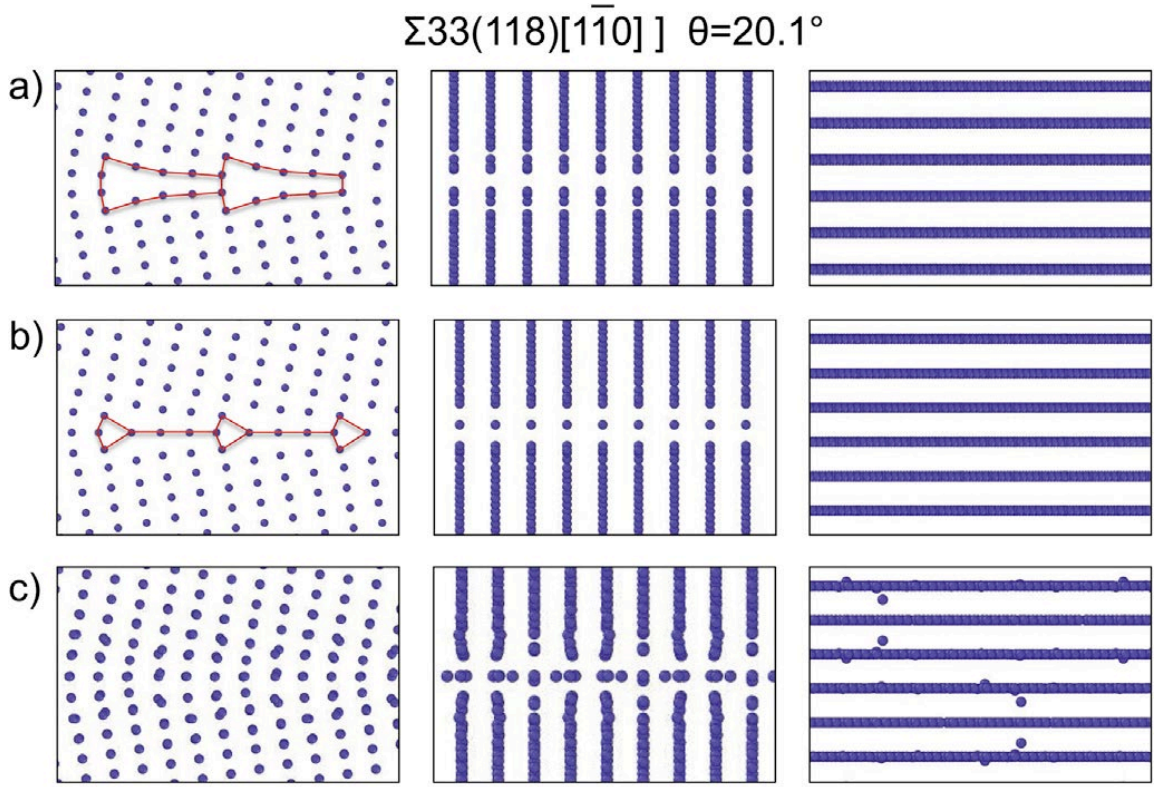

Figure 1. Tungsten GB phases for the $\Sigma 33\ (118)[1\bar{1}0]$ symmetric tilt boundary (θ=20.1°). The structure shown in panel c) is the ground state at zero temperature. The other structures are metastable, generated using the gamma-surface approach. The GB may undergo discontinuous structural transformations as conditions such as temperature change. At higher temperatures, entropy can stabilize other phases and atomic diffusion enables the density at the boundary to change so the phase transformations can happen. Reprinted from Reference [5] with permission.

More recently, the mechanisms of GB phase transformation in tungsten have been identified [7,8]. The phase transformation progresses by nucleation and growth. Nucleation is inhibited by an energetic barrier, and small fluctuations that produce sub-critical patches of the stable phase will quickly vanish despite the new phase having a lower energy because of other contributions to the energy: interfacing stresses and GB phase junction line tension and elastic interactions [7]. The functional form of this energy has been derived analytically using elasticity theory, comparing well to the results of molecular dynamics simulation. The GB phase junction is a new kind of defect, a line defect similar to a dislocation but confined to a GB where it separates two distinct phases. Methods have been developed to detect, characterize, and visualize GB phase junctions [8], an important step toward the formulation of GB thermodynamics accounting for impurities like hydrogen.

To determine the effect of hydrogen on tungsten GBs, we have introduced hydrogen into configurations created using the advanced genetic search algorithms and machine learning [3]. We have examined several distinct cases involving different boundaries and phases of those boundaries. Molecular dynamics is then used to simulate hydrogen diffusion into, out of, and along the GBs. Hydrogen diffuses rapidly through the lattice, although it still requires somewhat lengthy molecular dynamics simulations of up to 20 ns to observe the redistribution of the hydrogen. It segregates to the GBs, as shown for two phases of the 20° symmetric tilt boundary in Figure 2. Segregation was not observed for all boundaries. Two GB phases are considered for each boundary. We introduced hydrogen into the simulation at a range of concentrations. Here we focus on W-1atm%H at a temperature of 500K. The system was then equilibrated with molecular

dynamics as described for pure metal in Reference [3]. The figure shows the resulting distribution of hydrogen. There is significant segregation of hydrogen to the GB. There are two boundaries: both run vertically through the image, at the center. Not only is the hydrogen concentration greater at the boundary, but it is ordered in a way that is complementary to the tungsten structure.

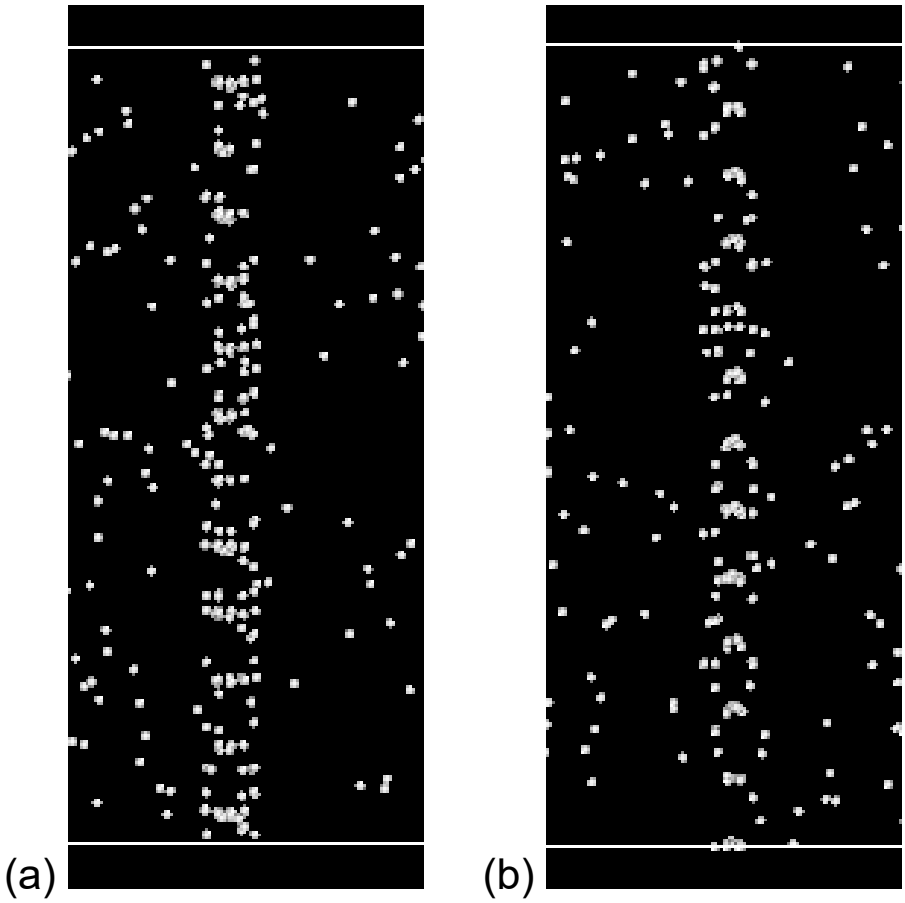

Figure 2. Tungsten 20° symmetric tilt boundary with hydrogen (W-1atm%H at T=500K). The two panels show the hydrogen atoms only, and their increased concentration at the GB running vertically through each panel is evident. The regular pattern of hydrogen atoms in panel (a) is complementary to the positions of the tungsten atoms. The positions of those atoms and the free volume at the GB is different in the phase of the boundary in panel (b), and the hydrogen atoms are seen to occupy different locations.

Tokamak first-wall applications require materials with high melting temperature, high thermal conductivity, acceptable activation levels upon exposure to radiation, mechanical strength at elevated temperatures, and resistance to surface sputtering. Tungsten possesses these qualities, but it exhibits undesirable recrystallization and embrittlement. Recrystallization involves the nucleation of stress-free grains and the motion of GBs. The GB phase affects the motion of the boundaries. While we have observed hydrogen segregation to GBs, work is ongoing to understand whether the presence of the hydrogen allows further relaxation of the tungsten structure. Previous computational work has studied hydrogen and helium in tungsten GBs for fusion energy [9-15], but the interplay of hydrogen with GB phases has not been addressed previously and there is more to understand with regard to the structure and properties.

Future Work

The next topic to address is the response of hydrogenated tungsten GBs to stresses, i.e., their mobilities. We plan to address both the quantitative effect of the hydrogen on mobility and the mechanisms at play. We will subject the GBs to stress and determine whether the significant differences seen for some pure tungsten GBs continue, strengthen, or diminish when hydrogen is present. The mobilities are provided to improve the parameterization of the recrystallization model being developed by the Marian group at the University of California, Los Angeles. This approach should provide new guidance on tungsten behavior in first-wall applications.

Acknowledgments

This work was performed under the auspices of the United States Department of Energy (US DOE) by Lawrence Livermore National Laboratory (LLNL) under Contract DE-AC52-07NA27344. This material is based upon work supported by the US DOE, Office of Science, Office of Fusion Energy Sciences. Computing resources for this work were provided in part by the LLNL Institutional Computing Grand Challenge program.

References

[1] T. Frolov et al., Nature Commun. 4, 1899 (2013).
[2] T. Meiners, T. Frolov, R. E. Rudd, G. Dehm, and C. H. Liebscher, Nature 579, 375-378 (2020).
[3] Q. Zhu, A. Samanta, B. Li, R. E. Rudd, T. Frolov, Nature Commun. 9, 467 (2018).
[4] T. Frolov et al., Nanoscale 10, 8253 (2018).
[5] T. Frolov, Q. Zhu, T. Oppelstrup, J. Marian, and R. E. Rudd, Acta Mater. 159, 123 (2018).
[6] R. Freitas, R. E. Rudd, M. Asta, and T. Frolov, Phys. Rev. Mater. 2, 093603 (2018).
[7] I. S. Winter, T. Oppelstrup, T. Frolov, and R. E. Rudd, Acta Mater. 237, 118067 (2022).
[8] I. S. Winter, T. Oppelstrup, T. Frolov, and R. E. Rudd, Phys. Rev. Lett. 128, 035701 (2022).
[9] K. Ohsawa et al., Phys. Rev. B 82, 184117 (2010).
[10] W. Xiao and W. T. Geng, J. Nucl. Mater. 430, 132 (2012).
[11] K. D. Hammond, L. Hu, D. Maroudas and B. D. Wirth, EPL 110, 52002 (2015).
[12] N. Fernandez, Y. Ferro and D. Kato, Acta Mater. 94, 307 (2015).
[13] J. Marian et al., Nucl. Fusion 57, 092008 (2017).
[14] A. De Backer et al., Phys. Scr. T170, 014073 (2017).
[15] B. Fu, M. Qiu, J. Cui, J. Wang, and Q. Hou, J. Nucl. Mater. 543, 152599 (2021).

9.2 PREDICTIVE MODELING OF He BUBBLE ACCUMULATION IN NANOSTRUCTURED FERRITIC ALLOYS

—K.C. Pitike, W. Setyawan (Pacific Northwest National Laboratory)

SUMMARY

The overall objective of this work is to develop a predictive model of helium bubble accumulation and distribution in irradiated nanostructured ferritic alloys under relevant fusion environments. As a first step, we have developed an accurate Fe-He machine learning potential ([MLP] version MLP1) based of deep neural network that is intended to study defect binding in He clusters and small He_nV bubbles in pure BCC-Fe. This work was recently published in J. Nucl. Mater. [1]. In this reporting period, we employ MLP1 to calculate the activation energies of trap-mutation (a process in which an over-pressurized He cluster/bubble releases the pressure by creating one or more vacancies [Vs]) in He_nV bubbles and He_n clusters. These activation energies are intended to be used in kinetic Monte Carlo or rate theory simulations to study the growth of He bubbles. In addition, we are extending MLP1 to describe larger bubbles (i.e., He_nV_m bubbles with one or more Vs).

PROGRESS AND STATUS

Modelling trap-mutation in He_n clusters and He_nV bubbles in BCC-Fe with MLP1

Here we report our preliminary work on utilizing the previously developed Fe-He MLP [1] to study the self-trapping of He_n clusters and trap-mutation of He_nV bubbles.

It is well known that He atoms strongly bind with Vs. In our previous work [1], through density functional theory (DFT) calculations, we have shown that a monovacancy at T=0 K, can accommodate up to 16 He atoms. The $He_{17}V$ bubble spontaneously trap-mutates into a $He_{17}V_2$ + SIA complex. We define a critical ratio of the number of He to vacancies (N_{He}/N_V) as the maximum ratio that can be accommodated by the cluster or bubble. Trap-mutation occurs because the pressure inside the bubble exceeds the surface tension plus the critical shear stress of the matrix. As temperature increases, the matrix material softens. Thus, it is expected that the critical ratio would decrease. A question arises: can a bubble trap-mutate when its helium to V ratio is lower than the critical ratio? The developed MLP1 allows us to investigate this question through molecular dynamics simulations. Here, we study the thermal stability of He_nV bubbles. Indeed, we find that bubbles with N_{He}/N_V lower than 16 can trap-mutate at elevated temperatures. In fact, we find that trap-mutation reaction is a thermally activated process [2], with an associated activation energy barrier. We perform thermalization simulations for He_9V and $He_{10}V$ bubbles and record the time (Δt) needed to observe a trap-mutation event for each thermalization temperature. Figure 1 shows the plot of $\log(1/\Delta t)$ as a function of inverse temperature for these bubbles. The activation energy is then calculated using the Arrhenius equation:

$$k_B \log\left(\frac{1}{\Delta t}\right) = -E_a\left(\frac{1}{T}\right) + k_B \log(A)$$

k_B is the Boltzmann constant, Δt is the lifetime of a He_nV bubble before it trap mutates, E_a is the activation energy of the trap mutation reaction, T is the temperature of the system, A is the temperature independent preexponent factor which represents the attempt frequency of the trap-mutation event.

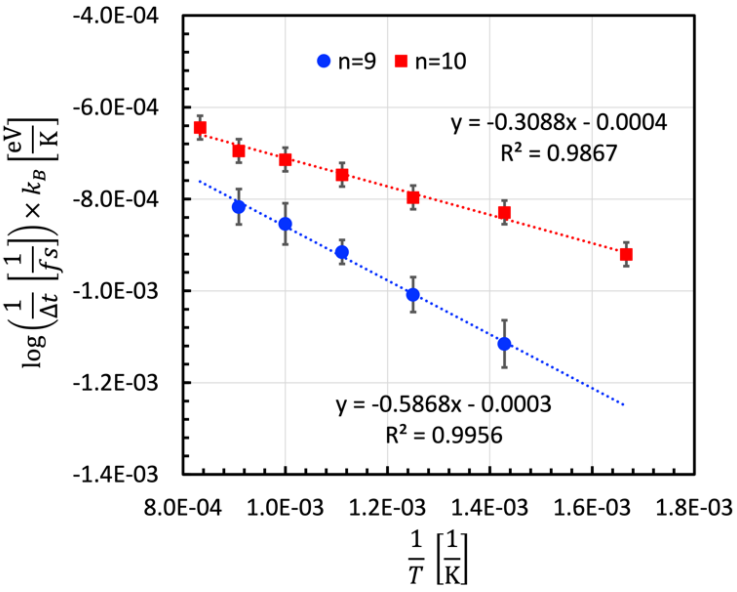

Figure 1. Arrhenius plot for the trap-mutation reactions of He$_n$*V* bubbles. *n*=9, *n*=10 bubbles are plotted in blue circles and red squares, respectively.

Hence, the slope of the lines in Figure 1 is the activation energy of trap mutation reactions for *n*=9 and *n*=10 bubbles. The error bars represent standard deviations, resulting from 10 simulations. We find that for n=9, $E_a = 0.59$ eV, which is greater than the value of $E_a = 0.31$ eV for n=10. Eventually we are planning to calculate the activation energies for all He$_n$ clusters and He$_n$*V* bubbles. Since the MLP is trained using the physically accurate DFT calculations, physical properties estimated employing MLP are expected to have near-DFT accuracy. These activation energies can be used to investigate the He bubble growth in ferritic steels through mesoscale kinetic Monte Carlo or rate theory simulations with high accuracy.

Developing Fe-He MLP to describe thermodynamics of He clusters and all He bubbles

Here we report our work on extending the Fe-He MLP to not only describe the thermodynamics of He$_n$ clusters and small He$_n$*V* bubbles but also for large He$_n$*V*$_m$ bubbles, which may contain more than one V.

Accurate estimation of the binding energies of He or *V* with He$_n$ cluster or He$_n$*V*$_m$ bubble is crucial to advance the fundamental understanding of radiation damage in nano structured ferritic alloys. First-principles based DFT is typically used to calculate the accurate binding energies. However, calculating the accurate binding energies for large He$_n$*V*$_m$ bubbles is prohibitively expensive due to the computational cost of large supercells. Hence, a MLP – trained on DFT data, obtained from relevant configurations – could be used to calculate accurate binding energies at a much smaller cost. In our previous work [1] we have developed a first Fe-He MLP to accurately describe the binding energies of He with He$_n$ clusters and small He$_n$*V* bubbles with only one V. Extending the MLP's ability to accurate estimation of binding energies for large He$_n$*V*$_m$ bubbles can be achieved by further training of the MLP with atomic configurations that represent larger He bubbles. So far, we have sampled the atomic configurations of He$_n$*V*$_2$ bubbles using DFT for the training data. Additional training data will be generated by sampling slab configurations in which the vacuum is filled with different number of He atoms. The slab configurations are intended to mimic He-matrix interaction in large bubbles.

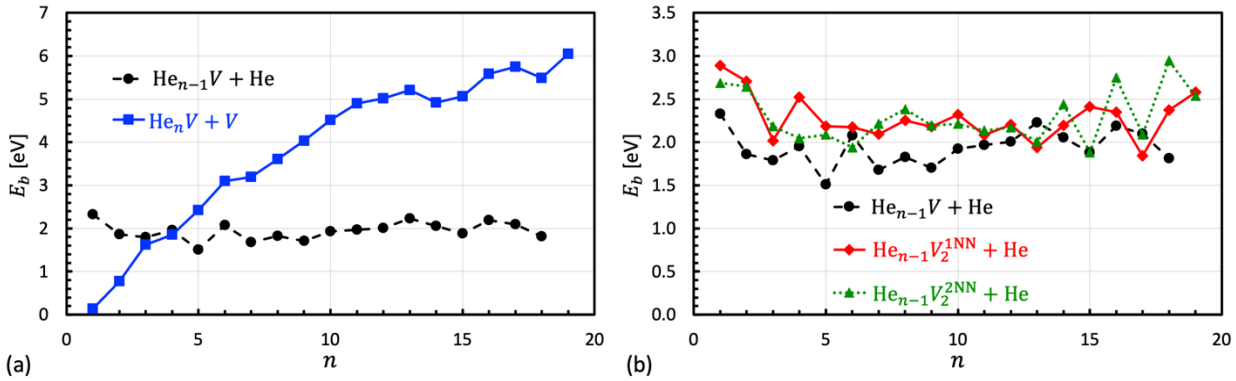

Figure 2. Binding energies of (a) V with He$_n$*V* bubble (b) He with He$_{n-1}$*V*$_2$ bubble where the divacancy takes first (red) and second (green) nearest neighbor.

Figure 2 presents the values of binding energies of (a) V, and (b) He atom with He$_n$*V* and He$_{n-1}$*V*$_2$ bubbles to form a larger He$_n$*V*$_2$ bubble. The binding energies of He with He$_{n-1}$*V* bubble are also plotted in both panels for reference. The defect reactions to form larger bubbles and the equations to calculate their binding energies are:

Defect reactions:

$$\begin{aligned}
\mathrm{He}_nV + V &\rightarrow \mathrm{He}_nV_2 \\
\mathrm{He}_{n-1}V_2^{1\mathrm{NN}} + \mathrm{He} &\rightarrow \mathrm{He}_nV_2^{1\mathrm{NN}} \\
\mathrm{He}_{n-1}V_2^{2\mathrm{NN}} + \mathrm{He} &\rightarrow \mathrm{He}_nV_2^{2\mathrm{NN}} \\
\mathrm{He}_{n-1}V + \mathrm{He} &\rightarrow \mathrm{He}_nV
\end{aligned}$$

Binding energy equations:

$$\begin{aligned}
E_b[\mathrm{He}_nV + V] &= E_{\mathrm{DFT}}[\mathrm{He}_nV] + E_{\mathrm{DFT}}[\mathrm{He}_{\mathrm{tet}}] - E_{\mathrm{DFT}}[\mathrm{He}_nV_2] - E_{\mathrm{DFT}}[\mathrm{Fe}_{\mathrm{pristine}}] \\
E_b[\mathrm{He}_{n-1}V_2^{1\mathrm{NN}} + \mathrm{He}] &= E_{\mathrm{DFT}}[\mathrm{He}_{n-1}V_2^{1\mathrm{NN}}] + E_{\mathrm{DFT}}[\mathrm{He}_{\mathrm{tet}}] - E_{\mathrm{DFT}}[\mathrm{He}_nV_2] - E_{\mathrm{DFT}}[\mathrm{Fe}_{\mathrm{pristine}}] \\
E_b[\mathrm{He}_{n-1}V_2^{2\mathrm{NN}} + \mathrm{He}] &= E_{\mathrm{DFT}}[\mathrm{He}_{n-1}V_2^{2\mathrm{NN}}] + E_{\mathrm{DFT}}[\mathrm{He}_{\mathrm{tet}}] - E_{\mathrm{DFT}}[\mathrm{He}_nV_2] - E_{\mathrm{DFT}}[\mathrm{Fe}_{\mathrm{pristine}}] \\
E_b[\mathrm{He}_{n-1}V + \mathrm{He}] &= E_{\mathrm{DFT}}[\mathrm{He}_{n-1}V] + E_{\mathrm{DFT}}[\mathrm{He}_{\mathrm{tet}}] - E_{\mathrm{DFT}}[\mathrm{He}_nV] - E_{\mathrm{DFT}}[\mathrm{Fe}_{\mathrm{pristine}}]
\end{aligned}$$

$E_b[\mathrm{He}_nV + V]$, $E_b[\mathrm{He}_{n-1}V + \mathrm{He}]$ are the binding energies of a *V* and a He with He$_n$*V* bubble and He$_{n-1}$*V* bubble to form He$_n$*V*$_2$ and He$_n$*V* bubbles, respectively. $E_b[\mathrm{He}_{n-1}V_2^{1\mathrm{NN}} + \mathrm{He}]$, $E_b[\mathrm{He}_{n-1}V_2^{2\mathrm{NN}} + \mathrm{He}]$ are the binding energies of He with $\mathrm{He}_{n-1}V_2$ bubble to form a bigger He$_n$*V*$_2$ bubble. The subscript 1NN and 2NN represent the relative first and second nearest neighboring Vs. $E_{\mathrm{DFT}}[defect]$ represents the DFT total energy of a defect embedded in BCC-Fe matrix. $\mathrm{He}_{\mathrm{tet}}$, $\mathrm{Fe}_{\mathrm{pristine}}$ represents He present at thermodynamically stable tetrahedral interstitial position and ideal BCC-Fe structures, respectively.

We find that the binding energy of a V with a He$_n$*V* bubble increases from 0.13 to 6.05 eV as the number of helium atoms in the bubble increases from *n*=1 to *n*=19. This result is consistent with the qualitative intuition that, as the pressure increases with *n* in He$_n$*V* bubbles, adding an extra V alleviates the bubble pressure thereby making the defect reaction highly exothermic as *n* increases to 19. For He$_n$*V*$_2$ bubble, 1NN and 2NN configurations are thermodynamically stable for *n*=1 to 17, and *n*=0,18,19. The binding energies of He with He$_{n-1}$*V*$_2$ bubble is shown in Figure 2b where the divacancy takes first (red) and second (green) nearest neighbor. The binding energies of He with a bubble containing divacancy is greater than the bubble containing a monovacancy, except for *n*=6,13,17. The configurations sampled for calculating the binding energies will be later used to train the Fe-He MLP. The sampling of configurations for larger bubbles, *n*≥3 is discussed in the following.

The interaction between large bubbles and BCC-Fe matrix can be considered as interaction between He gas and adjacent BCC-Fe surface. Hence, training the MLP with the surface-He interaction configurations will ensure that the MLP will accurately predict the thermodynamics of large He bubbles. So far, we have sampled the surface-He interaction configurations of (100), (110), (320), (210), (211), (311) surfaces. Next, we are planning to sample the high energy surface configurations: (331), (321), (221), (332), (322), (111). We find that the deep neural network has the capability to be accurately trained on both surface and bulk configurations with and without defects. Figure 3 presents the performance of Fe-He MLP, by comparing the DFT predicted (a) energies and (b) forces against the values predicted with MLP. We find that the energies and forces are predicted with a mean absolute error (MAE) of ≤1 meV/atom and 30 meV/Å, respectively.

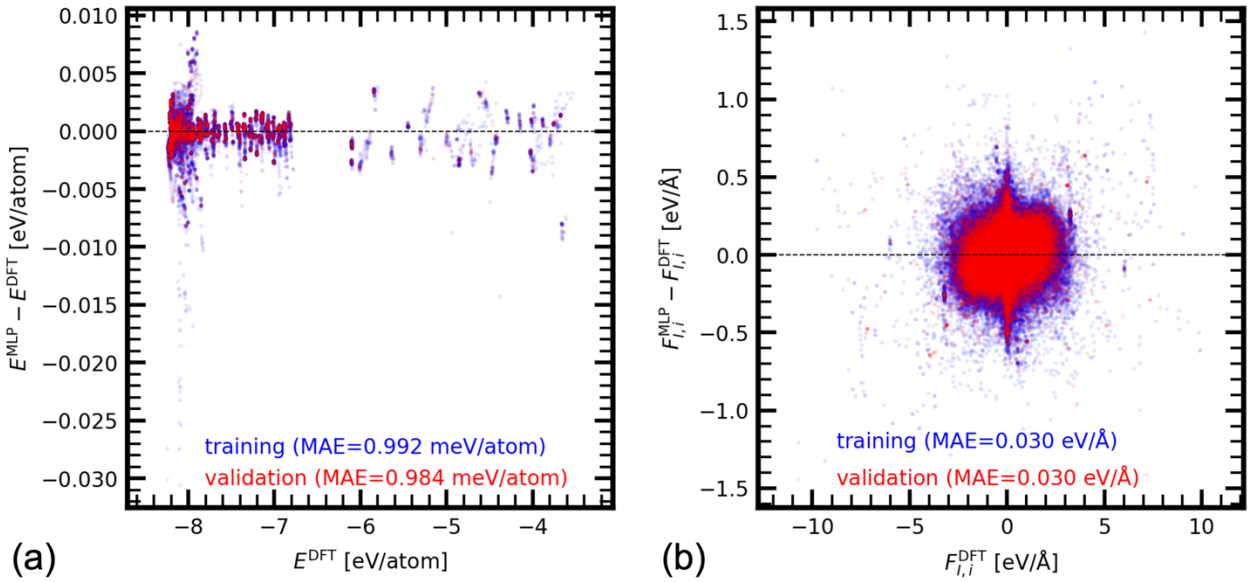

Figure 3. The MLP vs DFT density plots for (a) energies and (b) forces. The training and validation data sets are plotted in blue and red, respectively. The MAE values are also given in the plot legends.

Acknowledgments

This research was supported by the United States Department of Energy (US DOE), Office of Science, Office of Fusion Energy Sciences, through Contract No. AT2030110-13784 and was performed at the Pacific Northwest National Laboratory (PNNL), which is operated by Battelle for the US DOE under Contract No. DE-AC05-76RL0-1830. The research was performed using resources available through Research Computing at PNNL.

References

[1] K. C. Pitike, W. Setyawan, "Accurate Fe–He machine learning potential for studying He effects in BCC-Fe" J. Nucl. Mater. **574** (2023) 154183.

[2] J. Boisse, C. Domain, C.S. Becquart, “Modelling self-trapping and trap mutation in tungsten using DFT and Molecular Dynamics with an empirical potential based on DFT”, J. Nucl. Mater. **455** (2014) 10-15.

9.3 FINITE ELEMENT MODELING OF W/ODS-EUROFER TUNGSTEN COMPOSITES—B.N. Nguyen, W. Setyawan (Pacific Northwest National Laboratory)

This is an extended abstract of two manuscripts that have been submitted to Journal of Composite Materials. The manuscripts are titled "A Predictive Model for Mechanical Properties of Oxide Dispersion Strengthened Alloys - Part I: Constitutive Modeling" and "A Predictive Model for Mechanical Properties of Oxide Dispersion Strengthened Alloys - Part II: Application to Tungsten Brick-and-Mortar Composites."

Strengthening a matrix material in a composite with oxide particles that form coherent or semi-coherent interfaces with the matrix can produce a composite with significantly higher strength and toughness than the unstrengthened material. This research explores the use of oxide particles as strengthening materials for the ductile matrix in ductile-phase toughened tungsten (DPT-W) composites. The DPT-W composites that we consider employ Eurofer and Y_2O_3-Eurofer steels as the ductile phase. Based on experimental tensile data of Eurofer and 0.25wt.%Y_2O_3-Eurofer at 400 and 600°C [1], we derive the constitutive plastic behavior of the oxide/matrix interface. The derivation is based on an incremental Eshelby-Mori-Tanaka Approach (EMTA) combined with an inverse method. Subsequently, the interface constitutive model is used to predict the elastic-plastic behavior of Y_2O_3-Eurofer as a function of oxide volume fraction, as shown in Figure 1. The simulation shows that significant strengthening can be achieved with 0.3wt.% of Y_2O_3, while further increasing the oxide content up to 5wt.% only results in a modest additional strengthening.

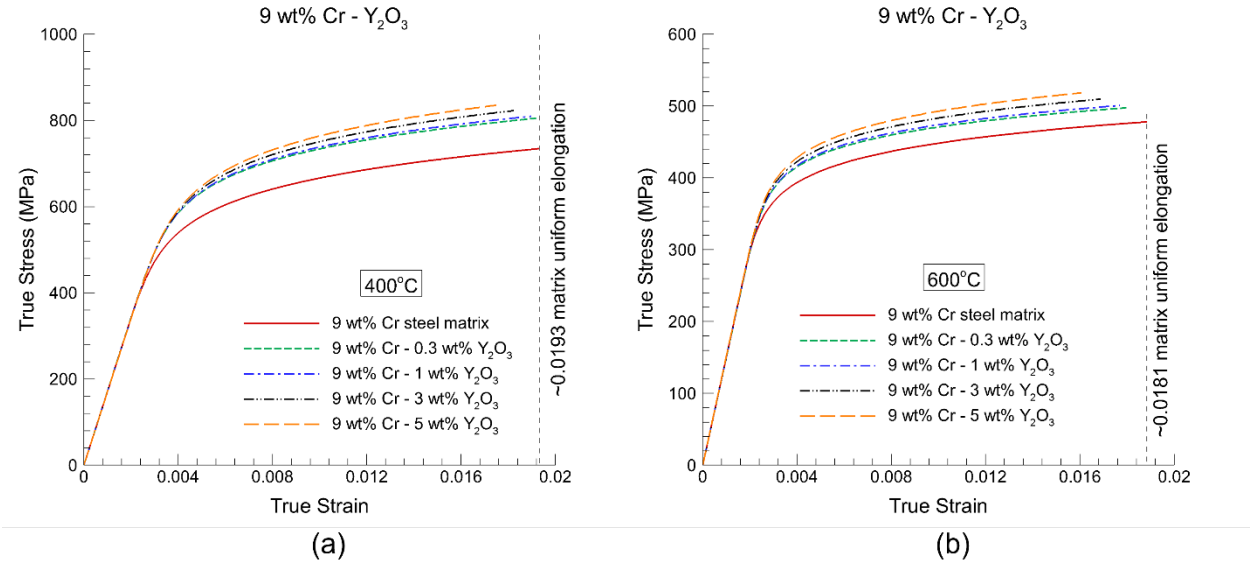

Figure 1. Predicted true stress versus true strain of 0.25wt.%Y_2O_3-Eurofer as a function of Y_2O_3 volume fraction at (a) 400°C and (b) 600°C.

Subsequently, we design DPT-W composites with a brick-and-mortar (BAM) architecture (the schematic is shown in Figure 2a). Different compositions of W-BAM composites are explored using Eurofer steels with various concentration of Y_2O_3 as the ductile phase. The derived constitutive models of the strengthened Eurofer steels are used in finite element simulations to investigate how the strengthened ductile phase improves the overall property of the W-BAM composites. Figure 2b shows the predicted tensile property of the W-BAM composites at 600°C. The results show that increasing the oxide content in the ductile matrix leads to a significant increase in both ductility and strength of the composites. This research suggests that employing oxide strengthening to DPT-W is feasible. Future research will apply a similar approach to strengthening of DPT-W with Ni-based ductile phase (in which the unstrengthened composite shows > 10

times fracture toughness than W at room-temperature). In addition, the oxides can serve as defect sinks for transmutation gases that will be produced by Ni and Fe to minimize their effects.

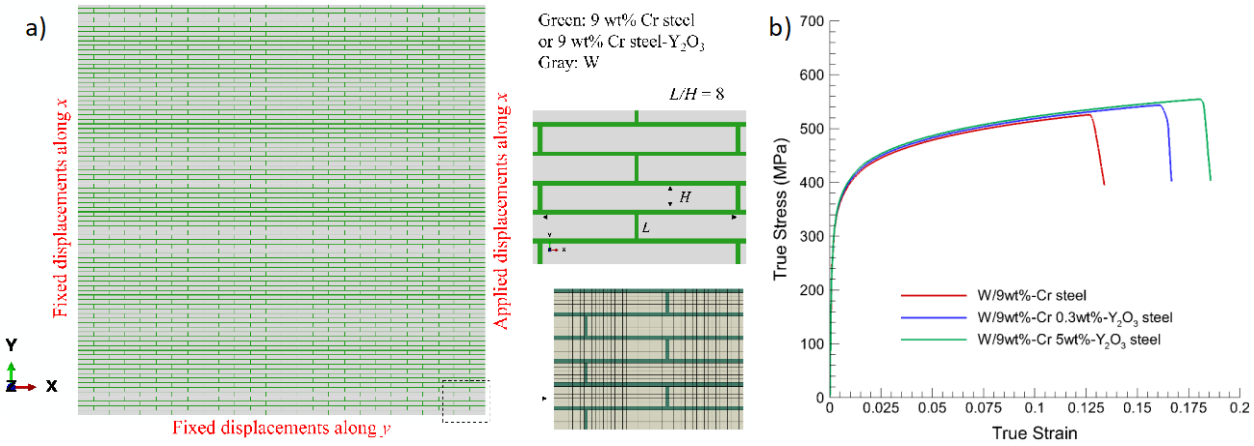

Figure 2. a) Schematic of BAM DPT-W composite architecture, b) predicted true stress versus true strain of DPT-W consisting of fine-grained W embedded in Eurofer, 0.3wt.%Y_2O_3-Eurofer, and 5wt.% Y_2O_3-Eurofer at 600°C.

Acknowledgements

This research was supported by the Office of Fusion Energy Sciences, United States Department of Energy and performed at Pacific Northwest National Laboratory under Contract DE-AC05-76RL01830.

References

[1] F. Siska, et al., Strengthening mechanisms of different oxide particles in 9Cr ODS steel at high temperatures, Mater Sci & Eng A 732 (2018) 112-119.

9.4 EFFECT OF NEUTRON SPECTRUM ON DAMAGE ACCUMULATION IN TUNGSTEN: 14 MEV VS. HIGH FLUX ISOTOPE REACTOR—G. Nandipati, W. Setyawan, K.J. Roche, R.J. Kurtz (Pacific Northwest National Laboratory), B.D. Wirth (University of Tennessee, Knoxville)

This is an extended abstract. The full manuscript will be submitted to a peer-reviewed journal.

Tungsten (W) is the main solid material choice for plasma-facing divertor components in future fusion reactors due to its high melting point, low sputtering coefficient, high thermal conductivity, low probability of transmutation, low tritium retention, and good mechanical strength [1–4]. Currently, there are no prototypic fusion neutron-sources for testing materials under fusion reactor-relevant conditions, especially with the necessary intensity and neutron energy spectrum. Therefore, a variety of neutron irradiation facilities are being used to explore radiation-induced degradation phenomena and microstructure evolution in W. Of these, only DT plasma-based devices provide a prototypic neutron fusion environment. However, such facilities have a much lower neutron flux than other sources based on spallation or fission reactors [5, 6]. Spallation neutron sources (SNS) produce a neutron spectrum with a high-energy tail and can reach damage levels > 10-20 dpa/year [6-9]. However, SNS produces pulsed irradiation and high-energy tail results in the production of He/dpa$_{NRT}$ and H/dpa$_{NRT}$ that are 5-10 times higher than the fusion ratios [7]. On the other hand, although mixed-spectrum reactors and fast reactors can also produce a high flux [6], the He/dpa$_{NRT}$ and H/dpa$_{NRT}$ production is lower compared to DT fusion conditions. Furthermore, different neutron sources will produce different concentrations of solid transmutations. [8–13]. Nevertheless, due to their availability, fission reactors and SNS are used to study neutron-induced damage in candidate fusion first wall and plasma-facing materials. Consequently, it is essential to construct physically based quantitative models of microstructure evolution for use in analyzing and interpreting irradiation experiments performed using alternative irradiation sources [14].

In addition to the initial microstructure of the material, temperature and energy spectrum of the radiation source also affect the accumulation of irradiation damage. For radiation sources, differences in radiation damage accumulation result from differences in the dose rate, transmutation rate, and primary knock-on atom (PKA) energy distribution, also called the PKA spectrum. If we consider the PKA's kinetic energy that is available for inducing a displacement cascade, PKAs with the same damage energy will produce a similar primage damage state, regardless of the neutron source. However, different radiation sources result in different PKA spectra. More importantly, the production of defects and their clustering within a single cascading event, also called in-cascade clustering, varies with PKA energy [15]. Therefore, the difference in the PKA spectrum leads to differences in the production rates of defect clusters of different sizes, leading to differences in damage accumulation. Therefore, understanding the dependence of damage accumulation on in-cascade defect clustering is important.

In our previous study, we explored the influence of confinement of self-interstitial atom (SIA) cluster diffusion by impurities on damage accumulation in W due to neutron irradiation with the 14MeV-PKA spectrum [15]. In the current study, we investigate the influence of PKA spectrum on damage accumulation by comparing damage accumulation in 14 MeV neutrons and High-flux Isotope Reactor (HFIR). We perform the study as a function of dose rate, de-trapping barrier of SIA clusters from impurities, and impurity (or trap) concentration. In the current simulations, the effect of transmutants on damage accumulation is ignored. We perform the simulations using the object kinetic Monte Carlo code KSOME (Kinetic Simulations of Microstructural Evolution) [15, 16]. The simulations are performed at 1025 K as a function of dose rate (≈ $10^{-4} - 10^{-8}$ dpa/s), impurity concentration, and different behaviors of trapping/de-trapping of SIA clusters by impurities. Displacement damage production is simulated by inserting primary cascade defects obtained from molecular dynamics simulations into the simulation domain according to the PKA spectrum of the corresponding neutron source. We find that the variance of vacancy and vacancy cluster densities and average vacancy cluster sizes as a function of dose rate, trap concentration, and de-trapping barrier are similar for both PKA spectra. When SIA clusters are permanently trapped, the densities of the vacancy and vacancy clusters increase with increasing trap concentration and are always higher than when SIA clusters

are allowed to de-trap. When de-trapping is allowed, vacancy density initially increases when the trap concentration is increased from 100 to 150 appm but starts to decrease with a further increase of trap concentration. However, there are key differences in the damage accumulation between the two neutron spectra. The main difference is that the accumulated damage at a given dose is always lower for HFIR. For example, with de-trapping, at a dose and dose rate of 1.0 dpa and 10^{-8} dpa/s and at the highest trap concentration simulated (250 appm), the density of vacancies ($\rho_V^{HIFR} = 0.46 \times 10^{27}/\mathrm{m}^3$) and vacancy clusters ($\rho_{VC}^{HFIR} = 0.38 \times 10^{25}/\mathrm{m}^3$) in HFIR is ≈ 2.1 and 1.4 times lower, respectively, than for the case of 14 MeV neutrons ($\rho_V^{14MeV} = 0.96 \times 10^{27}/\mathrm{m}^3$ and $\rho_{VC}^{14MeV} = 0.78 \times 10^{25}/\mathrm{m}^3$). Note that monovacancies are included in the calculation of vacancy cluster density.

Since impurities can reduce the energy barrier for 1D diffusing SIA clusters to change their Burgers vector direction upon de-trapping, we also investigated the impact of the change in the dimensionality of SIA cluster diffusion on the damage accumulation, which otherwise SIA clusters with sizes 5 and larger would only diffuse 1D. Note, SIA clusters of size 4 or less are always allowed to change their Burgers vector direction after de-trapping; in addition, they can rotate in the absence of impurities after overcoming an energy barrier. When large SIA clusters are allowed to rotate upon de-trapping, they undergo net-3D diffusion; otherwise, they undergo confined 1D diffusion between impurities. Our previous study [17] has shown that for 14 MeV, the damage is lower for the confined 1D diffusion case due to the increased probability of intracascade recombination. The difference between the two cases of SIA diffusion is sensitive to the dose rate and trap concentration. The present study shows that it is also sensitive to the PKA spectrum. In the case of HFIR, the impact of the change in the dimensionality of SIA cluster diffusion on damage accumulation is small.

Acknowledgments

The work described in this article was performed at Pacific Northwest National Laboratory (PNNL). The work was funded by the United States Department of Energy, Office of Fusion Energy Sciences, and Office of Advanced Scientific Computing Research through the SciDAC-4 program on Plasma-Surface Interactions [18] under Contract DE-AC05-76RL01830. The authors would like to thank Larry Greenwood of PNNL for providing the PKA spectra for 14-MeV neutrons and HFIR.

References

[1]. G. Janeschitz, J. Nucl. Mater. 290-293 (2001) 1-11.
[2]. H. Bolt et al., J. Nucl. Mater. 329-333, Part A (2004) 66-73.
[3]. J. Roth et al., Plasma Phys. Control. Fusion 50 (2008) 103001.
[4]. G. Pintsuk, in edited by R. J. M. Konings (2012).
[5]. E. Surrey et al., in 2013 IEEE 25th Symposium on Fusion Engineering (SOFE) (2013), pp. 1–6.
[6]. S. J. Zinkle and A. Möslang, Fusion. Eng. Des. 88 (2013) 472-482.
[7]. J. Knaster, A. Möslang, and T. Muroga, *Nat Phys* 12, 5 (2016), 424–434.
[8]. P. Vladimirov, A. Möslang, *J Nucl Mater* 329, (2004), 233–237.
[9]. H. Trinkaus and H. Ullmaier. *J Nucl Mater* 296, 1–3 (2001), 101–111.
[10]. Applications of Research Reactors Towards Research on Materials for Nuclear Fusion Technology (INTERNATIONAL ATOMIC ENERGY AGENCY, Vienna, 2013).
[11]. M. R. Gilbert, J. Marian, and J. –Ch. Sublet, J. Nucl. Mater. 467 (2015) 121.
[12]. M. E. Swan, Fusion Sci. Technol., 66 (2014) 272-277.
[13]. M. R. Gilbert and J. -Ch. Sublet, Nucl. Fusion 51 (2011) 043005.
[14]. A. Hasegawa et al., Fusion. Eng. Des. 89 (2014) 1568.
[15]. G. Nandipati, W. Setyawan, H. L. Heinisch, K. J. Roche, R. J. Kurtz, B. D. Wirth, *J. Nucl. Mater.* 462 (2015) 338–344; *Semi-annual Progress Report* DOE/ER-0313/54 (June 2013) 179–183.
[16]. G. Nandipati, Kinetic Simulations of Microstructural Evolution [Computer Software] (Version: 1.0) Repo: https://doi.org/10.11578/Dc.20200826.3, Docs: https://relaxednightingale-067fd1.netlify.app (2020).
[17]. G. Nandipati, W. Setyawan, H. L. Heinisch, K. J. Roche, R. J. Kurtz, B. D. Wirth, J. Nucl. Mater 542 (2020) 152402.

[18]. Plasma Surface Interactions: Bridging from the Surface to the Micron Frontier through Leadership Computing (https://tinyurl.com/te88h8q); Plasma Surface Interactions: Predicting the Performance and Impact of Dynamic PFC Surfaces (https://tinyurl.com/ru8mwqt).

10. IRRADIATION & TESTING ANALYSIS, METHODS, EXPERIMENTS, AND SCHEDULES

10.1 HIGH FLUX ISOTOPE REACTOR IRRADIATION EXPERIMENTS—C. On (Oak Ridge National Laboratory)

OBJECTIVE

The goal of this report is to describe the progress of the neutron irradiation experiments that were performed in the High Flux Isotope Reactor (HFIR) and the operating status of HFIR.

SUMMARY

During the six-month period starting from July 1st to December 31st, 2022, a total of thirty-eight rabbit capsules continued their irradiation. There were eighteen new capsules inserted into HFIR, while fourteen capsules were removed. The cycles 499 and 500 were completed during this period, but cycle 500 was split into two (500A and 500B) due to an unexplained increase in power.

PROGRESS AND STATUS

Neutron irradiation experiments were performed in support of the research and development of fusion reactor materials using various materials irradiation facilities in the HFIR. The reactor operating history for the period from July 1-December 31, 2022, is detailed in Table 1.

Table 1. The HFIR operating record for the semi-annual FY2022

Cycle Number	Cycle End Date	Power (MWD)
499	October 23	2163.05
500*	December 16	2062.91

*Cycle was split into two parts, due to an unexplained increase in power. Cycle 500A received 882.80 MWD, while cycle 500B received 1180.11 MWD.

All the fusion materials program irradiation experiments performed during this period (Fiscal Year [FY] 2022) used the nominally two-inch rabbit capsules, with neither full-length target rod nor instrumented reflector position capsules within that period. Thirty-eight target zone rabbit capsules remain in the reactor to complete their scheduled irradiations. Table 2 lists the new capsules that were loaded into HFIR in cycles 499 and 500. On the other hand, Table 3 lists the capsules that were removed from HFIR during cycles 499 or 500. The capsules listed in Table 4 were inserted either during or before FY2022 and will continue in FY2022 and beyond. Tables 2 through 4 give condensed information on the material, specimen type, temperature, fluence, and period of irradiation.

Table 2. New capsules starting irradiation in cycles 499 and 500

Experiment Designation	Primary Materials	Specimen Types	Irradiation Temperature (°C)	Max Exposure (dpa)	Number of Reactor Cycles	HFIR Cycles Start – End
FR03	Joint Tungsten Alloy	Disc (D6)	300	0.4	2	499 - 500
FR31	Joint Tungsten Alloy	Disc (D3)	300	0.2	1	499 - 499
FR51	Joint Tungsten Alloy	Disc (D3)	300	0.6	3	499 - 501
FR52	Joint Tungsten Alloy	Disc (D3)	500	0.6	3	499 - 501
SNF01	FeCrAl	Tensile	400	1.8	1	500A - 500A
SNF02	FeCrAl	Tensile	400	1.8	1	500A - 500A
SNF03	FeCrAl	Tensile	400	1.8	1	500A - 500A
SNF04	FeCrAl	Tensile	400	1.8	1	500A - 500A
SNF05	FeCrAl	Tensile	400	1.8	1	500A - 500A
FH31	F82H-IEA / F82H-mod3	Tensile	300	50	29	500 - 528
FH32	F82H-IEA / F82H-mod3	Tensile	400	50	29	500 - 528
FH33	F82H-IEA / F82H-mod3	Tensile	500	50	29	500 - 528
FH41	F82H-IEA / F82H-mod3	Bend Bar	300	50	35	500 - 534
FH42	F82H-IEA / F82H-mod3	Bend Bar	300	50	35	500 - 534
FH43	F82H-IEA / F82H-mod3	Bend Bar	400	50	29	500 - 528
FH44	F82H-IEA / F82H-mod3	Bend Bar	400	50	29	500 - 528
FH45	F82H-IEA / F82H-mod3	Bend Bar	500	50	29	500 - 528
FH46	F82H-IEA / F82H-mod3	Bend Bar	500	50	29	500 - 528

Table 3. The rabbit capsules removed from HFIR during cycles 499 or 500

Experiment Designation	Primary Materials	Specimen Types	Irradiation Temperature (°C)	Max Exposure (dpa)	Number of Reactor Cycles	HFIR Cycles Start – End
FR02	Joint Tungsten Alloy	Disc (D6)	300	0.4	2	498 - 499
FR14	Joint Tungsten Alloy	Disc (D6)	500	0.6	3	497 - 499
FR31	Joint Tungsten Alloy	Disc (D3)	300	0.2	1	499 - 499
FR41	Joint Tungsten Alloy	Fracture toughness	300	0.6	3	497 - 499
FR42	Joint Tungsten Alloy	Fracture toughness	500	0.6	3	497 - 499
FR43	Joint Tungsten Alloy	Fracture toughness	800	0.6	3	497 - 499
FR03	Joint Tungsten Alloy	Disc (D6)	300	0.4	2	499 - 500
FR11	Joint Tungsten Alloy	Disc (D6)	300	1.2	6	495 - 500
FR53	Joint Tungsten Alloy	Disc (D3)	800	0.6	3	498 - 500
SNF01*	FeCrAl	Tensile	400	1.8	1	500A - 500A
SNF02*	FeCrAl	Tensile	400	1.8	1	500A - 500A
SNF03*	FeCrAl	Tensile	400	1.8	1	500A - 500A
SNF04*	FeCrAl	Tensile	400	1.8	1	500A - 500A
SNF05*	FeCrAl	Tensile	400	1.8	1	500A - 500A

*SNF01-SNF05: These capsules were only irradiated for 10 days instead of one full cycle.

Table 4. The HFIR fusion materials program rabbit capsules to continue irradiation in FY2022

Experiment Designation	Primary Materials	Specimen Types	Irradiation Temperature (°C)	Max Exposure (dpa)	Number of Reactor Cycles	HFIR Cycles Start – End
FH11	F82H-IEA / F82H-mod3	Tensile	300	80	46	496 - 541
FH12	F82H-IEA / F82H-mod3	Tensile	400	80	46	496 - 541
FH13	F82H-IEA / F82H-mod3	Tensile	500	80	46	496 - 541
FH21	F82H-IEA / F82H-mod3	Bend Bar	300	80	55	496 - 550
FH22	F82H-IEA / F82H-mod3	Bend Bar	300	80	55	496 - 550
FH23	F82H-IEA / F82H-mod3	Bend Bar	400	80	55	496 - 550
FH24	F82H-IEA / F82H-mod3	Bend Bar	400	80	55	496 - 550
FH25	F82H-IEA / F82H-mod3	Bend Bar	500	80	48	496 - 543
FH26	F82H-IEA / F82H-mod3	Bend Bar	500	80	48	496 - 543
FH31	F82H-IEA / F82H-mod3	Tensile	300	50	29	500 - 528
FH32	F82H-IEA / F82H-mod3	Tensile	400	50	29	500 - 528
FH33	F82H-IEA / F82H-mod3	Tensile	500	50	29	500 - 528
FH41	F82H-IEA / F82H-mod3	Bend Bar	300	50	35	500 - 534
FH42	F82H-IEA / F82H-mod3	Bend Bar	300	50	35	500 - 534
FH43	F82H-IEA / F82H-mod3	Bend Bar	400	50	29	500 - 528
FH44	F82H-IEA / F82H-mod3	Bend Bar	400	50	29	500 - 528
FH45	F82H-IEA / F82H-mod3	Bend Bar	500	50	29	500 - 528
FH46	F82H-IEA / F82H-mod3	Bend Bar	500	50	29	500 - 528
FMP07	F82H	Tensile	300	20	21	487 - 507
FMP08	F82H	Tensile	300	80	45	487 - 531
FMP11	F82H	Tensile	385	20	21	488 - 508
FMP12	F82H	Tensile	385	80	45	488 - 532
FMP14	F82H	Tensile	525	20	21	484 - 504
FMP17	F82H	Tensile/MPC*	650	80	45	484 - 528
FMP22	F82H	Bend Bar	300	20	21	488 - 508
FMP23	F82H	Bend Bar	300	80	45	488 - 532
FR12	Joint Tungsten Alloy	Disc (D6)	300	1.2	6	497 - 502
FR51	Joint Tungsten Alloy	Disc (D3)	300	0.6	3	499 - 501
FR52	Joint Tungsten Alloy	Disc (D3)	500	0.6	3	499 - 501
JCR11-03	SiC/SiC	Mini Bend Bar	950	200	100	487 - 586
JCR11-05	SiC/SiC	Mini Bend Bar	950	200	115	444 - 568
JCR11-08	SiC/SiC	Mini Bend Bar	950	200	115	444 - 560
JCR11-11	SiC/SiC	Mini Bend Bar	950	100	55	448 - 524
SCF4	SiC/SiC	Miniature Flexure Bar	250	100	90	457 - 547
SCF5	SiC/SiC	Miniature Flexure Bar	250	200	45	457 - 511
SCF8	SiC/SiC	Miniature Flexure Bar	600	100	45	457 - 502
SCF9	SiC/SiC	Miniature Flexure Bar	600	200	90	457 - 548
SCF11	SiC/SiC	Miniature Flexure Bar	950	100	57	458 - 517

*MPC= Multi-Purpose Coupon

10.2 INFUSE – CHARACTERIZATION AND QUALIFICATION OF JK2LB ALLOY FOR ADDITIVE MANUFACTURING OF FUSION COMPONENTS—X. Chen, N. Russell, W. Zhong, Y. Yang, Y. Katoh (Oak Ridge National Laboratory), R. Volberg (Type One Energy)

OBJECTIVE

The application of additive manufacturing (AM) for building fusion components enables substantial savings in cost and time and a wider design envelope compared to conventional fabrication methods. However, additively manufactured materials may exhibit different microstructure features as compared to their counterparts made by conventional manufacturing methods. A critical concern for the AM technique is how the AM material behaves in a fusion environment. A nuclear-rated alloy of interest for AM qualification is JK2LB, a Japanese high manganese austenitic stainless steel designed for fusion components, e.g., International Thermonuclear Experimental Reactor (ITER) central solenoid. The JK2LB has high tensile strength, high ductility, and high resistance to fatigue at cryogenic temperatures. In addition, the material has a low Ni content so that it decays to safe radioactivity levels below the International Atomic Energy Agency (IAEA) clearance limit in a much shorter time compared with conventional austenitic stainless steels containing high Ni content. The project is for qualifying AM JK2LB for fusion applications by performing neutron irradiation in the High Flux Isotope Reactor (HFIR) at Oak Ridge National Laboratory (ORNL) and the following post-irradiation evaluation at the hot cell and the Low Activation Materials Development and Analysis (LAMDA) facilities.

SUMMARY

We adopted two rabbit capsule designs shown in Figures 1 and 2 for the 300°C and 80°C irradiations, respectively. The 300°C GENTEN design has been used in various irradiation campaigns and it relies on gamma heating and gas gap control for controlling the irradiation temperature. The rabbit can accommodate 24 SS-J3 specimens in total. More details for this design can be found in Reference [1]. The 80°C perforated rabbit capsule design is a relatively new design adopted from the irradiation campaign for SHINE Technologies. Since the specimens are in direct contact with the reactor coolant, the irradiation temperature is similar to the average coolant temperature of HFIR at 80°C. The perforated rabbit capsule design allows 30 SS-J3 specimens to be irradiated.

To fully utilize the available irradiation space, we designed the materials irradiation matrix shown in Table 1. Besides the AM JK2LB, we also include the baseline wrought JK2LB for comparing material properties differences due to the AM process. In addition, we will evaluate AM JK2LB with 3.3wt% of Y_2O_3 for additional oxide dispersion strengthening. Lastly, we will include the castable nanostructured alloy (CNA), an advanced reduced activation ferritic-martensitic (RAFM) steel developed at ORNL, for irradiation because limited post-irradiation mechanical properties available for this material.

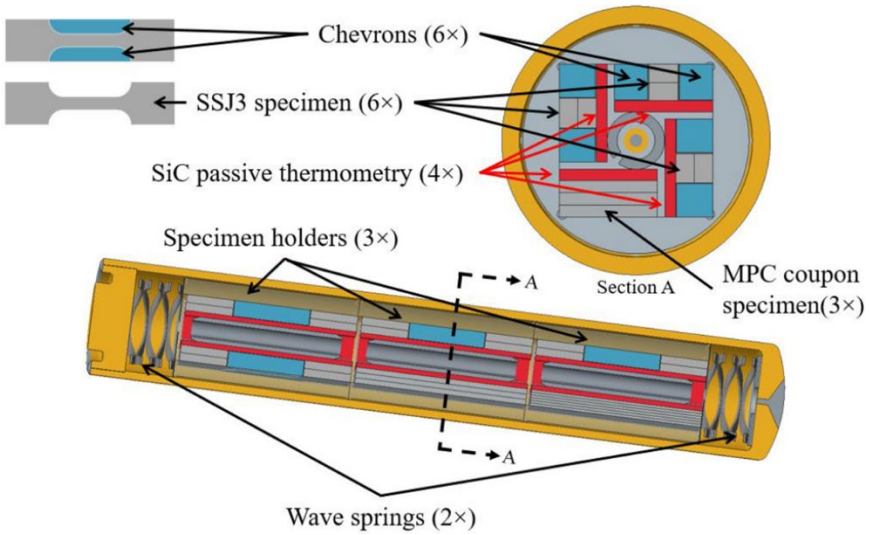

Figure 1. 300°C GENTEN rabbit capsule design [1].

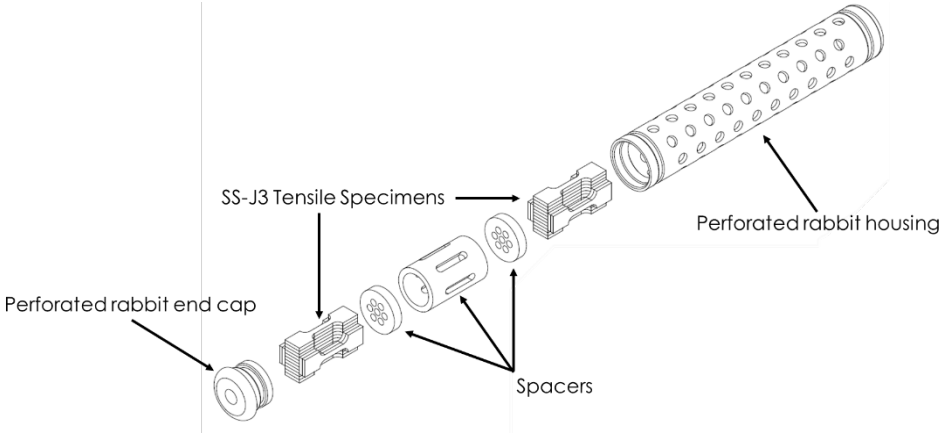

Figure 2. 80°C perforated rabbit capsule design.

Table 1. Materials irradiation matrix

Irradiation temperature (°C)	Number of SS-J3 specimens from different types of materials			
	ORNL CNA	JK2LB	AM-JK2LB	AM-JK2LB-Y_2O_3
80	3	3	11-12	11-12
300	6	2	8	8

In summary, the project aims for neutron irradiation and the following characterization of the mechanical properties and microstructures of AM JK2LB, a Japanese high manganese austenitic stainless steel designed for fusion applications. To date, we have completed the rabbit capsule design and parts ordering for two rabbit capsules for irradiating SS-J3 tensile specimens at 80°C to 5 dpa (displacements per atom) and at 300°C to 5 dpa. Our INFUSE partner, Type One Energy, has finalized the material matrix for irradiation with us and is currently performing additive manufacturing of JK2LB specimens for irradiation and additional characterization.

References

[1] R.H. Howard, K.R. Smith, “Development of a Flexible Design for Irradiation of Miniature Tensile and Charpy Test Specimens in the High Flux Isotope Reactor”, ORNL/TM-2018/872, 2018, doi:10.2172/1460197.

10.3 IRRADIATION OF QST F82H TENSILE AND BEND BAR SPECIMENS IN HIGH FLUX ISOTOPE REACTOR—N. Russell, C. On, X. Chen, W.J. Geringer (Oak Ridge National Laboratory)

OBJECTIVE

The objective of this task is the implementation of the general tensile (GENTEN) and general bend bar (GENBEN) capsule designs for irradiation of Quantum Science and Technology (QST) F82H specimens in High Flux Isotope Reactor (HFIR). There is a total of 21 irradiation capsules within this campaign consisting of three low dose capsules (5 dpa) and 18 high dose capsules (nine 50 dpa and nine 80 dpa). There are three different average specimen irradiation temperatures of 300°C, 400°C, and 500°C for these capsules.

SUMMARY

The temperature performance within an irradiation capsule is controlled by optimizing the specimen holder outer diameter (OD), holder material, and fill gas to create an insulating gas gap between the hot inner holder assembly and the cold capsule housing in direct contact with HFIR coolant. Much care and consideration was taken to apply the existing GENTEN and GENBEN designs. These designs developed a surface response model that allows the user to quickly and accurately determine a combination of holder OD, holder material, and fill gas to achieve an average specimen goal temperature. These two capsule designs can be seen below in Figure 1 and Figure 2.

The QST requested hold points be introduced to our standard irradiation capsule build procedure. These hold points give the Principal Investigators (PIs) an opportunity for input into the design and build. The first hold point was for holder design approval. This allowed the Oak Ridge National Laboratory (ORNL) PI and QST PI to be involved choosing appropriate holder ODs considering the neutron induced swelling. All the first hold point forms for the QST irradiation capsules have been reviewed and signed by the capsule designer, ORNL PI, and QST PI. The second hold point was introduced between assembly of the capsule parts and before welding. This hold point form for the capsules show pictures of every step in the assembly process so that QST could review the process and confirm specimen orientation. This hold form is approved for all capsules.

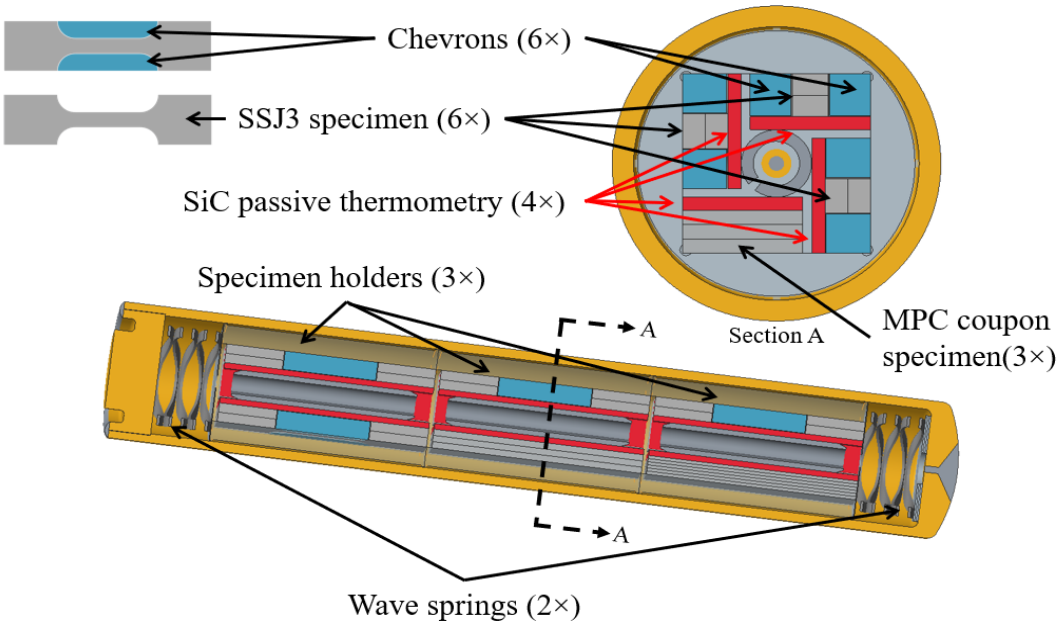

Figure 1. The GENTEN irradiation capsule design.

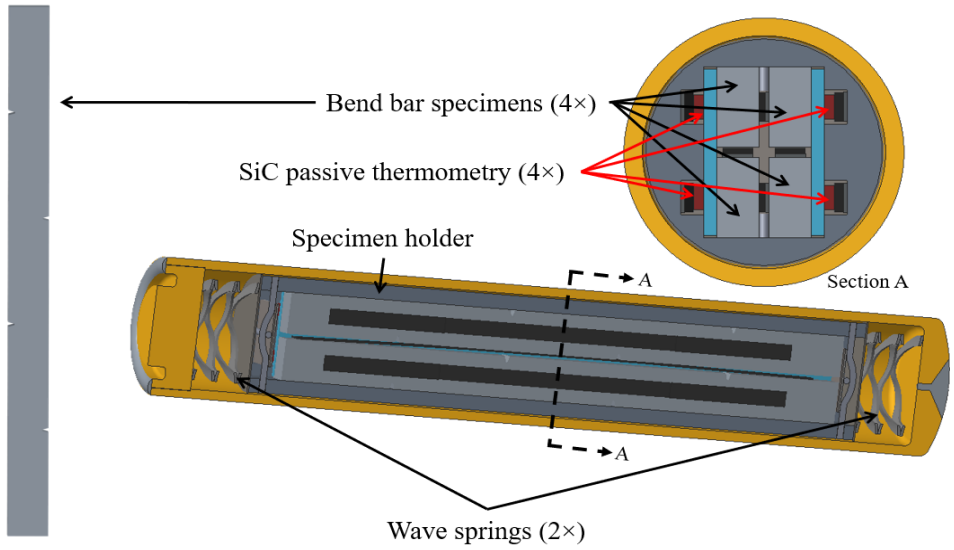

Figure 2. The GENBEN irradiation capsule design.

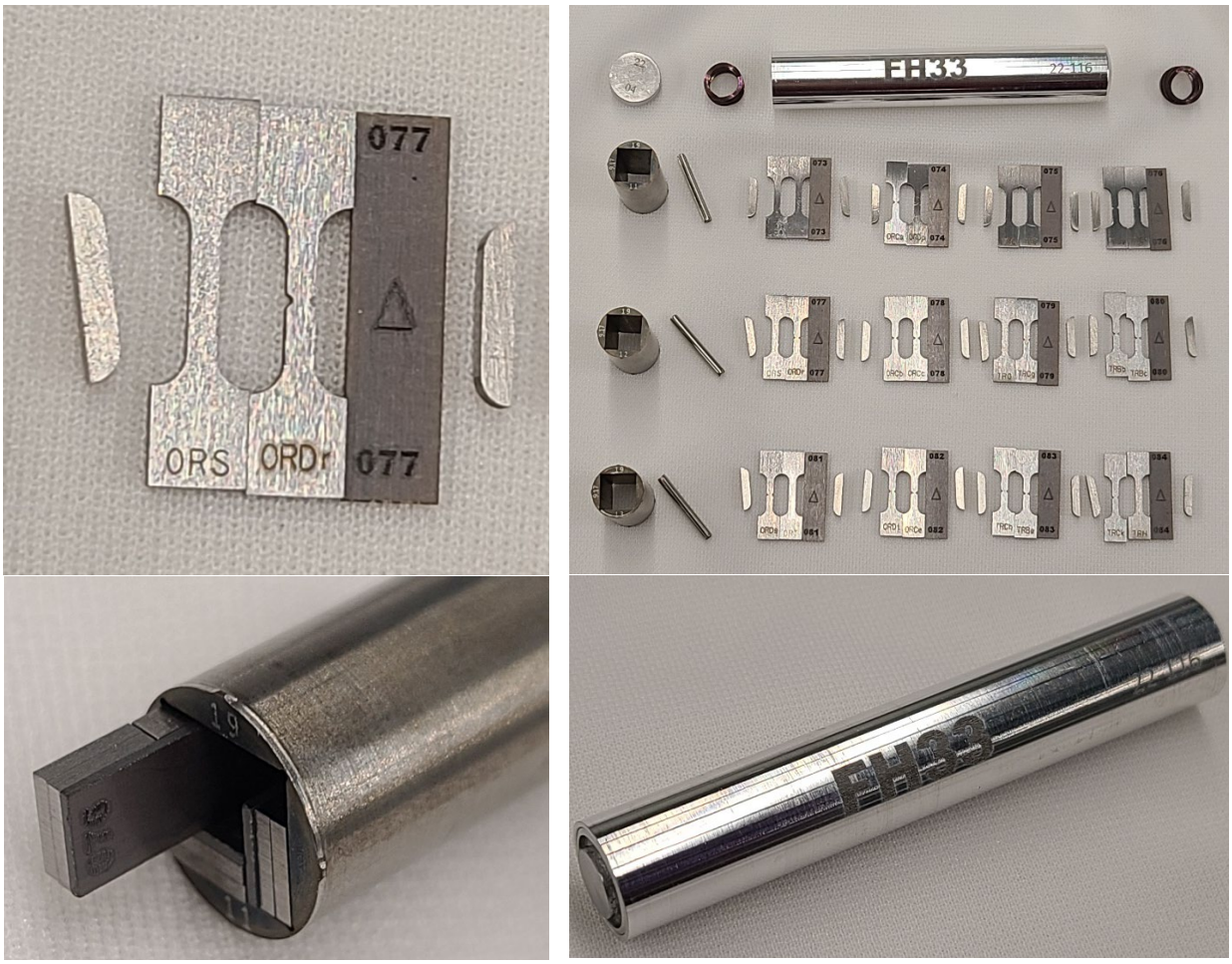

Figure 3. 50 dpa capsule GENTEN example (FH33)

Figure 4. 50 dpa GENBEN example (FH44)

PROGRESS AND STATUS

All the low dose capsules have completed irradiation in HFIR (cycles 490-493). The 80 dpa irradiation capsules began irradiation in HFIR cycle 496 with capsule removal estimated to begin after cycle 541. The 50 dpa irradiation capsules have begun irradiation in HFIR cycle 500A with capsule removal estimated to begin after cycle 528. Some example photos of the 50 dpa GENTEN assembly are shown in Figure 3, with a GENBEN example in Figure 4. All of the hold point forms for the capsules have been approved and are included with the fabrication packages.

10.4 FUSION 2022 FRONTIER TASK 3 IRRADIATION CAPSULE DESIGN—N. Russell (Oak Ridge National Laboratory)

OBJECTIVE

The Fusion 2022 FRONTIER Task 3 irradiation program plans to irradiate five capsules with a design temperature of 400°C. Loading will include FeCrAl tensile specimens and tin (Sn) shot designed to melt and interact with the specimens to test corrosion performance.

SUMMARY

The Fusion 2022 FRONTIER Task 3 irradiation program plans to irradiate FeCrAl tensile specimens submerged in molten Sn to determine corrosion effects during irradiation. The design has a target average specimen temperature of 400°C for one High Flux Isotope Reactor (HFIR) cycle. Images of the design and thermal analysis for the molten Sn corrosion experiment are shown in Figure 1.

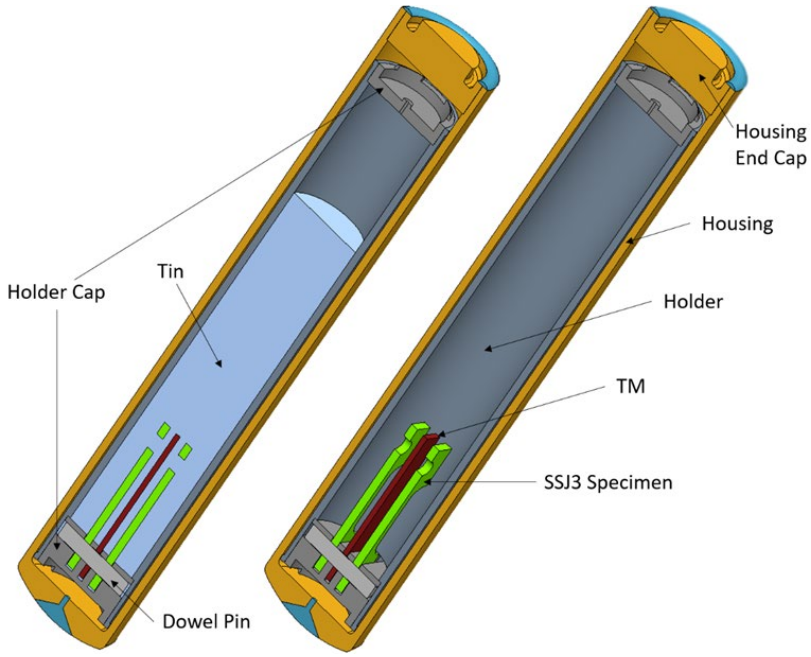

Figure 1. Computer Aided Design (CAD) representation (left) with Sn hidden for ease of viewing and representative thermal analysis (right) of FRONTIER Task 3 molten Sn corrosion irradiation capsules.

PROGRESS AND STATUS

These five rabbit capsules (SNF01-SNF05) completed irradiation in HFIR cycle 500A. Cycle 500A ran from November 8 to November 18, 2022, for a total length of 10.458 days and 882.8 MWD. The rabbit capsules are currently cooling in the HFIR pool before being shipped for disassembly.

A summary of the five rabbit capsule builds is shown in Table 1 with the predicted temperatures in Table 2. From the thermal analysis it is shown that the average melting temperature (Tm) is about 7.4°C hotter than the average specimen gauge region temperature. During post-irradiation examination, this temperature difference can be used to estimate the actual temperatures experienced in the specimen gauge region.

Table 1. Rabbit capsule build summary

Capsule ID	Holder OD (mm)	Housing ID (mm)	Gas gap (μm)	Fill Gas	Specimen Type (Specimen IDs)
SNF01	9.350	9.521	85.5	Helium	Japan ODS (J1, J2)
SNF02	9.355	9.523	84.0	Helium	Japan ODS (J3, J4)
SNF03	9.360	9.527	83.5	Helium	ORNL ODS (O1, O2)
SNF04	9.350	9.522	86.0	Helium	ORNL ODS (O3, O4)
SNF05	9.360	9.525	82.5	Helium	APMT (1, 2)

Table 2. Predicted rabbit capsule temperatures

Capsule ID	Part	Temperature (°C)		
		Avg	Max	Min
SNF01	Specimen	410.1	417.5	387.7
	Specimen Gauge	404.0	410.8	398.1
	TM	411.4	420.9	393.6
SNF02	Specimen	406.3	414.3	383.9
	Specimen Gauge	400.2	407.1	394.3
	TM	407.6	417.1	389.8
SNF03	Specimen	405.2	413.2	382.8
	Specimen Gauge	399.1	405.9	393.2
	TM	406.5	416.0	388.6
SNF04	Specimen	411.5	418.8	389.1
	Specimen Gauge	405.4	412.2	399.5
	TM	412.7	422.2	394.9
SNF05	Specimen	402.5	410.5	380.1
	Specimen Gauge	396.4	403.2	390.5
	TM	403.7	413.3	385.9